ANALYSIS AND DESIGN OPTIMISATION OF GRID-CONNECTED WOUND-ROTOR SYNCHRONOUS AND INDUCTION MOTORS

A PARAMETER AND PERFORMANCE STUDY OF CYLINDRICAL WOUND-ROTOR SYNCHRONOUS AND INDUCTION MOTORS

by

Mkhululi Mabhula

Dissertation presented for the degree of
Doctorate in Engineering in the
Faculty of Engineering at
Stellenbosch University

Department of Electrical Engineering,
Stellenbosch University,
Private Bag X1, Matieland, South Africa

Supervisor: Prof. Maarten J. Kamper

December 2019

Declaration

The work presented in this dissertation was carried out in the Department of Electrical and Electronic Engineering, University of Stellenbosch, South Africa, during the period January 2016 to December 2019 under the supervision of Prof. M.J. Kamper.

By submitting this dissertation electronically, the author declare that the entirety of the work contained therein is of own, original work, that he the sole author thereof (save to the extent explicitly otherwise stated), that reproduction and publication thereof by Stellenbosch University will not infringe any third party rights and that he have not previously in its entirety or in part submitted it for obtaining any qualification.

Date: ..... December 2019 .....

Synopsis

This dissertation is submitted to the Department of Electrical and Electronic Engineering, University of Stellenbosch, South Africa, as partial fulfilment of the requirements for the degree of Doctor of Philosophy (PhD) in Electrical Engineering. The research was carried out during a 4-year period of combined Masters and PhD as outlined in this dissertation.

Analysis and Design Optimisation of Grid-Connected Synchronous and Induction Wound-Rotor Motors

M. Mabhula
December 2019

Overall summary

The dissertation presents new approaches in the analysis, design and optimisation of three-phase cylindrical wound-rotor synchronous (WRSM) and induction (WRIM) motor types. The new approaches are based on the analysis of the steady-state finite element method (FEM) in which the parameters and performances of the motor types are predicted.

Absolute optimum designed WRSM and WRIM motor types can at best be obtained by the use of improved parameters and performance calculation methods in the design optimisation process. This dissertation proposes simple, fast and accurate parameter and performance calculation modern approaches for grid-connected WRSM and WRIM motor types using two-axes electromagnetic models. The modern approaches are based on non-classical models in which iterative processes are utilised using static FEM in conjunction with the motor types phasor diagrams. During the iterative processes, the electric circuit and magnetic field equations are coupled to access important parameters of the motor types. The access of parameters using iterative processes solves the excitation currents at different operating points of the motor. The parameters are accurately calculated using a FEM based method of freezing the motor core permeance. The dissertation investigates and expands the use of these parameters as an effective and powerful tool for explaining the motor behaviour under different operating points. A great deal of attention is also given to the design optimisation of the motor types during which a relatively efficient optimisation procedure is shown. In this study, the proposed model approaches are verified by employing a commercial FEM ANSYS-Maxwell and experimental tests in the laboratory. The study also gives the model approach and the design optimisation procedure of a 6 MW slip-ring motor used for milling purposes. In the analysis of this, the skin effects are perfectly fitted in the proposed model approaches.

The study presents a successful application of the proposed model approaches to the parameters and performance prediction and the design optimisation of the grid-connected WRSM and WRIM motor types. The proposed model approaches demonstrate accuracy, simplicity and fastness which are some of the key aspects in the electrical machine design.

Index terms

Cross-coupling, cylindrical wound-rotor, flux linkages, finite element method, frozen permeability method, grid-connected, induction motor, two-axes electromagnetic modelling, synchronous motor.

Sinopsis

Hierdie proefskrif word by die Departement Elektriese en Elektriese Ingenieurswese, Universiteit van Stellenbosch, Suid-Afrika ingedien as gedeeltelike vervulling van die vereistes vir die graad Doktor in die Filosofie (PhD) in Elektriese Ingenieurswese. Die navorsing is uitgevoer gedurende 'n periode van vier jaar van gekombineerde meesters en PhD word in hierdie proefskrif uiteengesit.

Analise en Ontwerp Optimering van Netwerk-Gekoppelde Bewikkelde-Rotor Sinchroon- en Induksiemotors

M. Mabhula
Desember 2019

Algehele opsomming

Die verhandeling stel nuwe benaderings vir die analise, ontwerp en optimering van drie-fase bewikkelde-rotor sinchroonmotor (WRSM) en induksiemotor (WRIM) tipes voor. Die nuwe benaderings is gebaseer op die analise van die bestendige toestand eindige element metodes (EEM) waarmee die vermoë van die motor tipes voorspel word.

Die optimum ontwerpte WRSM en WRIM motors kan verkry word deur die gebruik van verbeterde parameter en vermoë berekeningmetodes in die ontwerp optimeringsproses. Hierdie verhandeling stel 'n eenvoudige, vinnige en akkurate parameter en vermoë berekening vir netwerk-gekoppelde WRSM en WRIM voor deur gebruik te maak van twee-as elektromagnetiese modelle. Die moderne benaderings is gebaseer op nie-klassieke modelle waarin iteratiewe EEM in samewerking met die motor fasor diagramme gebruik word. Tydens die iteratiewe proses, word die elektriese stroombaan en magnetiese veld vergelykings gekoppel om belangrike motor parameters te kry. Die magnetiese veld vergelykings los die opweksstrome op by verskillende werkspunte van die motor. Die parameters word akkuraat bereken deur die gebruik van EEM gebaseer op die metode van die vries van die motor kern permeansies. Hierdie parameters word as 'n effektiewe hulpmiddel gebruik om die motorgedrag by verskillende werkspunte te verduidelik. Aandag word gegee aan die motorontwerp optimering, waartydens 'n effektiewe optimeringsproses gewys word. In die studie word die voorgestelde benaderingsmodelle deur 'n kommersiële EEM pakket (ANSYS-Maxwell) en toetse in die laboratorium geverifieer. 'n Benaderingsmodel en die ontwerp optimering van 'n 6 MW sleep-ring motor vir wals toepassings word ook gegee, waar die benaderingsmodel aangepas word om huid effekte in ag te neem.

Die studie wys ‘n suksesvolle toepassing van die voorgestelde benaderingsmodel vir parameter en vermoë voorspelling en ontwerp optimering van netwerk-gekoppelde WRSM en WRIM motor tipes. Die voorgestelde benaderingsmodel is akkuraat, vinnig en eenvoudig, wat van die sleutelaspekte in elektriese masjien ontwerp is.

Indeksterme

Dwars-koppeling, silindriese bewikkelde rotor, vloedkoppelings, eindige elementmetode, vries permiabiliteitsmetode, netwerk gekoppel, induksiemotor, twee-as elektromagnetiese modellering, sinchroonmotor

Acknowledgements

I would like to express my sincere appreciation to:

- Lord Jesus Christ, for things unseen and seen he have done during my study.
- my supervisor Professor M.J. Kamper for his inspiration guidance and encouragement through out the development of this dissertation;
- European Horizon 2020 and Department of Electrical Engineering for providing financial assistance;
- the technical personnel of the Department of Electrical Engineering, Mr. P.H. Petzer and Mr. K.J. Cloete for their help with technical support during the building of the prototype motors;
- colleagues at the Electrical Machine Laboratory for their support and help; and
- my family, this work is nothing but a result of their love and encouragement.

Dedications

**********To my father, Kiva Link and my mother, Nomsa**********

Quotes

'He gives power to the weak and strength to the powerless.'

**********Isaiah 40 : 29**********

Table of contents

List of figures

List of tables

Nomenclature

Acronyms

ac	alternating current
AMFEM	ANSYS-Maxwell FEM
CRIM	cage-rotor IM
CPU	central processing unit
dc	direct current
dol	direct-on-line
$dq0$	direct, quadrature, zero
emf	electromotive force
FE	finite element
FEA	finite element analysis
FEM	finite element method
GB	gigabyte
IHFEM	in-house FEM
IM	induction motor
mmf	magnetomotive force
NSS-CS	non-simultaneous-stator controlled switching
PM	permanent magnet
RAM	random access memory
RHR	right hand rule
RSM	reluctance SM
SEMFEM	Stellenbosch University Electrical Machine Finite Element Modelling
SM	synchronous motor
SS-CS	simultaneous-stator controlled switching
SR-CS	simultaneous-rotor controlled switching
Op-Al	optimisation algorithm
WRIM	wound-rotor IM
WRSM	wound-rotor SM
2D	two-dimensional
3D	three-dimensional

Latin

e.g.	for example
et al	and others
i.e.	that is

Symbol Conventions

X	magnitude or scalar
$\vec{X}$	phasor or vector

List of symbols

ω_s	stator waveform angular speed	(rad/s)
ω_r	rotor waveform angular speed	(rad/s)
ω_Δ	rotor waveform slip angular speed	(rad/s)
λ, Λ	flux linkage	(Wb-T)
$\vec{B}$	magnetic flux density	(Wb/m^2)
$\vec{A}$	vector potential	(Vs/m)
f_s	stator waveform frequency	(Hz)
f_g	grid waveform frequency	(Hz)
f_r	rotor waveform frequency	(Hz)
f_Δ	rotor waveform slip frequency	(Hz)
R_m	main-winding resistance	(Ω)
R_e	end-winding resistance	(Ω)
L_e	end-winding inductance	(H)
$\varnothing$	diameter	(mm)
ϕ	angle	(°)

Variables with units

D_s	stator outer diameter	(mm)
d_s	stator inner diameter	(mm)
D_r, D_f	rotor, field outer diameter	(mm)
d_r, d_f	rotor, field inner diameter	(mm)
g_a	air-gap length	(mm)
l	stack length	(mm)
l_m	main-conductor length	(mm)
l_e	end-conductor length	(mm)
P_o	output power	(W)
P_i	input power	(W)
P_l	total losses	(W)
P_{scl}	stator copper losses	(W)
P_{rcl}	rotor copper losses	(W)
P_{fcl}	field copper losses	(W)
P_c	core losses	(W)
P_b	bearing losses	(W)
P_w	windage losses	(W)

P_{bw}	bearing and windage losses	(W)

International system of units

A	ampere
°	degree
H	henry
Hz	hetz
g	gram
Nm	newton-metre
m	metre
s	second
W	watt
r/min	revolutions per minute
T	tesla
Wb	weber
Ω	ohm
℃	degree Celsius
%	percent

International system of units prefix

c	centi	10^{-2}
k	kilo	10^{3}
m	milli	10^{-3}
M	mega	10^{6}
μ	micro	10^{-6}

Indices

d	direct-axis variable
q	quadrature-axis variable
s	stator variable
r, f	rotor, field variable

Chapter 1

Motor technology overview and research motivation

This study is devoted to the analysis, design and optimisation of grid-connected three-phase cylindrical wound-rotor synchronous and induction motor types. Specific novel aspects for the motor types are addressed in a large number of informative and detailed literature provided by various citations at the leading edge of this field, both in this study work and application in the field. This chapter, however, sets out the motivation of the subject work including the background information.

1.1. Introduction

It is illuminating that, up-to-date conventional three-phase large grid-connected wound-rotor synchronous (WRSM) and induction (WRIM) motor types are still used in a wide range of industries. However, not restricted to power and energy, mining, oil and gas, cement production, water and waste-water, and for applications such as pumps, fans, compressors, grinding mills and more [2, 3]. The development and application of these motor types need a good grasp of complex mathematical formulation and operation. Moreover, the design process of the motor types requires simple and fast but accurate model approaches which are suited for optimisation processes.

This study focuses on the development of the simple, fast and accurate aspects of the model approaches for the analysis, design and optimisation of the grid-connected WRSM and WRIM motor types. The two-axes electromagnetic motor model (direct d and quadrature q axes) is adapted in the formulation of the model approaches proposed in this study. The proposed model approaches are used in the parameter and performance prediction of the motor types. With the work, the study also provides validation of the proposed model approaches based on the three mentioned aspects. The validation is done by:

- building ANSYS-Maxwell finite element method (AMFEM) commercial package models; and
- prototyping and testing;

the two motor types. In both cases, fulfilling simplicity, time efficiency and accuracy in the proposed model approaches is illustrated.

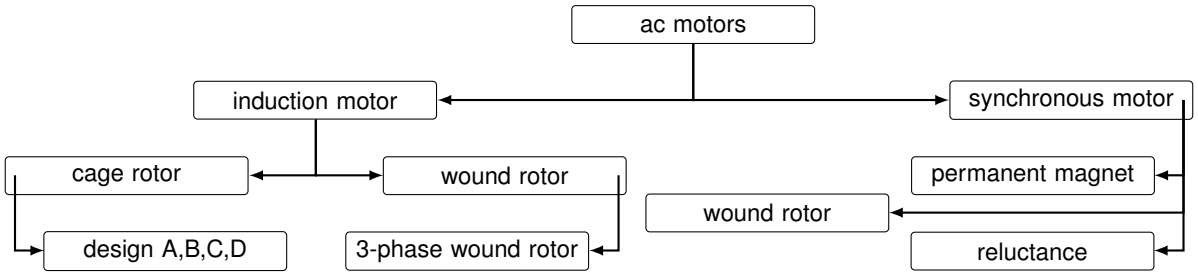

Figure 1.1: Alternating current electric motor class.

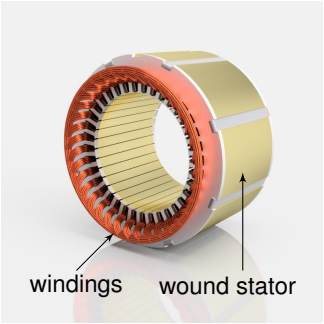

Figure 1.2: Identical synchronous and induction motor stator.

1.2. Electric motor background information

The electrical motor system of the subject work consists of the electromagnetic devices that convert electrical energy to mechanical energy. They are the interface between the electrical and mechanical frameworks of facilities. Even though various motor types exist, it is just the concise view of the outstanding motors relevant to this study work which are given hereafter.

Electrical motors are extensively classified into ac and dc motors, with the former the most common type in grid-connected operations. Figure 1.1 shows only the three-phase subdivisions within the ac motor class excluding linear motors.

Both IM and SM ac motors have identical three-phase stator, a typical one shown in Fig. 1.2. These motor types are further standardised according to their electrical characteristics.

1.2.1. Three-phase IM principle of operation

Three-phase IMs have been the workhorse of industry since their creation in 1888 by Mikhail Dolivo Pobrovolsky following the work of Galileo Ferraris in 1885 and Nikola Tesla in 1887 [62]. In industry, IMs account for about ninety percent of electrical motors, of which the majority are grid-connected [62]. The major drawback in IMs is not as good operating efficiency and power factor. To mitigate this, IMs are frequently fed through the variable frequency drives (VFDs) [15].

The working principle of the IM is that when the three-phase supply is given to the stator, due to interaction of the flux produced by the three-phase currents flowing through the stator, a rotating magnetic field which runs at synchronous speed is produced. This field is cut by the rotor conductors and an electro-magnetic force is induced in the rotor bars (for cage-rotor) or windings (for wound-rotor). Since the rotor circuit is closed, current flows through the bars or windings. The interaction between the stator produced field and the rotor induced currents produce torque. At standstill, the

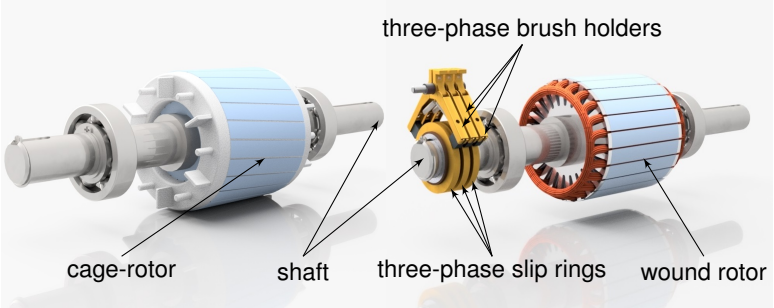

Figure 1.3: Induction motor cage (left) and wound rotors (right).

stator and rotor rotating fields have the same speed (synchronous) and the angle between these two fields is time-independent. Consequently, at standstill, the torque is not zero and the IM can start itself. The rotor can accelerate until the magnitude of the induced rotor current and the torque balances the applied mechanical load on the rotating rotor. Since rotating at synchronous speed would result in no induced rotor currents, IMs always operate slightly slower than synchronous speed. The difference in speed (slip) occurs when the motor begins to deliver torque to the load. The National Electrical Manufacturers Association (NEMA) offers design standard types A, B, C and D, shown in Fig. 1.1 designed to operate between $0.5 - 5\%$ slip.

As noted in Fig. 1.1, three-phase IMs are divided according to the rotor types, shown in Fig. 1.3 namely cage-rotor CR and wound-rotor WR IMs. The CRIM is so named because of the shape of the bar structure. The WRIM is named because of the presence of the coils of wire which turn the rotor windings. Cage rotors are most common in small to medium power level applications because they are simple to construct, robust and relatively inexpensive. Wound rotors are common in large power level applications because they offer control of the motor performance characteristics. Thus, wound rotors are often used for torque acceleration and adjustable speed application for large power levels.

1.2.2. Three-phase SM principle of operation

Three-phase SMs have become essential in industry over recent decades since motor technology was first developed by Friedrich August Haselwander in 1887 [9]. As with the IM working principle, the effect of the stator current is to set up a magnetic field rotating at synchronous speed. However, on account of the SM, the dc or permanent magnets (PMs) on the rotor will also produce a magnetic field rotating at the rotor speed. When the rotor speed is equal to that of the stator field, there is no load torque and the two magnetic fields tend to align with each other.

If a mechanical load is applied, the rotor retards with respect to stator rotating magnetic field, developing torque and continuing to be drawn by the rotating field. As the torque load increases, the angle between the stator and rotor fields increases until the rotor field lags the stator field by $\frac{\pi}{2}$ radians. At the instant of maximum accessible torque, application of more load torque stalls the motor. In general, non self-starting is the major drawback of the SMs since the torque is only produced at synchronous speed. The latter is because at the starting instant, the angle between the stator and the rotor fields is time-dependent and the torque is zero, i.e. the stator fields rotate at synchronous speed and the rotor field is constant [127].

Three-phase SMs are also categorised into three types according to how the rotor is magnetised namely: non-excited, PM-excited, and copper-excited. In non-excited (reluctance rotor) and PM-excited (PM rotor) SMs, the rotor is made of high-relatively steel, manufactured in the reluctance and PM designs. The copper-excited SMs such as salient-pole and synchronous-induction SMs require

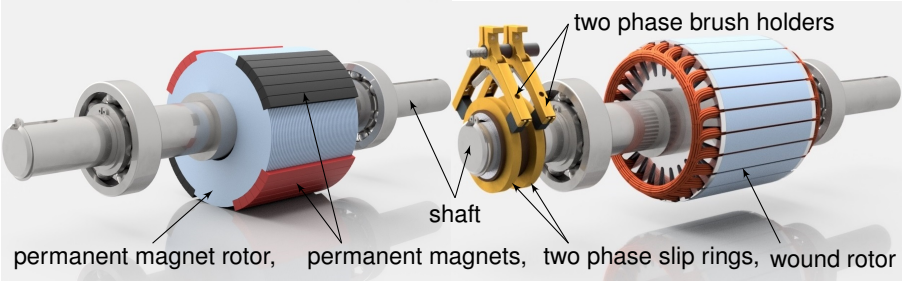

Figure 1.4: Synchronous motor permanent magnet: PM-excited (left) and wound: copper-excited (right) rotors.

dc supply for excitation through the slip rings [118]. With advancements in the SM topologies, the brushless WR doubly-fed electric motor forms the fourth type of SM.

Figure 1.4 shows the two typically selected types of PM-excited and wound copper-excited SMs. The PM-excited SMs are considered ideal SMs with their high torque density, almost unity power factor and high efficiency due to the absence of rotor copper excitation [21, 105, 129]. However, in recent research attention is drawn towards PM-free solutions. This is because of the high cost of PM materials and problems with the supply chain since most of the PM material comes from China [55, 56]. Thus the reluctance synchronous motor (RSM) is a good candidate, however, for VFD application [66]. The rotor of the RSM is made solely of iron and thus the efficiency of the motor is high when compared with the IM as there are no rotor copper losses [105]. In general, the disadvantage of the RSM is the low power factor but this can be moderated by proper design and assisting PMs [7, 21, 28, 129, 133]. A well-designed PM assisted RSM lowers the cost as fewer PM materials are used.

1.3. Grid-connected motor types

In general, the use of the variable frequency drives (VFDs) comes with a cost depending on the power level of the system and is the likely source of flaws. Decreased plant complexity usually translates into improved reliability and reduced costs due to large power VFDs and thus, large grid-connected motors remain largely when looking to reduce cost.

Even though the latest studies are interested in grid-connected RSM and PMSM motor types more applicable for small-medium power levels, these motor types can also be the promising future technology for large power application [25, 72]. For the grid-connected RSM, the rotor is armed with a short-circuited winding that gives the induction torque to accelerate the motor towards synchronous speed [22, 64, 123]. At steady-state the grid-connected RSM zero rotor currents flow permits an increase in efficiency compared to the IM. The main disadvantage of the grid-connected RSM is its low power factor, which can be moderated by a proper design and assisting PMs [21, 129, 133]. The grid-connected PMSM is considered as the classic SM with high torque density, nearly unity power factor and high efficiency due to the absence of rotor excitation currents [98]. For the grid-connected PMSM, the same technique as in the case of the grid-connected RSM is utilised for induction torque [13, 73, 80]. Under operation, if the PM flux is high enough to provide improved power factor, the stator copper losses can also be reduced [98]. The major drawbacks of the PMSM are the cost which comes with the PM material and problems with the supply chain [55, 56].

For large grid-connected motor types, it is evident that the traditional CRIM and WRIM are the most dominant. The CRIM's rotor construction is expensive and the motor has a problem with starting and this is why most industries rely on the WRIM. Large WRIM have low cost rotor construction and a

highly improved winding factor which gives a competitive performance over the CRIM [29,63,92,109].

In the analysis of the large grid-connected motor application, induction and synchronous operation of the motor bring complexity in the motor design, whether to sacrifice the starting for the synchronous running performance or vice versa [32, 53]. The wound-rotor synchronous-induction motor (WRSIM) type design has been used for grid-connected applications. The WRSIM likewise gives a competitive performance in the present era of large grid-connected cage-rotor and salient pole motor designs [48]. The WRSIM is designed to combine the superior starting of WRIMs with the desirable running characteristics of the WRSM motor type [102]. For the grid-connected WRSIM, the same rotor windings for induction and synchronous operation are used. The major advantage of the WRSIM is the accessibility of the rotor windings, which offer simple starting systems and better starting characteristics [15, 78]. Furthermore, when synchronised with the grid, the motor can operate at unity power factor which continuously minimises losses and heat in the stator winding. In large grid-connected applications, WRSIM can also be operated at leading power factor as a successful method for improving the overall power factor of the electrical load in the industrial plant to avoid power rates that may somehow be charged for low power factor loads.

As stated in Section 1.1, the complexity in the design of the grid-connected motor type is due to a lack of sufficient grasp of the already existing compound mathematical formulations. Hence, a separate analysis, design and optimisation is proposed in this study for the induction and synchronous operation of the grid-connected WRIM and WRSM motor types respectively, to give a good and clear understanding of both motor types.

1.4. Objectives and main contribution of the work

The general objective of this study is to analyse, design by optimisation, prototype and test grid-connected WRSM and WRIM motor types. The specific objective is to construct simple, fast and accurate model structures on which design optimisations can be carried out for both grid-connected small to large power level motor types. This has to be validated using the ANSYS-Maxwell commercial model package and practical test results only at a small power level.

Even though the work is divided into two motor type technologies, the research is dedicated to the development of grid-connected WRSIM as a promising electric motor type with room for improvement in both starting and steady-state operation. The main barriers in the motor design are the availability of robust but accurate and simple modelling methods in the calculation of the motor when operating as an IM and SM essentially under saturation. The contribution to design optimisation procedure is the use of the steady-state electric motor two-axes analysis in all operating conditions of both motor types, to meet the optimum design specifications. The modelling methods are also demonstrated at high power levels on the design optimisation using optimisation algorithms. Despite the traditional motor topologies being used in this study, the proposed modern design approaches give a clear and good understanding of obtaining a high efficiency, power factor and torque density in these motor types.

1.5. Outline of the document

The first chapter of this document sets forth the motivation of the subject work including background information on the application of grid-connected electric motor types. The electric motor system is

discussed and the wound-rotor motor type is proposed. The research objectives and significance are also given in this chapter.

Chapter 2 gives the WRSM and WRIM motor type models already available in the literature. Chapter 3 covers the proposed model approaches utilising the models of Chapter 2. In Chapter 4, the steady-state finite element based model approaches are demonstrated and conclusions are drawn in line with using the AMFEM. Chapter 5 focuses on the design optimisation procedures of the two motor types followed by a discussion of the optimum designs on a D160M frame size. Chapter 6 explains the prototyped WRSM and the WRIM and test results for the validation of the proposed model approaches in Chapter 3. In Chapter 7, a 6 MW WRIM used for industrial milling is also modelled using the model approaches in Chapter 3 and optimisation procedures described in Chapter 5. The findings of the study and other insights are summarised in Chapter 8. The conclusions regarding aspects claimed to be original and comparisons with other authors for this study work are also given in Chapter 8.

1.6. List of publications

Most of the work presented in this study has been published in both national and international conference papers and journals. The publications with the first author in **bold** are listed as follows.

1.6.1. Journal published papers

- **M. Mabhula** and M. J. Kamper, "Computational efficient parameter and performance prediction of wound-rotor induction motor," *2018 IEEE Transactions on Magnetics (Trans.Magn)*, vol. 54, no. 99, pp. 1-7.
- **M. Mabhula** and M. J. Kamper, "Parameter and performance calculation of cylindrical wound-rotor synchronous motors," *2019 IEEE Transactions on Industrial Application (IAS)*, submitted and under review.

1.6.2. National conference published papers

- **M. Mabhula** and M. J. Kamper, "Improving starting torque quality of wound-rotor induction motor for geared fan loads," *2017 25th Southern African Universities Power Engineering Conference (SAUPEC)*, Stellenbosch, South Africa, pp. 607-612.

1.6.3. International conference published papers

- **M. Mabhula** and M. J. Kamper, "Saliency and mutual inductance effect in cylindrical wound-rotor synchronous motor," *2017 IEEE Workshop on Electrical Machines Design, Control and Diagnosis (WEMDCD)*, Nottingham, UK, pp. 152-157.
- **M. Mabhula** and M. J. Kamper, "Design optimization of cylindrical-rotor synchronous-induction motor," *2018 IEEE Energy Conversion Congress and Exposition (ECCE)*, Portland, USA, pp. 5778-5785.
- **M. Mabhula** and M. J. Kamper, "Steady-state performance analysis of direct-on-line cylindrical wound-rotor synchronous motor," *2019 IEEE Workshop on Electrical Machines Design, Control and Diagnosis (WEMDCD)*, Athens, Greece, pp. 89-95.

Chapter 2

Classical two-axes electromagnetic modelling: WRSM and WRIM motor types

This chapter describes models of the WRSM and WRIM motor types which consist of the combination of a model structure and the corresponding parameters. Henceforth, the chapter is broken into two distinct junctures. The first juncture is the construction of the model structures which is the fundamental form for the motor types representation. The second juncture is the calculation of the model parameters.

2.1. Introduction

Both WRSM and WRIM motor types are primarily constructed with three phase stator windings as discussed in Chapter 1. The difference between the WRSM and WRIM is illustrated in Figs. 2.1 and 2.2 respectively. The former has an excited rotor winding (known as field) and the latter a three-phase short-circuited rotor winding.

In this clause, the two-axes mathematical formulation and theory background of the two motor types' model structures and parameters in stability analysis are described. The analysis of both motor types is done in two junctures which consist of the construction of the model structures and the parameter calculations. The model structures are formed from lumped equivalent circuits, differential equations, coupling magnetic fields and electrical circuit equations. The model parameters are determined from the motor types analytical formulations and sophisticated analyses that simulate the full internal electromagnetic phenomena occurring in the motor. For the internal electromagnetic phenomena in the motor, finite element methods (FEMs) are utilised. Using FEMs, the magnetic flux

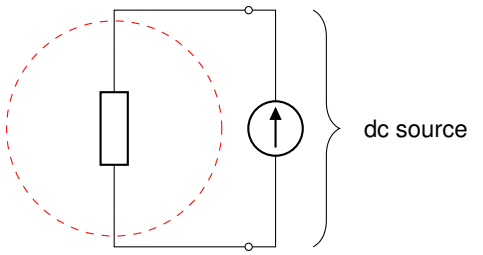

Figure 2.1: WRSM rotor winding connection.

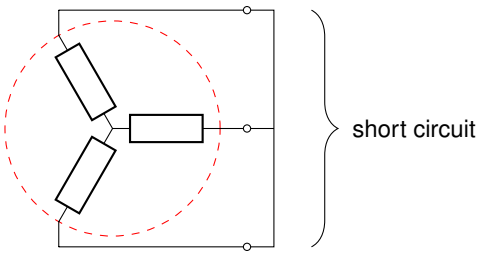

Figure 2.2: WRIM rotor winding connection.

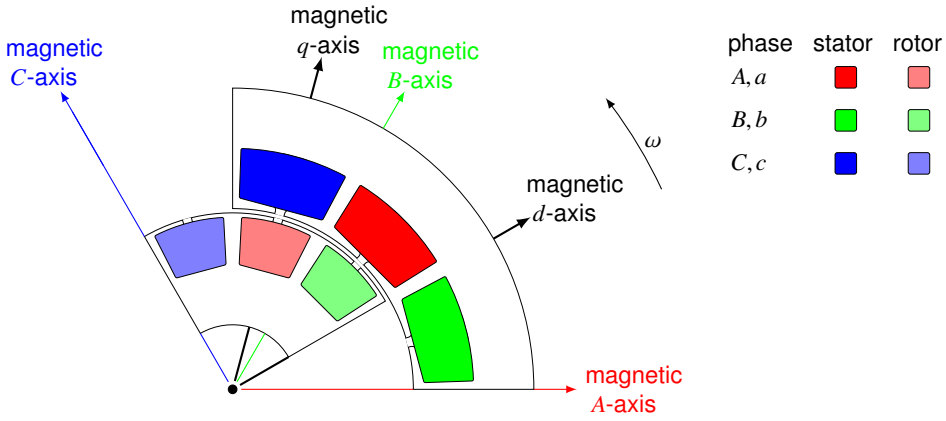

Figure 2.3: Pole face axial view motor geometry representation of d and q magnetic axes with respect to the stator phases.

distribution within the motor, including the non-linear properties of the magnetic saturation (explained in Appendix A.5), as well as the effects of eddy currents and rotor movements, are resolved.

It is important to state that during the analysis process, modelling is done based on the motor types stator and rotor, since both have windings. Additionally, only the fundamental values of the voltages, currents and flux linkages are considered. This is because the design optimisation of the motor types in this study is based on the fundamental quantities only.

2.2. WRSM and WRIM model structures

In the progression of developing skills for the analysis of electrical motors, it is accepted that analysis can significantly be simplified if the analysis is achieved in a reference frame rotating with the rotor. For the analysis, the stator and rotor parameters are transformed into two sets of variables which are orthogonal. The set of variables aligned with the axis of the rotor pole is known as the direct-axis (d-axis). The other set of variables in quadrature to the rotor pole is called the quadrature-axis (q-axis). This strategy transforms the motor stationary three-phase coordinates into a rotating dq-coordinate system as shown in Fig. 2.3. This simplification accompanied by such an approach originates from two distinct attributes of the analysis explained in [1] as:

- All of the motor parameters of both the rotor and the transformed stator windings have constant values under steady-state operation.
- By setting the two-axes to be orthogonal, the fluxes produced by one axis winding current do not produce flux linkages in the other axis. The latter simplifies the flux linkage-current relationship model and initiates a model structure of two independent systems, on the d and q axes.

Following the above mentioned attributes, what follows is the illustration of the two-axes model structures construction for the standard WRSM and WRIM motor types carried out under the following assumptions

- The stator of the motor is considered as three windings $\frac{2}{3}\pi$ electrical radians apart.
- Saturation effects (explained in Appendix A.5) are neglected to allow application of superposition as the motor is linear.

- A magneto-motive force setup by the stator windings is sinusoidal in space around the uniform air-gap, thus space harmonic effects in the field distribution are neglected.
- The magneto-motive forces along the d and q axes produce sinusoidal distribution flux linkages along the respective axes.

2.2.1. Stator winding voltage equations

Considering the above assumptions, the WRSM and WRIM stator three-phase voltages are given by Faraday's Law and the copper loss component represented in the conventional ABC phase reference frame fixed with the stator as

$$[v_{ABC}] = [r_{ABC}][i_{ABC}] + \frac{d}{dt}[\lambda_{ABC}], \tag{2.1}$$

where

$[r_{ABC}]$ - stator phase resistances,
$[i_{ABC}]$ - stator phase currents and
$[\lambda_{ABC}]$ - stator phase flux linkages,

are the matrices of the A, B and C phases, shown in Fig. 2.3. In (2.1), $\frac{d}{dt}$ is the time (t) derivative mathematical operator. For further simplification, the time varying stator quantities of (2.1) are transformed into time invariant dq-axes quantities using Park Transformation given in Appendix A.1 as

$$[T]^{-1}[v_{dqs}] = [r_s]([T]^{-1}[i_{dqs}]) + \frac{d}{dt}([T]^{-1}[\lambda_{dqs}]), \tag{2.2}$$

where

$[T]$ - Park transformation,
$[v_{dqs}]$ - stator voltage components,
$[i_{dqs}]$ - stator current components,
$[\lambda_{dqs}]$ - stator flux linkage components and
$[r_s]$ - equivalent to $[r_{ABC}]$.

The above last index is based on the assumption that the three-phase windings are identical. Also it is worth mentioning that the zero sequence of (2.2) is zero under the assumption of balanced voltage supply. Henceforth, the $dq0$ transformation is taken as dq transformation. This implies that the stator of the motor is represented by only two windings perpendicular to each other rotating synchronously with the rotor since the dq equations are still seen from the stator.

Writing (2.2) in terms of $[v_{dqs}]$ results in

$$[v_{dqs}] = [r_s][i_{dqs}] + \frac{d}{dt}[\lambda_{dqs}] + [T](\frac{d}{dt}[T]^{-1})[\lambda_{dqs}], \tag{2.3}$$

where

$$[T](\frac{d}{dt}[T]^{-1}) = [\omega_s] = \begin{bmatrix} 0 & -\omega_s \\ \omega_s & 0 \end{bmatrix}, \tag{2.4}$$

and

ω_s - stator waveform angular speed.

Finally, (2.3) can be expressed in terms of its respective components in dq reference frame, fixed to the rotor as

$$\begin{bmatrix} v_{ds} \\ v_{qs} \end{bmatrix} = \begin{bmatrix} r_s & 0 \\ 0 & r_s \end{bmatrix} \begin{bmatrix} i_{ds} \\ i_{qs} \end{bmatrix} + \frac{d}{dt} \begin{bmatrix} \lambda_{ds} \\ \lambda_{qs} \end{bmatrix} + \begin{bmatrix} 0 & -\omega_s \\ \omega_s & 0 \end{bmatrix} \begin{bmatrix} \lambda_{ds} \\ \lambda_{qs} \end{bmatrix}. \tag{2.5}$$

2.2.2. Rotor winding voltage equations

In the case of the WRSM, the rotor (field) winding voltages of Fig. 2.3 are excited by a single phase dc source as shown in Fig. 2.1. Considering the single phase dc source, the WRSM phase field voltage is given by

$$v_f = r_f i_f + \frac{d}{dt}\lambda_f, \tag{2.6}$$

where

v_f - field phase voltage ,
i_f - field phase current,
λ_f - field phase flux linkage and
r_f - field phase resistance.

Using Park Transformation (Appendix A.1), the WRSM field voltage components are given by

$$[v_{dqf}] = [r_f][i_{dqf}] + \frac{d}{dt}[\lambda_{dqf}], \tag{2.7}$$

where

$[v_{dqf}]$ - field voltage components,
$[i_{dqf}]$ - field current components and
$[\lambda_{dqf}]$ - field flux linkage components.

For an ideal WRSM, the d-axis is aligned with the rotor field, henceforth, (2.7) simplifies to

$$v_{df} = r_f i_{df} + \frac{d}{dt}\lambda_{df}. \tag{2.8}$$

In the case of the WRIM, the three-phase rotor windings of Fig. 2.3 are short-circuited as shown in Fig. 2.1. These rotor phases have induced ac, henceforth, it is correct to adapt the ABC stator voltage equations of (2.1) for the WRIM rotor voltages as

$$[v_{abc}] = [r_r][i_{abc}] + \frac{d}{dt}[\lambda_{abc}] = [0], \tag{2.9}$$

where

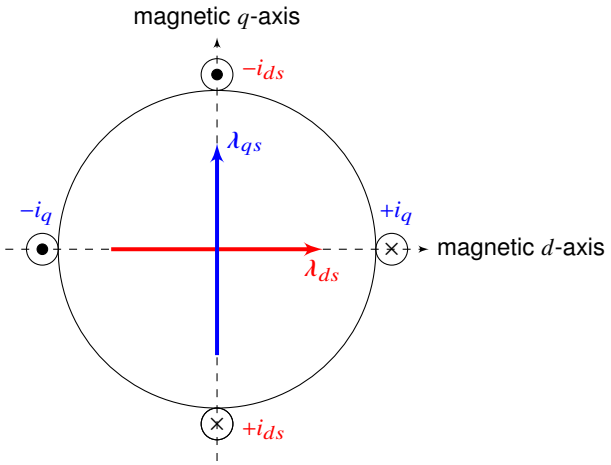

Figure 2.4: Stator winding representation in the dq-axes reference frame.

$[r_{abc}]$ - rotor phase resistances,
$[i_{abc}]$ - rotor phase currents,
$[\lambda_{abc}]$ - rotor phase flux linkages,

are the matrices of the a, b and c phases shown in Fig. 2.3. Following (2.5), the dq transformed WRIM rotor phase voltage equations of (2.9) become

$$\begin{bmatrix} v_{dr} \\ v_{qr} \end{bmatrix} = \begin{bmatrix} r_r & 0 \\ 0 & r_r \end{bmatrix} \begin{bmatrix} i_{dr} \\ i_{qr} \end{bmatrix} + \frac{d}{dt} \begin{bmatrix} \lambda_{dr} \\ \lambda_{qr} \end{bmatrix} + \begin{bmatrix} 0 & -\omega_\Delta \\ \omega_\Delta & 0 \end{bmatrix} \begin{bmatrix} \lambda_{dr} \\ \lambda_{qr} \end{bmatrix} = \begin{bmatrix} 0 \\ 0 \end{bmatrix}, \tag{2.10}$$

where

$$\omega_\Delta = \omega_s - \omega_r, \tag{2.11}$$

and

ω_r - rotor waveform angular speed,
ω_Δ - rotor waveform slip angular speed.

Equations of (2.5), (2.8) and (2.10) give the complete electrical model of the WRSM and WRIM motor types. The model parameters of these equations are calculated using analytical and numerical formulations given in Section 2.3.

2.2.3. Space phasor equations

Representation of the space phasor notation is to allow the transformation of the natural instantaneous values of the three-phase system to the dq-axes plane located on the cross-section of the motor, shown in Fig. 2.3. A good illustration of the stator winding representation in the dq transformation is shown in Fig. 2.4 [26]. In Fig. 2.4, the two independent planes containing the windings lying perpendicular to each other and the page are shown. In the setup, i_{ds} flows in the d-plane $\frac{\pi}{2}$ radians shifted from i_{qs}. i_{qs} flows in the q-plane. Fleming's Right Hand Rule (RHR), explained by E. Hughes *et al* [54] can be used to determine the direction of the flux produced by the currents in these windings.

Using the assumption of balanced stator phases, the star connected stator currents are given by

$$i_A + i_B + i_C = 0. \tag{2.12}$$

Each stator current of (2.12) varies in magnitude sinusoidal with the phase position as

$$\begin{bmatrix} i_A \\ i_B \\ i_C \end{bmatrix} = \begin{bmatrix} i_s & 0 & 0 \\ 0 & i_s & 0 \\ 0 & 0 & i_s \end{bmatrix} \begin{bmatrix} \cos(\theta_s) \\ \cos(\theta_s - \beta_e) \\ \cos(\theta_s - 2\beta_e) \end{bmatrix}, \tag{2.13}$$

where

- i_s - the maximum value of the stator current waveform,
- θ_s - stator electrical phase position angle,
- β_e - represents the electrical shift angle between the magnetic axes of the phases i.e. $\beta_e = \frac{2}{3}\pi$ radians for three phases.

The position origin $\theta_s = 0°$ is taken as the instance when phase A current is at its positive maximum. The combined effect of the sinusoidal currents of (2.13) can be represented as an equivalent current phasor $\vec{i}_s$ of magnitude i_s and phase angle θ_s which is frozen at some position. Thus current phase angle is measured between the phasor and A-phase magnetic axis. If only the fundamental component is considered, the current phasor rotates in an anti-clockwise direction at an angular speed given by

$$\omega_s = 2\pi f_s, \tag{2.14}$$

of one full revolution for every cycle, where

- f_s - stator waveform frequency.

Figure 2.5 shows the rotating phasor of the three-phase stator currents at $\theta_s = \frac{\pi}{12}$ radians. The components of the stator current phasor in Fig. 2.5 on the dq-axes are calculated by applying Park Transformation on (2.13) as

$$\vec{i}_s = [i_{dqs}] = [T][i_{ABC}]. \tag{2.15}$$

Since the d and q axes are orthogonal, the current phasor of (2.15) expressed in terms of magnitude and angle using Pythagoras Theorem is given by

$$\vec{i}_s = \sqrt{i_{ds}^2 + i_{qs}^2} \angle \alpha_s. \tag{2.16}$$

The derivation of (2.16) can also be applied to the three-phase voltage and flux linkages to result in the respective phasors given by

$$\begin{cases} \vec{v}_s = \sqrt{v_{ds}^2 + v_{qs}^2} \angle \delta_s \\ \vec{\lambda}_s = \sqrt{\lambda_{ds}^2 + \lambda_{qs}^2} \angle \beta_s. \end{cases} \tag{2.17}$$

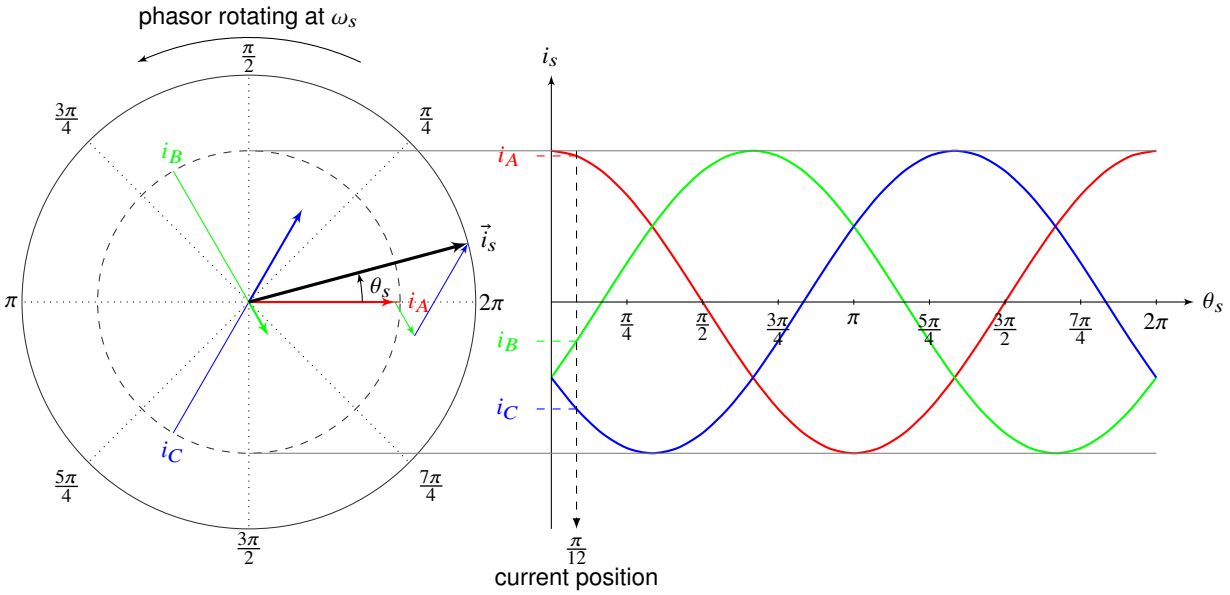

Figure 2.5: Rotating stator current phasor representation at $\theta_s = \frac{\pi}{12}$ radians.

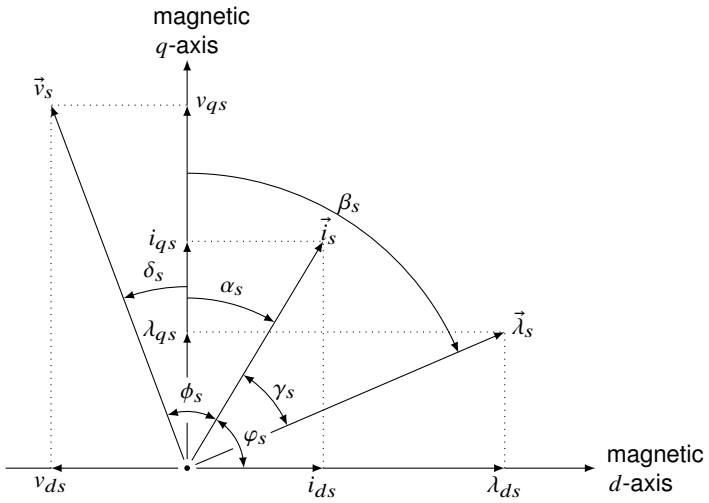

Figure 2.6: Stator voltage, current, and flux linkage space phasor diagram in the dq reference frame.

The current, voltage and flux linkage angles of (2.16) and (2.17) are respectively, calculated from

$$\begin{cases} \alpha_s = \tan^{-1}(\dfrac{i_{ds}}{i_{qs}}) \\ \delta_s = \tan^{-1}(\dfrac{v_{ds}}{v_{qs}}) \\ \beta_s = \tan^{-1}(\dfrac{\lambda_{ds}}{\lambda_{qs}}), \end{cases} \tag{2.18}$$

and are measured positive in the counter-clockwise direction from the q-axis. Figure 2.6 shows the relationship between the current, voltage and flux linkage phasors of (2.16) and (2.17) represented in the dq-axes plane. Although the current i_{ds} moves in a plane and the flux linkages λ_{ds} through that plane as shown in Fig. 2.4, i_{ds} and λ_{ds} are taken in the same direction as shown in Fig. 2.6.

2.2.4. Power factor equations

In an alternating current system, power factor is the cosine of the angle by which the current phasor lags or leads the voltage phasor, i.e. $\cos(\phi_s)$ where

$$\phi_s = (\delta_s - \alpha_s) \tag{2.19}$$

as shown in Fig. 2.6. The stator power factor of the motor is therefore, defined as

$$\cos(\phi_s) = cos(\alpha_s)\cos(\delta_s) + \sin(\alpha_s)\sin(\delta_s). \tag{2.20}$$

Considering Fig. 2.6, (2.20) can be written in terms of the dq-axes voltage and current phasor components as

$$\cos(\phi_s) = \frac{v_{ds}}{v_s}\frac{i_{ds}}{i_s} + \frac{v_{qs}}{v_s}\frac{i_{qs}}{i_s}. \tag{2.21}$$

2.2.5. Developed torque equations

As discussed in the overview of Section 1.2 in Chapter 1, electric motors convert electrical energy into mechanical energy using the principle of electromagnetism, which shows that a force is applied when an electric current is present in a magnetic field [87]. Thus, the concept of torque production is a very crucial motor parameter discussed in this section using Lorentz force law.

The developed torque is generated by the interaction between the current and flux linkage components shown in Fig. 2.4, represented as phasors in Fig. 2.6 and mathematically expressed as

$$T_d = \vec{\lambda}_s \times \vec{i}_s = |\vec{\lambda}_s|\ |\vec{i}_s| \sin(\gamma_s)\vec{u}_n, \tag{2.22}$$

where

$\vec{u}_n$ - unit vector perpendicular to the plane containing $\vec{\lambda}_s$ and $\vec{i}_s$ phasors.

Equation of (2.22) shows that the maximum torque can be achieved when both $\vec{\lambda}_s$ and $\vec{i}_s$ phasors are $\frac{\pi}{2}$ radians apart and the direction of this torque is given by RHR. Using this concept, it can be seen that the d-axis flux linkage with the q-axis current gives a positive torque while the q-axis flux linkage with the d-axis current gives a negative torque. Henceforth, the actual total torque for a one-pole pair motor is given by the sum of these two components of torque as

$$T_d = k[\lambda_{ds} i_{qs} + (-\lambda_{qs} i_{ds})], \tag{2.23}$$

where

$k = 1.5$ - power equaliser factor between the ABC and dq reference frames,

discussed in Appendix A.2.

The developed torque of (2.23) is the electro-mechanical torque which connects the electrical and mechanical models of the motor. The electrical model is obtained from the equivalent circuit and

power equations (given in Appendix A.2) and the mechanical model comprises the equivalent inertial, friction and torque of the load that is driven by the motor. Appendix A.3 gives more detail on torque production.

2.2.6. Magnetic field equations

To correctly construct the model structure, knowledge of the magnetic fields in the domain of the electrical motor is required. These fields are difficult to solve analytically due to the complex geometry of the motors and the non-linear properties of the materials used to assemble them. Finite element method FEM, which can be used to precisely solve magnetic fields, thus plays an important role in the development of electrical motors. Described hereafter is the analysis of these magnetic fields in the 2D geometry of the motor with extensive reference to [10, 46, 108, 125].

For the magnetic field equations, FEM computes the solution of the applicable partial differential equations given by Maxwell's equations that describe the simulation problem. Thus, it is the Maxwell's equations that result in the partial differential equations that FEM uses to solve the quasi-static problems e.g. magneto-static problems. For magneto-static problems the fields are independent of time and each other. Henceforth, the Maxwell magneto-static equations that describe such conditions are respectively, given by Gauss's law of magnetism and Ampere's law partial equations as

$$\nabla \cdot \vec{B} = 0, \tag{2.24}$$

$$\nabla \times \vec{H} = \vec{J}, \tag{2.25}$$

where

- ∇ - mathematical operator,
- $\vec{B}$ - magnetic flux density,
- $\vec{H}$ - magnetic field strength and
- $\vec{J}$ - phasor applied current density.

The magnetic flux density relation of (2.24) is defined by the curl of the magnetic vector potential as

$$\vec{B} = \nabla \times \vec{A}, \tag{2.26}$$

where

- $\vec{A}$ - magnetic vector potential.

Knowing the relation

$$\vec{B} = \mu \vec{H}, \tag{2.27}$$

equation of (2.25) can be written as

$$\vec{J} = \nabla \times (\frac{1}{\mu} \nabla \times \vec{A}), \tag{2.28}$$

where

μ - magnetic permeability.

In simulating electrical motors, FEM solves (2.24) and (2.25) using the vector potential approach by finding the vector potential which satisfies (2.28). Equation (2.28) is in the form of a curl of a scalar and a vector function, and henceforth, it can also be written as

$$\vec{J} = \frac{1}{\mu} \nabla \times (\nabla \times \vec{A}) - \vec{A} \times (\nabla \frac{1}{\mu}). \tag{2.29}$$

Considering a 2D FEM solution of the subject work, the magnetic vector potential and the current density only have the z-directed components respectively, defined as

$$\vec{A} = A(x, y)\vec{u}_z \quad \text{and} \quad \vec{J} = J(x, y)\vec{u}_z, \tag{2.30}$$

where

$\vec{u}_z$ - unit vector in the z-direction in Cartesian coordinates.

From the defined $0xy$ axes which results only on z-directed components of (2.30), (2.28) can be rewritten as

$$\vec{J} = -\frac{\partial}{\partial x}(\frac{1}{\mu}\frac{\partial}{\partial x}\vec{A}) - \frac{\partial}{\partial y}(\frac{1}{\mu}\frac{\partial}{\partial y}\vec{A}). \tag{2.31}$$

It is clear from (2.31) that for a current fed electric motor, the current density of (2.25) rewritten as in (2.31) can be solved by solving the vector potential.

In electrical motors, conductors are used as windings. For thin conductors, conductors are grouped in coils in which the current density flowing through the cross-section is considered uniform. However, for thick conductors, the current density is taken as non-uniform. To incorporate this behaviour using Maxwell's constitutive relation, the current density is given by

$$\vec{J} = \sigma\vec{E}, \tag{2.32}$$

where

σ - electric conductivity and
$\vec{E}$ - electric field intensity.

Furthermore, the curl of the field intensity of (2.32) is given by

$$\nabla \times \vec{E} = -\frac{\partial}{\partial t}\vec{B}. \tag{2.33}$$

Using the relation (2.26) into (2.33) yields

$$\nabla \times \vec{E} + \frac{\partial}{\partial t}\vec{B} = \nabla \times (\vec{E} + \frac{\partial}{\partial t}\vec{A}) = 0. \tag{2.34}$$

Also using the conservative field by Faraday's law, one can obtain

$$\vec{E} + \frac{\partial}{\partial t}\vec{A} = -\nabla v, \tag{2.35}$$

where

v - electric scalar potential.

The term on the right hand side of (2.35) is the gradient of the electric scalar potential. The current density of (2.32) in terms of v using (2.35) becomes

$$\vec{J} = \sigma(-\nabla v - \frac{\partial}{\partial t}\vec{A}). \tag{2.36}$$

Equation (2.31) can be rewritten using (2.36) as

$$\frac{\partial}{\partial x}(\frac{1}{\mu}\frac{\partial}{\partial x}\vec{A}) + \frac{\partial}{\partial y}(\frac{1}{\mu}\frac{\partial}{\partial y}\vec{A}) = \sigma\frac{\partial}{\partial t}\vec{A} + \sigma\nabla v. \tag{2.37}$$

The Dirichlet, Neumann and periodic boundary conditions are then imposed to solve for (2.37)

Furthermore, the Ampere's law in differential form is given by

$$\nabla \times \vec{B} = \mu\vec{J}. \tag{2.38}$$

Taking the divergence of the vector field on both sides, the divergence of the curl on the left hand side of (2.38) is zero. Therefore, the right hand side is also equivalent to zero and expressed as

$$\nabla \cdot \vec{J} \equiv 0. \tag{2.39}$$

With the magnetic vector potential $\vec{A}$ being constant in the z-direction, in 2D modelling using (2.39), one can get

$$\nabla \cdot (\sigma\frac{\partial}{\partial z}v\vec{u}_z) = \frac{\partial}{\partial z}(\sigma\frac{\partial}{\partial z}v). \tag{2.40}$$

The scalar electric field potential of (2.40) can be defined as

$$v = v_1\vec{u}_z. \tag{2.41}$$

Now, considering a thick bar conductor in each motor slot finite element (or main) region, the voltage across the conductor is given by

$$v_{mb} = \int_0^{l_m} -\nabla v dl_m = -v_1 l_m, \tag{2.42}$$

where

l_m - main conductor bar length in the z-direction (for the 2D problem).

The voltage v_{mb}, across the conductor bar winding in the finite element region can be physically illustrated as in Fig. 2.7. Integrating (2.36) in the z-direction over the conductor bar area as shown in Fig. 2.7 gives the total current in the bar as

$$i_{mb} = \int_{s_{mb}} \vec{J} ds = -\int_{s_{mb}} \sigma_m \frac{\partial}{\partial t}\vec{A} ds + \int_{s_{mb}} \sigma_m \frac{v_{mb}}{l_m} ds, \tag{2.43}$$

where

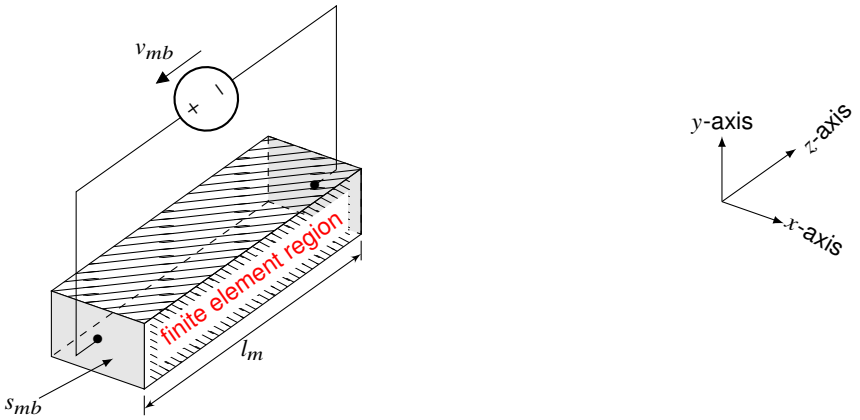

Figure 2.7: Applied voltage to the finite element region of a conductor bar winding.

s_{mb} - main conductor bar cross-section area and
σ_m - main conductor electric conductivity.

From (2.41) and (2.42), $\nabla v = v_1$ and $v_1 = \dfrac{-v_{mb}}{l_m}$ respectively, thus (2.43) can be written as

$$i_{mb} = \frac{v_{mb}}{r_{mb}} - \int_{s_{mb}} \sigma_m \frac{\partial}{\partial t}\vec{A} ds, \tag{2.44}$$

where

r_{mb} - main bar dc resistance,

is given by

$$r_{mb} = \frac{l_m}{\sigma_m s_{mb}}. \tag{2.45}$$

For a conductor bar using (2.43), the voltage across the bar in the motor slot is given by

$$v_{mb} = r_{mb} i_{mb} + r_{mb} \int_{s_{mb}} \sigma_m \frac{\partial}{\partial t}\vec{A} ds, \tag{2.46}$$

in which the last term of (2.46) is the voltage drop due to eddy currents. Using (2.31) and (2.36), one can also get

$$\frac{\partial}{\partial x}(\frac{1}{\mu}\frac{\partial}{\partial x}\vec{A}) + \frac{\partial}{\partial y}(\frac{1}{\mu}\frac{\partial}{\partial y}\vec{A}) - \sigma\frac{\partial}{\partial t}\vec{A} - \sigma \nabla v = 0, \tag{2.47}$$

which results in a bar equation given by

$$\frac{\partial}{\partial x}(\frac{1}{\mu}\frac{\partial}{\partial x}\vec{A}) + \frac{\partial}{\partial y}(\frac{1}{\mu}\frac{\partial}{\partial y}\vec{A}) - \sigma_m\frac{\partial}{\partial t}\vec{A} + \sigma_m\frac{v_{mb}}{l_m} = 0. \tag{2.48}$$

For thin conductors, the derivation of the thick conductor described above is also adapted. In the case of a series connected thin conductors in a slot, the current density is now considered uniform. Hence, the coil terminal voltage is the sum of all voltages across the thick conductor bars of (2.46) in

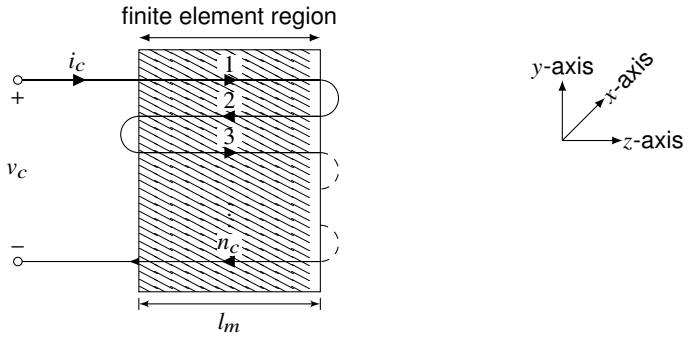

Figure 2.8: Series connected conductors to form a coil in the finite element region.

the coil given by

$$v_{mc} = n_{mc} v_{mb} = n_{mc} r_{mb} i_{mb} + n_{mc} r_{mb} \int_{s_{mb}} \sigma_m \frac{\partial}{\partial t} \vec{A} ds, \tag{2.49}$$

where

n_{mc} - main thin conductor bar number of turns in the coil.

The coil terminal voltage of (2.49) can be illustrated physically as shown in Fig 2.8. Also substituting (2.46) in (2.48), the following equation is obtained

$$\frac{\partial}{\partial x}(\frac{1}{\mu}\frac{\partial}{\partial x}\vec{A}) + \frac{\partial}{\partial y}(\frac{1}{\mu}\frac{\partial}{\partial y}\vec{A}) - \sigma_m \frac{\partial}{\partial t}\vec{A} + \frac{i_m}{s_m} + \sigma_m \frac{\partial}{\partial t}\vec{A} = 0, \tag{2.50}$$

where

i_m - main thin conductor total current and
s_m - main thin conductor cross-section area.

The last term in the left hand side of (2.50) is the uniform induced current density over the conductor cross-section area deduced from

$$\sigma_m \frac{\partial}{\partial t}\vec{A} = \frac{1}{s_m}\int_{s_m} \sigma_m \frac{\partial}{\partial t}\vec{A}. \tag{2.51}$$

For a total coil surface area $s_{mc} = n_{mc} s_m$, (2.50) is simplified to

$$\frac{\partial}{\partial x}(\frac{1}{\mu}\frac{\partial}{\partial x}\vec{A}) + \frac{\partial}{\partial y}(\frac{1}{\mu}\frac{\partial}{\partial y}\vec{A}) + \frac{n_{mc}}{s_{mc}} i_{mc} = 0, \tag{2.52}$$

where

i_{mc} - total current in the coil.

Using (2.51) into (2.49) yields

$$v_{mc} = r_{mc} i_{mc} + \frac{n_{mc} l_m}{s_{mc}} \int_{s_{mc}} \frac{\partial}{\partial t}\vec{A} ds, \tag{2.53}$$

where

r_{mc} - main coil dc resistance,

is given by

$$r_{mc} = \frac{n_{mc} l_m}{\sigma_m s_m}. \tag{2.54}$$

The second term on the right hand side of (2.53) is the voltage induced in the coil. Following the above, the equations for the series connected thin conductors are given by

$$\frac{\partial}{\partial x}(\frac{1}{\mu}\frac{\partial}{\partial x}\vec{A}) + \frac{\partial}{\partial y}(\frac{1}{\mu}\frac{\partial}{\partial y}\vec{A}) + \frac{n_{mc}}{s_{mc}} i_{mc} = 0. \tag{2.55}$$

and

$$v_{mc} = r_{mc} i_{mc} + \frac{n_{mc} l_m}{s_{mc}} \int_{s_{mc}} \frac{\partial}{\partial t}\vec{A} ds. \tag{2.56}$$

Since the slot cross-section is known, the individual voltages in (2.46) and (2.56) can be calculated using the stator current and the magnetic vector potential. Appendix A.4 gives the calculation of the vector potential using the FEM.

It is important to state that the equations described in this section are useful in the accurate calculation of magnetic fields of complex motor geometry using the FEM. The accuracy of the FEM essentially in complex electromagnetic problems is noted when compared to tradition methods such as magnetic circuit methods. The limitation in the magnetic circuit method is that it relies on the assumption of the magnetic flux paths as opposed to FEM which does not require any assumption of flux paths or related empirical formulas. FEM accurately computes magnetic fields and the related motor design parameters for motors of complicated geometry, with saturation, significant armature reaction, and with or without eddy currents [108, 125].

2.2.7. Electric circuit equations

The purpose of assuming that the magnetic fields in the motor are 2D as discussed in Sub-section 2.2.6, is to save computation time. To incorporate the parameters and conditions which cannot be included in 2D field equations, the 3D end-region fields are modelled approximately by constant end-region fields impedances in the external electric circuit equations of the windings.

2.2.8. Coupling magnetic field and electric circuit equations

In the case of a grid-connected electric motors type, i.e. voltage-fed motors, all the voltage drops must be simulated. Henceforth, the end-windings which are not taken into account in 2D have to be considered separately. As a result of the end-windings, simulation of the grid-connected motor is made up of magnetic field equations as well as electric circuit equations. To couple the magnetic field (Sub-section 2.2.6) and electric circuit (Sub-section 2.2.7) equations, the magnetic vector potential's direct relation with the magnetic flux is utilised in the analysis. Thus, the motor terminal voltage is the grid in which the vector potential and the excitation currents are calculated from the motor model

parameters using the combined magnetic field and electric circuit equations. Considering the motor stator terminal voltage equation of (2.1), the grid-connected motor terminal phase voltage to include the end-effect separately is now defined as

$$v_\phi = i_\phi r_s + \frac{d}{dt}\lambda_\phi, \tag{2.57}$$

where

$$\begin{cases} r_s = r_{ms} + r_{es} \\ \lambda_\phi = \lambda_{ms}(i_\phi, \theta_s) + \lambda_{es}(i_\phi), \end{cases} \tag{2.58}$$

with

- r_{ms} - main-winding stator phase resistance as of (2.45) and (2.54) given in Sub-section 2.3.1,
- r_{es} - series connected end-winding stator phase resistance given in Sub-section 2.3.3,
- λ_{ms} - main-winding stator phase flux linkage responsible for torque production and calculated from the vector potential as of (2.48) and (2.55) given in Sub-section 2.3.2 and
- λ_{es} - series connected end-winding stator phase flux linkage calculated from the end-winding inductance given in Sub-section 2.3.4.

Furthermore, considering (2.58), λ_{ms} is a function of phase current i_ϕ and the stator electrical rotor position angle θ_s while λ_{es} only the phase current, hence, (2.57) is expressed as

$$v_\phi = i_\phi r_{ms} + i_\phi r_{es} + \frac{\partial}{\partial t}\lambda_{ms}\frac{d}{dt}i_\phi + \frac{\partial}{\partial \theta_s}\lambda_{ms}\frac{d}{dt}\theta_s + \frac{\partial}{\partial t}\lambda_s\frac{d}{dt}i_\phi, \tag{2.59}$$

simplified to

$$v_\phi = \underbrace{\underbrace{i_\phi \omega_s L_{es} + i_\phi r_{es}}_{\text{end-winding}} + \underbrace{i_\phi r_{ms} + \frac{d}{dt}\lambda_{ms}}_{\text{main-winding}}}_{\text{model parameters}}, \tag{2.60}$$

where ω_s is the stator waveform angular speed. The coupling voltage equation of (2.60) is in the form of simulated voltage drops across the main and end-winding impedances, and all model parameters in which the end-winding inductances L_{es} and resistance r_{es} are constant. Thus (2.60) serves to couple the finite element (main-winding) region, represented by Z_{ms}, to the external circuits (end-winding) and sources (grid), represented by Z_{es} and v_g using the total current i_ϕ, shown in Fig. 2.9 for series connected coils. In Fig. 2.9, v_{es} given by (2.60) is the voltage applied to the external terminals of the winding, and v_{ms} given by (2.56) for a single coil is the terminal voltage of the finite element region.

The stator voltage equation approach described above of coupling field and electric circuit equations can also be applied to the rotor voltage equations.

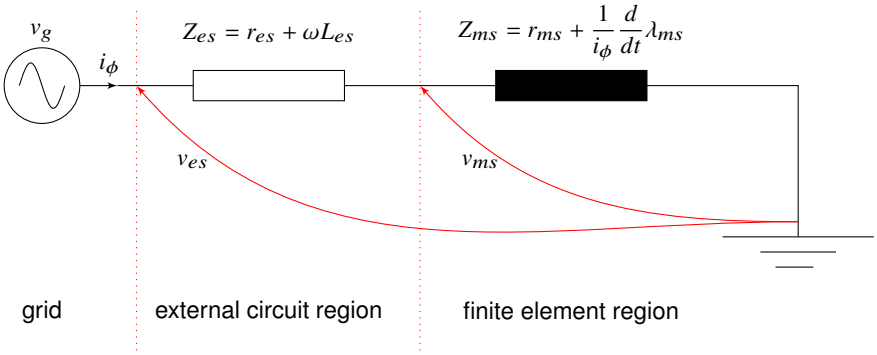

Figure 2.9: Circuit diagram showing coupled magnetic field and electric circuit equations with series connected conductors in a coil.

2.3. WRSM and WRIM model parameter calculation

The model parameters which include resistance, end-winding inductance and flux linkage, as earlier stated, are calculated from analytical formulations and analysis that simulate the full electromagnetic phenomenon occurring in the motor respectively. It is evident that the basic equations of the motor model structure discussed in Section 2.2 are complicated because of the inductances which are a function of rotor motion, and hence, they vary with time. However, in dq reference frame steady-state operation under study, the inductances are independent of the rotor motion i.e. $\frac{d}{dt}\lambda = 0$. To denote steady-state operation, the model parameters of this section and the rest of the study, determined at steady-state, are written in capital letters.

The WRSM dq-axes terminal voltage equations of (2.5) and (2.8) in steady-state matrix form become

$$\begin{bmatrix} V_{ds} \\ V_{qs} \\ V_{df} \end{bmatrix} = \begin{bmatrix} (R_{ms} + R_{es}) & -\omega_s L_{es} & 0 \\ \omega_s L_{es} & (R_{ms} + R_{es}) & 0 \\ 0 & 0 & (R_{mf} + R_{ef}) \end{bmatrix} \begin{bmatrix} I_{ds} \\ I_{qs} \\ I_{df} \end{bmatrix} + \begin{bmatrix} 0 & -\omega_s & 0 \\ \omega_s & 0 & 0 \\ 0 & 0 & 0 \end{bmatrix} \begin{bmatrix} \Lambda_{ds} \\ \Lambda_{qs} \\ 0 \end{bmatrix}. \tag{2.61}$$

In (2.61), the effect of end-winding has been included as discussed in Sub-section 2.2.8.

The corresponding WRIM steady-state dq-axes terminal voltage equations following (2.5) and (2.10) become

$$\begin{bmatrix} V_{ds} \\ V_{qs} \\ V_{dr} \\ V_{qr} \end{bmatrix} = \begin{bmatrix} (R_{ms} + R_{es}) & \omega_s L_{es} & 0 & 0 \\ \omega_s L_{es} & (R_{ms} + R_{es}) & 0 & 0 \\ 0 & 0 & (R_{mr} + R_{er}) & -\omega_\Delta L_{er} \\ 0 & 0 & \omega_\Delta L_{er} & (R_{mr} + R_{er}) \end{bmatrix} \begin{bmatrix} I_{ds} \\ I_{qs} \\ I_{dr} \\ I_{qr} \end{bmatrix} + \begin{bmatrix} 0 & -\omega_s & 0 & 0 \\ \omega_s & 0 & 0 & 0 \\ 0 & 0 & 0 & -\omega_\Delta \\ 0 & 0 & \omega_\Delta & 0 \end{bmatrix} \begin{bmatrix} \Lambda_{ds} \\ \Lambda_{qs} \\ \Lambda_{dr} \\ \Lambda_{qr} \end{bmatrix}, \tag{2.62}$$

where

$$V_{dr} = V_{qr} = 0. \tag{2.63}$$

The dq-axes voltage equations of (2.61) and (2.62) result in the dq-axes equivalent circuit diagrams of Figs. 2.10 and 2.11 respectively. These rotor parameters can be referred to the stator (for common ground) by using the effective winding ratio.

The calculation of the circuit parameters of Figs. 2.10 and 2.11 are given in the following sections.

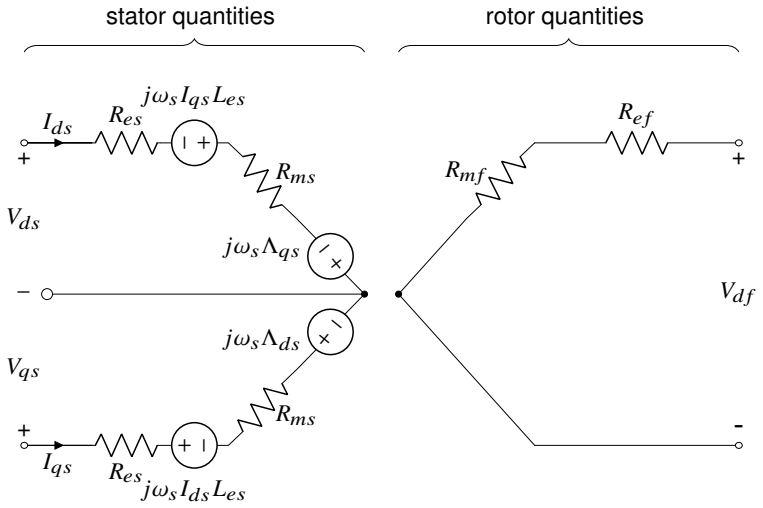

Figure 2.10: WRSM equivalent circuit diagrams represented in the steady-state dq-reference frame.

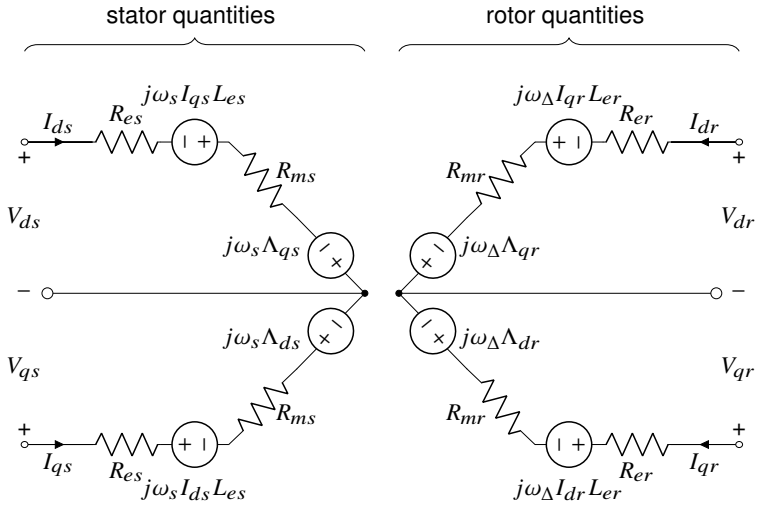

Figure 2.11: WRIM equivalent circuit diagrams represented in the steady-state dq-reference frame.

The parameters are classified as main-winding and end-winding circuit parameters, both forming the model parameters. The circuit parameters such as R_m, R_e and L_e are determined using analytical formulas. The FEM is used to simulate the electromagnetic behaviour in the motor in which the effect of saturation, explained in Appendix A.5, is included. The FEM magnetic vector potential explained in Sub-section 2.2.8 in the coil region is then utilised to obtain the flux linked by the coil energised by a current source.

Furthermore, the steady-state dq-axes torque equation of (2.23) is redefined as

$$T_d = 1.5p(\Lambda_{ds} I_{qs} - \Lambda_{qs} I_{ds}). \tag{2.64}$$

2.3.1. Main-winding resistance

The general dc main-winding resistance (i.e. skin effect ignored) in Figs. 2.10 and 2.11 are of (2.54) given by

$$R_m = \frac{n_{mc} l_m}{\sigma_m s_m} W_m, \tag{2.65}$$

where

W_m - main-winding number of turns per phase.

In (2.65), σ_m is temperature dependent calculated from the reciprocal of the known electric resistivity ρ, at an operating temperature $℃$ given by [127] as

$$\rho_{℃} = \rho_{20}[1 + \frac{1}{273}(℃ - 20)], \tag{2.66}$$

where

ρ_{20} - electric resistivity of copper winding at a temperature of $20℃$.

Furthermore, when ac current at high frequencies is injected through a thick conductor, the skin effect becomes important in the computation of the main-winding resistance [15, 65]. This effect is illustrated in the last term of (2.46) which is the voltage drop due to eddy currents. J. Lammeraner and M. Štafl in [71] explain the skin effect as being due to opposing currents induced (eddy currents) by changing magnetic fields resulting from ac current. This effect in turn causes non-uniform distribution of current density in the considered cross-section of the conductor, consequently causing the effective (dc) resistance as of (2.65) to increase more than expected which results in higher copper losses. In addition, according to IEC-60050 definition [[58], entry 121.13.18], skin effect for ac in a conductor is a phenomenon in which the current density is greater near the surface than in the interior of the conductor. P. Ponomarev further demonstrated and explained the skin effect phenomenon in [100] that if the frequency is high and the conductor dimensions are large enough, the current density at the centre of the conductor along its axis can be practically zero, and most of the current is concentrated near the surface of the conductor within the skin depth. This skin depth (considering the main-winding) is defined as the distance from the conductor surface at which current density is e^{-1} given as [47]

$$\delta_m = \sqrt{(\frac{1}{\pi f_m \mu_r \mu_o \sigma_m})}, \tag{2.67}$$

where

μ_o - permeability of free space,
μ_r - relative permeability of the winding material and
f_m - main-winding frequency.

In order to limit the skin effect, it is advisable to have conductor dimensions less than the skin depth so that the path for eddy currents along the conductor length will be cut [71]. In this way, the conductor experiences a uniformly distributed current density and as a result a low effective resistance. In practice, a bunch of insulated strands of cross-section dimensions lower than the skin

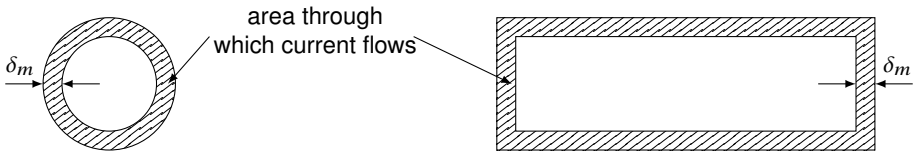

Figure 2.12: Cross-section of a cylindrical and rectangular conductor demonstration skin depth.

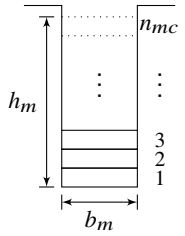

Figure 2.13: Rectangular conductors located in a slot of an electrical motor.

depth are normally used (as assumed in (2.65)). Figure 2.12 demonstrates the skin depth in which the high-frequency current in a cylindrical and rectangular conductor is contained within thickness of one skin depth of the surface.

To include the skin effect in the main-winding resistance calculation, the dc resistance of (2.65) is redefined as

$$R'_m = k_{mr} R_m, \tag{2.68}$$

where

k_{mr} - main-winding resistance coefficient,

in which the effective resistance increment is due to the skin effect.

The work of J. Lammeraner *et al* [71] is well appreciated in the calculation of k_{mr}. In derivations, the authors considered eddy currents in the conductors located in the slots of an electric motor as shown in Fig. 2.13. In the arrangement, assuming all the n_{mc} identical conductors in the slot are carrying equal currents, the resistance coefficient defined as the increase in copper losses caused by eddy currents is expressed as [71]

$$k_{mr} = \varphi(\xi_m) + \frac{0.81 n_{mc}^2 - 1}{3} \psi(\xi_m), \tag{2.69}$$

where

ξ_m - main-winding relative height,

given by

$$\xi_m = \frac{h_m}{\delta_m}. \tag{2.70}$$

The real functions of ξ_m in (2.70) are explicitly given in [71] as

$$\begin{cases} \varphi(\xi_m) = \xi_m(\dfrac{\sinh\ 2\xi_m + \sin\ 2\xi_m}{\cosh\ 2\xi_m - \cos\ 2\xi_m}) \\ \psi(\xi_m) = 2\xi_m(\dfrac{\sinh\ \xi_m - \sin\ \xi_m}{\cosh\ \xi_m + \cos\ \xi_m}). \end{cases} \tag{2.71}$$

2.3.2. Main-winding flux linkage

The dq-axes flux linkage model parameters in Figs. 2.10 and 2.11 are calculated using the total phase flux linkage solution. As stated in Sub-section 2.2.8, the flux linkage solution is obtained directly from the vector potential $\vec{A}$. This is illustrated in Appendix A.4 in which FEM is utilised in the computation of $\vec{A}$. The literature of [66, 82, 108] is followed in the derivation hereafter following the formulation in Sub-section 2.2.8.

For the 2D magnetic vector potential problems, a contour of constant potential is a flux line. This is due to the derivation of the magnetic vector potential of (2.26) as

$$\nabla \times \vec{A} = \vec{B}, \tag{2.72}$$

where following (2.30), $\vec{A}$ has only the z-directed component i.e. $\vec{A} = A\vec{u}_z$. The net total flux of the main-winding through surface S_m is calculated from

$$\varphi_m = \int_{S_m} \vec{B} \cdot dS. \tag{2.73}$$

From (2.72) and using Stokes' integral theorem, (2.73) becomes

$$\varphi_m = \int_{S_m} (\nabla \times \vec{A}) \cdot dS = \oint_C \vec{A} \cdot dl_m. \tag{2.74}$$

It is (2.74) which is the portion of the problem analysed with finite elements where the problem is discretised (meshed) in space, shown in Fig. A.2. Considering (2.74) for a coil area S_m divided into n_m first-order triangle mesh finite elements, n_{mc} turns and length l_m along the z-direction, the flux linkage of the coil is given by

$$\Lambda_m = n_{mc}\varphi_m = n_{mc} \sum_{j=1}^{n_m} \frac{\triangle_j}{S_m} (\Im \frac{1}{3} \sum_{i=1}^{3} \vec{A}_{ij}) l_m, \tag{2.75}$$

where

- $\triangle_j$ - j^{th} triangle element,
- $\vec{A}_{ij}$ - vector potential of nodal point $i = 1$, $i = 2$ or $i = 3$ of the $\triangle_j$ and
- $\Im$ - denotes the direction of the integral into $+1$ or out -1 of the plane.

Considering (2.75) and one meshed pole, the net total flux linkage of the phase main-winding is

expressed as

$$\Lambda_m = \frac{2pn_{mc}l_m}{S_m}\sum_{j=1}^{u_m}\left(\frac{\triangle_j \Im}{3}\sum_{i=1}^{3}\vec{A}_{ij}\right), \tag{2.76}$$

where

u_m - total number of elements of the meshed phase coil area in the pole main region.

The total net flux linkage of (2.76) includes high order harmonic and leakage fluxes produced by the winding, slotted air-gap and magnetic saturation. Thus the total phase flux linkages are given by (2.76), which are transformed into the dq reference frame to represent the Λ_d and Λ_q in Figs. 2.10 and 2.11.

2.3.3. End-winding resistance

The dc main-winding resistance formulation of (2.65) is adapted for the calculation of the end-winding resistance, shown in Figs. 2.10 and 2.11. Assuming an equal number of winding turns, cross-section area and temperature, the end-winding resistance from (2.65), is given by

$$R_e = \frac{n_{ec}l_e}{\sigma_e s_e}W_e, \tag{2.77}$$

where

n_{ec} - end thin conductor number of turns in the coil,
σ_e - end conductor electric conductivity,
s_e - end thin conductor cross-section area,
W_e - end-winding number of turns per phase and
l_e - end-winding length.

l_e is determined from a pole pitch length τ_p as [15]

$$l_e = \begin{cases} 2\tau_p - 0.02 & \text{when } p = 2 \\ 0.5\pi\tau_p + 0.018 & \text{when } p = 3. \end{cases} \tag{2.78}$$

For thick end-winding conductors, eddy effects are also noticeable and the ac resistance of (2.68) is adapted using (2.77) as

$$R'_e = k_{er}R_e, \tag{2.79}$$

where

k_{er} - end-winding resistance coefficient.

2.3.4. End-winding flux linkage

Given the currents, the end-winding flux linkages i.e. $I_d L_e$, $I_q L_e$, of Figs. 2.10 and 2.11 are calculated from the end-winding inductance L_e. The end-winding inductance is calculated from the formulation of M.J. Kamper [67]. Kamper [67] gave a modified end-winding inductance formula by Honsinger 1959 to accommodate both single and double layer windings. He further modified the formula method of Lawrenson of 1970, in which the effect of mutual flux linkage between end-winding groups is taken into account. However, the formula does not take into account effect of flux linkage coupling between stator and rotor end-windings in the case of wound rotor motors. The end-winding inductance formula by Kamper for m winding phases is defined as

$$L_e = \frac{1}{2\pi} V_{(u)} m D \left(\frac{W_e k_d k_{p(u)}}{p}\right)^2 k_{e(p)} (10^{-8}), \tag{2.80}$$

where

D - either stator inside diameter d_s or rotor outside diameter D_r.

Other variables of (2.80), V_u the shape-factor, k_d the distribution-factor, k_p the pitch-factor and k_e the end-winding factor are given in Appendix A.6.

2.4. Chapter conclusions

An overall electric motor model which consists of the combination of the model structure and the parameter calculations with the focus on the WRSM and WRIM motor types is described. Not only for simplicity reasons, the two-axes motor model is illustrated as the best model approach in which all the important effects of the motor can be perfectly added to give accurate motor behaviour. Only important aspects and citations of the subject work are studied for the purpose of creating a simplified compatible model approach for a grid-connected motor type as given in Chapter 3.

Chapter 3

Proposed two-axes electromagnetic modelling: Grid-connected WRSM and WRIM

This chapter presents the proposed two-axes electromagnetic model approaches for grid-connected WRSM and WRIM motor types in which the classical electric models described in Chapter 2 are adapted. The proposed model approaches are as a result of non-reliable performance prediction in classical models, hence, the available models may not be used with enough confidence to model the motor types. The attention is directed towards making appropriate modifications to the classical two-axes model using FEM in steady-state operations. The objectives are to achieve improved accuracy by integrating all major effects such as magnetic saturation, while at the same time, keeping the calculations relatively efficient and simple.

3.1. Introduction

Economic use of lamination material in electric motors dictates that the magnetic material will be operated near saturation [16, 93]. Furthermore, it has been recognised that the motor magnetic material is often heavily saturated [109]. Consequently, steady-state parameters such as inductances for modelling vary with operating loads [75, 78, 122]. This introduces increased complexity in motor modelling than assumed by classical models, resulting in the simulation process being more and more time consuming in order to attain accuracy.

There is no doubt that FEM is a very accurate numerical method, broadly used for electrical motor analysis as discussed in Chapter 2. Among others, the Time-Stepping (TS) FEM has been used for the transient performance prediction of electric motors [42, 52, 79, 94, 95, 117, 121]. Also recently, Time-harmonic (TH) FEM has been widely used in addition to determine the motor parameters and performance [77,91,107,110,130,136]. However, both these FEMs are found not to be computational time efficient especially when steady-state analysis in the motor design optimisation is required. The major drawback in TH FEM is that only linear regions of the motor are considered which is a big problem because of saturation, as stated earlier in this introduction.

To avoid weighty errors and time-consuming approaches in the motor analysis using FEM when considering either TS or TH FEMs given above, this chapter demonstrates steady-state model approaches which use the total overall flux linkages of the motor. The flux linkages are the net flux

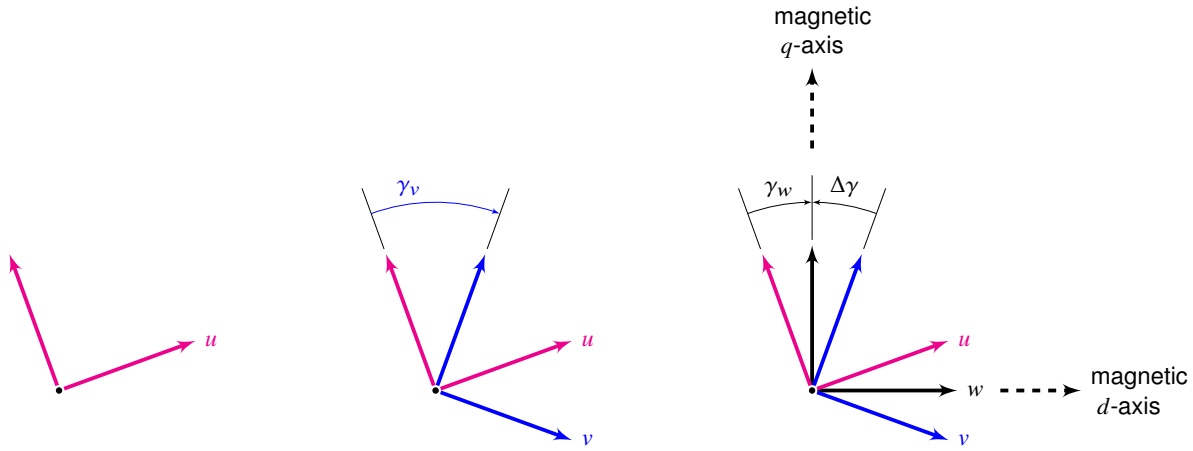

Figure 3.1: Shifting motor magnetic axis under load.

linkages produced by the three phases in which the parameters and performance of the motor are determined. For the field solution, a FEM based analysis which has the ability to separate the loaded motor flux linkages into components is utilised as in [81, 85] for the WRSM and [82] for the WRIM. The segregated flux linkage components are used in the simplified proposed models which utilise iterative processes in solving excitations for the grid-connected motor types. During the iterative processes, electrical circuits and magnetic field equations are coupled as explained in the model structure given in Chapter 2. With the proposed modelling approaches, it is not only the non-linear operating region of the motor types dealt with, but also the cross-magnetisation, saturation-saliency and asymmetric-saturation effects on the motor parameters incorporating all leakage flux linkages.

3.2. Modelling magnetic axis definition

The importance and existence of cross-magnetisation, saturation saliency and asymmetric saturation phenomena have been practically verified and are currently well recognised [8, 33, 69]. Owing to the above mentioned issue, non-classical methods are required to determine the most important motor characteristics. The purpose of this section is to define the shifted non-classical magnetic axis under the load of the proposed magnetic approaches based on the electric model described in Chapter 2. This is to take into account all the important effects of saturation in the motor modelling.

The position of the magnetic axis on the motor can be defined in three shifted dq-axes identified as u, v and w as shown in Fig. 3.1. The u-axis is the classic textbook-defined magnetic axis in which the motor is analysed on the d and q axes assuming they are decoupled. On this axis, the effects of cross-magnetisation, saturation-saliency and asymmetric-saturation are ignored. Consequently, the total flux linkage components for the WRSM and WRIM in matrix form following (2.61) and (2.62), on the u-axis are respectively, defined as

$$u\text{-axis model} \begin{cases} \begin{bmatrix} \Lambda_{ds} \\ \Lambda_{qs} \end{bmatrix} = \begin{bmatrix} L_{dsds} & 0 & L_{dsdf} \\ 0 & L_{qsqs} & 0 \end{bmatrix} \begin{bmatrix} I_{ds} \\ I_{qs} \\ I_{df} \end{bmatrix} & (3.1) \\ \begin{bmatrix} \Lambda_{ds} \\ \Lambda_{qs} \\ \Lambda_{dr} \\ \Lambda_{qr} \end{bmatrix} = \begin{bmatrix} L_{dsds} & 0 & L_{dsdr} & 0 \\ 0 & L_{qsqs} & 0 & L_{qsqr} \\ L_{drds} & 0 & L_{drdr} & 0 \\ 0 & L_{qrqs} & 0 & L_{qrqr} \end{bmatrix} \begin{bmatrix} I_{ds} \\ I_{qs} \\ I_{dr} \\ I_{qr} \end{bmatrix}. & (3.2) \end{cases}$$

In (3.1) and (3.2), there are no mutual cross-coupling inductances and for round-rotor, the respective stator and rotor self inductances are taken as equal to each other.

Due to saturation, the classical u-axis is shifted by angle γ_v (saliency shift angle) to another magnetic axis identified as v as shown in Fig. 3.1. The v-axis is characterised by the phenomenon of cross-magnetisation [41]. Including cross-axes magnetisation, the WRSM and WRIM total flux linkages of (3.1) and (3.2) are respectively, redefined as

$$v\text{-axis model}\begin{cases} \begin{bmatrix}\Lambda_{ds}\\ \Lambda_{qs}\end{bmatrix} = \begin{bmatrix}L_{dsds} & M_{dsqs} & L_{dsdf}\\ M_{qsds} & L_{qsqs} & 0\end{bmatrix}\begin{bmatrix}I_{ds}\\ I_{qs}\\ I_{df}\end{bmatrix} & (3.3)\\ \begin{bmatrix}\Lambda_{ds}\\ \Lambda_{qs}\\ \Lambda_{dr}\\ \Lambda_{qr},\end{bmatrix} = \begin{bmatrix}L_{dsds} & M_{dsqs} & L_{dsdr} & 0\\ M_{qsds} & L_{qsqs} & 0 & L_{qsqr}\\ L_{drds} & 0 & L_{drdr} & M_{drqr}\\ 0 & L_{qrqs} & M_{qrdr} & L_{qrqr}\end{bmatrix}\begin{bmatrix}I_{ds}\\ I_{qs}\\ I_{dr}\\ I_{qr}\end{bmatrix}. & (3.4)\end{cases}$$

Furthermore, due to the stator and rotor reaction during operation, the motor magnetic axis is dragged away from the original dq-axes because of asymmetric saturation. Henceforth, the v-axis is shifted by an angle $\Delta\gamma$ (magnetic axis position error) to an axis identified as w shown in Fig. 3.1. Modelling on the w-axis, redefines respectively, (3.3) and (3.4) as

$$w\text{-axis model}\begin{cases} \begin{bmatrix}\Lambda_{ds}\\ \Lambda_{qs}\end{bmatrix} = \begin{bmatrix}L_{dsds} & M_{dsqs} & L_{dsdf}\\ M_{qsds} & L_{qsqs} & M_{qsdf}\end{bmatrix}\begin{bmatrix}I_{ds}\\ I_{qs}\\ I_{df}\end{bmatrix} & (3.5)\\ \begin{bmatrix}\Lambda_{ds}\\ \Lambda_{qs}\\ \Lambda_{dr}\\ \Lambda_{qr}\end{bmatrix} = \begin{bmatrix}L_{dsds} & M_{dsqs} & L_{dsdr} & M_{dsqr}\\ M_{qsds} & L_{qsqs} & M_{qsdr} & L_{qsqr}\\ L_{drds} & M_{drqs} & L_{drdr} & M_{drqr}\\ M_{qrds} & L_{qrqs} & M_{qrdr} & L_{qrqr}\end{bmatrix}\begin{bmatrix}I_{ds}\\ I_{qs}\\ I_{dr}\\ I_{qr}\end{bmatrix}. & (3.6)\end{cases}$$

As mentioned in the introduction of this chapter, most industrial motors either operate near saturation or heavily saturated, thus the phenomena of cross-magnetisation, saturation-saliency and asymmetric-saturation will always exist in most saturated electric motors. Hence, modelling on the w-axis which results into (3.5) and (3.6) for the WRSM and WRIM respectively, is considered complete in the modelling of the motor types under study. Corresponding to the equations of (2.61) and (2.62), the respective motor terminal voltages for the performance calculation can only be correctly computed by determining the self-inductances (L_{dsds}, L_{qsqs}, L_{drdr}, L_{qrqr}), the effect of d-axis current on the d-axis inductance (L_{dsdf}, L_{dsdr}, L_{drds}), the effect of the q-axis current on the q-axis inductance (L_{qsqr}, L_{qrqs}) and cross-axis inductances (M_{dsqs}, M_{qsds}, M_{qsdf}, M_{dsqr}, M_{qsdr}, M_{drqs}, M_{qrds}, M_{drqr}, M_{qrdr}) as expressed in (3.1)-(3.6).

In addition to the above magnetic axis analysis, it is worth mentioning here that the relationship between the u, and v axes using γ_v (saliency-shift angle) and the u and w axes using γ_w (field-shift angle) of Fig.3.1 is of great importance in both the design and control of electrical machines, especially cylindrical rotor synchronous machines. This is because the rotor types suffer heavily from asymmetric saturation due to the magnetic field drag in the available cylindrical space caused by the field reaction.

Formulations have been derived for SMs to give the relationships between the magnetic axes of Fig. 3.1. One typical example is where sensorless control designers have relied on the saliency-shift angle γ_v. In the analysis, γ_v is derived for the permanent magnet machines in zeroing the mutual

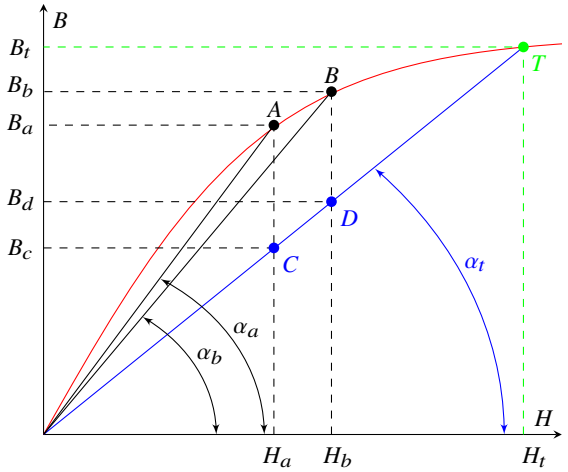

$$H_t = H_a + H_b$$
$$B_t = B_a + B_b$$
$$\alpha_a < \alpha_t$$
$$\alpha_b < \alpha_t$$

Figure 3.2: First-quadrant BH curve for frozen permeability approach.

inductances M_{dsqs}, M_{qsds} of (3.3) as [12]

$$\gamma_v = 0.5 \tan^{-1}\left(\frac{M_{dsqs} + M_{qsds}}{|L_{dsds} - L_{qsqs}|}\right). \tag{3.7}$$

This (3.7) shifts the magnetic axis from the u-axis axis to the v-axis and vice versa, using the transformation angle shift technique (shown in Section 4.3).

Despite of the saliency-shift angle being well known, the field-shift angle is rarely analysed in literature [97]. In this study, the rotation matrix is used to formulate γ_w in zeroing M_{qsdf} of (3.5). Using the rotation matrix, the field inductances of the new w-axis from the u-axis for a p-pole pair motor are expressed as

$$\begin{cases} L'_{dsdf} = L_{dsdf}\cos(\theta_s) - M_{qsdf}\sin(\theta_s) = L_{af}\cos[p(\theta_m + \gamma_w)] \\ M'_{qsdf} = L_{dsdf}\sin(\theta_s) + M_{qsdf}\cos(\theta_s) = L_{af}\sin[p(\theta_m + \gamma_w)], \end{cases} \tag{3.8}$$

where $L_{af} = \sqrt{L_{dsdf}^2 + M_{qsdf}^2}$ and

$$\gamma_w = -0.5 \tan^{-1}\left(\frac{M_{qf}}{L_{df}}\right). \tag{3.9}$$

In (3.9), θ_m is the mechanical angle of the rotor position defined in Section 3.4. The application of (3.9) on the considered WRSM geometry managed to shift the magnetic axis from the v-axis to the w-axis, as shown later in the application example of Sub-section 4.2 in Chapter 4.

3.3. Frozen permeability method

Despite the modelling the motor on the w-axis of Fig. 3.1 being complete, the accuracy of (3.5) and (3.6) depends on the estimation accuracy of the inductances, and hence the method of inductance estimation is crucial. This is not an easy task due to non-uniform saturation and the presence of the heavy armature reaction especially in case of the WRSM.

In [81, 82], the frozen permeability method is used for the first time on WRSM and WRIM, which

is generally applied these days to PM machines [11, 20, 23, 38, 44, 124, 132]. Authors such as M. Ge [45] and N. Kumar [31] have also used the method in the separation of torque components of hybrid PM variable-flux machines, and C. Hittinger [19] in modelling IPMSM for sensorless position estimation. J.A. Walker and D. G. Dorrell [131] verified the frozen permeability method on the IPMSM. The authors concluded that the accuracy of the method can be increased by refining the mesh. Currently, the frozen permeability method is well recognised in both the design and control of electric machines.

To have a better understanding and illustration of the principle of the frozen permeability method, the above-cited literature including [24, 124] and [138] are good examples followed in this study. The method is implemented in the FEM for the separation of the total magnetic flux linkage of the electric motor into the corresponding contributions from different excitations.

Considering the magnetic curve of Fig. 3.2 to which the BH curve of a ferrous lamination material is shown, the total flux linkages at an operating point (position T) can be separated into two single excitation components. The components consist of flux linkages due to the rotor (position A) and stator (position B) excitations. In Fig. 3.2, it is clear to perceive that without using frozen method

$$B_t \neq B_a + B_b = H_a \tan(\alpha_a) + H_b \tan(\alpha_b), \tag{3.10}$$

when using the conventional non-linear FEM. In (3.10), the unfrozen permeabilities are given by

$$\begin{cases} \mu_a = \dfrac{B_a}{H_a} = \tan(\alpha_a) \\ \mu_b = \dfrac{B_b}{H_b} = \tan(\alpha_b). \end{cases} \tag{3.11}$$

However, in the case of the frozen permeability method, the magnetic permeabilities of every mesh element obtained from the double excitation non-linear FEM solution are frozen. At this instant, the problem becomes linear, i.e. using the frozen μ_t shown in Fig. 3.2 with all the excitations. The solution for stator and rotor excitations are then shown in Fig. 3.2 as positions C and D. The transformed non-linear to linear problem relationship becomes

$$B_t = \begin{cases} B_c + B_d \\ H_t \tan(\alpha_t), \end{cases} \tag{3.12}$$

where the frozen permeabilities are given by

$$\mu_t = \begin{cases} \dfrac{B_t}{H_t} \\ \tan(\alpha_t). \end{cases} \tag{3.13}$$

Thus the implementation procedure described above makes it possible to separate self and mutual inductances of (3.1)-(3.6) to the accurate calculation of the motor types' terminal voltages of (2.61) and (2.62) for the motor performance. Figure 3.3 shows a flow diagram of the simulation procedure using the frozen permeability method according to [81].

Note in this study it is perceived that the principle of the frozen permeability method is essential to reveal the influence of magnetic saturation, as well as carry out the separation of torque components.

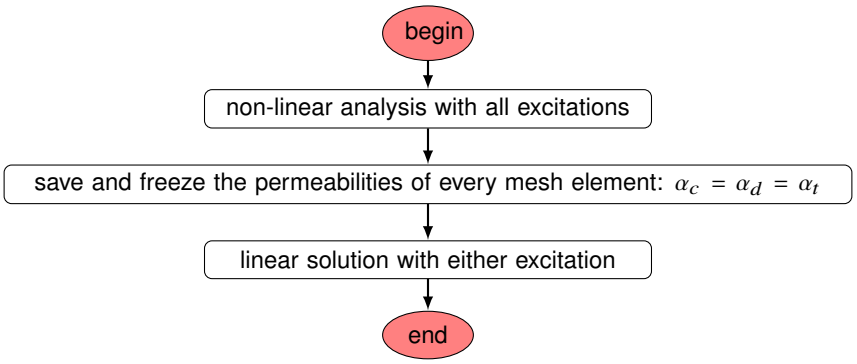

Figure 3.3: Implementation procedure of the frozen permeability method.

3.4. Grid-connected WRSM model approach

As explained in [85], one of the important calculations for grid-connected WRSM is the computation of the excitation requirements under load i.e. finding the necessary currents for a given load. Furthermore, in FEM as explained in Sub-section 2.2.8, the current is normally an input which also allows for the position of the d-axis to be known. With the above mentioned issues, the analysis of the grid-connected WRSM generally becomes complicated when using the FEM. This is because the stator terminal voltages, i.e. grid voltage, is fixed with only varying voltage angle δ_s, shown in Fig. 2.6 caused by the load.

The proposed grid-connected model approach presented in this section is a classical adapted FEM analysis approach in which the FEM model is solved in conjunction with the motor phasor diagram equations using iterative processes as given in [85]. The purpose of the approach is to provide simple, fast but very accurate techniques to predict the grid-connected WRSM motor type performance, as illustrated in the following sections.

3.4.1. Current solution calculation using iterative processes

In Section 2.2.3, the instantaneous values of the three-phase system are represented on space as a phasor rotating at synchronous speed ω_s in the dq-axes plane located in the cross-section of the motor. Thus in the FEM model, the steady-state stator current components on the synchronous rotating dq-axes reference frame using (2.15), are given by

$$[I_{dsqs}] = [T(\theta_s)][I_{ABC}], \tag{3.14}$$

where

θ_s - stator electrical phase position angle.

The steady-state three-phase currents $[I_{ABC}]$ of (3.14) at this stage are of (2.13) given as

$$\begin{bmatrix} I_A \\ I_B \\ I_C \end{bmatrix} = \begin{bmatrix} I_s & 0 & 0 \\ 0 & I_s & 0 \\ 0 & 0 & I_s \end{bmatrix} \begin{bmatrix} \cos(\theta_s + \varphi_s) \\ \cos(\theta_s + \varphi_s - \beta_e) \\ \cos(\theta_s + \varphi_s - 2\beta_e) \end{bmatrix}, \tag{3.15}$$

where

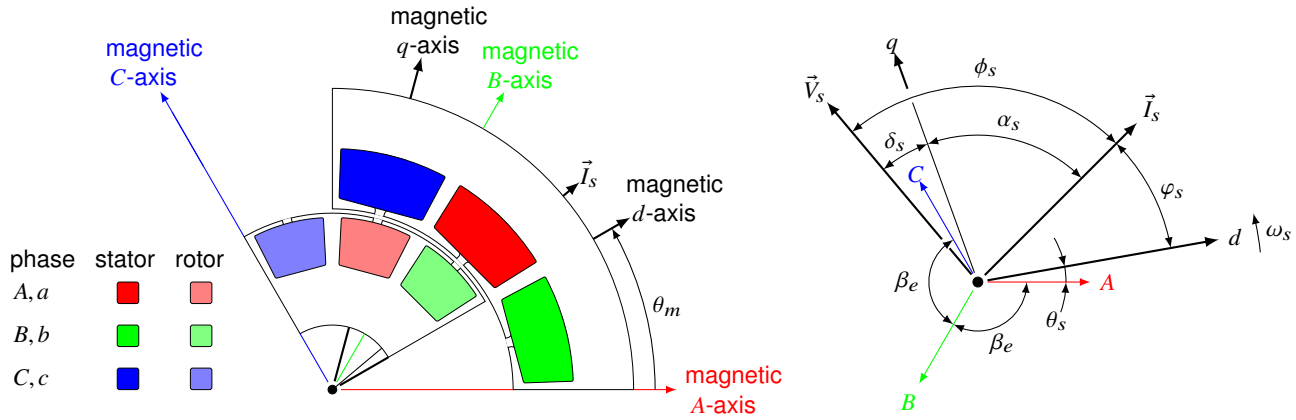

Figure 3.4: Pole face axial view representation showing the dq-axes, voltage and current phasors relationships.

φ_s - electrical angle between the stator current phasor and the magnetic d-axis.

As illustrated in Fig. 2.5 of Section 2.2.3, (3.14) and (3.15) can be represented equivalently by a current phasor $\vec{I}_s$ which if only the fundamental is considered, rotates at ω_s. The rotating current phasor components given in (3.14) are thus given by

$$\vec{I}_s = \begin{bmatrix} I_{ds} \\ I_{qs} \end{bmatrix} = \begin{bmatrix} 0 & I_s \\ I_s & 0 \end{bmatrix} \begin{bmatrix} \sin(\varphi_s) \\ \cos(\varphi_s) \end{bmatrix}. \tag{3.16}$$

In light of the above derivations, Fig. 3.4 shows the relations between the rotating stator current phasor and the dq-axes located on the cross-section of the motor. In Fig. 3.4, the left and right figures show the mechanical and electrical phasor representation respectively. The link between the two figures is through the relationship between mechanical rotor position θ_m and the electrical phase position or transformation angle θ_s (used in the analysis) through the number of motor pole pairs p as

$$\theta_s = p\theta_m. \tag{3.17}$$

From (3.16), the current phasor is shifted by angle φ_s from the d-axis, as defined in Fig. 3.4. Thus, knowing the current phasor of (3.16), the motor stator terminal voltage phasor $\vec{V}_s$ leading the current phasor by angle ϕ_s (i.e. power factor angle) is defined by

$$\vec{V}_s = \begin{bmatrix} V_{ds} \\ V_{qs} \end{bmatrix} = \begin{bmatrix} 0 & -V_s \\ V_s & 0 \end{bmatrix} \begin{bmatrix} \sin(\phi_s + \varphi_s) \\ \cos(\phi_s + \varphi_s) \end{bmatrix}, \tag{3.18}$$

where

V_s - maximum value of the stator voltage waveform.

The maximum value of the stator voltage waveform defining the phasor of (3.18) is the sum of the voltage drops across the main- and end-winding impedances as discussed in Sub-section 2.2.8. Using (2.61) for steady-state analysis, the motor terminal voltages of (3.18) and rotor are respectively expressed as

$$\begin{bmatrix} V_{ds} \\ V_{qs} \end{bmatrix} = \begin{bmatrix} 0 & -V_s \\ V_s & 0 \end{bmatrix} \begin{bmatrix} \sin(\phi_s + \varphi_s) \\ \cos(\phi_s + \varphi_s) \end{bmatrix} = \begin{bmatrix} R_s & -\omega_s L_{es} \\ \omega_s L_{es} & R_s \end{bmatrix} \begin{bmatrix} I_{ds} \\ I_{qs} \end{bmatrix} + \begin{bmatrix} 0 & -\omega_s \\ \omega_s & 0 \end{bmatrix} \begin{bmatrix} \Lambda_{ds} \\ \Lambda_{qs}, \end{bmatrix} \tag{3.19}$$

and

$$V_{df} = k_{dc} R_f I_{df}, \tag{3.20}$$

where

R_s - sum of stator main- and end-winding resistance,
R_f - sum of rotor main- and end-winding resistance and
k_{dc} - rotor resistance constant calculated from the equivalent rotor resistance.

The model parameters of (3.19) and (3.20) are calculated as described in Section 2.3 in which Λ_{ds} and Λ_{qs} are of (3.5).

The important feature of the above described approach to determine (3.19), is based on the fact that the FEM in its basic form requires defined currents, i.e. $\vec{I}_s$ and I_{df}, whereas for grid-connected motors relates to the defined grid voltage, i.e. $\vec{V}_g$. For that, iterative processes are proposed to solve for currents of (3.16), in alternation with the FEM, in evaluate the motor flux distribution for the prescribed grid voltage. This grid voltage phasor is defined by

$$\vec{V}_g = \begin{bmatrix} V_{dg} \\ V_{qg} \end{bmatrix} = \begin{bmatrix} -V_g & 0 \\ 0 & V_g \end{bmatrix} \begin{bmatrix} \sin(\delta_g) \\ \cos(\delta_g) \end{bmatrix}, \tag{3.21}$$

where

V_g - maximum value of the grid voltage waveform and
δ_g - grid voltage or load angle.

From (3.21), the grid voltage V_g is shifted by angle δ_g from the q-axis which is orthogonal to the d-axis. For simulation purposes and following (3.21), (3.19) is redefined using the stator voltage angle δ_s as

$$\begin{bmatrix} V_{ds} \\ V_{ds} \end{bmatrix} = \begin{bmatrix} -V_s & 0 \\ 0 & V_s \end{bmatrix} \begin{bmatrix} \sin(\delta_s) \\ \cos(\delta_s) \end{bmatrix} = \begin{bmatrix} R_s & -\omega_s L_{es} \\ \omega_s L_{es} & R_s \end{bmatrix} \begin{bmatrix} I_{ds} \\ I_{qs} \end{bmatrix} + \begin{bmatrix} 0 & -\omega_s \\ \omega_s & 0 \end{bmatrix} \begin{bmatrix} \Lambda_{ds} \\ \Lambda_{qs}, \end{bmatrix} \tag{3.22}$$

where $\vec{V}_s$ is shifted by δ_s from the q-axis. Figure 3.5 shows the phasor diagram of the current solution calculation method resulting from (3.21) and (3.22) at an instant when the A and d magnetic axes shown aligned, thus $\theta_m = 0$ from Fig. 3.4. From the voltage equations of (3.20) and (3.22), the WRSM equivalent circuit diagram of Fig. 2.10 is also valid for the steady-state analysis of the grid-connected motor.

To find the current solution for the WRSM performance calculation, the FEM model is solved in conjunction with the phasor diagram of Fig. 3.5 using an iterative process as explained in Fig. 3.6. Combining (3.20), and (3.22) and modelling on the w-axis, shown in Fig. 3.1, which results in flux linkages of (3.5), the motor stator and rotor assembled terminal voltages of Fig. 3.6 result in a column matrix as

$$\begin{bmatrix} V_{ds} \\ V_{qs} \\ V_{df} \end{bmatrix} = \begin{bmatrix} (R_s - \omega_s M_{qsds}) & -\omega_s (L_{qsqs} + L_{es}) & \omega_s M_{qsdf} \\ \omega_s (L_{dsds} + L_{es}) & (R_s + \omega_s M_{dsqs}) & \omega_s L_{dsdf} \\ 0 & 0 & k_{dc} R_f \end{bmatrix} \begin{bmatrix} I_{ds} \\ I_{qs} \\ I_{df} \end{bmatrix}, \tag{3.23}$$

simplified to

$$[V] = [Z][I], \tag{3.24}$$

where

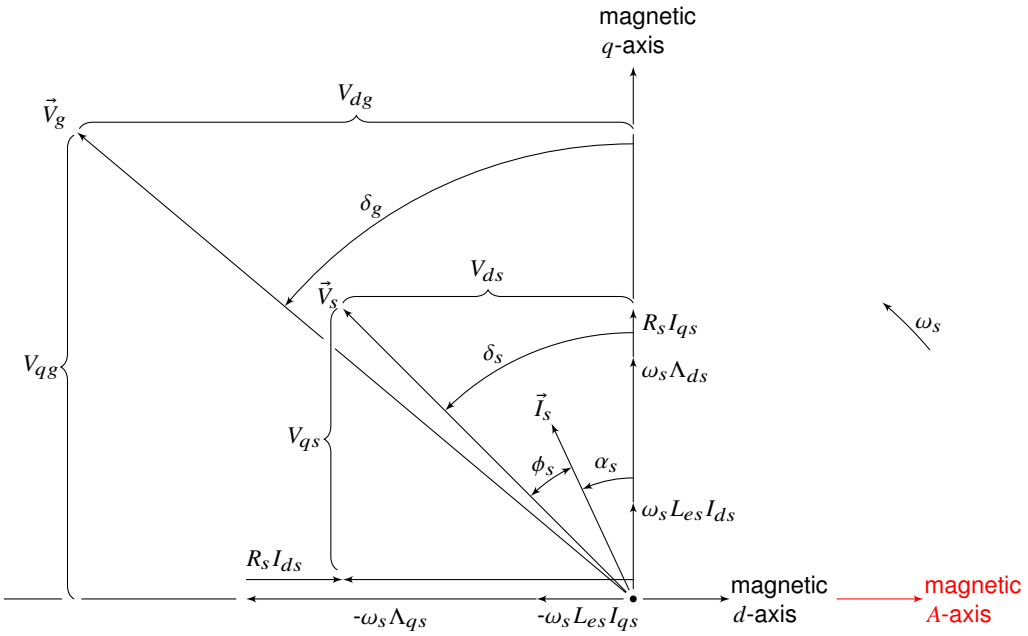

Figure 3.5: Grid-connected WRSM grid voltage, stator terminal voltage and current relationship phasor diagram.

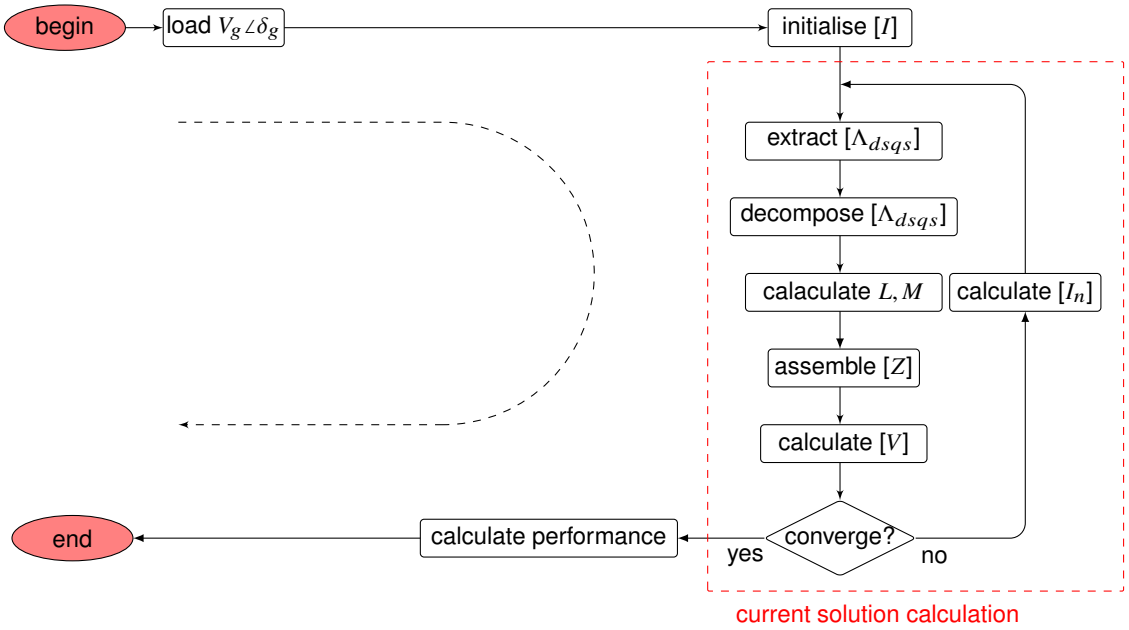

Figure 3.6: Grid-connected WRSM iterative process flow diagram for parameter and performance calculation.

$[V]$ - voltage matrix,
$[Z]$ - impedance matrix and
$[I]$ - current matrix.

Thus the voltage matrix of (3.24) is in the form of the product of the impedance and current matrices.

As explained in the principle operation of the SM in Sub-section 1.2.2, on the application of the mechanical load on the motor shaft, the rotor slows with respect to the rotating magnetic field of the stator, developing torque, continuously drawn around by the rotating field. The angle between the stator and the rotor fields (i.e. load angle) increases as the load torque increases until maximum accessible torque of the motor is reached. For constant field excitation I_{df}, the motor loading (load $V_g \angle \delta_g$ step) in the iterative process of Fig. 3.6 is facilitated on the defined V_g using the grid load angle

δ_g.

From Fig. 3.6, the initial current $[I]$ is used to calculate the inductance parameters to assemble $[Z]$. With the $[I]$ and $[Z]$, $[V]$ of (3.23) is computed. The computed stator voltage in $[V]$ might not be equal to the defined grid voltage V_g and angle δ_g. For that, new currents are computed iteratively until the grid and stator voltages converge. At this point, the performance of the motor can be determined.

Since the motor is modelled on the w-axis, to extract the total flux linkages of (3.5) the motor at its loading point is excited in the FEM by all the currents I_{ds}, I_{qs} and I_{df}. The inverse Park Transformation $[T]^{-1}$ is then used from (3.14) to get the initial stator phase current of (3.15) as

$$[I_{ABC}] = [T]^{-1}[I_{dsqs}]. \tag{3.25}$$

The phase currents of (3.25) are then used to compute the three-phase total net flux linkages $[\Lambda_{ABC}]$ from the non-linear FEM analysis under the stated current operating point. The Park Transformation is again used to compute the total dq-axes flux linkages of (3.5) (extract $[\Lambda_{dsqs}]$ step in Fig. 3.6), and shown in Fig 3.5 as

$$[\Lambda_{dsqs}] = [T][\Lambda_{ABC}]. \tag{3.26}$$

Because it is impossible to implement the conventional non-linear FEM analysis to decompose the total flux linkages of (3.26), the frozen permeability method discussed in Section 3.3 is employed to separate the total magnetic flux of the motor into corresponding contributions of the different excitations. Three FEM linear solutions due to either I_{ds}, I_{qs} and or I_{df} are necessary to decompose the total flux linkage of (3.26) as expressed in (3.5). Note that the summation of the different dq-axes linear flux linkage solution components must be equal to the non-linear total flux linkage solution.

The above WRSM total flux linkage decomposition using the frozen permeability method, following Fig. 3.3 is described in the following steps:

i. A non-linear FEM solution at the desired operating point at a rotor position is conducted. From this solution, the total flux linkages produced in the active stack length are calculated, defined by

$$\left.\begin{aligned} \Lambda_{ds} &= L_{ds}I_{ds} = \Lambda_{ds}(I_{ds}, I_{qs}, I_{df}) \\ \Lambda_{qs} &= L_{qs}I_{qs} = \Lambda_{qs}(I_{ds}, I_{qs}, I_{df}) \end{aligned}\right\} \quad \text{with all} \quad I_{ds},\ I_{qs} \ \text{and} \ I_{df} \ \text{excitation}, \tag{3.27}$$

which in turn can be used to calculate the electromagnetic torque according to (2.64) and also the actual torque of the motor by means of the magnetic stress tensor method.

ii. The FEM permeabilities of all the mesh elements of step (i) are saved and frozen. This enables saturation levels remain constant with different excitations.

iii. Using the frozen permeabilities and the same model of steps (i) and (ii), the decomposed dq-axes flux linkages from (3.5) are solved using the single excitations defined as

$$\left.\begin{aligned} \Lambda_{dsds}(I_{ds}) &= L_{dsds}I_{ds} = \Lambda_{ds}(I_{ds}, 0, 0) \\ \Lambda_{qsds}(I_{ds}) &= M_{qsds}I_{ds} = \Lambda_{qs}(I_{ds}, 0, 0) \end{aligned}\right\} \quad \text{when} \quad I_{qs} = I_{df} = 0, \tag{3.28}$$

$$\left.\begin{aligned} \Lambda_{dsqs}(I_{qs}) &= M_{dsqs}I_{qs} = \Lambda_{ds}(0, I_{qs}, 0) \\ \Lambda_{qsqs}(I_{qs}) &= L_{qsqs}I_{qs} = \Lambda_{qs}(0, I_{qs}, 0) \end{aligned}\right\} \quad \text{when} \quad I_{ds} = I_{df} = 0, \tag{3.29}$$

$$\left.\begin{array}{ll} \Lambda_{dsdf}(I_{df}) & = L_{dsdf} I_{df} = \Lambda_{ds}(0,0,I_{df}) \\ \Lambda_{qsdf}(I_{df}) & = M_{qsdf} I_{df} = \Lambda_{qs}(0,0,I_{df}) \end{array}\right\} \quad \text{when} \quad I_{ds} = I_{qs} = 0. \tag{3.30}$$

The self L and mutual M inductance parameters of Fig. 3.6 are calculated from the three linear solutions of (3.28)-(3.30) respectively, as

$$\begin{cases} L_{dsds} = \dfrac{\Lambda_{dsds}}{I_{ds}} \\ M_{qsds} = \dfrac{\Lambda_{qsds}}{I_{ds}}, \end{cases} \tag{3.31}$$

$$\begin{cases} M_{dsqs} = \dfrac{\Lambda_{dsqs}}{I_{qs}} \\ L_{qsqs} = \dfrac{\Lambda_{qsqs}}{I_{qs}}, \end{cases} \tag{3.32}$$

$$\begin{cases} L_{dsdf} = \dfrac{\Lambda_{dsdf}}{I_{df}} \\ M_{qsdf} = \dfrac{\Lambda_{qsdf}}{I_{df}}. \end{cases} \tag{3.33}$$

From (3.31)-(3.33), the total flux inductance of (3.27), are thus given by

$$\begin{cases} L_{ds} = \dfrac{\Lambda_{ds}}{I_{ds}} = L_{dsds} + M_{dsqs}\dfrac{I_{qs}}{I_{ds}} + L_{dsdf}\dfrac{I_{df}}{I_{ds}} \\ L_{qs} = \dfrac{\Lambda_{qs}}{I_{qs}} = M_{qsds}\dfrac{I_{ds}}{I_{qs}} + L_{qsqs} + M_{qsdf}\dfrac{I_{df}}{I_{qs}}. \end{cases} \tag{3.34}$$

Following Fig. 3.6, using calculated inductance parameters of (3.31)-(3.33), the impedance matrix $[Z]$ is assembled which is used to calculate the motor terminal voltages of (3.23).

As observed from Fig. 3.6, the process is repeated in an iterative manner at the defined grid voltage, each cycle calculating new currents $[I_n]$ until convergence. The new currents are calculated from

$$[I_n] = [Z]^{-1}[V_n] \tag{3.35}$$

where the $[V_n]$ is defined by the grid voltage of (3.21) as

$$[V_n] = \begin{bmatrix} V_{dg} \\ V_{qg} \\ V_{df} \end{bmatrix}. \tag{3.36}$$

The convergence state is defined when there is no significant change noticed in all the motor parameters and performances. The convergence is facilitated by using any motor parameter or performance, e.g. using V_s, the cycle can be terminated when

$$|V_s - V_g| \leqslant \nu(\frac{V_s + V_g}{2}), \tag{3.37}$$

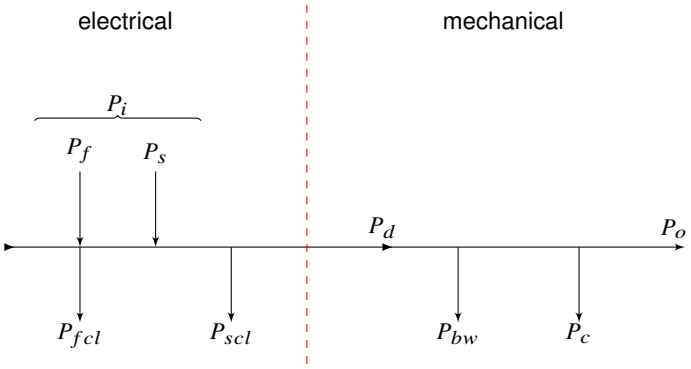

Figure 3.7: Grid-connected WRSM simplified power flow diagram.

where

ν - fraction tolerance (significance in parameter change) in the parameter value.

At the point of convergence, it can be confirmed that the solved new current $[I_n]$ of (3.35) is the correct required excitation for the WRSM at the set $[V_n]$ of (3.36) holding the defined grid voltage.

3.4.2. Performance calculation

It is the solved currents of (3.35), after the iterative process convergence, that are used to excite the motor in order to calculate other important performances of the motor. Knowing the voltage and current phasors, the power factor is easily computed using (2.21) as

$$\cos(\phi_s) = \frac{V_{ds}I_{ds}}{V_s I_s} - \frac{V_{qs}I_{qs}}{V_s I_s}. \tag{3.38}$$

The percentage efficiency of the motor is calculated from the simplified power flow diagram of Fig. 3.7 as

$$\eta = \frac{P_o}{P_i} \times 100, \tag{3.39}$$

where

P_i - electrical input power and
P_o - mechanical output power.

In (3.39), the electrical power is defined as the sum of the stator and rotor electrical input power, given as

$$P_i = P_s + P_f = P_o + P_l. \tag{3.40}$$

The total energy supplied to the field coils P_f is constant and all of it is consumed as copper losses in the field windings. In (3.40), excluding stray losses, P_l is the total losses expressed as

$$P_l = P_{scl} + P_{fcl} + P_{bw} + P_c, \tag{3.41}$$

where

P_{scl} - stator copper losses,
P_{fcl} - field copper losses,
P_{bw} - bearing and windage losses and
P_c - core losses.

The stator and field windings copper losses of (3.41) are respectively, given by

$$\begin{cases} P_{scl} = 1.5 I_s^2 R_s \\ P_{fcl} = k_{dc} I_{df}^2 R_f. \end{cases} \tag{3.42}$$

The mechanical losses, which are comprised of bearing and windage losses i.e. $P_{bw} = P_b + P_w$ are, respectively given in [63] as

$$\begin{cases} P_b = 0.5 \omega_r \mu_f F d_b \\ P_w = k_\rho D_r (l + 0.6\tau_p) v_r^2, \end{cases} \tag{3.43}$$

where

F - bearing load,
μ_f - bearing friction coefficient,
v_r - shaft surface speed,
τ_p - pole pitch length,
d_b - inner diameter of the shaft taken as the rotor inner diameter and
ω_r - shaft angular frequency.

For the 2D lamination of the motor shown in Fig. 3.8, the core losses are estimated from

$$P_c = \overbrace{c f_s^x (B_{ts}^y M_{ts} + B_{ys}^y M_{ys})}^{\text{stator}} + \overbrace{c f_r^x (B_{tr}^y M_{tr} + B_{yr}^y M_{yr})}^{\text{rotor}}, \tag{3.44}$$

where for the respective motor stator and rotor

B_t - teeth maximum flux density,
B_y - yoke maximum flux density,
M_t - teeth mass and
M_y - yoke mass.

The core-loss equation constants c, x and y are given in Appendix B.2 according to [83]. Figure 3.8 indicates the positions of the teeth and yoke where samples are done to obtain the flux densities and mass of (3.44).

From Fig. 3.7 , the mechanical power output of (3.39) is calculated from

$$P_o = P_d - (P_{bw} + P_c). \tag{3.45}$$

P_d is the mechanical developed power expressed as

$$P_d = \omega_r T_d, \tag{3.46}$$

where the developed torque T_d (of three components) defined by (2.23) is calculated from the total

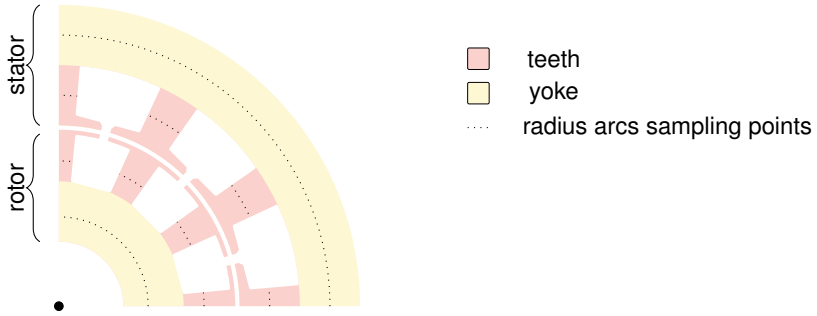

Figure 3.8: Pole face axial view lamination showing stator-rotor teeth and yoke sampling points for core loss calculation.

flux linkages expressed as functions of inductance parameters given by

$$T_d = T_f + T_s + T_m. \tag{3.47}$$

The torque components of (3.47) for a p pole pair grid-connected WRSM following (3.31)-(3.33) are given by [81]

$$\begin{cases} T_f = 1.5p(L_{dsdf} I_{qs} - M_{qsdf} I_{ds}) I_{df} \\ T_s = 1.5p(L_{dsds} - L_{qsqs}) I_{ds} I_{qs} \\ T_m = 1.5p(M_{dsqs} I_{qs}^2 - M_{qsds} I_{ds}^2, \end{cases} \tag{3.48}$$

where

T_f - field flux torque,
T_s - saliency torque and
T_m - cross-magnetisation torque.

The stator apparent, real and reactive power are respectively, calculated from

$$\begin{cases} S_s = 1.5 V_s I_s \\ P_s = P_i - P_{fcl} \\ Q_s = \sqrt{S_s^2 - P_s^2}. \end{cases} \tag{3.49}$$

The above described modelling equations (3.14)-(3.48) are used in solving the WRSM excitation currents and performances using the iterative process shown in Fig. 3.6. The iterative process utilises static FEM solutions in conjunction with the phasor diagram shown in Fig. 3.5. In all, forms the proposed model approach for parameter and performance prediction of the grid-connected WRSM.

3.5. Grid-connected WRIM modelling approach

In the analysis of the grid-connected WRSM, the problem of finding the stator excitation using phasors is presented, which is also valid in the analysis of the grid-connected WRIM. However, the drawback in the WRIM analysis is the existence of the alternating current not only in the stator but also in the rotor. Thus both stator and rotor current phasors must be determined at defined stator (grid) and rotor (short-circuit) voltage phasors. The defined voltage phasors give complexity in the analysis of grid-connected WRIM. The purpose of the proposed approach is also to provide simple, fast and accurate techniques to predict the grid-connected WRIM motor type performance.

3.5.1. Current solution calculation using iterative processes

To solve the grid-connected WRIM current solution for the excitation problem, the modelling approach of the WRSM in Section 3.4 is followed. The difference is on the rotor side. In the case of WRIM, the rotor voltages are zeroed in which external resistors can be added for start up. This proposed model approach for the WRIM is also discussed in [82].

As mentioned in Section 3.5, the alternating input current in the WRIM rotor side, complicates more the analysis of the motor type when using FEM of the already solved problem in Section 3.4 (stator side currents). It is correct to adapt (3.22) as the known WRIM rotor terminal voltage phasor $\vec{V}_r$ rotating with slip angular speed ω_Δ, given by

$$\begin{bmatrix} V_{dr} \\ V_{dr} \end{bmatrix} = \begin{bmatrix} V_r & 0 \\ 0 & -V_r \end{bmatrix} \begin{bmatrix} \sin(\delta_r) \\ \cos(\delta_r) \end{bmatrix} = \begin{bmatrix} R_r & -\omega_\Delta L_{er} \\ \omega_\Delta L_{er} & R_r \end{bmatrix} \begin{bmatrix} I_{dr} \\ I_{qr} \end{bmatrix} + \begin{bmatrix} 0 & -\omega_\Delta \\ \omega_\Delta & 0 \end{bmatrix} \begin{bmatrix} \Lambda_{dr} \\ \Lambda_{qr} \end{bmatrix}, \tag{3.50}$$

where

R_r - sum of rotor main- and end-winding resistance,

and solve for the unknown rotor current phasor $\vec{I}_r$. Thus, for the grid-connected WRIM, Fig. 3.9 shows the phasor diagram of the current solution calculation method defining the stator δ_s and rotor δ_r voltage angles of (3.22) and (3.50) at an instant when the A and d-axes shown aligned, thus $\theta_m = 0$ from Fig. 3.4. It is important to state that even though $V_r = 0$, it is shown in Fig. 3.9 as $V_r \neq 0$. This is as to have a better understanding of how V_r zeros to the defined rotor voltage $V_0 = 0$ using the proposed WRIM iterative process for parameter and performance calculation. Following the voltage equation of (3.22) and (3.50), the WRIM equivalent circuit of Fig. 2.11 is also valid in the steady-state analysis of the motor type.

Finally, to find the current solution for the motor performance calculations, as in Section 3.4, the iterative process explained in Fig. 3.6 is followed, however, using the FEM in conjunction with the phasor diagram of Fig. 3.9. The current solution calculation is shown in the grid-connected WRIM iterative process flow diagram of Fig. 3.10. Thus combining (3.22) and (3.50) and modelling on the w-axis shown in Fig. 3.1, which results in flux linkages of (3.6), the WRIM stator and rotor assembled terminal voltages of Fig. 3.10 result in a column matrix given by

$$\begin{bmatrix} V_{ds} \\ V_{qs} \\ V_{dr} \\ V_{qr} \end{bmatrix} = \begin{bmatrix} (R_s - \omega_s M_{qsds}) & -\omega_s(L_{qsqs} + L_{es}) & -\omega_s M_{qsdr} & -\omega_s L_{qsqr} \\ \omega_s(L_{dsds} + L_{es}) & (R_s + \omega_s M_{dsqs}) & \omega_s L_{dsdr} & \omega_s M_{dsqr} \\ -\omega_\Delta M_{qrds} & -\omega_\Delta L_{qrqs} & (R_r - \omega_\Delta M_{qrdr}) & -\omega_\Delta(L_{qrqr} + L_{er}) \\ \omega_\Delta L_{drds} & \omega_\Delta M_{drqs} & \omega_\Delta(L_{drdr} + L_{er}) & (R_r + \omega_\Delta M_{drqr}) \end{bmatrix} \begin{bmatrix} I_{ds} \\ I_{qs} \\ I_{dr} \\ I_{qr} \end{bmatrix}, \tag{3.51}$$

and also following (3.24), simplified to

$$[V] = [Z][I]. \tag{3.52}$$

As explained in the principle operation of the IM in Sub-section 1.2.1, the difference in speeds (slip speed) of the stator produced field and the rotor induced field occurs when the motor begins to deliver torque to the load. In the FEM, the rotor does not rotate, it remains stationary $\omega_r = 0$ and the slip speed ω_Δ is the stator speed $\omega_\Delta = \omega_s$. Varying the rotor speed in the FEM from 0 to the stator speed ω_Δ means that the magnetic fields rotate at slip speed with slip speed varying from 0 to synchronous speed ω_s. Hence, the motor loading (load ω_r step) in the iterative process of Fig. 3.10 is facilitated using the slip speed approach in simulating the rotor motion based on the relationship of (2.11). From Fig. 3.10, the initial motor current $[I]$ is used to calculate the inductance parameters to assemble $[Z]$.

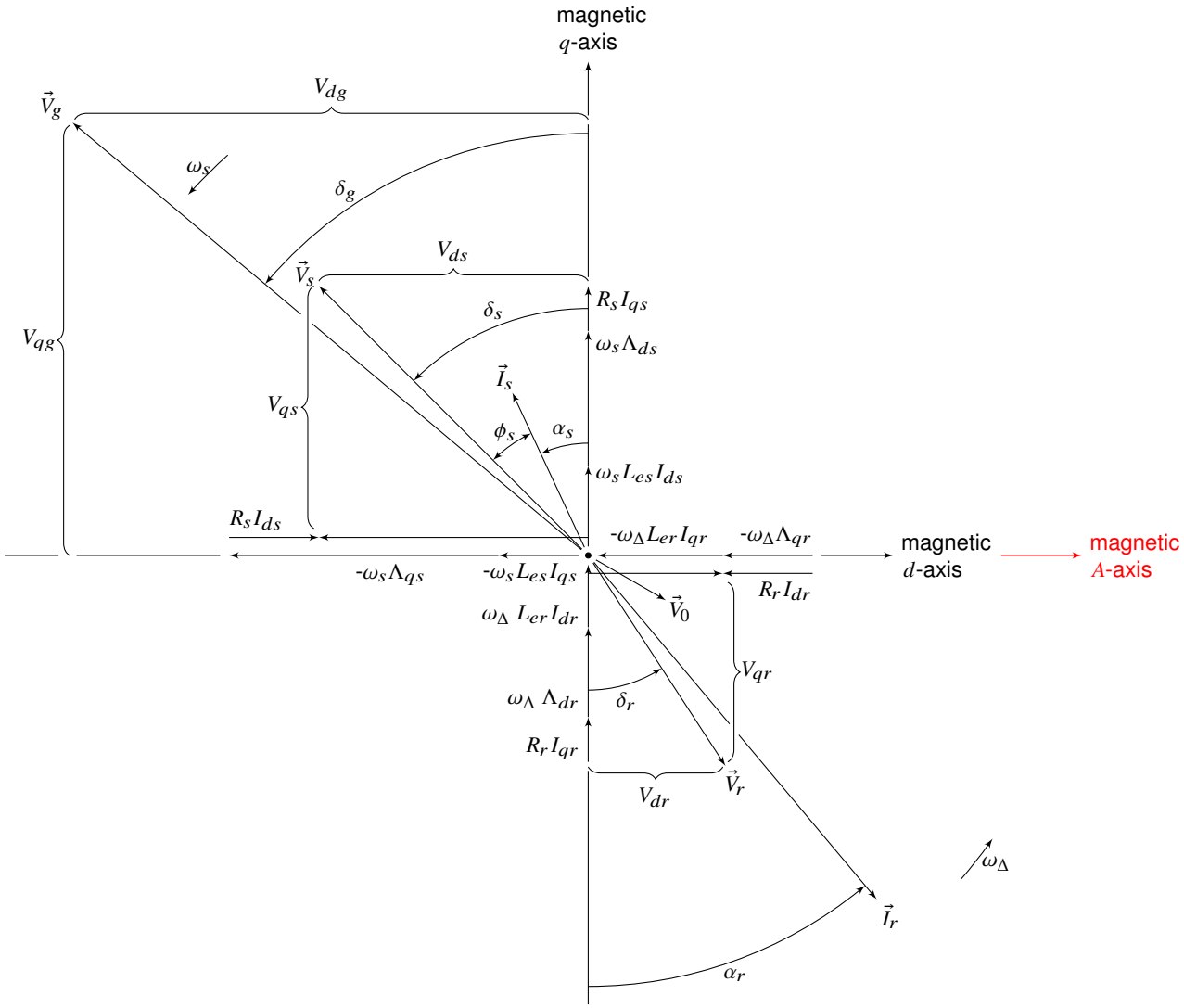

Figure 3.9: Grid-connected WRIM grid voltage, terminal voltages and current phasor diagram.

Using $[I]$ and $[Z]$, $[V]$ of (3.52) is calculated. This calculated stator and rotor voltage might not be equal to the defined grid voltage magnitude V_g and the rotor voltage magnitude of zero $V_0 = 0$ at the specified load. For that, the new currents are computed iteratively until the stator and defined grid voltage converge at the specified motor load. At this instant, the performance of the WRIM can be determined. The desired rotor voltage phasor following (3.21) in Fig. 3.9 is defined by

$$\vec{V}_0 = \begin{bmatrix} V_{d0} \\ V_{q0} \end{bmatrix}. \tag{3.53}$$

Following the WRSM modelling approach in Section 3.5, the WRIM is also modelled on the w-axis. To extract the total flux linkages of (3.6) the WRIM at its loading point is excited in the FEM by all the currents I_{ds}, I_{qs}, I_{dr} and I_{qr}. The inverse Park Transformation is then used to get initial stator of (3.25) and rotor phase currents given by

$$[I_{abc}] = [T(\theta_\Delta)]^{-1}[I_{dsqr}]. \tag{3.54}$$

In (3.54),

$$\theta_\Delta = \theta_s - \theta_r, \tag{3.55}$$

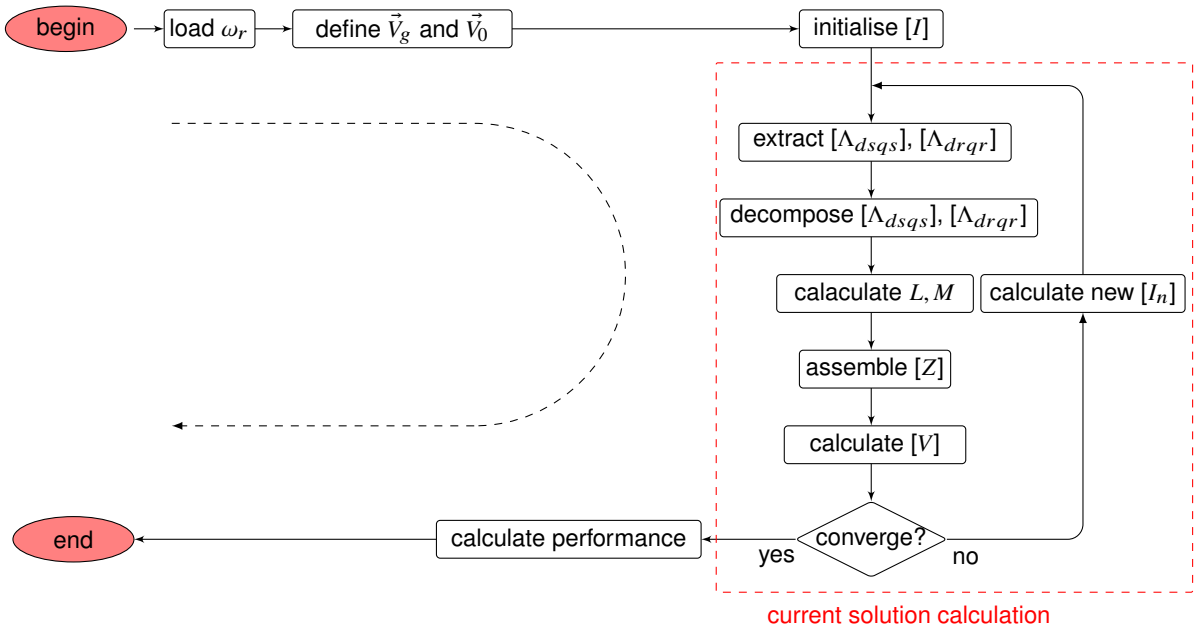

Figure 3.10: Grid-connected WRIM iterative process flow diagram for parameter and performance calculation.

where

θ_Δ - rotor slip electrical phase position angle and
θ_r - rotor electrical phase position angle.

The stator and rotor phase currents of (3.25) and (3.54) respectively are then used to compute the corresponding three-phase total net flux linkages of the stator $[\Lambda_{ABC}]$ and rotor $[\Lambda_{abc}]$ from the non-linear FEM analysis under the stated current operating point. The Park Transformation is also used to compute the total dq-axes flux linkages of (3.6) (extract $\Lambda_{dsqs}, \Lambda_{drqr}$ step in Fig. 3.10). These flux linkages are shown in Fig. 3.9 for the stator as in (3.26) and for the rotor given by

$$[\Lambda_{drqr}] = [T(\theta_\Delta)][\Lambda_{abc}]. \tag{3.56}$$

The FEM based frozen permeability method discussed in Section 3.3 is also used to separate the WRIM rotor total flux linkages of (3.56) as illustrated on the WRSM stator of (3.26). In the case of the WRIM, four FEM linear solutions due to either I_{ds}, I_{qs}, I_{dr} and I_{qr} are necessary to decompose the total flux linkage of stator (3.26) and rotor (3.56) as expressed in (3.6). Note that the summation of the different stator and rotor dq-axes flux linkages solution components must be equal to the respective stator and rotor non-linear total flux linkage solutions.

The above WRIM total flux linkage decomposition using the frozen permeability method, following Fig. 3.3 is described in the following steps:

i. A non-linear FEM solution at the desired operating point at a rotor position is conducted. From this solution, the total flux linkages produced in the active stack length are calculated, defined

by

$$\left.\begin{aligned}\Lambda_{ds} &= L_{ds}I_{ds} = \Lambda_{ds}(I_{ds}, I_{qs}, I_{ds}, I_{qs})\\ \Lambda_{qs} &= L_{qs}I_{qs} = \Lambda_{qs}(I_{ds}, I_{qs}, I_{ds}, I_{qs})\\ \Lambda_{dr} &= L_{dr}I_{dr} = \Lambda_{dr}(I_{ds}, I_{qs}, I_{ds}, I_{qs})\\ \Lambda_{qr} &= L_{qr}I_{qr} = \Lambda_{qr}(I_{ds}, I_{qs}, I_{ds}, I_{qs})\end{aligned}\right\} \text{ with all } I_{ds}, I_{qs}, I_{dr} \text{ and } I_{qr} \text{ excitation,} \tag{3.57}$$

which in turn can be used to calculate the electromagnetic torque according to (2.64) and also the actual torque of the motor by means of the magnetic stress tensor method.

ii. The FEM permeabilities of all the mesh elements of step (i) are saved and frozen. This enables saturation levels not to change with different excitations.

iii. Using the frozen permeabilities and the same model of steps (i) and (ii), the decomposed dq-axes flux linkages from (3.5) are solved using single excitations defined as

$$\left.\begin{aligned}\Lambda_{dsds}(I_{ds}) &= L_{dsds}I_{ds} = \Lambda_{ds}(I_{ds}, 0, 0, 0)\\ \Lambda_{qsds}(I_{ds}) &= M_{qsds}I_{ds} = \Lambda_{qs}(I_{ds}, 0, 0, 0)\\ \Lambda_{drds}(I_{ds}) &= L_{drds}I_{ds} = \Lambda_{dr}(I_{ds}, 0, 0, 0)\\ \Lambda_{qrds}(I_{ds}) &= M_{qrds}I_{ds} = \Lambda_{qr}(I_{ds}, 0, 0, 0)\end{aligned}\right\} \quad \text{when} \quad I_{qs} = I_{dr} = I_{qr} = 0, \tag{3.58}$$

$$\left.\begin{aligned}\Lambda_{dsqs}(I_{qs}) &= M_{dsqs}I_{qs} = \Lambda_{ds}(0, I_{qs}, 0, 0)\\ \Lambda_{qsqs}(I_{qs}) &= L_{qsqs}I_{qs} = \Lambda_{qs}(0, I_{qs}, 0, 0)\\ \Lambda_{drqs}(I_{qs}) &= M_{drqs}I_{qs} = \Lambda_{dr}(0, I_{qs}, 0, 0)\\ \Lambda_{qrqs}(I_{qs}) &= L_{qrqs}I_{qs} = \Lambda_{qr}(0, I_{qs}, 0, 0)\end{aligned}\right\} \quad \text{when} \quad I_{ds} = I_{dr} = I_{qr} = 0, \tag{3.59}$$

$$\left.\begin{aligned}\Lambda_{dsdr}(I_{dr}) &= L_{dsdr}I_{dr} = \Lambda_{ds}(0, 0, I_{dr}, 0, 0)\\ \Lambda_{qsdr}(I_{dr}) &= M_{qsdr}I_{dr} = \Lambda_{qs}(0, 0, I_{dr}, 0, 0)\\ \Lambda_{drdr}(I_{dr}) &= L_{drdr}I_{dr} = \Lambda_{dr}(0, 0, I_{dr}, 0, 0)\\ \Lambda_{qrdr}(I_{dr}) &= M_{qrdr}I_{dr} = \Lambda_{qr}(0, 0, I_{dr}, 0, 0)\end{aligned}\right\} \quad \text{when} \quad I_{ds} = I_{qs} = I_{qr} = 0, \tag{3.60}$$

$$\left.\begin{aligned}\Lambda_{dsqr}(I_{qr}) &= M_{dsqr}I_{qr} = \Lambda_{ds}(0, 0, 0, I_{qr})\\ \Lambda_{qsqr}(I_{qr}) &= L_{qsqr}I_{qr} = \Lambda_{qs}(0, 0, 0, I_{qr})\\ \Lambda_{drqr}(I_{qr}) &= M_{drqr}I_{qr} = \Lambda_{dr}(0, 0, 0, I_{qr})\\ \Lambda_{qrqr}(I_{qr}) &= L_{qrqr}I_{qr} = \Lambda_{qr}(0, 0, 0, I_{qr})\end{aligned}\right\} \quad \text{when} \quad I_{ds} = I_{qs} = I_{dr} = 0. \tag{3.61}$$

The self L and mutual M inductance parameters of Fig. 3.10 are calculated from the four linear solutions of (3.58)-(3.61) as

$$\begin{cases} L_{dsds} = \dfrac{\Lambda_{dsds}}{I_{ds}} \\ M_{qsds} = \dfrac{\Lambda_{qsds}}{I_{ds}} \\ L_{drds} = \dfrac{\Lambda_{drds}}{I_{ds}} \\ M_{qrds} = \dfrac{\Lambda_{qrds}}{I_{ds}}, \end{cases} \tag{3.62}$$

$$\begin{cases} M_{dsqs} = \dfrac{\Lambda_{dsqs}}{I_{qs}} \\ L_{qsqs} = \dfrac{\Lambda_{qsqs}}{I_{qs}} \\ M_{drqs} = \dfrac{\Lambda_{drqs}}{I_{qs}} \\ L_{qrqs} = \dfrac{\Lambda_{qrqs}}{I_{qs}}, \end{cases} \tag{3.63}$$

$$\begin{cases} L_{drdr} = \dfrac{\Lambda_{drdr}}{I_{dr}} \\ M_{qrdr} = \dfrac{\Lambda_{qrdr}}{I_{dr}} \\ L_{dsdr} = \dfrac{\Lambda_{dsdr}}{I_{dr}} \\ M_{qsdr} = \dfrac{\Lambda_{qrdr}}{I_{dr}}, \end{cases} \tag{3.64}$$

$$\begin{cases} M_{drqr} = \dfrac{\Lambda_{drqr}}{I_{qr}} \\ L_{qrqr} = \dfrac{\Lambda_{qrqr}}{I_{qr}} \\ M_{dsqr} = \dfrac{\Lambda_{dsqr}}{I_{qr}} \\ L_{qsqr} = \dfrac{\Lambda_{qsqr}}{I_{qr}}. \end{cases} \tag{3.65}$$

From (3.62)-(3.65), the total flux inductances of (3.57) are given by

$$\begin{cases} L_{ds} = \dfrac{\Lambda_{ds}}{I_{ds}} = L_{dsds} + L_{dsdr}\dfrac{I_{dr}}{I_{ds}} + M_{dsqs}\dfrac{I_{qs}}{I_{dr}} + M_{dsqr}\dfrac{I_{qr}}{I_{ds}} \\ L_{qs} = \dfrac{\Lambda_{qs}}{I_{qs}} = L_{qsqs} + L_{qsqr}\dfrac{I_{qr}}{I_{qs}} + M_{qsds}\dfrac{I_{ds}}{I_{qs}} + M_{qsdr}\dfrac{I_{dr}}{I_{qs}} \\ L_{dr} = \dfrac{\Lambda_{dr}}{I_{dr}} = L_{drdr} + L_{drds}\dfrac{I_{ds}}{I_{dr}} + M_{drqr}\dfrac{I_{qr}}{I_{dr}} + M_{drqs}\dfrac{I_{qs}}{I_{dr}} \\ L_{qr} = \dfrac{\Lambda_{qr}}{I_{qr}} = L_{qrqr} + L_{qrqs}\dfrac{I_{qs}}{I_{qr}} + M_{qsds}\dfrac{I_{ds}}{I_{qr}} + M_{qsdr}\dfrac{I_{dr}}{I_{qr}}. \end{cases} \tag{3.66}$$

Using calculated inductance parameters of (3.62)-(3.65), the impedance matrix $[Z]$ is assembled which is used to calculate the motor terminal voltages of (3.51).

As observed from Fig. 3.10, the process is repeated in an iterative manner at the defined grid and rotor voltage, each cycle calculating new current $[I_n]$ until convergence. This new current is calculated from

$$[I_n] = [Z]^{-1}[V_n] \tag{3.67}$$

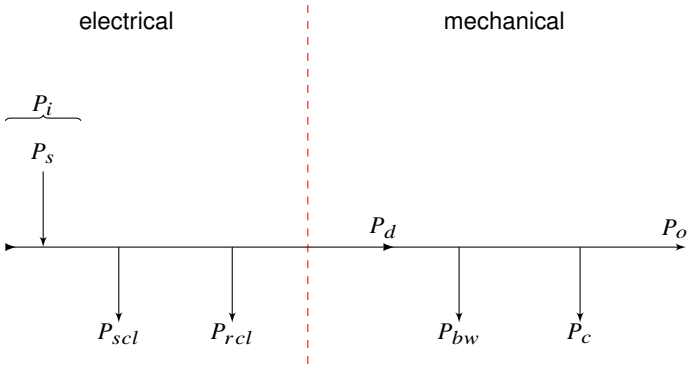

Figure 3.11: Grid-connected WRIM simplified power flow diagram.

where $[V_n]$ is defined by both grid and rotor voltages of (3.21) and $\vec{V}_0$ of (3.53) respectively, as

$$[V_n] = \begin{bmatrix} V_{dg} \\ V_{qg} \\ V_{d0} \\ V_{q0} \end{bmatrix}. \tag{3.68}$$

The convergence state is also facilitated by using any motor parameter or performance e.g. as of (3.37).

At this point of convergence, it can be confirmed that the solved new current of (3.67) is the correct required excitation for the WRIM at the set $[V_n]$ of (3.68) holding the defined grid and rotor voltage.

3.5.2. Performance calculation

It is the solved current of (3.67) after the iterative process convergence which is used to excite the WRIM in the FEM in order to calculate the motor performance. As the stator voltage and current phasors are now known, the WRIM power factor is calculated as of (3.38).

The percentage efficiency of the motor is calculated from the simplified power flow diagram of Fig. 3.11 as

$$\eta = \frac{P_o}{P_i} \times 100, \tag{3.69}$$

where

P_i - electrical input power and
P_o - mechanical output power.

In (3.69), the electrical power is the stator electrical input power, given as

$$P_i = P_s = P_o + P_l. \tag{3.70}$$

In (3.70), excluding stray losses, P_l is the total losses expressed as

$$P_l = P_{scl} + P_{rcl} + P_{bw} + P_c, \tag{3.71}$$

where

P_{scl} - stator copper losses,
P_{rcl} - rotor copper losses and
P_c - core losses.

The stator and rotor windings copper losses in (3.71) are of (3.42) expressed as

$$\begin{cases} P_{scl} = 1.5 I_s^2 R_s \\ P_{rcl} = 1.5 I_r^2 R_r. \end{cases} \tag{3.72}$$

The mechanical and core losses in (3.71) are of (3.43) and (3.44) respectively.

Following Fig. 3.11, the mechanical power output of (3.69) is the same as of (3.46) where the WRIM developed torque T_d defined by (2.23) is calculated from the total flux linkages expressed as functions of inductance parameters given by

$$T_d = T_r + T_s + T_m. \tag{3.73}$$

The torque components of (3.73) following (3.62)-(3.65) are given by [82] as

$$\begin{cases} T_r = 1.5p[(M_{dsqr} I_{qr} + L_{dsdr} I_{dr}) I_{qs} - (M_{qsdr} I_{dr} + L_{qsqr} I_{qr}) I_{ds}], \\ T_s = 1.5p(L_{dsds} - L_{qsqs}) I_{ds} I_{qs}, \\ T_m = 1.5p(M_{dsqs} I_{qs}^2 - M_{qsds} I_{ds}^2), \end{cases} \tag{3.74}$$

where

T_r - rotor flux torque,
T_s - saliency torque and
T_m - cross-magnetisation torque.

The above described modelling equations (3.50)-(3.74) in solving excitation currents using an iterative process shown in Fig. 3.10 which utilises static FEM solutions in conjunction with phasor digram shown in Fig. 3.9, forms the proposed model approach for parameter and performance prediction of the grid-connected WRIM.

3.6. Chapter conclusions

The chapter provides proposed model approaches for grid-connected WRSM and WRIM motor types. The approaches are based on non-classical models in which iterative processes are utilised using static FEM in conjunction with phasor diagrams to calculate important motor parameters and performances at any operating point. It is illustrated that the simple proposed model approaches are effective and powerful tools in the motor types modelling. The latter is validated in Chapter 4 in which commercial FEM performance results are directly compared with the proposed model approaches results.

Chapter 4

Proposed two-axes electromagnetic modelling: Application examples

This chapter presents the parameter and performance calculation application examples of the proposed grid-connected WRSM and WRIM motor types model approaches in Chapter 3. The results are verified by direct comparison of the performance characteristics of both motor types with ANSYS-Maxwell commercial FEM. Further discussions are also given in terms of time efficiency in simulation when using these methods.

4.1. Introduction

The purpose of the application examples presented in this chapter is to implement and validate the proposed model approaches in Chapter 3. This is done by calculating the WRSM and WRIM motor types parameter and performance characteristics resulting from the proposed methods and directly compare them with those of the ANSYS-Maxwell commercial FEM (AMFEM) package. Since the proposed model approaches are FEM based, a modified in-house FEM (IHFEM) described in Appendix B.3 is used for the flux linkage solution calculation. Some of the reasons for implementing IHFEM are:

- user-friendly tool allowing non-expect users to analyse in detail the magnetic field;
- its script based interface allows large adaptability with respect to motor model advancements;
- its use of first-order mesh elements with negligible reduction in analysis accuracy, heavily decreases solution extraction time which is critical for motor design optimisation; and
- the IHFEM package is open source.

A note has to be made that any FEM package (commercial or non-commercial) can be utilised alongside the proposed model approaches of Chapter 3 as long as the package can execute static FE solutions and is capable of freezing the core-element permeabilities. As mentioned in Section 3.2, the total net flux linkages implemented in (3.5) and (3.6) using the IHFEM include high-order harmonic and leakage fluxes produced by the winding, slotted air-gap and magnetic saturation. These total

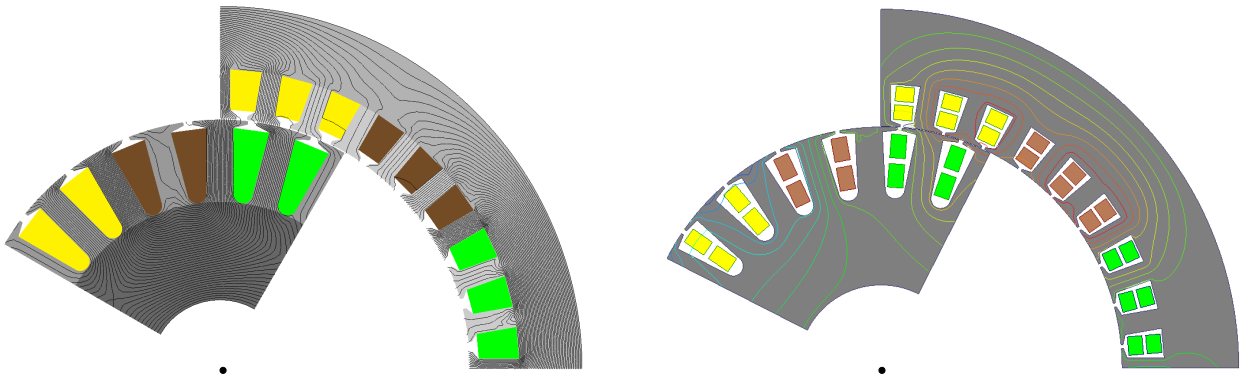

(a) IHFEM model **(b)** AMFEM model

Figure 4.1: Typical WRSM and WRIM FEM pole model axial view for the application examples. phase A/a, phase B/b, phase C/c.

Table 4.1: D160M FRAME AND SHAFT DATA

variable	symbol	value	units
stator outer diameter	D_s	260	mm
rotor inner diameter	d_r	60	mm
stack length	l	125	mm

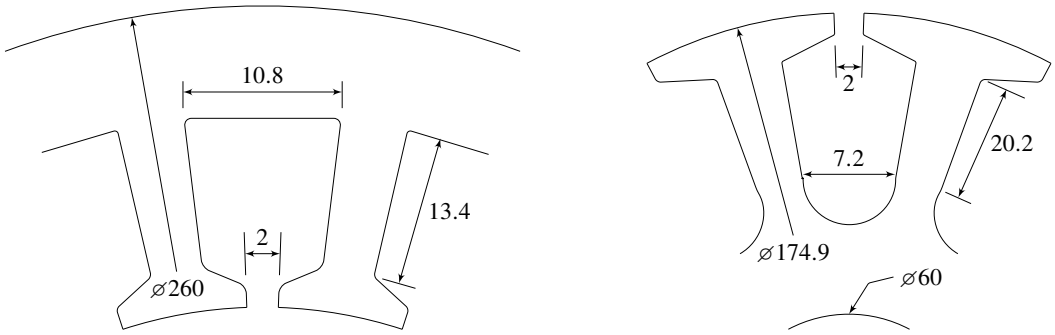

(a) stator **(b)** rotor

Figure 4.2: Grid-connected WRSM and WRIM application example cut-off lamination cross-section and dimensions, (mm).

flux linkages are essential because with these flux linkages a complete parameter and performance prediction model of the motor is obtained.

Following the above described, the IHFEM allows the study an opportunity to solve complicated models of the motor types. The IHFEM allows models of complicated internal structure and magnetic saturation within the motor to be solved to a high degree of accuracy. Because of large amount of computational time and memory requirements in the FEM, IHFEM concentrates on the steady-state analysis operation of the motor in which phasor quantities are employed, which suits well with the proposed model approach discussed in this study.

In this chapter, the same motor specifications except for rotor excitations are used for both WRSM and WRIM application examples. Figure 4.1 shows typical IHFEM and AMFEM pole face models of the wound-rotor motor type constructed using the geometry construction in Appendix B.4. Symmetry for the four pole models of Fig. 4.1 is utilised to drastically save simulation time. A standard D160M motor frame peripheral dimensions tabulated in Table 4.1 are used. The lamination dimensions with peripheral dimensions given in Table 4.1 are shown in Fig. 4.2. Other important parameter specifications for the application examples are given in Table 4.2 with both stator and rotor three-phase

Table 4.2: GRID-CONNECTED WRSM AND WRIM APPLICATION EXAMPLES SPECIFIED PARAMETERS

variable	symbol	stator	rotor
slots	Q_s, Q_r	36	24
turns per slot	n_s, n_f	20	32
slots per pole per phase	q_s, q_f	3	2
winding layers	N_L	2	
slots fill factor	k_{fill}	0.4	
operating temperature	℃	75	
pole pairs	p	2	
copper coil winding material		cu	
lamination material		m400-50a	

Table 4.3: ANALYTICAL RESISTANCE AND END-WINDING INDUCTANCE VALUES FOR THE APPLICATION EXAMPLE

variable	stator	symbol	rotor	unit
resistance	R	0.75	0.75	Ω
end-winding inductance	L_e	1.52	1.74	mH

winding full pitched and star connected. Since the slot area of the motor can be calculated using slot dimensions of Fig. 4.2, the phase dc resistance using (2.65) and (2.77) with series connected conductor coils of variable specifications given in Table 4.2 is calculated from

$$R = \frac{N_L n_c^2 pq(l_m + l_e)}{\sigma S_{slot} k_{fill}}, \tag{4.1}$$

where

S_{slot} - stator or rotor slot area and
q - stator or rotor slots per pole per phase.

In (4.1), the electrical conductivity and coil turns of the corresponding main- and end-windings are taken to be equal to each other. The calculated stator and rotor resistance using (4.1) and end-winding inductances using (2.80) for the considered above motor specifications are tabulated in Table 4.3. Furthermore, the above described motor for both the WRSM and WRIM is fed from a 400 V line-to-line 50 Hz grid. More details concerning the winding connection are given with respect to the motor type in Sections 4.2 and 4.4.

4.2. Grid-connected WRSM application example

The described motor of Section 4.1 is used in the application example of the grid-connected WRSM except for the rotor (field) winding connection for excitation and excluding end-winding inductance values. The field end-winding inductances are excluded because of the dc excitation. The chosen three-phase winding to dc winding connection is shown in Fig. 4.3. Using field winding connection of Fig. 4.3, k_{dc} of (3.42) is 1.5.

It is important to state that there are numerous field winding connections that can be considered for the WRSM as described in [48]. However, only one type of the field winding connection of Fig. 4.3 is considered in this study. Despite of the advantage that when the field exciter fails the whole winding setup can run as a normal grid-connected WRIM until the exciter is fixed, the field winding setup gives an excellent start since the three-phase field windings are short-circuited or connected in series with

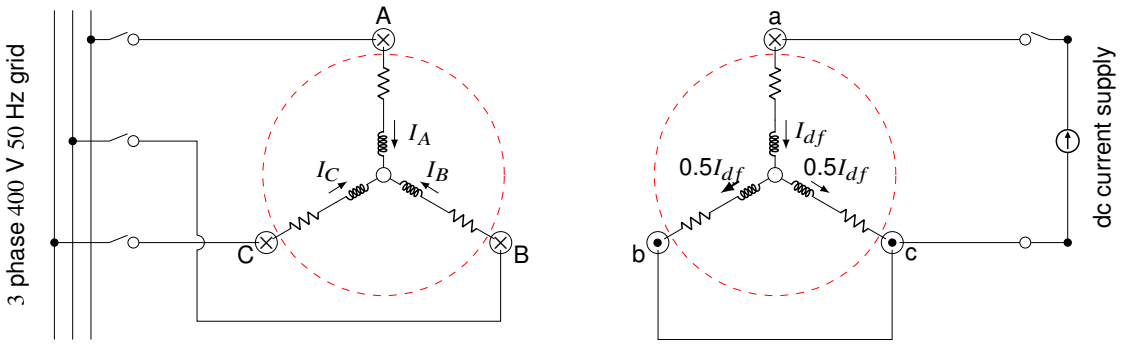

(a) stator winding connection **(b)** rotor winding connection

Figure 4.3: Grid-connected WRSM (a) stator and (b) field winding connection for excitation.

external resistors and or controlled switched as described in Appendix B.5 [86,104]. The field winding connection also does not complicate manufacturing parts. Furthermore, with this type of winding, not only is the WRIM speed prior to synchronisation at maximum, but, also, since the field connections are virtually unchanged for synchronous running, the motor is readily synchronised [83, 109]. This is on the premise that the induction torque is always available throughout the synchronising period except for the brief instant during which the change over is operated [48]. It is clear from Fig. 4.3(b), field phases a and b can be permanently connected, in which only two slip-rings will be necessary for the induction and synchronous torque production. This can be implemented using stator soft start techniques on the stator as in [86]; otherwise using three-slip rings will work for existing industrial systems which utilise external resistors and or resistive fluids. The presence of the closed loop delta circuit, apart from through the exciter, inherent good damping properties, which is important in avoiding hunting with pulsating loads [83].

Despite the above stated advantages, the drawback of the field winding configuration is the non-uniform distribution of the copper losses, because only one-phase of the field winding carries the whole dc exciting current and other two parallel field winding carry only a half dc current. However, this can be smoothed out by high thermal conductivity of insulation [102].

Following the parameters and performance calculation flow diagram of Fig. 3.6, the desired grid voltage and load angle matrix of (3.21) for the grid-connected WRSM application example is defined as

$$\begin{bmatrix} V_{dg} \\ V_{qg} \end{bmatrix} = \begin{bmatrix} -400\sqrt{\frac{2}{3}}\sin(\delta_g) \\ 400\sqrt{\frac{2}{3}}\cos(\delta_g) \end{bmatrix}. \tag{4.2}$$

The initial current $[I]$ in Fig. 3.6 is set to an arbitrary stator current phasor and field current. The chosen field current $I_{df} = 23$ A is kept constant through out the simulation process.

Figure 4.4 shows the voltage and current phasors components during the iterative process with the load angle of (4.2) varied from $0°$ to $90°$ i.e. $(0 \leqslant \delta_g \leqslant 90)°$. The robustness of the proposed approach can be observed from Fig. 4.4(a) in which the iterative process has a stator voltage magnitude V_s convergence behaviour to the rated grid voltage magnitude V_g of 327 V within 6 iterations. This is when the iterative process is terminated using the fraction tolerance of (3.37) as $\nu = 0.001$. At the set grid voltage magnitude, it can be confirmed that within these 6 iterations, the corresponding solved current phasor components in Fig. 4.4(b) are the current solution needed for the excitation of the motor at a specified load angle.

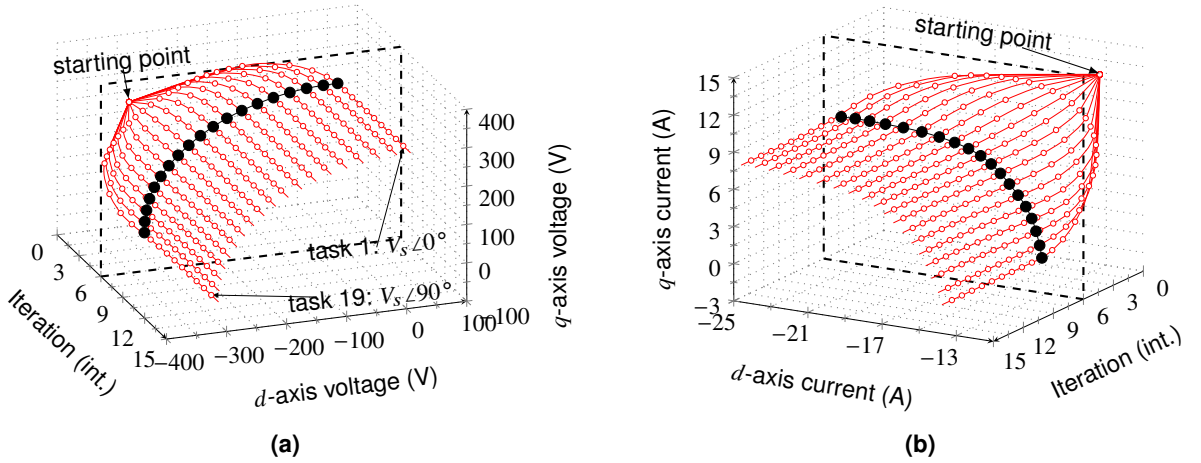

(a) **(b)**

Figure 4.4: Grid-connected WRSM stator (a) voltage and (b) current phasor components variation during the iteration process.

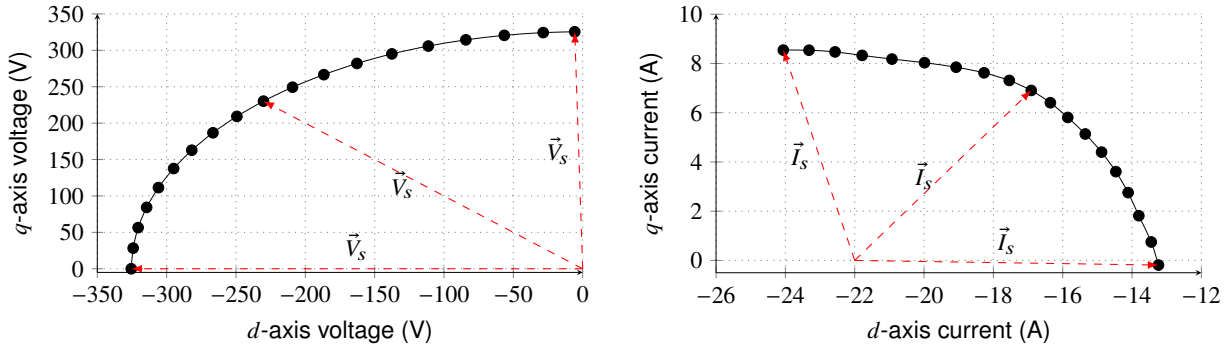

(a) **(b)**

Figure 4.5: Grid-connected WRSM q-axis versus d-axis components of the stator (a) voltage (b) current over the cross-section plane of Fig. 4.4.

Because the proposed mode approaches in Chapter 3 are script based interface, the maps of Fig. 4.4 are constructed in a quick manner by utilising Python script multiprocessing described in Appendix A.7 in which the iterative process of Fig. 3.6 for a given V_g, I_{df} and motor geometry, is distributed into tasks of different load angle e.g. shown in Fig. 4.4 for δ_g equal to $0°$: task 1 and $90°$: task 19. On a 3.6 GHz CPU with 16 GB RAM Intel(R) Core(TM) i7 computer, each iteration ($1\times$ non-linear plus $3\times$ linear FEM solutions) takes 8.71 s for the considered mesh which is fast when compared to other methods such as Time-stepping and Time-harmonic FEMs [107, 121].

The solved phasor components of the stator voltage and current in Fig. 4.4 can be viewed through the cross-section plane shown, at the sixth iteration i.e. filled markers as shown in Fig. 4.5. The origin of the current phasor of Fig. 4.5(b) is shifted to the left by 22 A for better presentation of the current phasor I_s. Now to validate the results in Fig. 4.5, an analysis in AMFEM is done for the grid-connected WRSM. In AMFEM, the motor is supplied with stator and rotor three-phase voltage

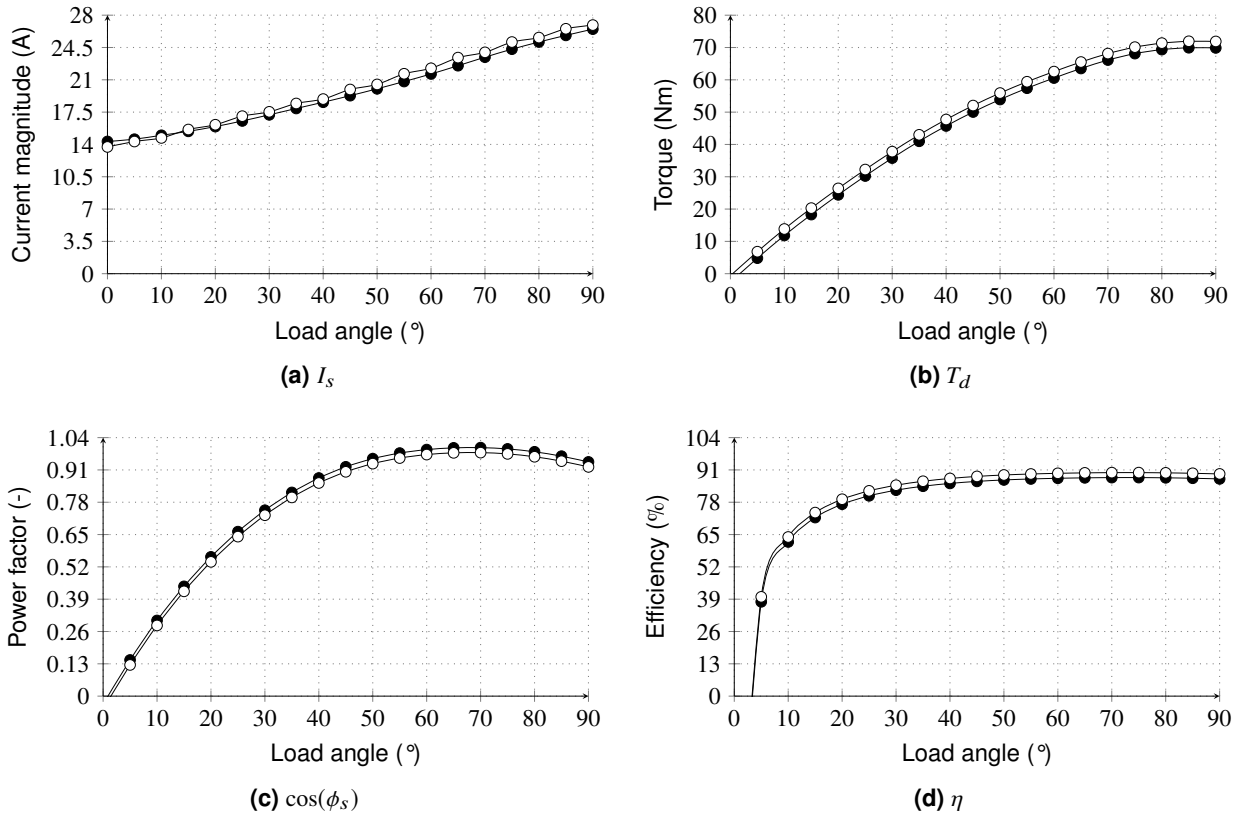

(a) I_s **(b)** T_d **(c)** $\cos(\phi_s)$ **(d)** η

Figure 4.6: Validation of the grid-connected WRSM performance characteristics versus the load angle using IHFEM (-●-) by AMFEM (-○-).

matrices, respectively given by

$$\begin{cases} \begin{bmatrix} V_A \\ V_B \\ V_C \end{bmatrix} = \begin{bmatrix} V_g & 0 & 0 \\ 0 & V_g & 0 \\ 0 & 0 & V_g \end{bmatrix} \begin{bmatrix} \cos(\theta_s + \delta_g) \\ \cos(\theta_s + \delta_g - \beta_e) \\ \cos(\theta_s + \delta_g - 2\beta_e) \end{bmatrix} \\ \begin{bmatrix} V_a \\ V_b \\ V_c \end{bmatrix} = \begin{bmatrix} V_{df} & 0 & 0 \\ 0 & V_{df} & 0 \\ 0 & 0 & V_{df} \end{bmatrix} \begin{bmatrix} \frac{2}{3} \\ \frac{1}{3} \\ \frac{1}{3} \end{bmatrix}, \end{cases} \tag{4.3}$$

where β_e is defined in Fig. 3.4. In (4.3), V_{df} is calculated from

$$V_{df} = k_{dc} R_f. \tag{4.4}$$

where $k_{dc} = 1.5$ from Fig. 4.3. In the AMFEM WRSM analysis, the motor grid voltage angle of (4.3) is also varied in the range $(0 \leqslant \delta_g \leqslant 90)°$ as in the case when using the iterative process.

Figures (a)-(d) of Fig. 4.6 show the variation of the grid-connected WRSM calculated stator current magnitude I_s, torque T_d of (3.47), power factor $\cos(\phi_s)$ of (3.38) and efficiency η of (3.39) respectively, with the load angle when using the IHFEM and AMFEM. The filled markers in Fig. 4.6 denote the proposed iterative process results when using IHFEM. During the simulation, on the same computer, the iterative process using IHFEM was found to be sixteen times faster than the AMFEM, which is critical when it comes to design optimisation of the motor.

The correlation between the proposed model approach and AMFEM results concurs. The agreement proves the validity of the modelling of the grid-connected WRSM discussed in Section 3.4.

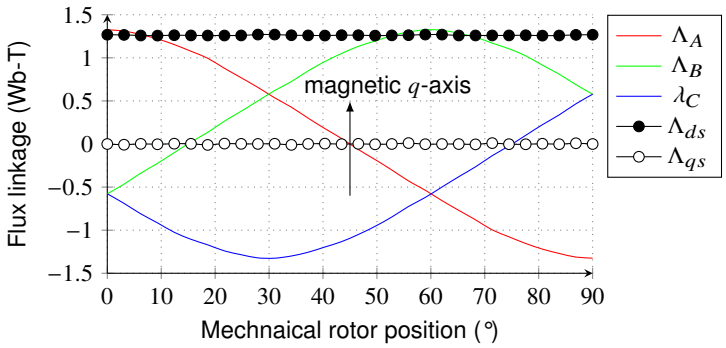

Figure 4.7: WRSM non-linear FEM flux linkages versus rotor position with only field excitation.

4.3. Transformation angle shift technique

Having modelled the WRSM on the complete w-axis of Fig.3.1 and having validated it as in Section 4.2, the validation of the saliency-shift angle γ_v of (3.7) and field-shift angle γ_w of (3.9) is done using the transformation angle shift technique. The transformation angle shift technique is simulated by using the frozen permeability method in Section 3.3 for the flux linkage components solution. The technique used to find the mechanical shift angles γ_v and γ_w such that the electrical transformation angle in $T[\theta_s]$ of (3.14) is redefined as

$$\theta_s = p(\theta_m + \Theta_m), \tag{4.5}$$

where

Θ_m - mechanical transformation shift angle,

such that

$$\begin{cases} \gamma_v = \Theta_m \text{ when } M_{dsqs} = M_{qsds} = 0 \text{ and} \\ \gamma_w = \Theta_m \text{ when } M_{qsdf} = 0. \end{cases} \tag{4.6}$$

In (4.5), θ_m is the mechanical angle of the rotor position defined in Fig. 3.4. For the transformation angle shift technique analysis, the positive d-axis must be aligned with the magnetic axis of the field winding (i.e. $\theta_m = 0$ at $t = 0$ in Fig. 3.4). This is demonstrated in Fig. 4.7 showing the stator non-linear flux linkage solutions extracted when the WRSM is exciting with only the field current.

With correct d and A magnetic axes initial alignment as shown in Fig. 4.7, Fig. 4.8 shows the FEM flux linkage solutions of (3.28)-(3.30) versus the transformation shift angle Θ_m with stator current angle α_s as a parameter. Before finding Θ_m to satisfy (4.6), Fig. 4.9 shows the inductances calculated from the flux linkages of Fig. 4.8 when $\Theta_m = 0°$. The inductances of Fig. 4.9 are used in the calculation of (3.7) and (3.9). Now, Fig. 4.10 shows the top view cross-section over the plane of Fig. 4.8 where the flux linkage solutions are zero to find γ_v and γ_w using the transformation angle shift Θ_m.

Using the above transformation angle shift technique, from Fig. 4.10 the study identifies that $\gamma_v \neq \gamma_w$, which confirms the existence of the three magnetic axes (i.e. u, v and w-axes) of Fig. 3.1. The agreement in Fig. 4.8 is evidence that using the transformation angle shift technique, the saliency- and field-shift angles formulation of (3.7) and (3.9) can be adapted to give the relationship between the three magnetic axes of Fig. 3.1. Furthermore, it is important to state that even though

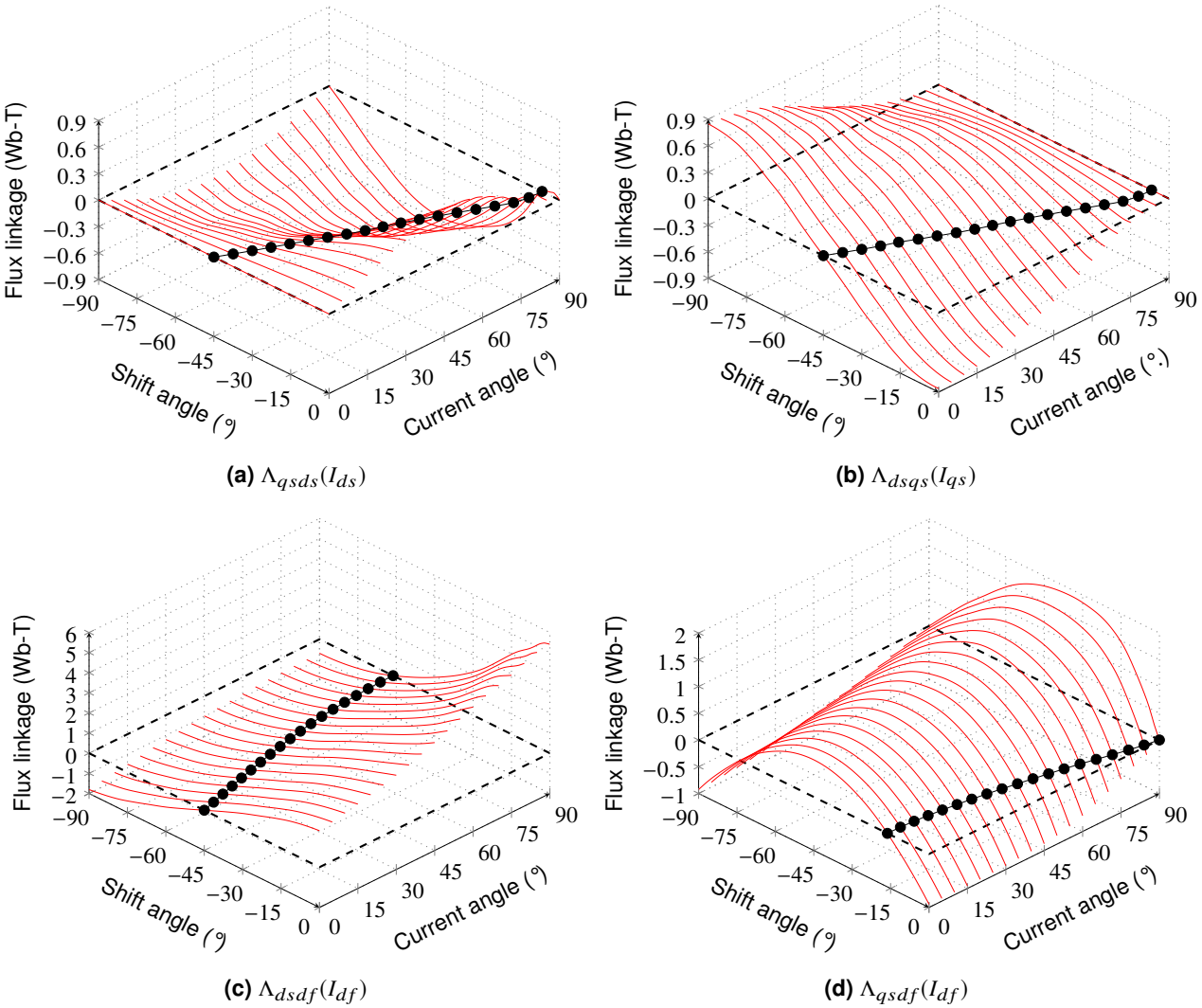

(a) $\Lambda_{qsds}(I_{ds})$ **(b)** $\Lambda_{dsqs}(I_{qs})$

(c) $\Lambda_{dsdf}(I_{df})$ **(d)** $\Lambda_{qsdf}(I_{df})$

Figure 4.8: WRSM flux linkage versus shift angle with current angle as a parameter.

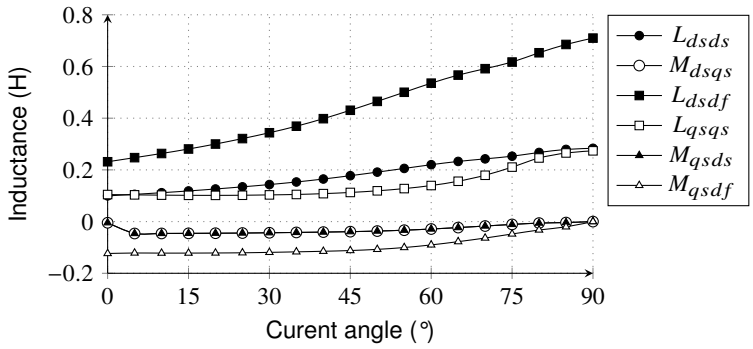

Figure 4.9: WRSM inductance versus current angle with $\Theta_m = 0°$.

(3.7) is derived for permanent magnet machines, it gives correct results for the considered WRSM as shown in Fig. 4.10.

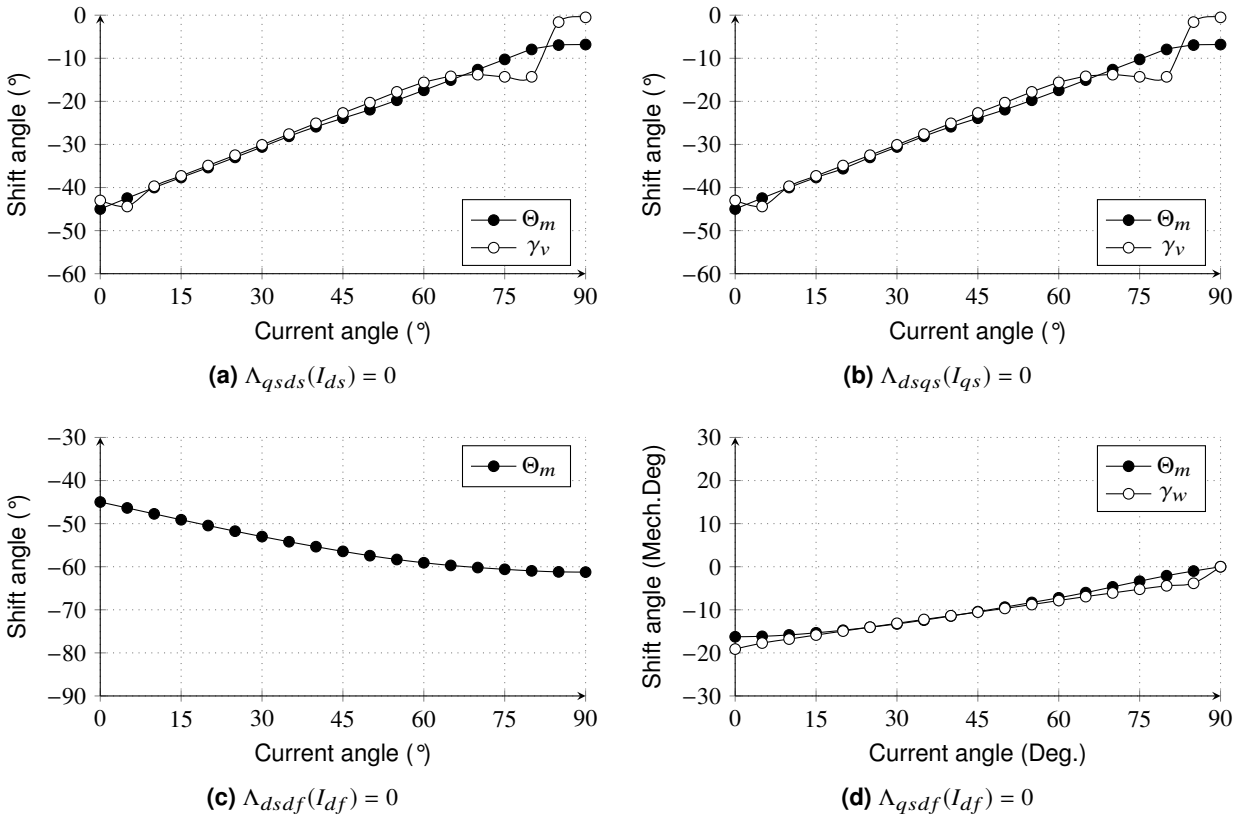

(a) $\Lambda_{qsds}(I_{ds}) = 0$ **(b)** $\Lambda_{dsqs}(I_{qs}) = 0$

(c) $\Lambda_{dsdf}(I_{df}) = 0$ **(d)** $\Lambda_{qsdf}(I_{df}) = 0$

Figure 4.10: WRSM transformation shift angle versus current angle over the cross-section of Fig. 4.8.

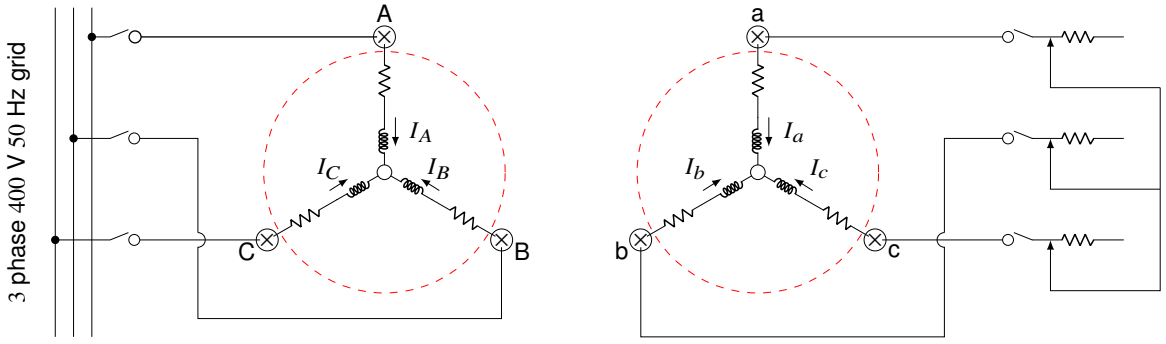

(a) stator winding connection **(b)** rotor winding connection

Figure 4.11: Grid-connected WRIM (a) stator and (b) rotor winding connection for excitation.

4.4. Grid-connected WRIM application example

The typical IHFEM and AMFEM package models shown in Fig. 4.1 are used in the application example of the WRIM model approach of Section 3.5, discussed here. Thus also Fig. 4.2 and Tables 4.1, 4.2, and 4.3 give the parameter specifications of the grid-connected WRIM. Since there is ac in the rotor side of the WRIM, the rotor end-winding inductances of Table 4.3 are not assumed zero as in the case of the WRSM in Section 4.2.

The three-phase windings in the WRIM stator and rotor are full pitched star connected as shown in Fig. 4.11. The rotor windings are short-circuited (normal operation of the WRIM) as shown in Fig. 4.11(b). Following the WRIM parameter and performance calculation flow diagram of Fig. 3.10 and

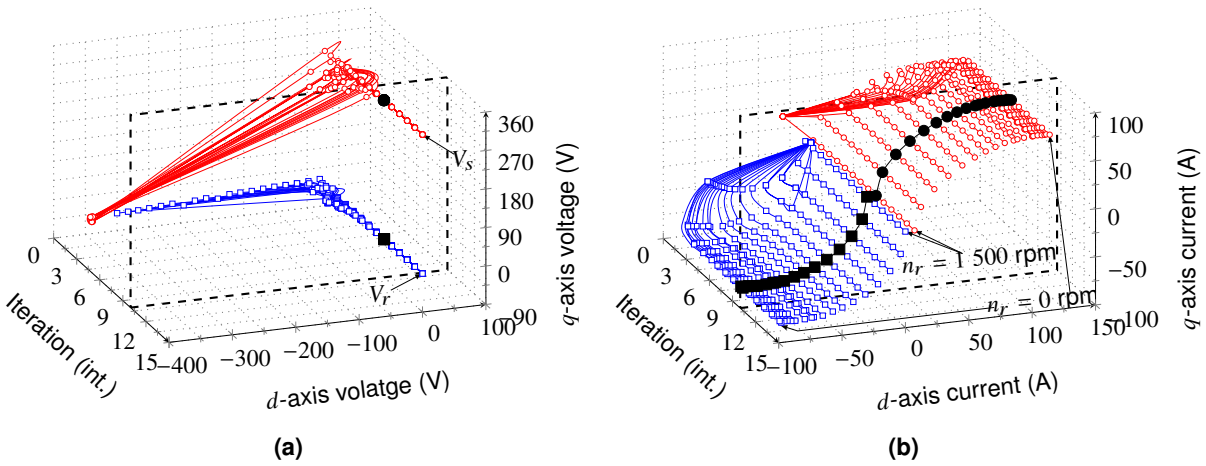

Figure 4.12: Grid-connected WRIM (a) voltage and (b) current phasor components variation during the iteration process.

only considering the positive q-axis grid voltage component (i.e. $\delta_g = 0°$ of Fig. 3.9), the desired grid voltage of (3.21) and rotor of (3.53) defined by $\vec{V}_g$ and $\vec{V}_0$ respectively, are given by

$$\begin{cases} \begin{bmatrix} V_{dg} \\ V_{qg} \end{bmatrix} = \begin{bmatrix} 0 \\ 400\sqrt{\frac{2}{3}} \end{bmatrix} \\ \begin{bmatrix} V_{d0} \\ V_{q0} \end{bmatrix} = \begin{bmatrix} 0 \\ 0 \end{bmatrix}. \end{cases} \tag{4.7}$$

The initial current matrix of (3.51) in Fig. 3.10 is set to an arbitrary stator and rotor current phasors. Different rotor speeds (ω_r in Fig. 3.10) are used to facilitate loading on the WRIM. Figure 4.12 shows the voltage and current phasor components during the iterative process when the motor rotor speed calculated from

$$n_r = \frac{30}{\pi p}\omega_r, \tag{4.8}$$

is varied in the range $(0 \leqslant n_r \leqslant 1500)$ rpm.

The robustness of the proposed WRIM model approach can also be observed from Fig. 4.12(a) in which the iterative process has a convergence behaviour of the stator voltage V_s to the desired grid voltage $V_g = 327$ V and rotor $V_0 = 0$ V magnitudes within eight iterations when the iterative process is terminated using the fraction tolerance of (3.37) of $\nu = 0.001$. At these desired voltage magnitudes, it can also be confirmed that within these eight iterations, the corresponding solved stator and rotor current phasors of Fig. 4.12(b) are the current solutions needed for the excitation of the motor at a specific speed or load.

The technique of utilising Python multiprocessing as in Section 4.2 is also employed to quickly obtain maps of Fig. 4.12. In the case of the WRIM, the iterative process of Fig. 3.10, for the defined grid and rotor voltages and motor geometry, is distributed into tasks of different rotor speeds e.g 0 rpm: task 1 to 1500 rpm: task 19. Using the 3.6 GHz CPU computer with 16 GB RAM Intel(R) Core(TM) i7, each iteration ($1\times$ non-linear plus $4\times$ linear FE solutions) takes 9.35 s for the considered mesh. This is also much faster with accuracy in calculation of IM when compared to Time-stepping and Time-harmonic FEMs [**?**]. The solved phasor components of the voltage and currents can be viewed through the cross-section plane shown in Fig. 4.12, i.e. filled markers at the eighth iteration as in Fig. 4.13.

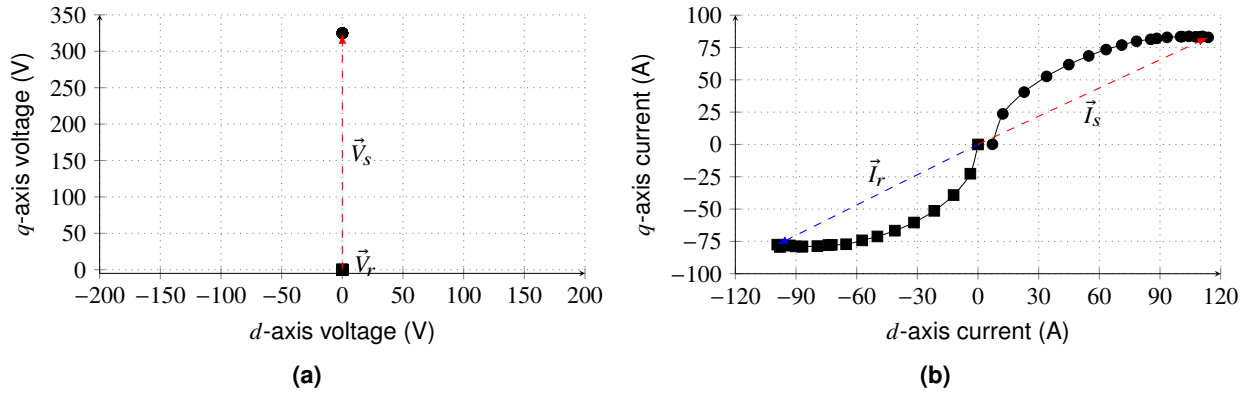

(a) **(b)**

Figure 4.13: Grid-connected WRIM q-axis versus d-axis components of the stator rotor (a) voltage and (b) current over the cross-section plane of Fig. 4.12.

To validate the results of Fig. 4.13, an analysis also in AMFEM is done for the grid-connected WRIM. In AMFEM, the motor is supplied with stator and rotor three-phase voltage matrices given by

$$\begin{cases} \begin{bmatrix} V_A \\ V_B \\ V_C \end{bmatrix} = \begin{bmatrix} V_g & 0 & 0 \\ 0 & V_g & 0 \\ 0 & 0 & V_g \end{bmatrix} \begin{bmatrix} \cos(\theta_s) \\ \cos(\theta_s - \beta_e) \\ \cos(\theta_s - 2\beta_e) \end{bmatrix} \\ \begin{bmatrix} V_a \\ V_b \\ V_c \end{bmatrix} = \begin{bmatrix} 0 \\ 0 \\ 0 \end{bmatrix}. \end{cases} \tag{4.9}$$

The motor speed as of (4.8) is also varied, as is the case when using the WRIM iterative process described above. Figures (a)-(e) of Fig. 4.14 show the variation of the grid-connected WRIM stator I_s, and rotor I_r magnitude currents, torque of T_d of (3.73), power factor $\cos(\phi_s)$ of (3.38) and efficiency η of (3.69) respectively, with rotor speed when using IHFEM and AMFEM. The filled markers denote the proposed grid-connected WRIM model approach results when using the IHFEM. Again, during the simulation, on the same computer, the iterative process using the IHFEM was found to be eighteen times faster than the AMFEM, which is essential when it comes to the design optimisation of the motor type. The agreement between the proposed WRIM model approach and AMFEM results shows a satisfying correlation. Hence, the results prove the validity of the model of the grid-connected WRIM discussed in Section 3.5.

4.5. Chapter conclusions

The steady-state model approaches presented in Chapter 3 are utilised in the application examples in this chapter. The approaches not only demonstrated simplicity, but also accuracy and computational time efficiency when compared with the AMFEM commercial FEM. The further advantage of the proposed method is the knowledge of parameter values, which one does not have with AMFEM. It also confirms that classical expressions cannot be employed for grid-connected motor types essentially facing heavy saturation.

From the results obtained in the considered grid-connected WRSM and WRIM model approaches, saturation saliency, cross-magnetisation and asymmetric saturation phenomena must always be taken in account in cylindrical wound-rotor motors. This is because the magnetic field paths can

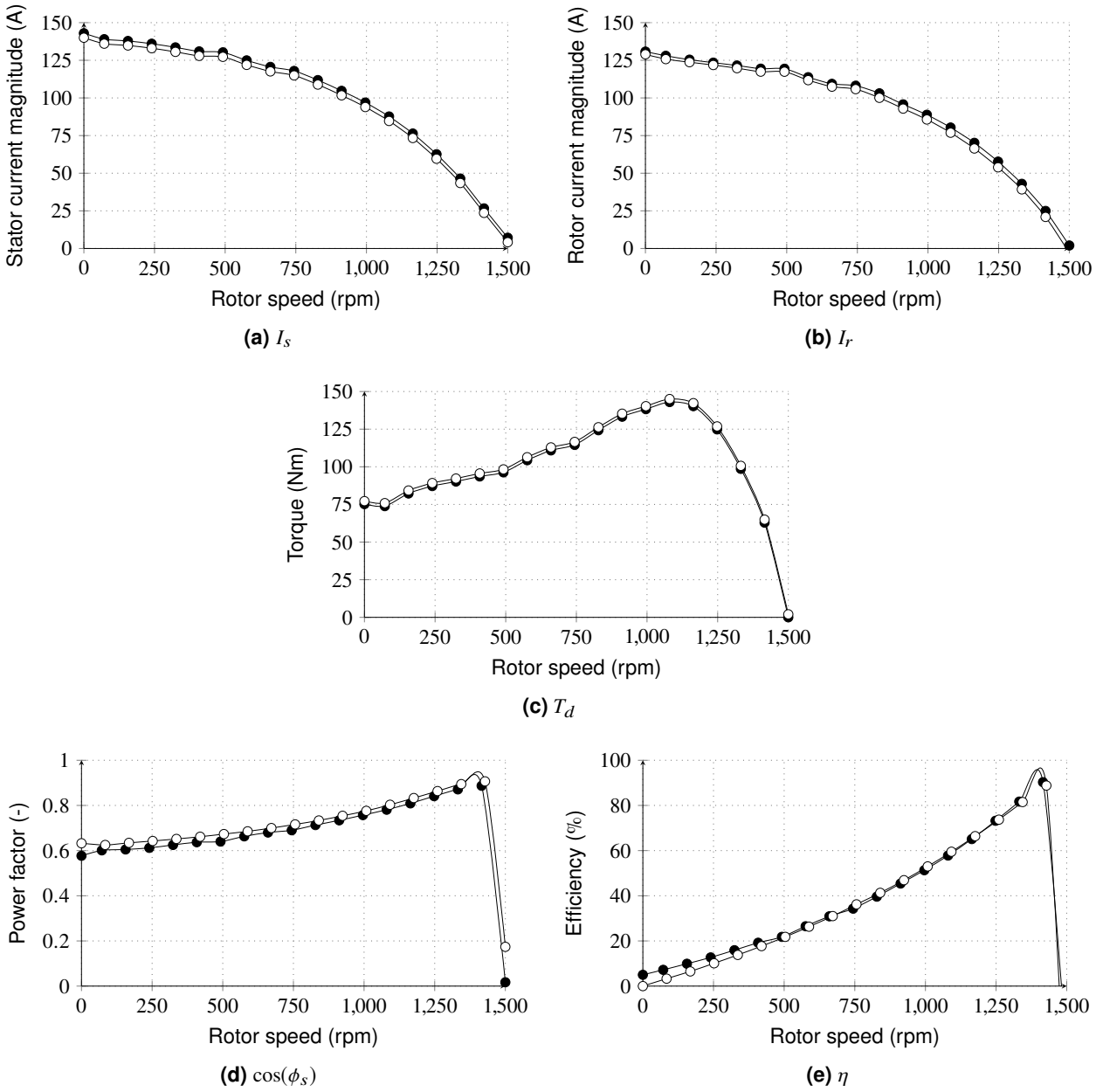

(a) I_s **(b)** I_r **(c)** T_d **(d)** $\cos(\phi_s)$ **(e)** η

Figure 4.14: Validation of the grid-connected WRIM performance characteristics versus rotor speed using IHFEM (-●-) and AMFEM (-○-).

easily be shifted on the rotor core space when the motor is loaded. This is demonstrated using the transformation angle shift technique to verify the formulation of the saliency and field shift angles introduced in Chapter 3. The saliency- and field-shift angles calculated from the formulations and using the transformation angle shift technique were found to be in agreement.

The compatibility of the method enables parameter and performance mapping by loading the motor types using the iterative process. Hence, not only accuracy is demonstrated, but also simplicity and speed, which are all important in the design optimisation of the motor. Thus the performance calculation method also works well in the design of energy efficient electrical motors in terms of accuracy in parameter calculation and time efficiency in performance prediction. The optimum design of the motor types using the performance calculation method is well demonstrated in Chapter 5. Furthermore, even though the investigations here are done on small motor types, the proposed model approaches for performance calculation are also applicable in large power level applications, i.e.

given in Chapter 7 for the WRIM.

Chapter 5

Design optimisation: Grid-connected WRSM and WRIM

This chapter presents a multi-objective optimum performance and lamination design of both grid-connected WRSM and WRIM motor types to suit the prospective objectives for the given active core volume by improving the overall motor performance. In this chapter the two motor types are optimised separately to look at the possible application of the proposed model approaches in Chapter 3, utilising optimisation algorithms on the performance enhancement. Equations are formulated using the optimisation algorithms, gradient and non-gradient based, for the optimum design of both the stator and rotor laminations of the motor types. Discussions in terms of motor performances on the separate incidents resulting from the design optimisation are also given.

5.1. Introduction

Apart from improving the parameter and performance calculation methods, lamination dimensions necessary for the optimum performance of the motor are also of great importance. The combination of the optimal modelling approach and lamination dimension results in high-efficiency motors, seen here as a way to improve electrical drive systems which reduce energy consumption in a rising energy-cost world.

The design optimisation of electrical motors involves a considerable number of variables which dictate the motor performances. The process requires reviewing preceding motor performance events to select the compound of variables which yields to the desired performance, and then investigating further for the possibility of generating designs which give better performance, but at the same time, satisfy the desired requirements [49, 115, 137]. The design optimisation process is well dealt with by utilising digital computing to reduce the processing time. Despite digital computing making it possible to synthesise for any type of motor in a reduced time, it is obvious that the process of optimisation is still time-consuming. Thus, it is necessary that both the optimisation algorithms (Op-Al) and the analysis program are fast and accurate. These aspects receive considerable attention in this chapter.

Following the above described, this chapter demonstrates the use of Op-Al tools and techniques to achieve the optimal defined design optimisation problem function. The problem function is usually different because the criteria for optimisation are influenced by the multiple designers requirements

and application [17, 37, 50, 90, 126]. S.S. Murthy [89] discusses the history of the design of electric motors for performance optimisation. The author gives the trend shift over the past years for decreasing the motor size for the same power to energy efficient rating motors. It can be observed from this that performance optimisation aimed at energy conservation in motor is, in every case, related to efficiency as an objective function, since efficiency has a direct bearing on power consumption and energy conservation [89]. Hence, the multi-objective problem function in this study also focuses on the separate performance optimisation of the two grid-connected WRSM and WRIM using the proposed model approaches for time-efficient and accurate analysis. The focus proves the feasibility of the application of the proposed model approaches in the development of energy efficiency motors, keeping in sight of existing motor frame size. The performance optimisation of both motor types is done using a commercial optimisation package called *VisualDoc*, following a defined performance optimisation procedure.

5.2. Multi-objective design optimisation problem function

The design optimisation problem function comprises mathematically formulated design parameters namely: constraint, and objective functions, and design variables. The constraint and objective functions are required performance candidates and the functions are either maximised or minimised respectively. Both functions depend on the design variables. Mathematically, the general non-linear multi-variable constrained performance optimisation problem function is defined as

find the design variables

$$x_1, x_2, \ldots, x_K, \tag{5.1}$$

such that the objective functions

$$f_i(x_1, x_2, \ldots, x_K) \qquad i = 1, 2, \ldots, I \tag{5.2}$$

are minimum subjected to constraint functions

$$\begin{cases} g_j(x_1, x_2, \ldots, x_K) = 0 & j = 1, 2, \ldots, j_e \\ g_j(x_1, x_2, \ldots, x_K) \leqslant 0 & j = (j_e + 1), \ldots, J \end{cases} \tag{5.3}$$

and boundary conditions

$$x_k^l \leqslant x_k \leqslant x_k^u \qquad k = 1, 2, \ldots, K \tag{5.4}$$

In the above defined problem function (5.1)-(5.4), x_k are set of unknown independent design variables, f_i are the objective functions and g_j are equality, and inequality constraint functions. The unknown design variables x_k are bound by lower x_k^l and upper x_k^u limits for feasible designs.

Another group of design parameters also indirectly incorporated into the design problem are defined as fixed design variables. This is a group of variables with little influence on the constraint or objective functions of the considered optimisation problem function. The fixed design variables are used here to minimise the number of design variables of the problem function for time-efficient optimisation. Fixed design variables are taken as the number of slots, winding layout and slot fill factors. In addition to the bound design variables, constraint functions are also imposed on the performance optimisation problem function to meet the performance requirements of the motor types.

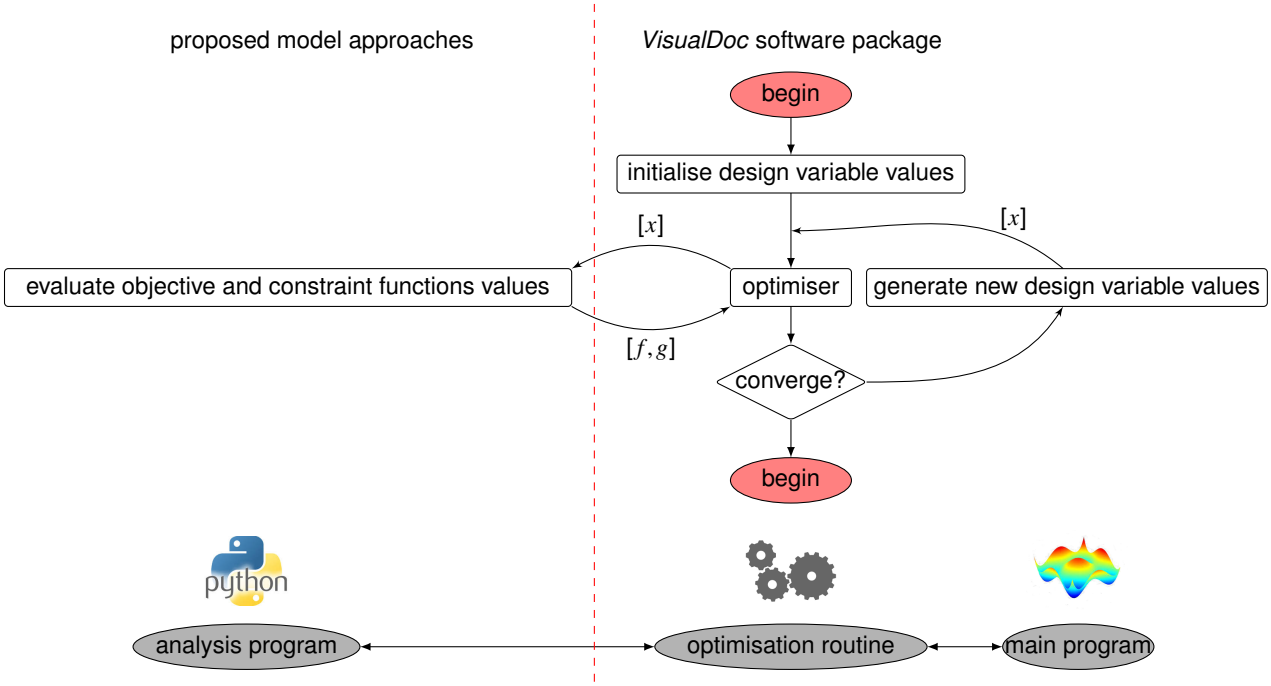

Figure 5.1: Optimisation procedure using directly the proposed model approaches.

5.3. Optimisation procedure

To solve the optimisation problem function defined in Section 5.2, the procedure followed in this study is to try and use the proposed FEM based models of Chapter 3 directly with the Op-AI. The procedure is explained in Fig. 5.1. The analysis program which utilises Python scripting package, i.e. the proposed model approaches of Chapter 3, is used to evaluate the objective $[f]$ and constraint $[g]$ function values. The function values are read in the first call of the optimisation package (*VisualDoc* commercial package) using initial design variable values $[x]$ passed to and from the package. The optimisation routine (optimiser) is either a gradient or non-gradient based Op-AI. Both routines control parameters are well explained in the literature of *VisualDoc* [128]. Depending on the optimisation routine, the other prime operators for the package passed to the main program are the lower x^l, and upper x^u bounds of the design variables, population (N) and maximum or minimum number of iterations (G). The main program of the optimisation package reads all these design variables and constraint function values including their upper and lower bounds. It is also here where constraint functions can be defined as the objective functions, or equalities or inequalities. The process from the analysis program is repeated in an iterative manner with new design variables from the main program until the desired routine control parameters are satisfied, i.e. converge. At this instant, it can be confirmed that the solution found in the optimisation problem function is the optimum one.

5.4. Optimisation algorithms

The Op-AI which utilise digital computing to find and solve problems are used to enhance the motor types' performance and help to accomplish period arranged objectives. The routines additionally help with user friendly solutions, thus making the whole coding and advanced procedures easier for the designer. Although there are a couple of optimisation routes that are applicable in this study, the gradient and non-gradient routines have been chosen. These routines, which come with *VisualDoc*,

are:

- modified method of feasible direction (MMFD); and
- non-dominated sorting genetic algorithm (NSGA-II).

Because the MMFD Op-Al is gradient based, the algorithm gives good results in the shortest period of time, but they are not the best results. On the other hand, NSGA-II Op-Al which is non-gradient is slow but gives the best selection of optimised results [115].

5.5. Design optimisation techniques

In addition to the designer's skill, accuracy and time efficiency in motor analysis, the optimum solution techniques are to help the Op-Al locate the global optimum. If poor optimisation techniques are used, improvements can be achieved that can not be justified by change in the existing designs, which will mean additional tests that consumes time must be used to achieve satisfactory results.

Following the problem function (5.1)-(5.4) to be solved using the optimisation procedure of Fig. 5.1, the objective, and constraint functions, and design variables are respectively, defined in matrix form as

$$[f] = \begin{bmatrix} f_1 \\ f_2 \\ \vdots \\ f_I \end{bmatrix}, \qquad [g] = \begin{bmatrix} g_1 \\ g_2 \\ \vdots \\ f_J \end{bmatrix}, \qquad [x] = \begin{bmatrix} x_1 \\ x_2 \\ \vdots \\ x_K \end{bmatrix}. \tag{5.5}$$

During the optimisation process, the main program of Fig. 5.1 assumes each design variable x_k holds an equal weight. Thus if x_k produces a small change on objective function f_i compared to the other design variable, e.g $x_{(k+1)}$, the main function will make an analogously bigger change on x_k. This phenomenon does not take into account the relative importance of the individual design variable. Also if a value of a particular constraint function g_j is very high and its relative significance compared to the other constraint function, e.g. $g_{(j+1)}$ is low, then g_j will dominate in satisfying the optimum condition thereby giving unsatisfactory results.

To overcome the above-mentioned problem, the technique of smoothing of the problem function by scaling each design parameter to obtain an even weighting is utilised [36]. This is achieved by strengthening or weakening some of the design parameters to restrict them to fall within a given range as seen by the Op-Al. Thus, generally in arbitrary given range of bounds (a and b), the normalised objective, and constraint functions and design variables are defined by

$$\begin{cases} f_i' = a + \dfrac{(f_i - f_i^{min})(b-a)}{(f_i^{max} - f_i^{min})} \\ g_j' = a + \dfrac{(g_j - g_j^{min})(b-a)}{(g_j^{max} - g_j^{min})} \\ x_k' = a + \dfrac{(x_k - x_k^{min})(b-a)}{(x_k^{max} - x_k^{min})}, \end{cases} \tag{5.6}$$

where the superscript $'$ denotes the normalised parameters. In (5.6), superscripts max and min

denote maximum and minimum actual values of the corresponding normalised parameters which depend on the designer's experience.

Although multi-objective optimisation using Op-Al like NSGA-II provides much more information and insight into the problem function, it is also possible to combine different objectives into a single objective optimisation using Op-Al like MFFD to save solution time. This is implemented during the optimisation process by utilising the residual errors left by a set of objective functions not satisfying a set of targeted objective functions. It is these residual errors of each objective function that are used to define the combined multi-objective effect of objective functions to a single-objective as

$$f = \sum_{i=1}^{I} \epsilon_i^2, \tag{5.7}$$

where

$$\epsilon_i = \begin{cases} 0 & : f_i \geqslant f_i^{min} \\ \dfrac{f_i^{min} - f_i}{f_i^{min}} & : f_i < f_i^{min}, \end{cases} \tag{5.8}$$

for f_i no less than f_i^{min} or

$$\epsilon_i = \begin{cases} 0 & : f_i \leqslant f_i^{max} \\ \dfrac{f_i - f_i^{max}}{f^{max}} & : f_i > f_i^{max}, \end{cases} \tag{5.9}$$

for f_i less than f_i^{max}. In (5.7), it is only necessary to utilise penalty functions when the optimisation package does not have the option of built-in constraints, later seen in the application examples. Furthermore, following the function scaling of (5.6) the actual design variables x_k from the normalised values x_k' in an arbitrary given range, a and b are generally calculated from

$$x_k = x_k^{min} + \frac{(x_k' - a)(x_k^{max} - x_k^{min})}{(b - a)}. \tag{5.10}$$

Unlike NSGA-II (non-gradient based Op-Al), MFFD (gradient-based Op-Al) get stuck in the local minimum or maximum and their performances are dependent on initial or starting values of design variables [111, 140]. To control this problem, the technique of different starting design variables $[x]$ of (5.5) is utilised. In each case, the problem function is defined using different initial design variable $[x]_0$ as

- CASE I:

$$[x]_0^1 = \begin{bmatrix} x_1^l \\ x_2^l \\ \vdots \\ x_K^l \end{bmatrix}, \tag{5.11}$$

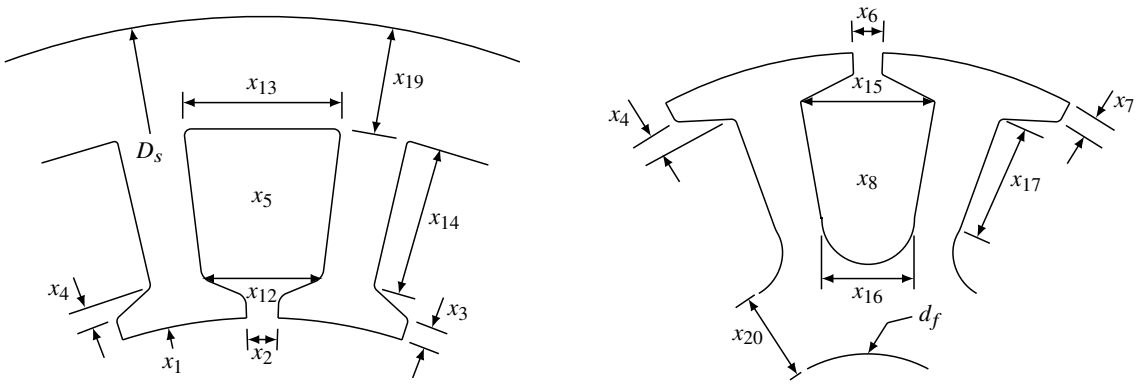

(a) stator **(b)** rotor

Figure 5.2: WRSM cut-off lamination showing design variables to be optimised.

- CASE II:

$$[x]_0^2 = \begin{bmatrix} x_1^{avg} \\ x_2^{avg} \\ \vdots \\ x_K^{avg} \end{bmatrix} \tag{5.12}$$

- CASE III:

$$[x]_0^3 = \begin{bmatrix} x_1^u \\ x_2^u \\ \vdots \\ x_K^u \end{bmatrix}, \tag{5.13}$$

where

$$x_k^{avg} = 0.5(x_k^l + x_k^u). \tag{5.14}$$

The matrix superscript in (5.11)-(5.13) denotes the case number i.e. CASE I-III. Each of the cases of (5.11)-(5.13) is further defined by the set of targeted constraint and objective function values. In addition to scaling design parameters and the use of different starting design variables, minimum and maximum bounds are included with the constraints to avoid valid but undesirable results.

5.6. Grid-connected WRSM design optimisation

This section gives a multi-objective design optimisation of the grid-connected WRSM utilising MFFD and NSGA-II Op-Al following the considerations given in Section 5.5. Figure 5.2 shows the dimensional design variables of the WRSM used in the optimisation procedure with specification given in Section 4.1 of Chapter 3 including the winding connection for excitation. In the optimisation problem function, the objective is to find the design variables for an optimum performance WRSM using the selected objective functions. From the optimisation problem function given in Section 5.2, a total of eleven design variables of (5.5) are selected in the optimisation problem as:

Table 5.1: WRSM DESIGN OPTIMISATION FIXED DESIGN VARIABLES

fixed design variable	symbol	value
stator slots per pole per phase	q_s	3
rotor slots per pole per phase	q_f	2
stator and rotor phases	m	3
stator outer diameter (mm)	D_s	260
rotor inner diameter (mm)	d_f	60
stator and rotor pole pairs	p	2

eight of Fig. 5.2 defined by

$$[x] = \begin{bmatrix} x_1 \\ x_2 \\ \vdots \\ x_8 \end{bmatrix}, \tag{5.15}$$

and three additional current loading variables defined by

$$[x] = \begin{bmatrix} x_9 \\ x_{10} \\ x_{11} \end{bmatrix} = \begin{bmatrix} J_s \\ J_f \\ \alpha_s \end{bmatrix}, \tag{5.16}$$

in which x_5 and x_8 are the stator and rotor slot cross-sectional areas. It is from design variables of (5.15) where other dimensions of Fig. 5.2 x_{12} - x_{20} are computed using the parallel teeth width of the stator and rotor discussed in Appendix B.4. In (5.16), J_s, and α_s are stator peak current density and angle and J_f is the peak field current density. The current densities are limited by the ability to cool the motor and the maximum allowable motor temperature. It is important to note that after the optimisation process the grid-voltage can be easily attained by choosing correct turns without affecting the obtained optimum performance. The selected objective matrix of (5.5) contains two objective functions defined by

$$[f] = \begin{bmatrix} f_1 \\ f_2 \end{bmatrix} = \begin{bmatrix} T_d \\ \eta \end{bmatrix}, \tag{5.17}$$

where T_d is the motor torque of the components of (3.48) and the efficiency η of (3.39). The constraint matrix of (5.5) contains only one selected constraint function viz. power factor defined by

$$g = \cos(\phi_s). \tag{5.18}$$

The power factor constraint function is of (3.38). The chosen fixed design variables are given in Table 5.1.

Each design variable of (5.15) and (5.16) to be passed from the Op-AI is given variable bounds chosen between $a = 0$ and $b = 1$, thus (5.10) is simplified to be

$$x_k = x_k^{min} + (x_k')(x_k^{max} - x_k^{min}). \tag{5.19}$$

The dimensional parameters defined by the design variables of (5.19) are used in the IHFEM program for the geometry creations as discussed in Appendix B.4. Using symmetry the IHFEM geometry model is shown in Fig. 5.3.

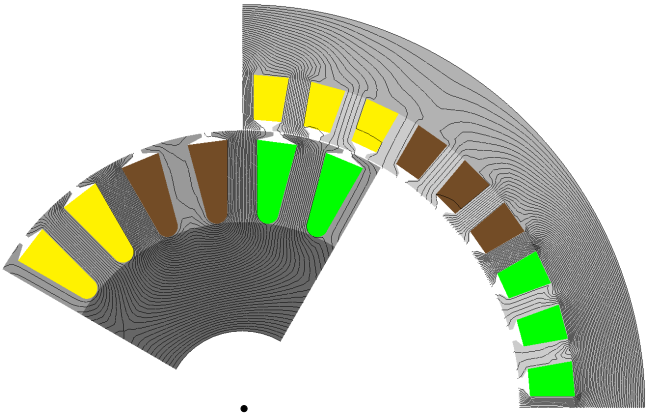

Figure 5.3: Typical IHFEM pole model axial view to be optimised. phase A/a, phase B/b, phase C/c.

5.6.1. WRSM MFFD optimisation

As stated in Section 5.5, MFFD performance is heavily influenced by the starting or initial design variables values. Hence, following (5.19) the cases (5.11)-(5.13) are adapted into (5.15) and used in the initial design variable matrices as

- CASE I:

$$[x]_0^1 = \begin{bmatrix} x_1 \\ x_2 \\ \vdots \\ x_{11} \end{bmatrix} = \begin{bmatrix} 0 \\ 0 \\ \vdots \\ 0 \end{bmatrix}, \tag{5.20}$$

- CASE II:

$$[x]_0^2 = \begin{bmatrix} x_1 \\ x_2 \\ \vdots \\ x_{11} \end{bmatrix} = \begin{bmatrix} 0.5 \\ 0.5 \\ \vdots \\ 0.5 \end{bmatrix}, \tag{5.21}$$

- CASE III:

$$[x]_0^3 = \begin{bmatrix} x_1 \\ x_2 \\ \vdots \\ x_{11} \end{bmatrix} = \begin{bmatrix} 1.0 \\ 1.0 \\ \vdots \\ 1.0 \end{bmatrix}. \tag{5.22}$$

The optimisation problem is further defined using the square of the objective functions residual errors as of (5.6) in (5.17) given by

$$f = \sum_{i=1}^{2} \epsilon_i^2. \tag{5.23}$$

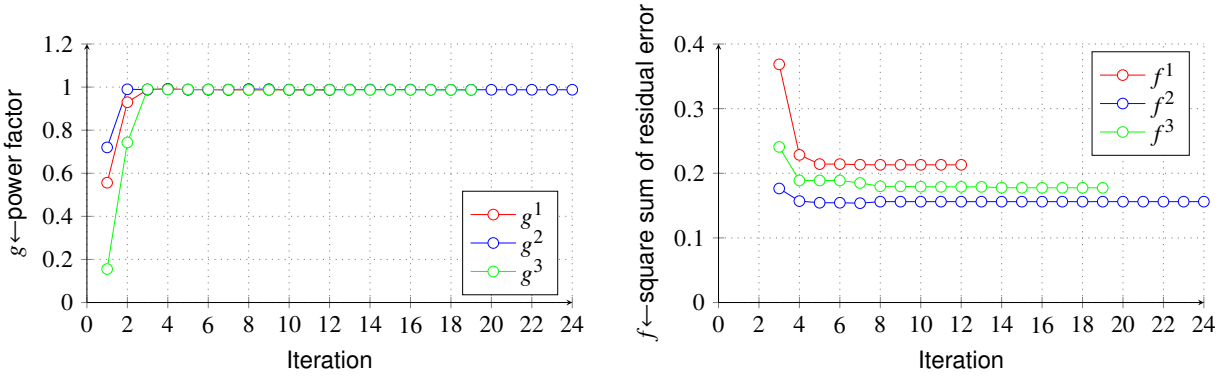

(a) constraint function **(b)** objective function

Figure 5.4: WRSM normalised constraint and objective functions results during MFFD optimisation.

Table 5.2: WRSM MFFD OPTIMISATION RESULTS

CASE	total iterations	ϵ_1	ϵ_2	f
I	11	0.44626	0.11894	0.21309
II	23	0.37518	0.12373	0.15607
III	18	0.39931	0.13555	0.1775

Large targeted objective function values are chosen in which the residual errors of (5.8) in (5.23) are given by

$$\epsilon_1 = \begin{cases} 0 & : f_1 \geqslant f_1^{max} \\ \dfrac{f_1^{max} - f_1}{f_1^{max}} & : f_1 < f_1^{max} \end{cases} \quad \text{where} \quad f_1^{max} = 100 \text{ Nm},$$
$$\epsilon_2 = \begin{cases} 0 & : f_2 \geqslant f_2^{max} \\ \dfrac{f_2^{max} - f_2}{f_2^{max}} & : f_2 < f_2^{max} \end{cases} \quad \text{where} \quad f_2^{max} = 100 \text{ \%}. \tag{5.24}$$

In (5.24), f_1 and f_2 are torque and efficiency of (5.17). Following (5.24), 100 Nm and 100 % even though large to be achieved, are exaggerated targeted torque and efficiency values which the MFFD Op-AI is forced to achieve. The constraint function of (5.18) is restricted to a unit power factor.

To summarise the above-described optimisation problem, MFFD optimisation of the WRSM is achieved by combining the two objective functions T_d and η of (5.17) into a single objective function of the square sum of residual errors as of (5.23). It is then the function of (5.23) which is minimised by the MFFD gradient-based Op-AI.

Figure 5.4 shows the constraint and objective functions' results during the MFFD optimisation after the application of the above described problem function. The superscripts (1-3) in the constraint g and objective f functions shown in Fig. 5.4 denote the different cases (CASE I-III) of (5.20)-(5.22). It can be seen from Fig. 5.4 that the optimisation process using MFFD managed to achieve a unity power factor as shown in Fig. 5.4(a), of the motor type whilst minimising the objective function, as shown in Fig. 5.4(b).

Table 5.2 gives the values of the minimised sum square error function f of (5.23) in Fig. 5.4 together with components ϵ_1 and ϵ_2 of (5.24).

It can be observed from the results of Fig. 5.4 and Table 5.2 that the effect of using different initial design variable values as of (5.20)-(5.22) results in different optimum results, i.e. f values in Table

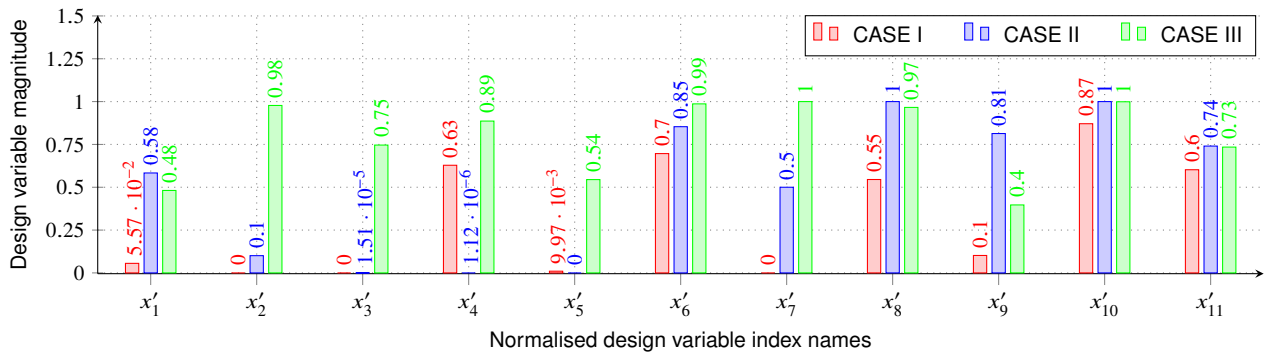

Figure 5.5: WRSM MFFD isolated normalised design variables.

Table 5.3: WRSM MFFD ACTUAL DESIGN VARIABLES OF FIG. 5.5 DESIGNS

variable	CASE I	CASE II	CASE III	unit
x_1	167.9	176.9	175.2	mm
x_2	2.0	2.2	4.0	mm
x_3	1.2	1.2	3.3	mm
x_4	2.3	1.2	2.8	mm
x_5	150.3	150.0	166.3	mm^2
x_6	3.4	3.7	4.0	mm
x_7	1.2	1.2	3.3	mm
x_8	228.2	260.0	257.6	mm^2
x_9	4.2	5.6	4.8	Amm^{-2}
x_{10}	5.7	6.0	6.0	Amm^{-2}
x_{11}	54.0	66.2	65.7	°

Table 5.4: WRSM MFFD ACTUAL OBJECTIVE AND CONSTRAINT FUNCTIONS

objective	CASE I	CASE II	CASE III	unit
f_1	55.4	62.5	60.1	Nm
f_2	88.1	87.6	86.4	%
constraint	**CASE I**	**CASE II**	**CASE III**	**unit**
g	1.0	1.0	1.0	-

5.2. The results of Table 5.2 also include the different number of iterations for convergence in the optimisation procedure given in Table 5.2. This is due to different starting points in the considered cases to satisfy the gradient-based MFFD Op-AI termination criteria of the optimisation procedure.

Figure 5.5 shows the resultant normalised design variables of the selected minimised objective functions shown in Table 5.2. It can be observed that even after convergence, most of the design variables are relatively close to their initial set of design variables. This behaviour is because MFFD gradient based Op-AI seldom changes optimisation direction during the optimisation process. Using the normalised design variables of Fig. 5.5, the actual design parameters using (5.19) are given in Tables 5.3 and 5.4. Figure 5.6 shows the corresponding IHFEM pole axial view models which resulted from the actual design variables of Table 5.3.

The results depicted in this section prove the feasibility of the application of the WRSM proposed model approach on the MFFD Op-AI defined optimisation problem function using the optimisation procedure of Fig. 5.1. It can be observed from Table 5.4 that CASE II gives the best results in terms of torque magnitude even though CASE I gives a slightly better efficiency value. However, for comparison purposes with NSGA-II optimisation results in the next section, CASE II's results of Table 5.4 of the IHFEM model shown in Fig. 5.6(b) are considered the best obtained results.

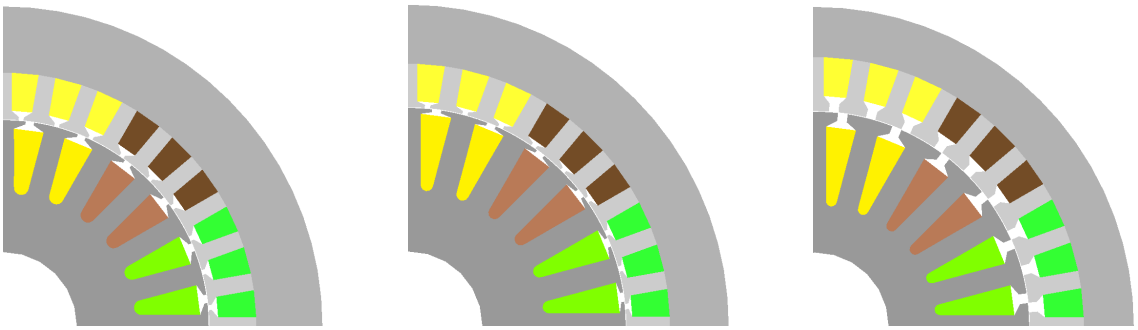

(a) CASE I **(b)** CASE II **(c)** CASE III

Figure 5.6: WRSM MFFD isolated optimum IHFEM model. phase A/a, phase B/b, phase C/c.

Table 5.5: NSGA-II CONTROL PARAMETERS

parameter	symbol	value
crossover and mutation probabilities	p_c, p_m	0.95, 0.09
crossover and mutation distribution indices	n_c, n_m	20, 20
population and iterations	N, G	50, 100

5.6.2. WRSM NSGA-II optimisation

The defined optimisation problem of Sub-section 5.6.1 is investigated, instead, using NSGA-II Op-AI in the optimisation procedure of Fig. 5.1. Thus the design variables of (5.15), and (5.16), objective function of (5.17) and constraint function of (5.18) are used. The chosen fixed design variables are given in Table 5.1.

In the case of NSGA-II, there is no need for cases as of (5.20)-(5.22) for the initial design variables since the NSGA-II is a non-gradient based Op-AI, and its performance is not influenced by starting design variable values. NSGA-II has four main control parameters namely:

- cross over probability p_c;
- mutation probability p_m;
- cross over distribution n_c; and
- mutation distribution n_m.

These control parameters are explained well in the book of J. Branke *et al* [61]. In Table 5.5, p_c, n_c and n_m are chosen according to recommendations of [27,57,135]. The reciprocal length of the design variables $[x]$ is adapted as p_m. In addition to the above NSGA-II control parameters, population (N) and iteration (G) sizes are chosen so as to not slow down the optimisation at the same time as utilising the genetic operators techniques discussed in [96].

Figure 5.7 shows the normalised converged Pareto optimal solutions' results using the NSGA-II Op-AI in *VisualDoc* following the above sub-section described problem at a unity power factor. There is no doubt that for the given feasibility design boundary specifications, the best option to present the prime design solution using the trade-off or compromise between two multi-objective functions, is well investigated using Pareto optimisation. This is demonstrated in Fig. 5.7 as compared to Fig. 5.4.

Because the front obtained by mapping the non-dominated solutions into objective space (Pareto-optimal front) is a good compromise objective space, given the results in Fig. 5.7, only the Pareto

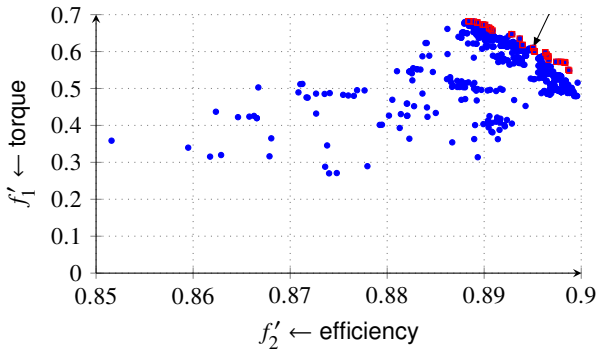

Figure 5.7: WRSM characteristics of normalised NSGA-II results performance space. □ and ● scatter points represent all Pareto-optimal and feasible solutions respectively.

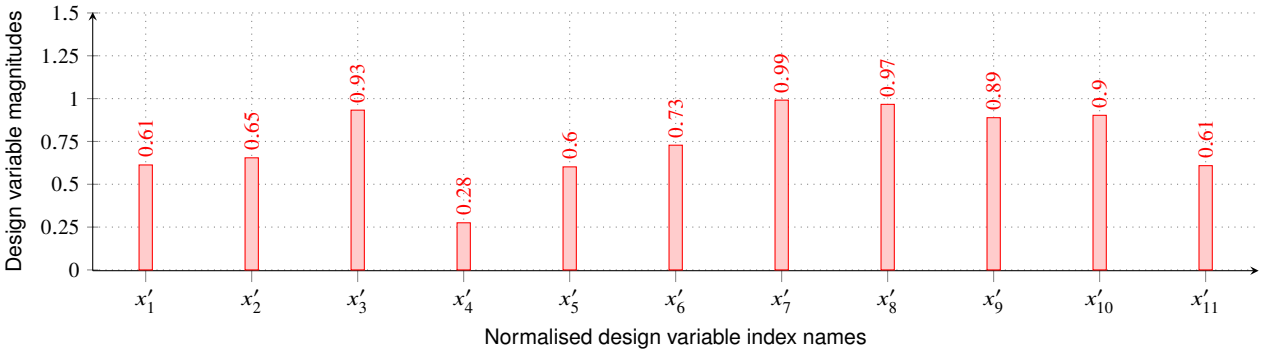

Figure 5.8: WRSM NSGA-II isolated normalised design variables

front (red scatter points) solution is investigated in this study. It can be observed that NSGA-II Pareto front solution results in high values of efficiency in the range 88.8 - 90 % when compared to MFFD results given in Table 5.4 of range 86.4 - 88.1 %. Furthermore, the NSGA-II results of Fig. 5.7 give a range of optimum designs that are a feasible solution for the design problem function, other than in the case of MFFD which results in a single final solution. This is demonstrated in Fig. 5.7 where NSGA-II gives normalised maximum torque of up to 0.7 at a normalised efficiency of 0.89 which is not attained when using MFFD.

It is important to mention that different methods (goal programming, the epsilon constraints method and weighted sum) can be used for the multi-objective optimisation problem to isolate a single Pareto optimal solution from the Pareto optimal front. Here, the isolated design is indicated by an arrow in Fig. 5.7. Figure 5.8 gives the normalised design variables of the isolated optimum WRSM design using NSGA-II Op-AI.

Using the normalised design variables of Fig. 5.8, the actual parameters of the WRSM using (5.19) are given in Tables 5.6 and 5.8. Tables 5.7 and 5.9 show the CASE II MFFD considered best results of Tables 5.3 and 5.4. The results of Tables 5.6-5.9 show different design variables and objective functions obtained when NSGA-II and MFFD Op-AI are used to find an optimum solution of a defined optimisation problem function. Figure 5.9 shows the corresponding WRSM IHFEM pole axial view model which resulted from the design variable values of Table 5.6. Figure 5.10 shows the MFFD IHFEM model (also shown in Fig. 5.6(b)) results from the design variables of Table 5.7. NSGA-II results in a WRSM selected design of different geometry as seen in Figs. 5.9 and 5.10 with design variables and performance values given in Tables 5.6-5.9. A note has to be made that the NSGA-II selected design is on the collar of the Pareto front which gives fewer torque results than MFFD, in this case. However, because NSGA-II gives more than one optimum result, it can be noted from Fig. 5.7 that better torque and efficiency results can be obtained using NSGA-II.

Table 5.6: WRSM NSGA-II ACTUAL DESIGN VARIABLES OF FIG. 5.8

variable	value	unit
x_1	171.0	mm
x_2	1.3	mm
x_3	0.9	mm
x_4	1.1	mm
x_5	120.3	mm^2
x_6	1.5	mm
x_7	1.0	mm
x_8	227.1	mm^2
x_9	5.3	Amm^{-2}
x_{10}	5.4	Amm^{-2}
x_{11}	54.8	°

Table 5.7: WRSM CASE II MFFD ACTUAL DESIGN VARIABLES OF FIG. 5.5 DESIGNS

variable	CASE II	unit
x_1	176.9	mm
x_2	2.2	mm
x_3	1.2	mm
x_4	1.2	mm
x_5	150.0	mm^2
x_6	3.7	mm
x_7	1.2	mm
x_8	260.0	mm^2
x_9	5.6	Amm^{-2}
x_{10}	6.0	Amm^{-2}
x_{11}	66.2	°

Table 5.8: WRSM NSGA-II ACTUAL OBJECTIVE AND CONSTRAINT FUNCTIONS

objective	value	unit
f_1	61.0	Nm
f_2	89.5	%
constraint	**value**	**unit**
g	1.0	-

Table 5.9: WRSM CASE II MFFD ACTUAL OBJECTIVE AND CONSTRAINT FUNCTIONS

objective	CASE II	unit
f_1	62.5	Nm
f_2	87.6	%
constraint	**CASE II**	**unit**
g	1.0	-

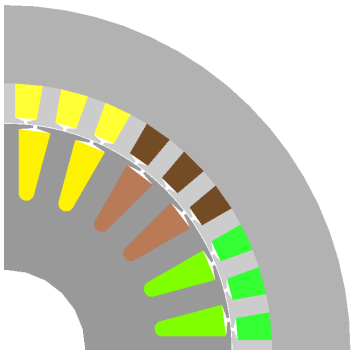

Figure 5.9: WRSM NSGA-II isolated optimum IHFEM model. phase A/a, phase B/b, phase C/c.

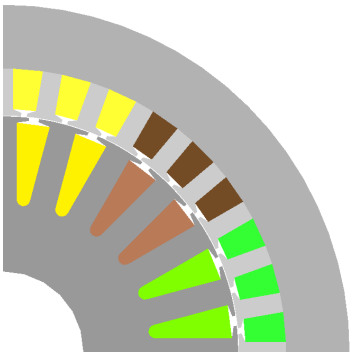

Figure 5.10: WRSM CASE II MFFD isolated optimum IHFEM model. phase A/a, phase B/b, phase C/c.

As in the application example of Sub-section 5.6.1 using MFFD, the results depicted in this section show the feasibility in application of the WRSM proposed model approach on the NSGA-II Op-Al defined optimisation problem function using the optimisation procedure of Fig. 5.1. Even though slower than the MFFD application results, the application of the NSGA-II on the WRSM design optimisation problem function gives better results and furthermore, additional possible optimal designs on the Pareto-front.

5.7. Grid-connected WRIM design optimisation

This section presents the application of the optimisation procedure of Fig. 5.1 using the WRIM proposed model approach alongside MFFD and NSGA-II Op-Al. In the design optimisation process of the grid-connected WRIM, the methodology of defining the problem function as of Section 5.6 is adapted for both scenarios when using MFFD and NSGA-II Op-Al with however, a few changes.

Figure 5.2 shows the dimensional design variables of the WRIM used in the design optimisation with the specifications given in Section 4.1 of Chapter 3 including the winding connection for stator and rotor excitation.

In the optimisation problem function, the objective is to find the design variables for an optimal performance WRIM using selected objective and constraint functions. In the case of the WRIM, eight design variables of (5.15) shown in Fig. 5.2 given by

$$[x] = \begin{bmatrix} x_1 \\ x_2 \\ \vdots \\ x_8 \end{bmatrix}, \tag{5.25}$$

and two additional loading variables defined by

$$[x] = \begin{bmatrix} x_9 \\ x_{10} \end{bmatrix} = \begin{bmatrix} n_s \\ f_\Delta \end{bmatrix}, \tag{5.26}$$

where n_s and f_Δ are stator turns per slot and slip frequency respectively, are used in the definition of the problem function. The geometric structure of the WRIM is similar to the WRSM with parallel stator and rotor teeth width. The additional loading parameters of (5.26) are selected because for a fixed grid voltage on the WRIM stator terminals with short-circuited rotor terminals, n_s and f_Δ influence the performance of the motor when changed. This is not the case on WRSM as seen in Section 5.6.

The selected objective of the optimisation is to improve the overall efficiency and power factor of the motor, hence, two separate objective matrices of (5.5) are considered as rounds, given by

- ROUND A:

$$[f]_a = \begin{bmatrix} f_1 \\ f_2 \end{bmatrix} = \begin{bmatrix} T_d \\ \cos(\phi_s) \end{bmatrix}, \tag{5.27}$$

- ROUND B:

$$[f]_b = \begin{bmatrix} f_3 \\ f_4 \end{bmatrix} = \begin{bmatrix} T_d \\ \eta \end{bmatrix}, \tag{5.28}$$

where T_d is the motor torque of components of (3.73) , $\cos(\phi_s)$ is the power factor of (3.38) and η is the efficiency of (3.69). In both optimisation of the objective function values of (5.27) and (5.28), the constraint matrix of (5.5) contains two selected constraints which are stator J_s and rotor J_r peak current densities and are separately defined in each round of (5.27) and (5.28) as

- ROUND A:

$$[g]_a = \begin{bmatrix} g_1 \\ g_2 \end{bmatrix} = \begin{bmatrix} J_s \\ J_r \end{bmatrix}, \tag{5.29}$$

- ROUND B:

$$[g]_b = \begin{bmatrix} g_3 \\ g_4 \end{bmatrix} = \begin{bmatrix} J_s \\ J_r \end{bmatrix}, \tag{5.30}$$

respectively. The chosen fixed design variables are given in Table 5.1, however, the subscript for the rotor is taken as r not f, e.g. B_f for WRSM is B_r in the case of the WRIM. Each design variable of

(5.25) and (5.26) to be passed from the Op-AI is given variable bounds chosen between $a = 0$ and $b = 1$ and is expressed as (5.19). The design variables are then used in the IHFEM program for the geometry creation as discussed in Appendix B.4. Symmetry is also utilised for the WRIM IHFEM geometry model which results in the identical motor model as of Fig. 5.3 to be optimised.

5.7.1. WRIM MFFD optimisation

The grid-connected WRIM MFFD optimisation is done using the two rounds of (5.27) ROUND A and (5.28) ROUND B, in which each round consists of the three cases as of (5.20), (5.21) and (5.22). Thus, the problem is further defined using the square of the objective function residual errors as of (5.6) given by

$$f_a = \sum_{i=1}^{2} \epsilon_i^2, \tag{5.31}$$

$$f_b = \sum_{i=3}^{4} \epsilon_i^2. \tag{5.32}$$

The residual errors of (5.31) and (5.32) are calculated from the targeted objective functions (a technique used in (5.24)) and are given by

$$\begin{aligned}
\epsilon_1 &= \begin{cases} 0 & : f_1 \geqslant f_1^{max} \\ \dfrac{f_1^{max} - f_1}{f_1^{max}} & : f_1 < f_1^{max} \end{cases} \quad \text{where} \quad f_1^{max} = 100 \text{ Nm}, \\
\epsilon_2 &= \begin{cases} 0 & : f_2 \geqslant f_2^{max} \\ \dfrac{f_2^{max} - f_2}{f_2^{max}} & : f_2 < f_2^{max} \end{cases} \quad \text{where} \quad f_2^{max} = 100 \text{ \%}, \\
\epsilon_3 &= \begin{cases} 0 & : f_3 \geqslant f_3^{max} \\ \dfrac{f_3^{max} - f_3}{f_3^{max}} & : f_3 < f_1^{max} \end{cases} \quad \text{where} \quad f_3^{max} = 100 \text{ Nm}, \\
\epsilon_4 &= \begin{cases} 0 & : f_4 \geqslant f_4^{max} \\ \dfrac{f_4^{max} - f_4}{f_4^{max}} & : f_4 < f_4^{max} \end{cases} \quad \text{where} \quad f_4^{max} = 1.0.
\end{aligned} \tag{5.33, 5.34}$$

In (5.33) and (5.34), f_1, and f_3 are torques of ROUND A and B respectively and f_2, and f_4 are efficiencies, and the power factor again of ROUND A and B respectively.

From (5.33) and (5.34), 100 Nm, 100 % and 1.0 are chosen as the exaggerated targeted torque, efficiency and power factor which the MFFD Op-AI is forced to achieve. Thus, MFFD optimisation of the WRIM is achieved by combining either T_d and η or T_d and $\cos(\phi_s)$ objective functions into the respective single objective functions of the square sum of residual errors f_a and f_b of (5.31) and (5.32) respectively.

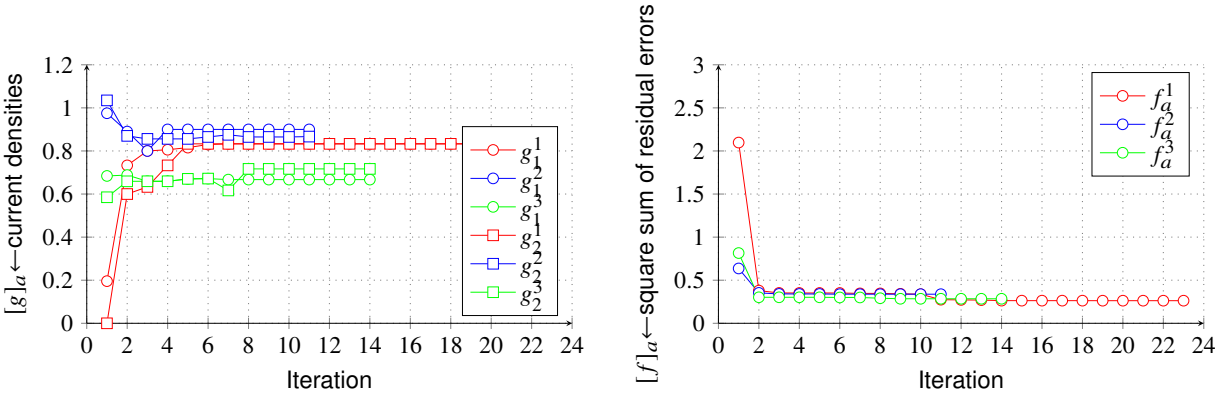

(a) constraint function **(b)** objective function

Figure 5.11: WRIM normalised constraint and objective functions ROUND A results during MFFD optimisation.

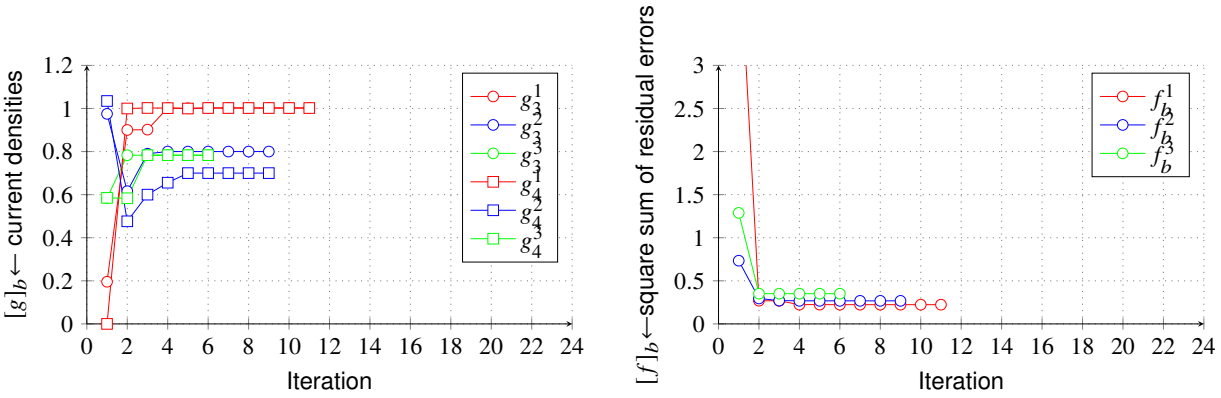

(a) constraint function **(b)** objective function

Figure 5.12: WRIM normalised constraint and objective functions ROUND B results during MFFD optimisation.

Table 5.10: WRIM MFFD OPTIMISATION RESULTS

CASE	ROUND A				ROUND B			
	total iterations	ϵ_1	ϵ_2	f_a	**total iterations**	ϵ_3	ϵ_4	f_b
I	22	0.49703	0.12404	0.26239	10	0.44932	0.14525	0.22269
II	10	0.54735	0.19656	0.33770	8	0.45154	0.25336	0.26756
III	13	0.51246	0.14997	0.28464	6	0.49032	0.33253	0.35067

Figures 5.11 and 5.12 show the constraint and objective functions' results during the MFFD optimisation after the application of the above-defined optimisation problem function. The superscript in the functions denotes the different cases (I-III) of (5.20)-(5.22). Table 5.10 gives the values of the minimised sum square error functions f_a and f_b of (5.31) and (5.32) in Figs. 5.11 and 5.12 respectively, together with the corresponding components ϵ_1 and ϵ_2 of (5.33) and ϵ_3 and ϵ_4 of (5.34).

It can be observed from Figs. 5.11 and 5.12 and Table 5.10 that the effect of using different initial design variable values and also objective functions (as expected from the results of Sub-section 5.6.1) results in different optimum results. Figure 5.13 shows the resultant normalised design variables of the selected minimised objective functions given in Table 5.10. The same phenomenon as observed in the results of Fig. 5.5 is observed in the results of Fig. 5.13 in which the optimum design variables are relatively closer to their initial set of the design variables. This is because MFFD seldom changes optimisation direction during the optimisation process since the algorithm is gradient-based.

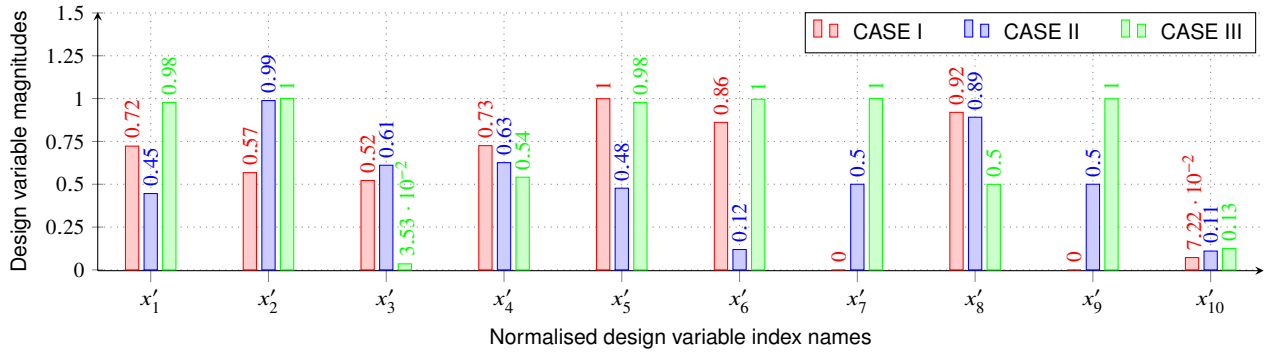

(a) ROUND A

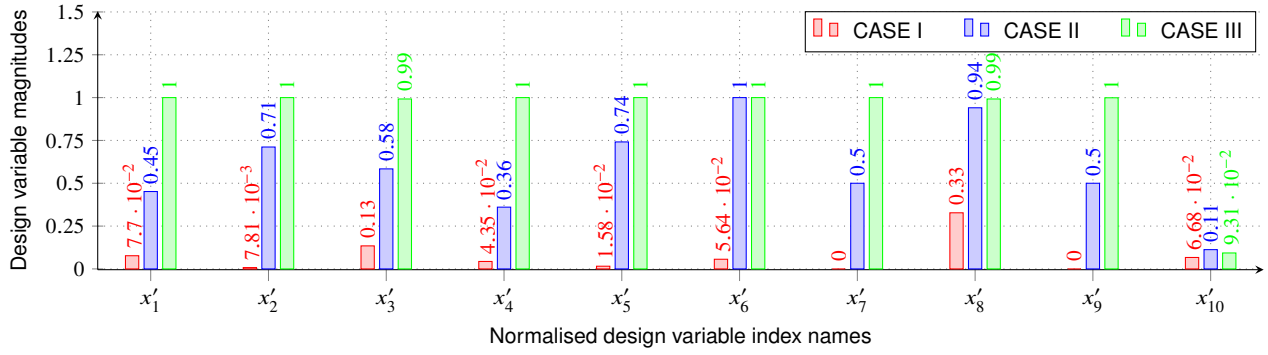

(b) ROUND B

Figure 5.13: WRIM MFFD isolated normalised design variables for (a) ROUND A and (b) ROUND B.

Table 5.11: WRIM MFFD ACTUAL DESIGN VARIABLES OF FIG. 5.13 DESIGNS

variable	ROUND A			ROUND B			unit
	CASE I	CASE II	CASE III	CASE I	CASE II	CASE III	
x_1	179.3	174.6	183.6	168.3	174.7	184.0	mm
x_2	3.1	4.0	4.0	2.0	3.4	4.0	mm
x_3	2.7	2.9	1.3	1.6	2.8	3.9	mm
x_4	2.5	2.3	2.2	1.3	1.9	3.0	mm
x_5	180	164.3	179.3	150.5	172.2	180.0	mm^2
x_6	3.7	2.2	4.0	2.1	4.0	4.0	mm
x_7	2.7	2.9	1.3	1.6	2.8	3.9	mm
x_8	254.4	252.4	225.0	212.9	255.8	259.9	mm^2
x_9	24	62	100	24	62	100	-
x_{10}	3.6	5.5	6.3	3.3	5.6	4.7	Hz

Using the normalised design variables of Fig. 5.13, the actual parameters using (5.19) are given in Tables 5.11 and 5.12. Figures 5.14 and 5.15 show the corresponding IHFEM pole axial view models which resulted from design variables of Table 5.11 for ROUND A and B, respectively.

From Table 5.12, it can be observed that CASE I in both ROUND A and ROUND B gives good results, however, with ROUND B being the best in terms of performance. Hence, for the defined WRIM problem function, optimising for torque and efficiency results in good performance of the motor type.

Table 5.12: WRIM MFFD ACTUAL OBJECTIVE AND CONSTRAINT FUNCTIONS

objective	ROUND A			objective	ROUND B			unit
	CASE I	CASE II	CASE III		CASE I	CASE II	CASE III	
f_1	50.3	45.3	48.8	f_3	55.1	54.9	51.0	Nm
f_2	0.88	0.80	0.84	f_4	85.5	74.7	66.8	–, %
constraint	**ROUND A**			**constraint**	**ROUND B**			**unit**
	CASE I	**CASE II**	**CASE III**		**CASE I**	**CASE II**	**CASE III**	
g_1	5.0	5.4	4.0	g_3	6.0	4.8	4.7	Amm^{-2}
g_2	5.0	5.2	4.3	g_4	6.0	4.2	4.7	Amm^{-2}

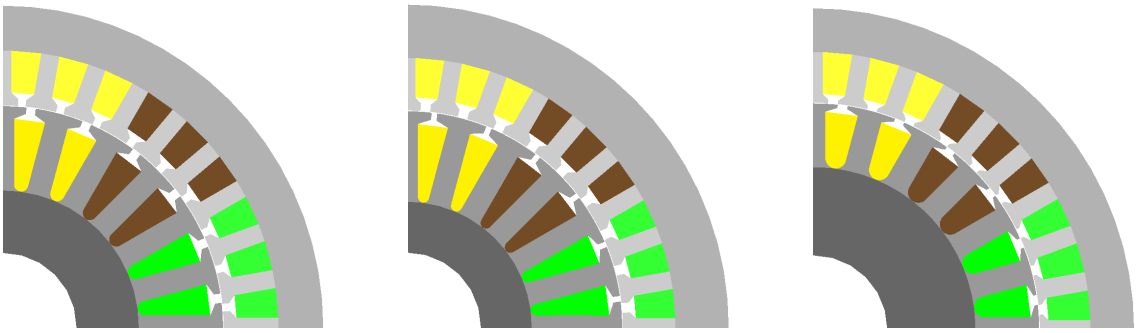

(a) CASE I **(b)** CASE II **(c)** CASE III

Figure 5.14: WRIM MFFD isolated optimum round A IHFEM model. phase A/a, phase B/b, phase C/c.

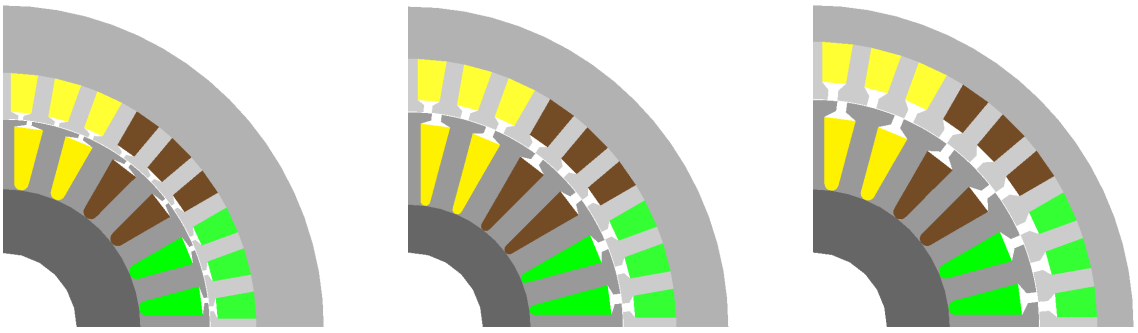

(a) CASE I **(b)** CASE II **(c)** CASE III

Figure 5.15: WRIM MFFD isolated optimum ROUND B IHFEM model. phase A/a, phase B/b, phase C/c.

5.7.2. WRIM NSGA-II optimisation

The defined optimisation problem of Sub-section 5.7.1 for the WRIM is investigated in this section, however, using NSGA-II. Thus the design variables of (5.25), and (5.26), objective functions of (5.27), and (5.28) and constraint function of (5.29), and (5.30) are used. The chosen fixed design variables are given in Table 5.1 as discussed in Sub-section 5.7.1. As mentioned, in the case of the NSGA-II Op-AI, there is no need of the cases (5.20)-(5.22) for the initial design variables since the NSGA-II is a non-gradient based Op-AI, and its performance is not influenced by starting design variable values. The four main control variables of the NSGA-II Op-AI given in Table 5.5 are also used in the optimisation of the WRIM.

Figure 5.16 shows the normalised converged Pareto optimal solution results using the NSGA-II Op-AI in *VisualDoc* following the above herein sub-section described problem. As earlier stated, a good compromise in a multi-objective function optimisation is well represented using Pareto optimi-

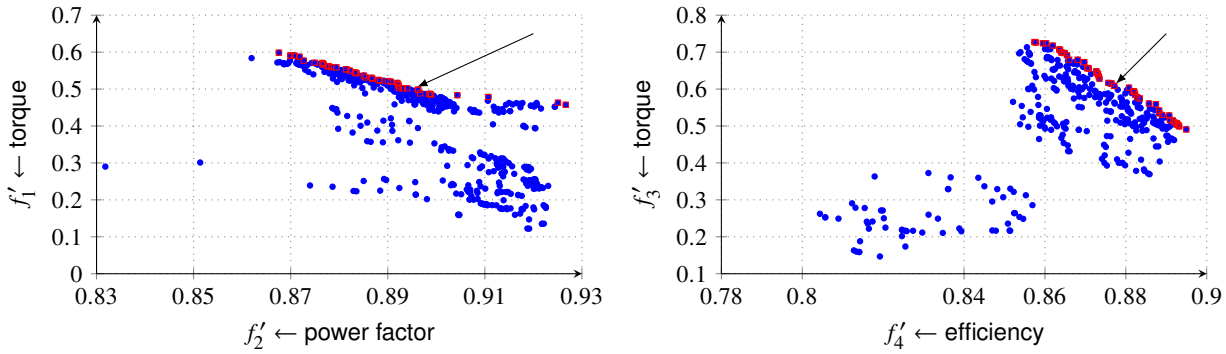

(a) ROUND A **(b)** ROUND B

Figure 5.16: WRIM characteristics of normalised optimisation results performance space. □ and ● scatter points represent all Pareto-optimal and feasible solutions respectively.

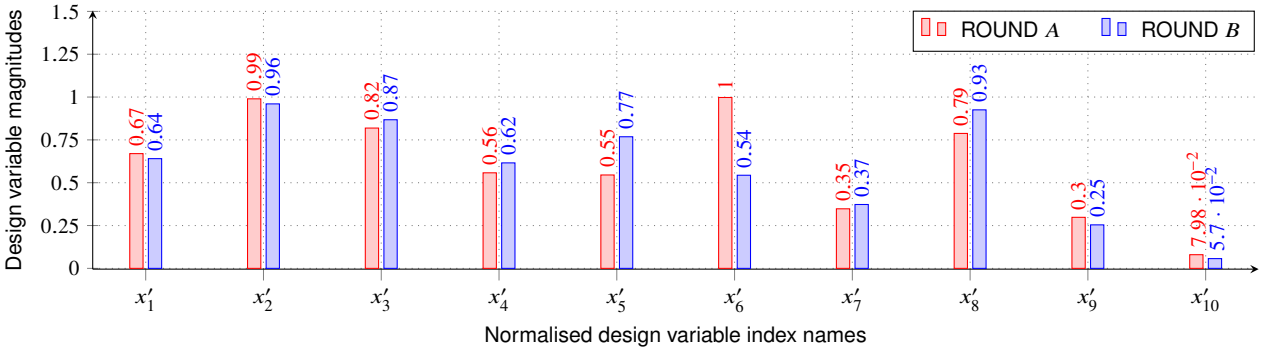

Figure 5.17: WRIM NSGA-II isolated normalised design variables of ROUND A and ROUND B.

Table 5.13: WRIM NSGA-II ACTUAL DESIGN VARIABLES OF FIG. 5.8

variable	ROUND A	ROUND B	unit
	value		
x_1	174.2	166.5	mm
x_2	4.0	3.8	mm
x_3	3.3	3.5	mm
x_4	1.7	1.8	mm
x_5	163.5	230.5	mm^2
x_6	4.0	3.4	mm
x_7	1.4	1.5	mm
x_8	236.3	277.6	mm^2
x_9	14	20	-
x_{10}	4.0	2.8	Hz

sation as shown in Fig 5.16 compared with Fig. 5.11. Again, since the front obtained by mapping the non-dominated solutions into objective space (Pareto-optimal front) is a good compromise objective space, the Pareto front (red scatter points) solution is only considered for further results evaluation. Figure 5.17 gives the normalised design variables of the isolated optimum WRIM design of ROUND A and B using NSGA-II, shown by the arrow in Fig. 5.16.

Using the normalised design variables of Fig. 5.17, the actual parameters of the motor type using (5.19) are given in Tables 5.13 and 5.14. Figure 5.18 shows the corresponding IHFEM pole axial view model which resulted from the design variables of Table 5.13.

For comparison purposes, Tables 5.15 - 5.18 give optimisation results considered to be the best

Table 5.14: WRIM NSGA-II ACTUAL OBJECTIVE AND CONSTRAINT FUNCTIONS

objective	ROUND A	objective	ROUND B	unit
	value		value	
f_1	49.2	f_3	63.3	Nm
f_2	0.896	f_4	87.7	%, –
constraint	**ROUND A**	**constraint**	**ROUND B**	**unit**
	value		**value**	
g_1	5.9	g_3	4.4	Amm^{-2}
g_2	5.8	g_4	4.1	Amm^{-2}

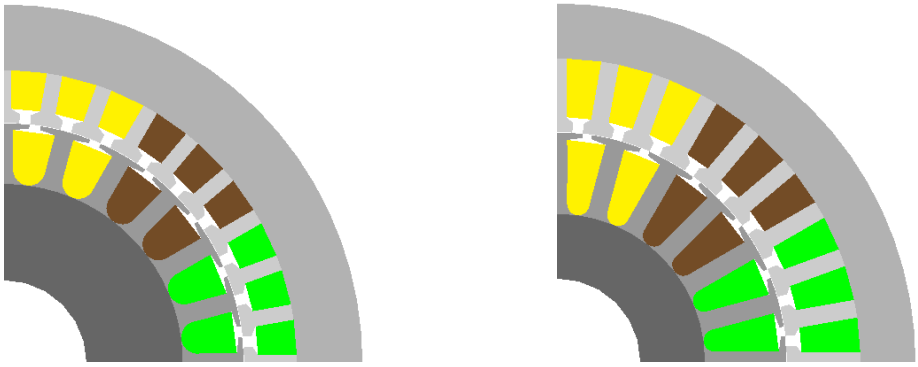

(a) ROUND A **(b)** ROUND B

Figure 5.18: WRIM NSGA-II isolated optimum IHFEM models. phase A/a, phase B/b, phase C/c.

Table 5.15: WRIM NSGA-II ACTUAL OPTIMUM DESIGN VARIABLES OF FIG. 5.8

variable	ROUND B	unit
	value	
x_1	166.5	mm
x_2	3.8	mm
x_3	3.5	mm
x_4	1.8	mm
x_5	230.5	mm^2
x_6	3.4	mm
x_7	1.5	mm
x_8	277.6	mm^2
x_9	20	-
x_{10}	2.8	Hz

Table 5.16: WRIM MFFD ACTUAL OPTIMUM DESIGN VARIABLES OF FIG. 5.13 DESIGNS

variable	ROUND B	unit
	CASE I	
x_1	168.3	mm
x_2	2.0	mm
x_3	1.6	mm
x_4	1.3	mm
x_5	150.5	mm^2
x_6	2.1	mm
x_7	1.6	mm
x_8	212.9	mm^2
x_9	24	-
x_{10}	3.3	Hz

when using NSGA-II in this section and MFFD in Section 5.7.1. The corresponding pole face axial view IHFEM model resulting from Tables 5.15 and 5.16 is shown in Fig. 5.19. It can be seen from Fig. 5.19 that the optimum solution of NSGA-II and MFFD results in different motor geometries.

In general as expected from the findings of Section 5.6, the application of the NSGA-II in this section on the defined WRIM optimisation problem gives better results in terms of performance, i.e. NSGA-II Table 5.17 results when compared to the MFFD Table 5.18 results in Section 5.7.1. From the results of Table 5.17, optimising for torque and efficiency of (5.28) gives better results.

Table 5.17: WRIM NSGA-II ACTUAL OPTIMUM OBJECTIVE AND CONSTRAINT FUNCTIONS

objective	ROUND B	unit
	value	
f_3	63.3	Nm
f_4	87.7	%
constraint	**ROUND B**	**unit**
	value	
g_3	4.4	Amm^{-2}
g_4	4.1	Amm^{-2}

Table 5.18: WRIM MFFD ACTUAL OPTIMUM OBJECTIVE AND CONSTRAINT FUNCTIONS

objective	**ROUND B**	**unit**
	CASE I	
f_3	55.1	Nm
f_4	85.5	%
constraint	**ROUND B**	**unit**
	CASE I	
g_3	6.0	Amm^{-2}
g_4	6.0	Amm^{-2}

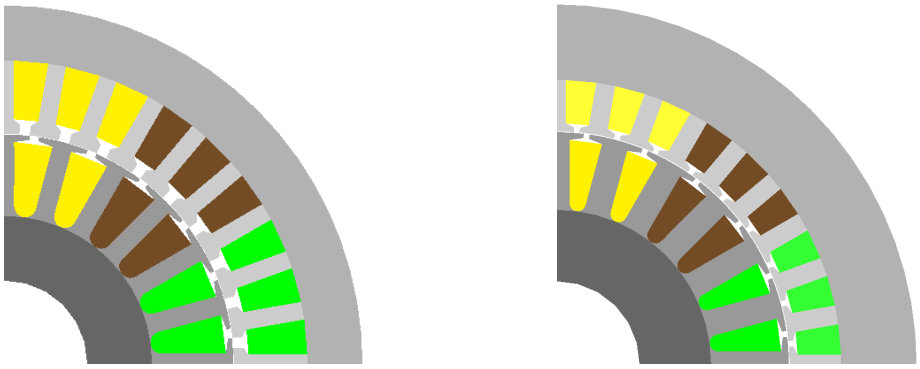

(a) NSGA-II optimum design **(b)** MFFD optimum design

Figure 5.19: WRIM NSGA-II and MFFD optimum IHFEM models. phase A/a, phase B/b, phase C/c.

5.8. Chapter conclusions

This chapter herein presents a study on the WRSM and WRIM motor types performance optimisation. Mathematically formulated multi-objective problems are used to determine optimum motor design variable values derived from a defined optimisation procedure using MFFD and NSGA-II Op-Al. Both Op-Al processes prove to be effective in design optimisation of motor types. However, the application of the Op-Al result in different optimal designs in NSGA-II gives much better problem function solutions. It is also shown that the formulation of the design optimisation problem function is important in helping the Op-Al to locate the global minimum or maximum solution of the problem. An important conclusion is that the proposed model approaches can be used successfully alongside both gradient and non-gradient based Op-Al optimisation of the defined problem function motor types.

Chapter 6

Manufacturing and laboratory measurements: Grid-connected WRSM and WRIM

This chapter presents the experimental validation of the proposed model approaches described in Chapter 3. The built grid-connected WRSM and WRIM motor types are optimum designed motors found after using the techniques given in Chapter 5. The experimental set-up is described in detail in which a dynamometer is utilised as a load and results are depicted.

6.1. Introduction

With few exceptions, the work presented in this chapter is the validation of the WRSM and WRIM motor types proposed model approaches. The validation is done by laboratory studies carried out to experimentally test the performance of the prototyped grid-connected motor types. Furthermore, the continuous accessibility of the motor types' parameters in the proposed model approaches is used in this chapter as an effective and powerful tool to explain the behaviour of the test motor types under different operating points. It is important also to take note that the proposed model approaches are also validated in Chapter 4 using a commercial package, ANSYS-Maxwell FEM and the results agreed.

6.2. Prototyping and experimental setup

Figure 6.1 shows the WRSM and WRIM m400-50a lamination cuttings. Details of the lamination steel are given in Appendix B.1. Figure 6.2 shows the corresponding dimensional parameters of Fig. 6.1 for the WRSM and WRIM motor type lamination cuttings. Figure 6.3 shows stamping of the WRSM and WRIM rotors. Since both motor types' stators need special tools for clitting, the stator laminations were sent to a manufacturing company (not shown here). Both the WRSM and WRIM motor types have stacks lengths of 125 mm for both the stator and rotor lamination stacks. Figure 6.4 shows the WRSM and WRIM stator and rotor wound stacks. Both the stator and rotor of both the WRSM and WRIM motor types have a distributed winding configuration as described in Appendix C.1. This choice is based on the need to have a general motor built for the validation of model approaches in this study.

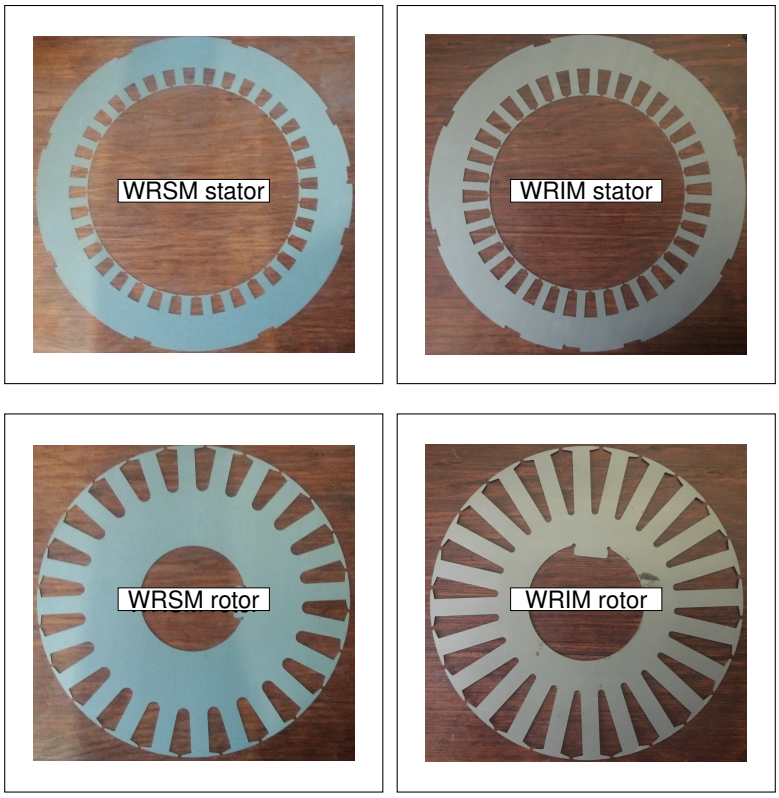

Figure 6.1: WRSM and WRIM m400-50A lamination cuttings.

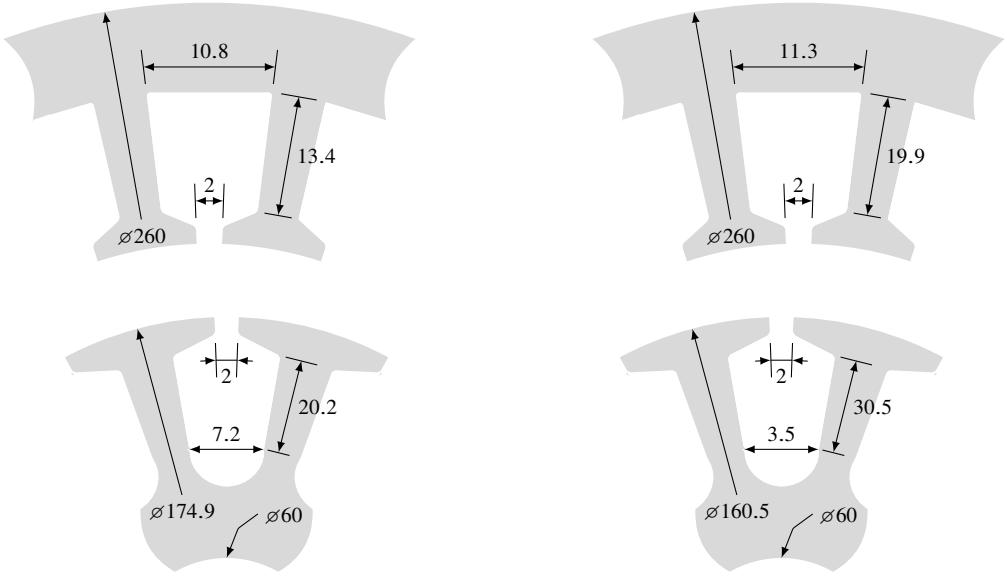

(a) WRSM **(b)** WRIM

Figure 6.2: Prototyped motor stator and rotor lamination cuttings dimensions of (a) WRSM and (b) WRIM. Dimensions in mm.

Figure 6.5 shows a D160M motor frame size used for both the grid-connected WRSM and WRIM motor types. The choice of the motor frame is based on the availability of the frame. In Fig.6.5 the finished assembled motor is shown. Appendix C gives mechanical drawings for the prototyped motor types. Table 6.1 shows some other motor parameters. Figure 6.6 shows the laboratory set-up process. The dynamometer is mechanically coupled through the torque sensor to the motor to

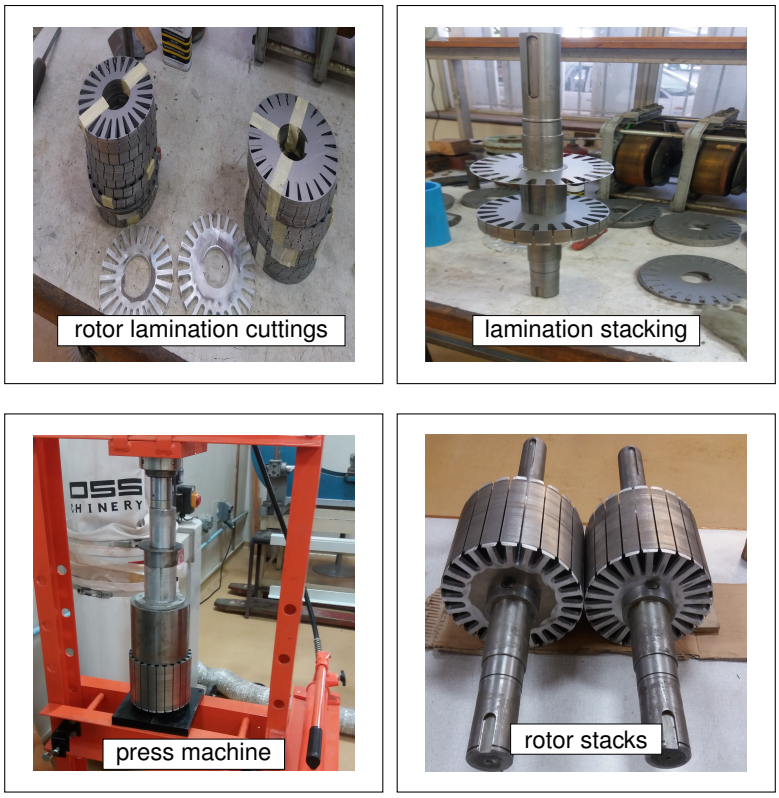

Figure 6.3: WRSM and WRIM rotor lamination stacking.

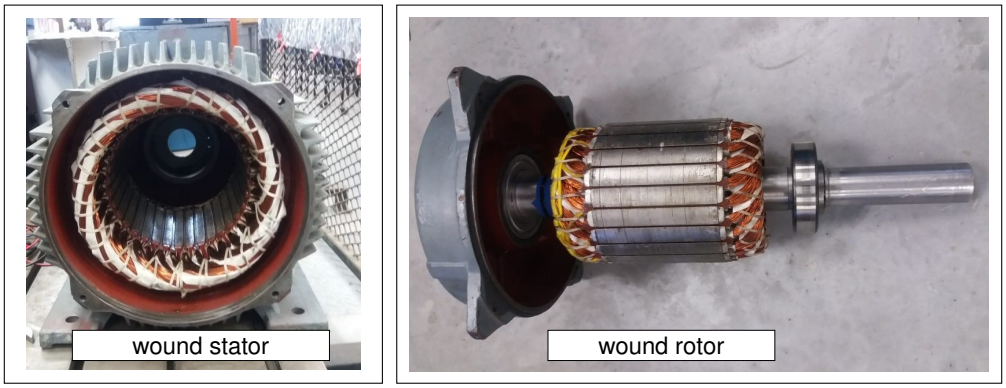

Figure 6.4: Stator and rotor wound lamination stacks.

Table 6.1: PROTOTYPED WRSM AND WRIM MOTOR PARAMETERS

variable	WRSM		WRIM	
	stator	**rotor**	**stator**	**rotor**
resistance, $R_s, R_{(f,r)}$ (Ω)	0.5	0.8	0.7	0.6
slots, $Q_s, Q_{(f,r)}$	36	24	36	24
turns per slot, $n_s, n_{(f,r)}$	16	32	24	30
pole pairs, p	2			
slots per pole per phase, $q_s, q_{(r,f)}$	3, 2			
air gap, g_a (mm)	0.305			
stack length, l (mm)	125			

provide the mechanical load for both motors. Since the WRSM only develops torque at synchronous speed, a dc pony motor also mechanically coupled to the dynamometer, is used to facilitate the

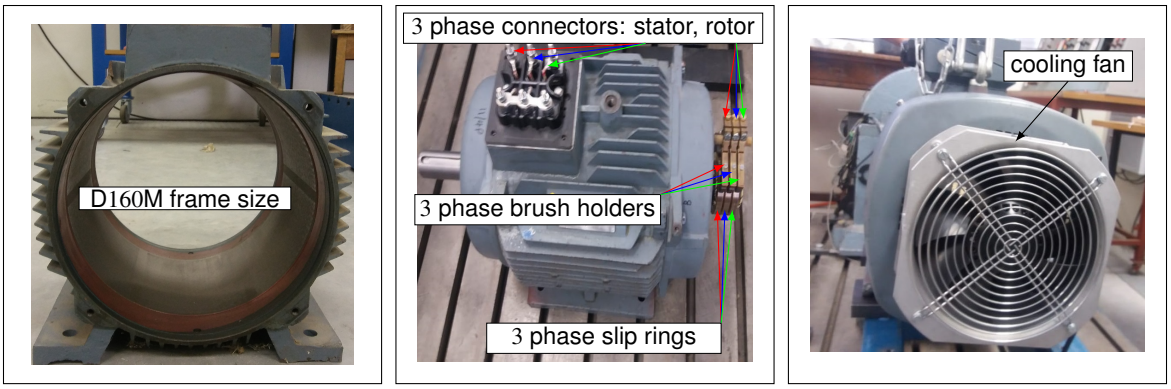

Figure 6.5: WRSM and WRIM motor assembled on a D160M frame.

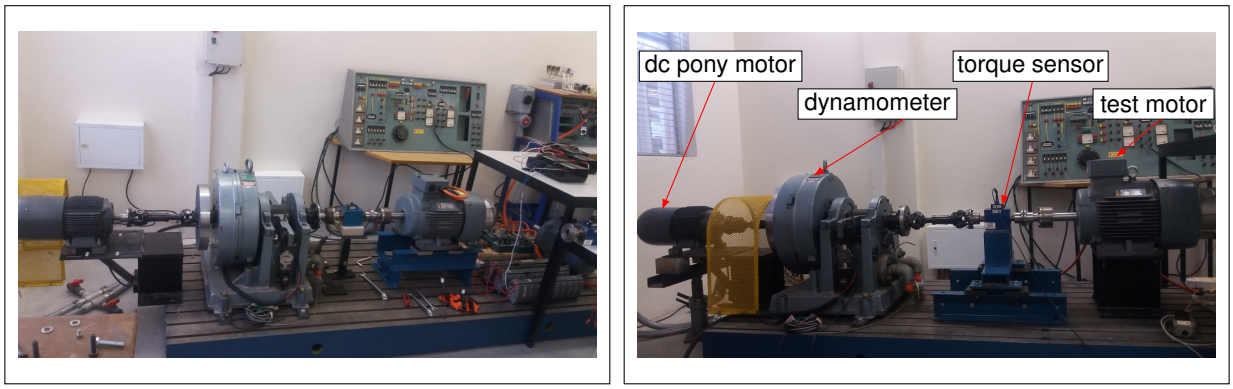

Figure 6.6: Laboratory set-up.

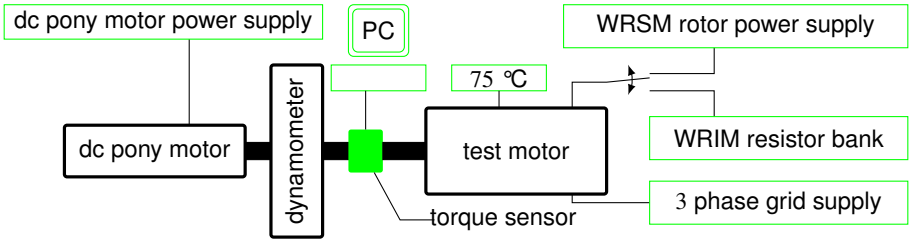

Figure 6.7: Laboratory setup block diagram.

starting when the WRSM is under test.

6.3. Experimental tests measurements reading

Figure 6.7 shows the laboratory setup block diagram of the test bench shown in Fig. 6.6 which is used to test the motor types at a winding operating temperature monitored at $75\ ℃$. The torque sensor is used to measure the speed and mechanical output power of (3.45). Figures 6.8 and 6.9 show connections for the winding excitation of the WRSM and WRIM respectively as illustrated in the block diagram of Fig. 6.7. For both motor types experiments, tests are carried out on a 400 V line-line 50 Hz grid power supply. Finally, the power factor, power, voltage and currents of the supply to the stator were measured.

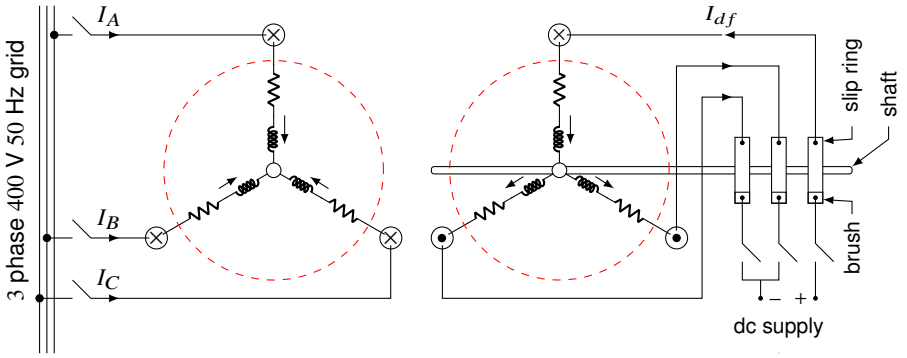

(a) stator connection **(b)** rotor connection

Figure 6.8: WRSM excitation connection for (a) stator and (b) rotor windings.

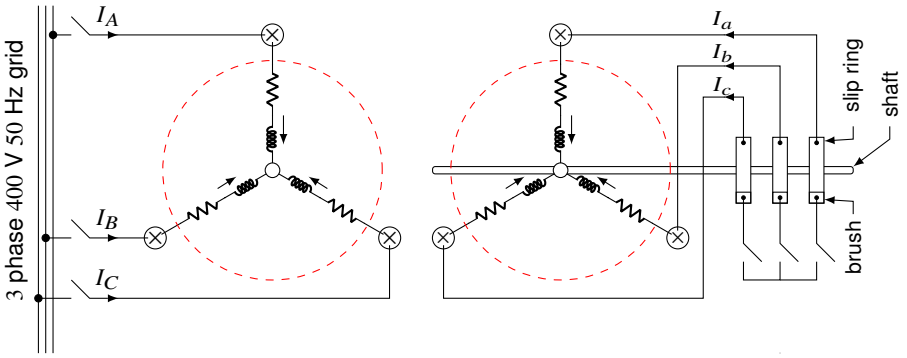

(a) stator connection **(b)** rotor connection

Figure 6.9: WRIM excitation connection for (a) stator and (b) rotor windings.

6.4. WRSM experimental results

In this section, the proposed model approach of the grid-connected WRSM is validated using the experimental test results. Further discussions are given using the model approach evaluated parameters to explain the motor type behaviour when subjected to different load conditions [84].

6.4.1. Open and short circuit tests results

The open and short circuit curves of the motor are obtained by operating the motor at constant synchronous speed and measuring the stator open circuit voltage and short circuit current as a function of field current respectively. In the tests, the field current was limited to 17 A due to the dc pony motor's limited power. With the measured stator open circuit voltage V_{rms}, the measured stator open circuit field inductances are calculated from

$$\begin{cases} L_{dsdf} = \dfrac{V_{qs}}{\omega_s I_{df}} = \dfrac{\sqrt{2}V_{rms}}{\omega_s I_{df}} \\ M_{qsdf} = -\dfrac{V_d}{\omega_s I_{df}} = 0. \end{cases} \tag{6.1}$$

Using the proposed WRSM model approach in Section 3.5, setting the stator current and voltage

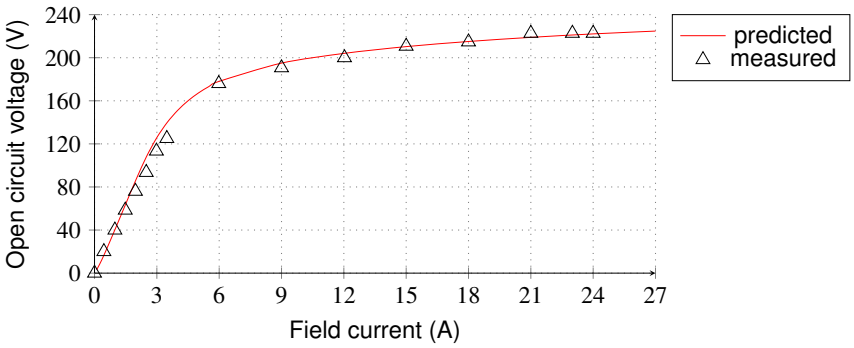

Figure 6.10: WRSM predicted and measured stator open circuit voltage versus field current at synchronous speed.

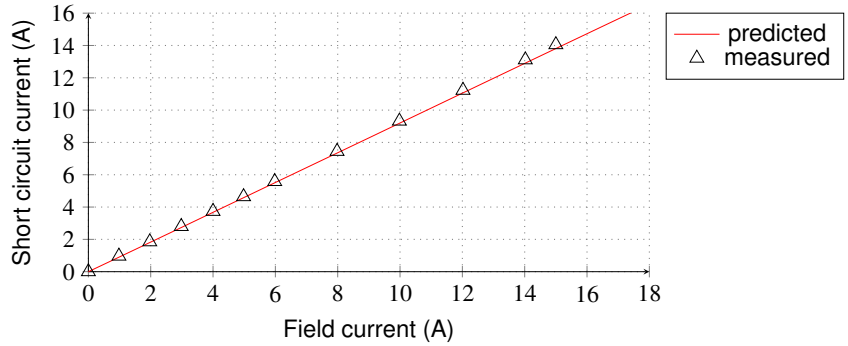

Figure 6.11: WRSM predicted and measured stator short circuit current versus field current at synchronous speed.

magnitudes to zero, the respective stator open circuit voltage and short circuit current phasors are predicted from

$$[V_{oc}] = [Z_{oc}][I_{oc}] \quad \text{where} \quad I_s = 0, \tag{6.2}$$

and

$$[I_{sc}] = [Z_{sc}]^{-1}[V_{sc}] \quad \text{where} \quad V_s = 0. \tag{6.3}$$

The predicted field inductances using (6.2) are calculated from the non-linear FEM solutions as

$$\begin{cases} L_{dsdf} = \dfrac{\Lambda_{dsdf}}{I_{df}} \\ M_{qsdf} = \dfrac{\Lambda_{qsdf}}{I_{df}}. \end{cases} \tag{6.4}$$

Hence, only one non-linear FEM solution is necessary per field current value to obtain (6.4) as a function of field current.

Figures 6.10 and 6.11 show good concurrence between the measured and predicted WRSM open and short circuit curves as a function of field current.

Figure 6.12 also shows an excellent concurrence between the measured and predicted open circuit field inductances of (6.1) and (6.4), respectively. Also shown in Fig. 6.12 are the FEM used m400-50a lamination BH characteristics, which explain the behaviour of the predicted field inductance of (6.4) at low H values. Figure 6.12 illustrates the expected phenomenon of saturation in the motor which decreases the field inductances as the field current increases.

Figure 6.13 shows the predicted current phasor components of (6.3) of magnitude shown in Fig.

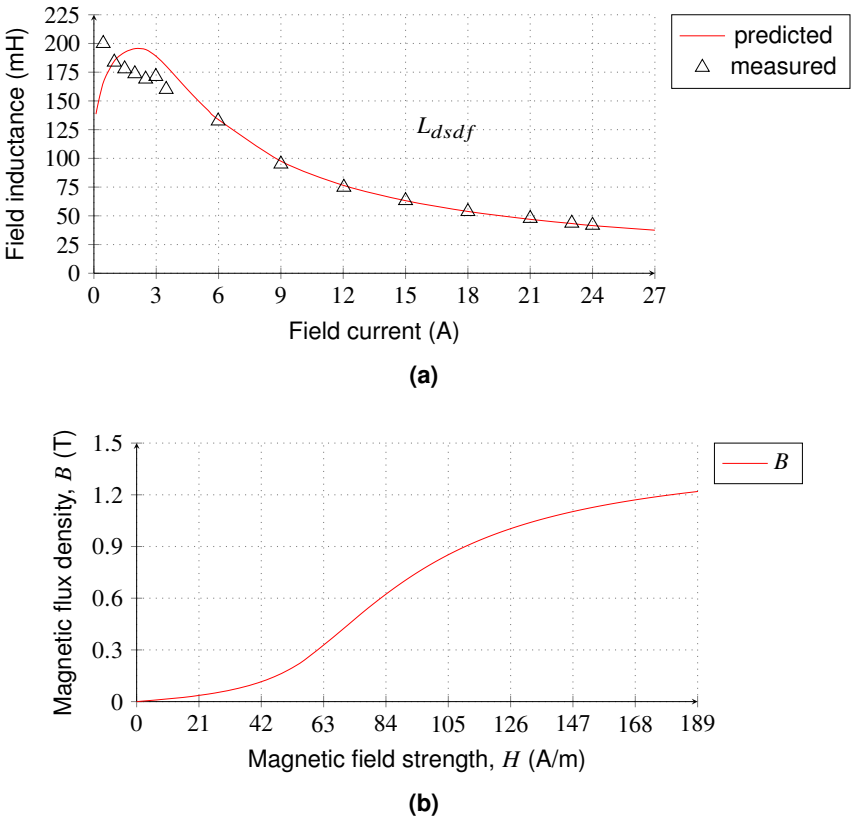

Figure 6.12: WRSM (a) predicted and measured stator open circuit field inductance and (b) manufacturer's m400-50a BH curve.

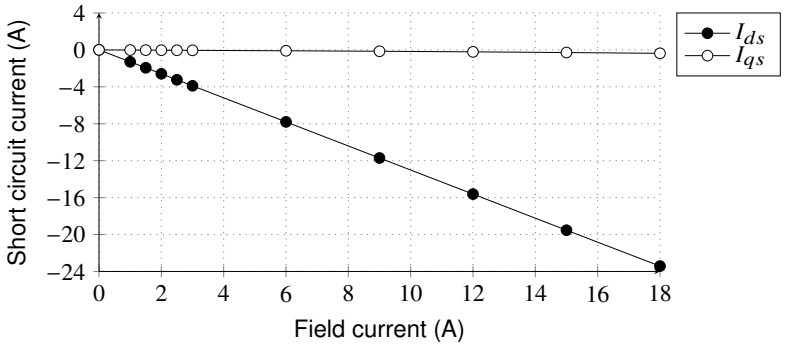

Figure 6.13: WRSM calculated stator short circuit dq-axes currents versus field current at synchronous speed.

6.11 in which $I_{qs} \approx 0$. Furthermore, the short-circuit flux linkages and inductances due to the I_{ds}, I_{qs} and I_{df} currents of Fig. 6.13 are shown in Fig. 6.14, calculated from (3.27)-(3.33). As expected, both the short-circuit mutual flux linkages $M_{dsqs}I_{qs} = M_{qsds}I_{ds} = M_{qsdf}I_{df} \approx 0$ and inductances $M_{dsqs} = M_{qsds} = M_{qsdf} \approx 0$ since $I_{qs} \approx 0$, hence they are not shown in Fig. 6.14. However, what is illuminating from the results of Fig. 6.14(c) is the increase in the short-circuit inductance (up to 19%) with field current, which is classically assumed constant in literature. This assumption is incorrect in the considered motor, and saturation saliency should be always taken into account due to the increase of the main flux $\Lambda_s = \sqrt{\Lambda_{ds}^2 + \Lambda_{qs}^2}$ of Fig. 6.14(b).

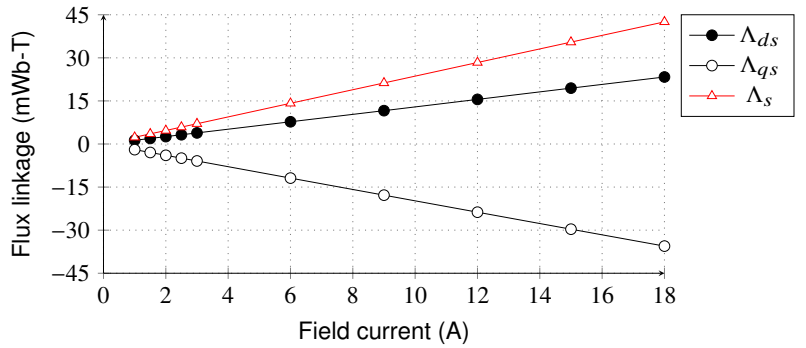

(a)

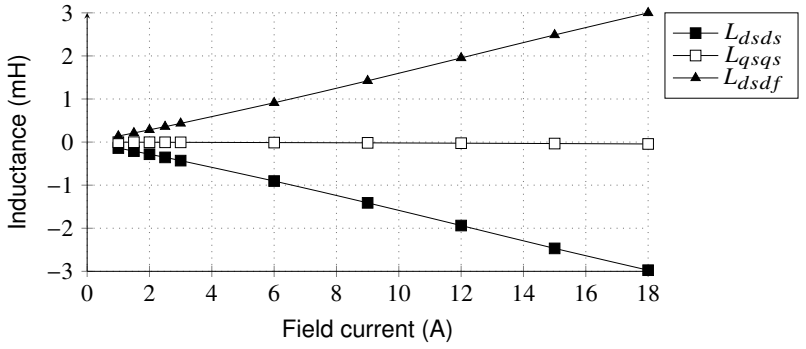

(b)

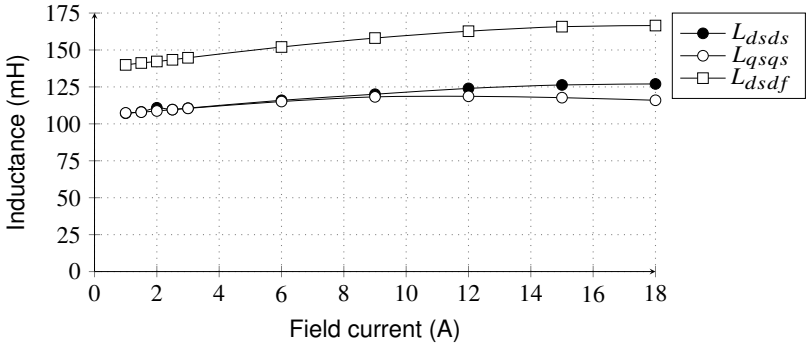

(c)

Figure 6.14: WRSM calculated stator short circuit (a) total flux linkages, (b) flux linkage components and (c) inductances versus field current at synchronous speed.

6.4.2. Mechanical and core losses test results

The mechanical power required to drive the test motor with excited rotor is the sum of bearing, windage and open-circuit core losses [40]. These losses are shown in Fig. 6.15 for the measured and predicted sum of mechanical and core losses as a function of the motor speed. A good agreement is noticed, however, with the predicted core losses of (3.44) multiplied by a constant factor of 1.63 to take into account other additional core losses. It must be noted that core losses in electrical machines are generally difficult to compute accurately and (3.44) only consider the maximum flux densities of the teeth and yoke for the estimation [66, 113].

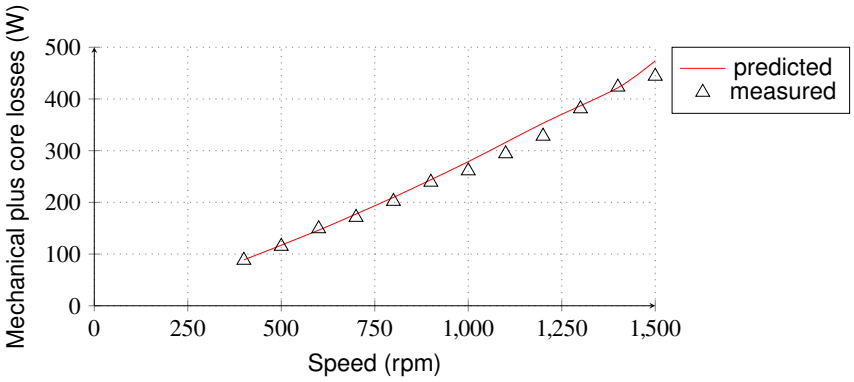

Figure 6.15: WRSM predicted and measured mechanical and core losses versus rotor speed.

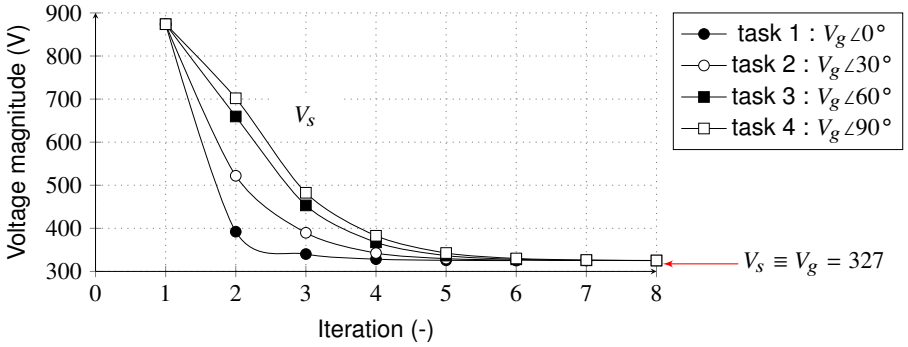

Figure 6.16: WRSM calculated stator voltage magnitude variation with the iterative process.

6.4.3. Parameters and performance measurement results

The same experimental setup of Fig. 6.7 of the test bench shown in Fig. 6.6 excited as in Fig. 6.8 is used to measure the WRSM parameters and performances at different operating points by changing the dynamometer power to vary the load on the test motor. To predict the motor parameters and performances, the simulated operating point parameter and performance maps are used. These maps are quickly constructed using python multiprocessing (Appendix A.7) also done in Section 4.2. Thus, the iterative process of Fig. 3.6 for the desired grid voltage V_g, field excitation I_{df} and motor geometry is distributed into tasks of the load angle δ_g of parallel running processes e.g. shown in Fig. 6.16 when δ_g is equal to $0°$ task 1, $30°$ task 2 $60°$ task 3 and $90°$ task 4. In Fig. 6.16, the calculated stator voltage magnitude V_s converges to the desired grid voltage $V_g = 327$ V at different load angles.

The corresponding above-described performance maps constructed are shown in Fig. 6.17 for P_o. As an example, for a measured $P_o = 3.5$ kW excited by 327 V grid and $0 \leqslant I_{df} \leqslant 29$ A, the corresponding load angle values ($11.4 \leqslant \delta_g \leqslant 42.9°$) for the iterative process are found by using Python splines on the maps as shown in Fig. 6.17. The load angle determination can be repeated for different measured output power $3 \leqslant P_o \leqslant 16°$ kW which results in δ_g maps as shown in Fig. 6.18. The construction of the parameters and performance maps shows the effectiveness, power and compactivity of the iterative process.

Figure 6.19 shows the relationship between the output power P_o of (3.45) and input power P_i of (3.40) while Figs. 6.20, 6.21 and 6.22 show the relationship between the stator current $I_s/\sqrt{2}$ of (3.35), efficiency η of (3.39) and power factor $\cos(\phi_s)$ of (3.38), respectively. Also from Figs. 6.19-6.22 are measured experimental results. A constant dc current of $I_{df} = 23$ A into the motor field windings is used because it is the simplest dc regulator method type used in industry besides the reactive

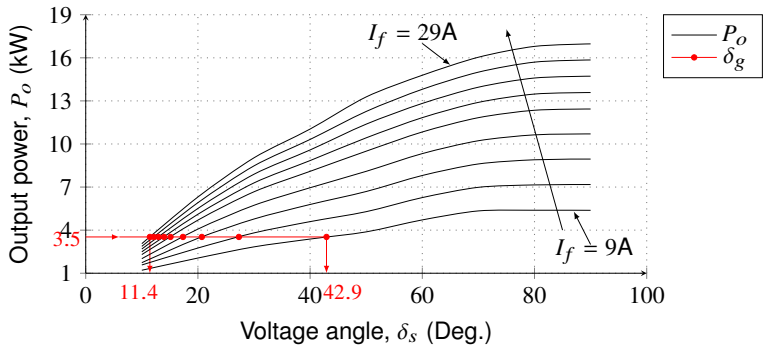

Figure 6.17: WRSM calculated power output map at 400 V, 50 Hz supply with field current a parameter and supply voltage a constant versus load angle.

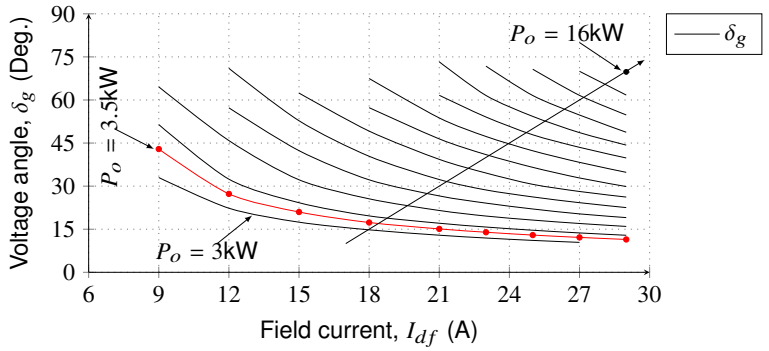

Figure 6.18: WRSM stator voltage angle map with power output a parameter.

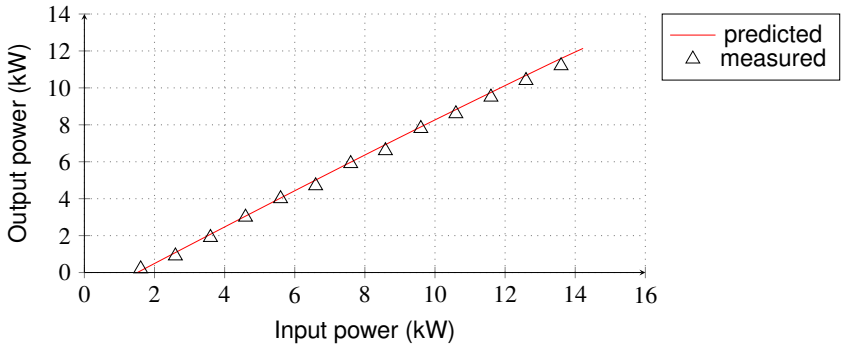

Figure 6.19: WRSM predicted and measured mechanical power output versus electrical power input.

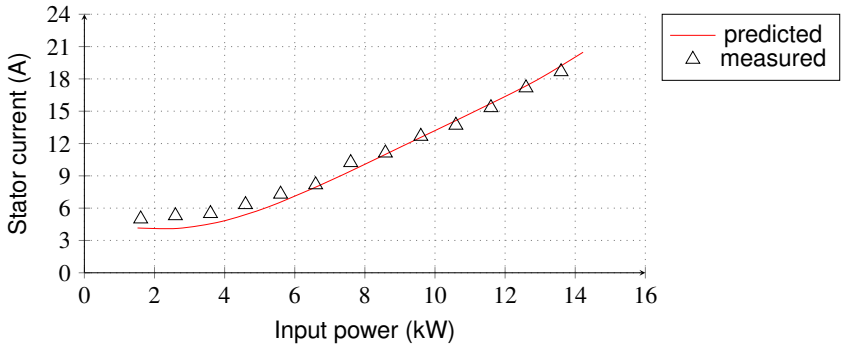

Figure 6.20: WRSM predicted and measured stator current versus electrical power input.

power and power regulations [88]. However, the capability of the motor is set back since there is no field current control. From Figs. 6.19-6.22 a good agreement between the measured and predicted results can be noticed.

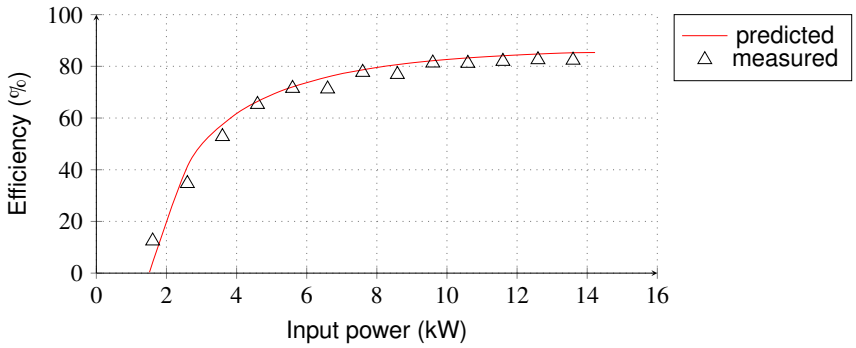

Figure 6.21: WRSM predicted and measured efficiency versus electrical power input.

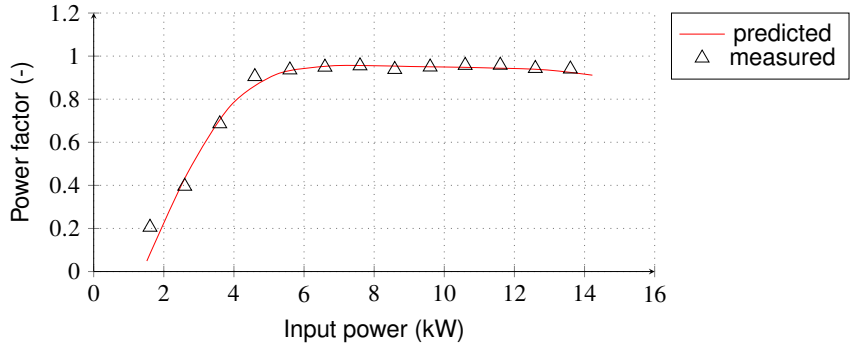

Figure 6.22: WRSM predicted and measured power factor versus electrical input power.

It is notable to mention that the advantage of the WRSM proposed model approach using iterative processes is the continuous access to the motor parameters for better motor analysis. To illustrate this, Fig. 6.23 shows the corresponding solved current phasor angle and components of the predicted performances in Figs. 6.19-6.22. It can be seen from the positive d-axis current at lower input power that the motor is under excited.

For further motor analysis, Figs. 6.24-6.26 show other motor parameters in which the effect of saturation can be noticed. It is evident that cross-magnetisation, saturation saliency and asymmetric saturation have significant effect on the parameter of the test motor. As the motor is loaded, the d-axis comes out of saturation as shown by the decrease in the d-axis flux linkages of Fig. 6.24. Consequently, the d-axis L_{dsds} and field L_{dsdf} inductances increase with an increase in the d-axis negative current shown in Fig. 6.25 due to less saturation in the corresponding magnetic axis. At lower q-axis current, the d-axis inductance is not significantly affected by cross-magnetisation, i.e. $M_{dsqs} \approx 0$. However, as the q-axis current increase, the effect of cross-magnetisation is noticed. The above described d-axis inductance analysis can be repeated for the q-axis inductances. The effect of asymmetric saturation is also noticed in Fig. 6.25 which introduces the negative q-axis mutual field inductance M_{qsdf} which is larger than the cross-axes inductances M_{dsqs}, M_{qsds} as the motor is loaded.

Figure 6.26 shows the different torque components which are directly calculated from the inductances of Fig. 6.25 using (3.48). In Fig. 6.26, T is the average of the FEM calculated torque. The effect of saturation saliency and cross-magnetisation brings in negative and positive mutual T_m and saliency T_s torques, which drastically reduce the resultant torque T_d from the field torque T_f.

Figure 6.27 shows the saliency ξ_s and field ξ_f shift ratios calculated from

$$\xi_s = \frac{L_{qsqs}}{L_{dsds}}, \qquad \xi_f = \frac{M_{qsdf}}{L_{dsdf}}. \tag{6.5}$$

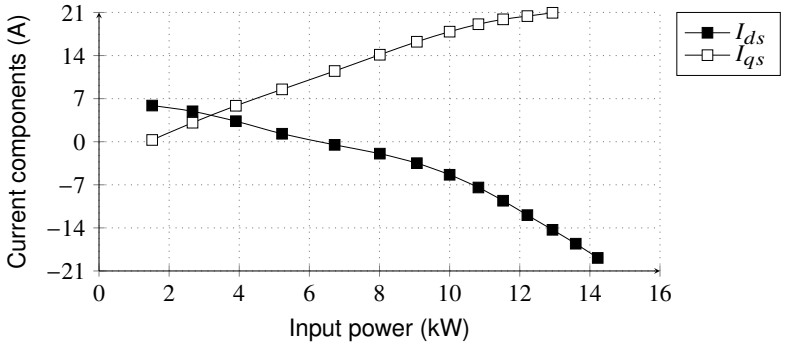

(a)

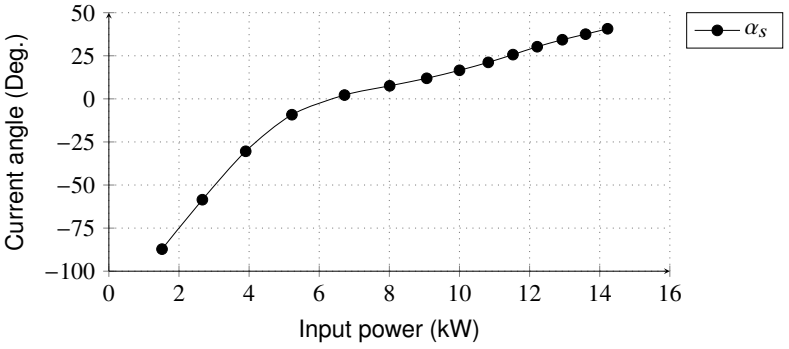

(b)

Figure 6.23: WRSM calculated stator current phasor (a) components and (b) angle at a constant field current.

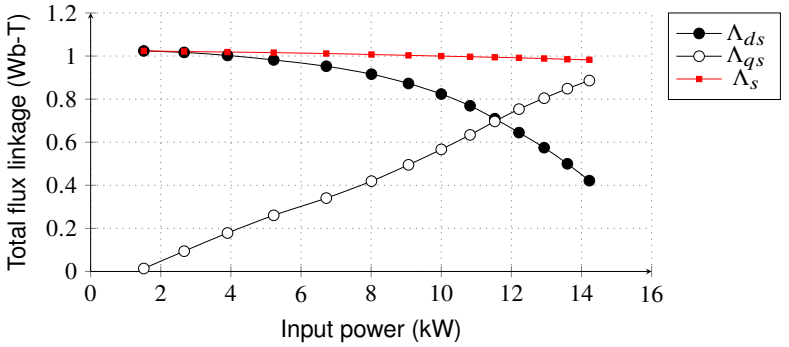

Figure 6.24: WRSM calculated flux linkages versus electrical power input with constant field current.

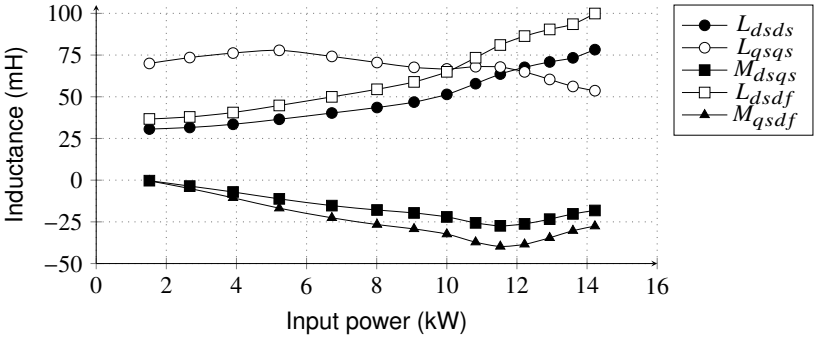

Figure 6.25: WRSM calculated inductances versus electrical power input with constant field current.

Figure 6.28 also shows the saliency γ_v and field γ_w shift angles of (3.7) and (3.9) respectively. These parameters of Figs. 6.27 and 6.28 can be used as a measure of the severity of the magnetic axis shift phenomenon, which shows the importance of incorporating saturation into the modelling

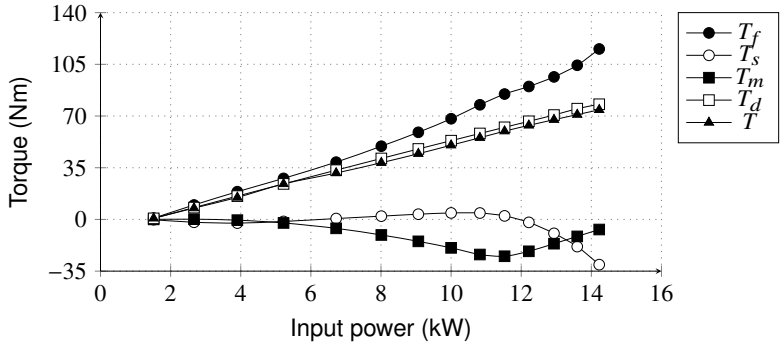

Figure 6.26: WRSM calculated torque versus electrical power input with constant field current.

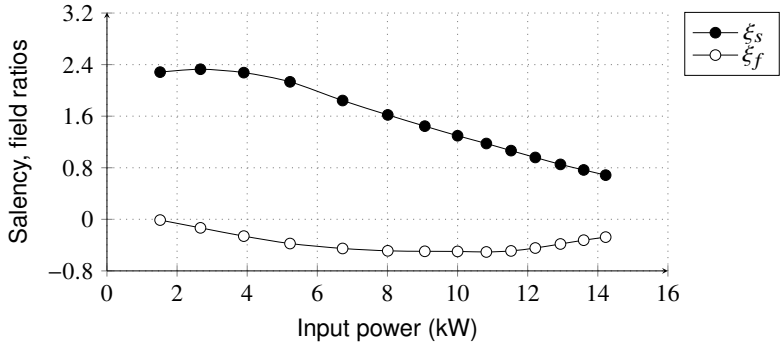

Figure 6.27: WRSM calculated saliency and field ratios versus voltage angle, all at constant field current.

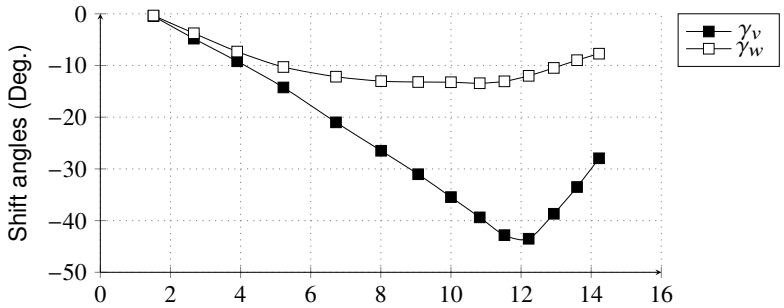

Figure 6.28: WRSM calculated saliency, and field shift angles versus voltage angle, all at constant field current.

Table 6.2: WRSM FIELD CURRENT AND LOAD ANGLE AT $P_o = 3.5$ kW

I_{df} (A)	δ_g (°)	I_{df} (A)	δ_g (°)	I_{df} (A)	δ_g (°)
9	42.9	18	17.3	25	12.9
12	27.3	21	15.1	27	12.2
15	20.7	23	13.9	29	11.4

of electric motors. What is interesting are the ξ_s and ξ_f parameter values of Fig. 6.27 which are classically taken as $\xi_s = 1$ and $\xi_f = 0$ for the uniform air-gap motors. As the motor power increases, the ξ_f increases (negatively) and ξ_s decreases.

Figure 6.29 shows a good correlation between the measured and predicted reactive power of (3.49) at the corresponding fixed load of $P_o = 3.5$ kW, by varying the field current. For the predicted reactive power, the load angles for the corresponding field currents at the fixed load are determined using the technique discussed in Figs. 6.17 and 6.18 as shown in Table 6.2. The results of Fig. 6.29 also show the advantage of the proposed WRSM calculation method in terms of accuracy when improving the plant power factor by motor field current control.

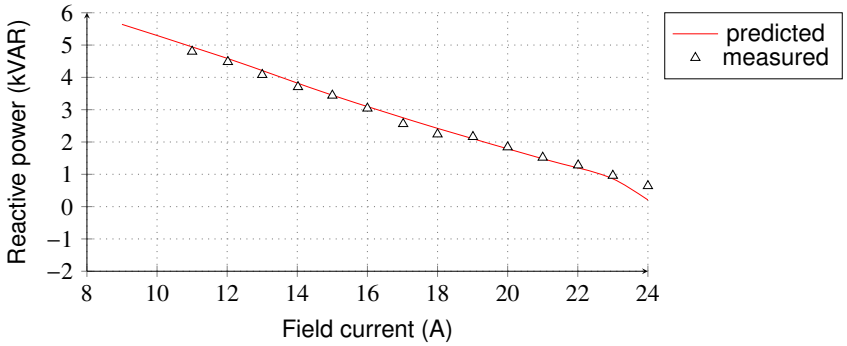

Figure 6.29: WRSM predicted and measured reactive power versus field current at constant load.

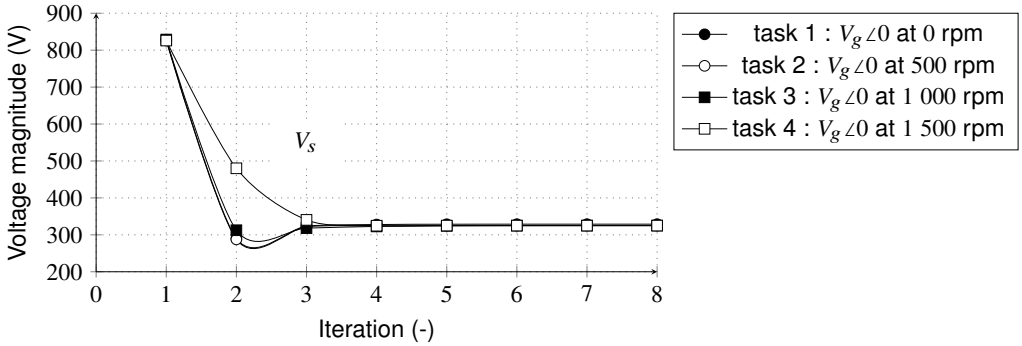

Figure 6.30: WRIM calculated voltage magnitude variation with the iterative process.

6.5. WRIM experimental results

In this section, the proposed model approach of the grid-connected WRIM is validated using the experimental test results. Further discussions are also given using the model approach evaluated parameters in explanation of the motor type behaviour when subjected to different load conditions. The procedures described in Sub-sections 6.4.1 and 6.4.2 in measuring and predicting the open, and short circuit test results and the mechanical and core losses' results are also followed for the prototyped WRIM. The measured and predicted results agreed and it is also applicable to use the predicted parameters of the motor with better explanation of these tests as illustrated in Section 6.4.

6.5.1. Parameter and performance prediction measurements results

The experimental setup of Fig. 6.7 of the test bench shown in Fig. 6.6 excited as in Fig. 6.9 is used to measure the WRIM parameters and performances at different operating points by changing the dynamometer power to vary the load on the test motor. To predict the measured results, following Sub-section 6.4.3, the operating point parameter and performance maps are also used. These maps are quickly constructed using Python multiprocessing as discussed in Appendix A.7, and also demonstrated in Section 3.5. Thus, the iterative process of Fig. 3.10 is distributed into tasks of rotor speed n_r (4.8) of parallel running processes, using the slip speed approach ($\omega_\Delta = \omega_s - \omega_r$) to put the load on the simulated motor.

Shown in Fig. 6.30 is a typical example of the WRIM under study here (i.e. desired V_g and V_0 are $400\sqrt{\frac{2}{3}}$ and 0 V respectively) when n_r is equal to 0 rpm task 1, 500 rpm task 2, $1\ 000$ rpm task 3 and $1\ 500$ rpm task 4. The results of the WRIM in Fig. 6.30 are interesting when compared with those of

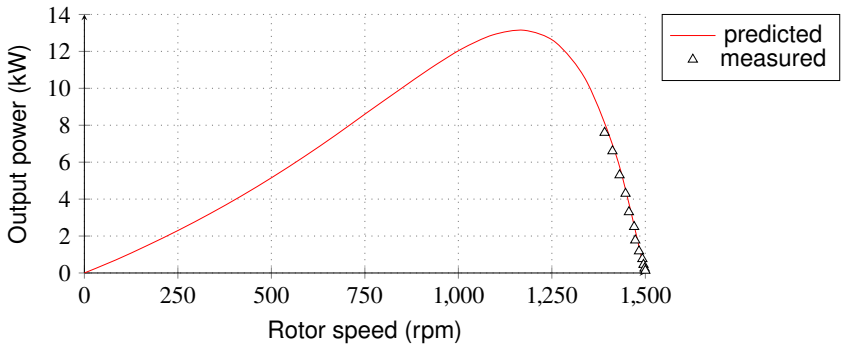

Figure 6.31: WRIM predicted and measured mechanical power output versus rotor speed.

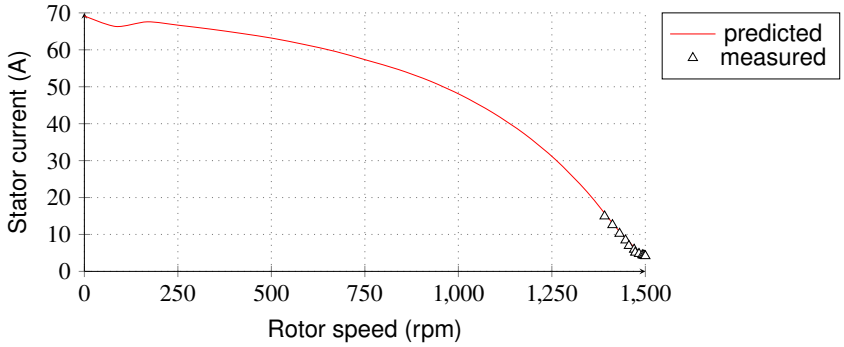

Figure 6.32: WRIM predicted and measured stator current versus rotor speed.

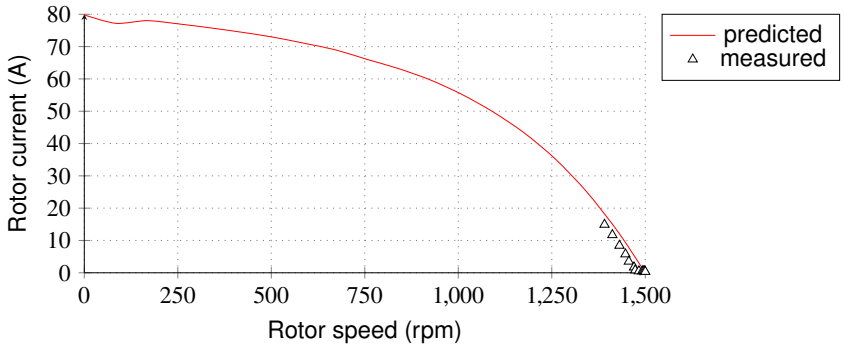

Figure 6.33: WRIM predicted and measured rotor current versus rotor speed.

the WRSM in Fig. 6.16 in terms the number of iterations to convergence. It can be observed that the proposed model approach using iterative processes is independent of the load on the WRIM.

Figure 6.31 shows the relationship between the output power P_o of (3.45) and rotor speed n_r of (4.8) while Figs. 6.32, 6.33, 6.34 and 6.35 show the relationship between the stator and rotor currents $I_s/\sqrt{2}$, $I_r/\sqrt{2}$ of (3.67), efficiency η of (3.69) and power factor $\cos(\phi_s)$ of (3.38), respectively. Also in Figs. 6.31-6.35 are measured experimental results. The measured results are limited to within 10% slip speed as this covers the motor operating speed. From Figs. 6.31-6.35 a good agreement between the measured and predicted results can be noticed.

Also as mentioned in Section 6.4, the advantage of the proposed model approaches in Chapter 3 which utilise iterative processes is continuous access to the quickly and accurately predicted motor parameters for a clear and better understanding of the motor analysis. On the considered WRIM,

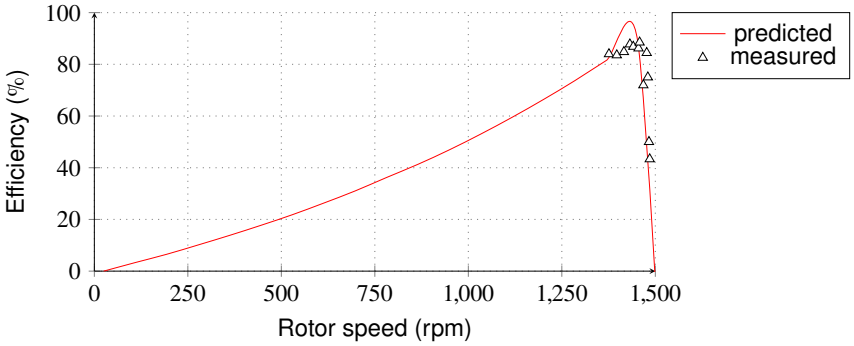

Figure 6.34: WRIM predicted and measured efficiency versus rotor speed.

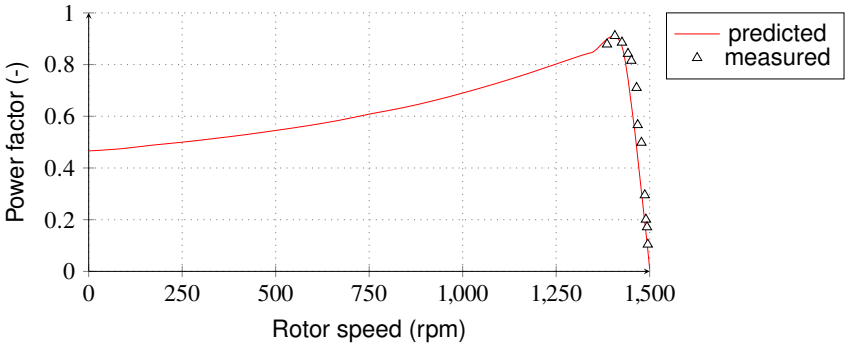

Figure 6.35: WRIM predicted and measured power factor versus rotor speed.

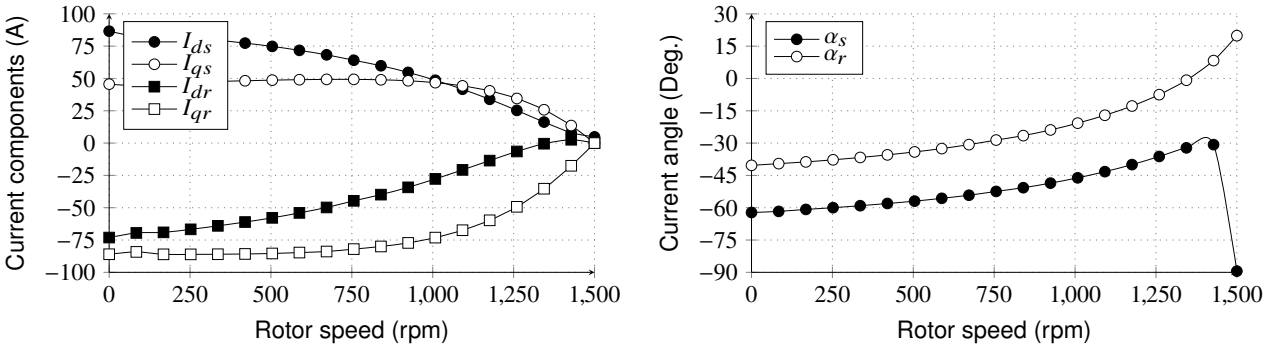

(a) **(b)**

Figure 6.36: WRSM calculated stator and rotor current phasor (a) components and (b) angle versus rotor speed.

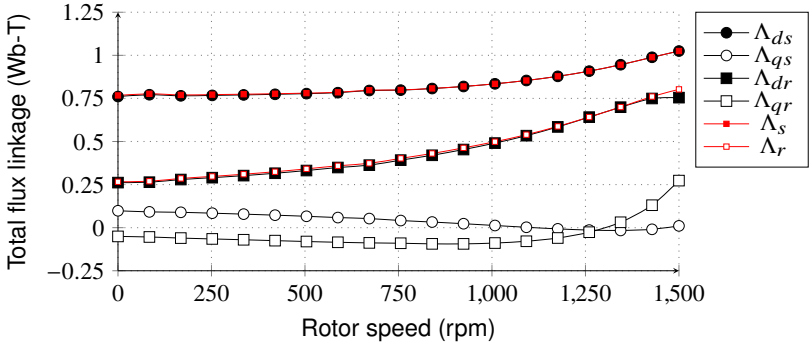

(a)

Figure 6.37: WRIM calculated flux linkages versus rotor speed.

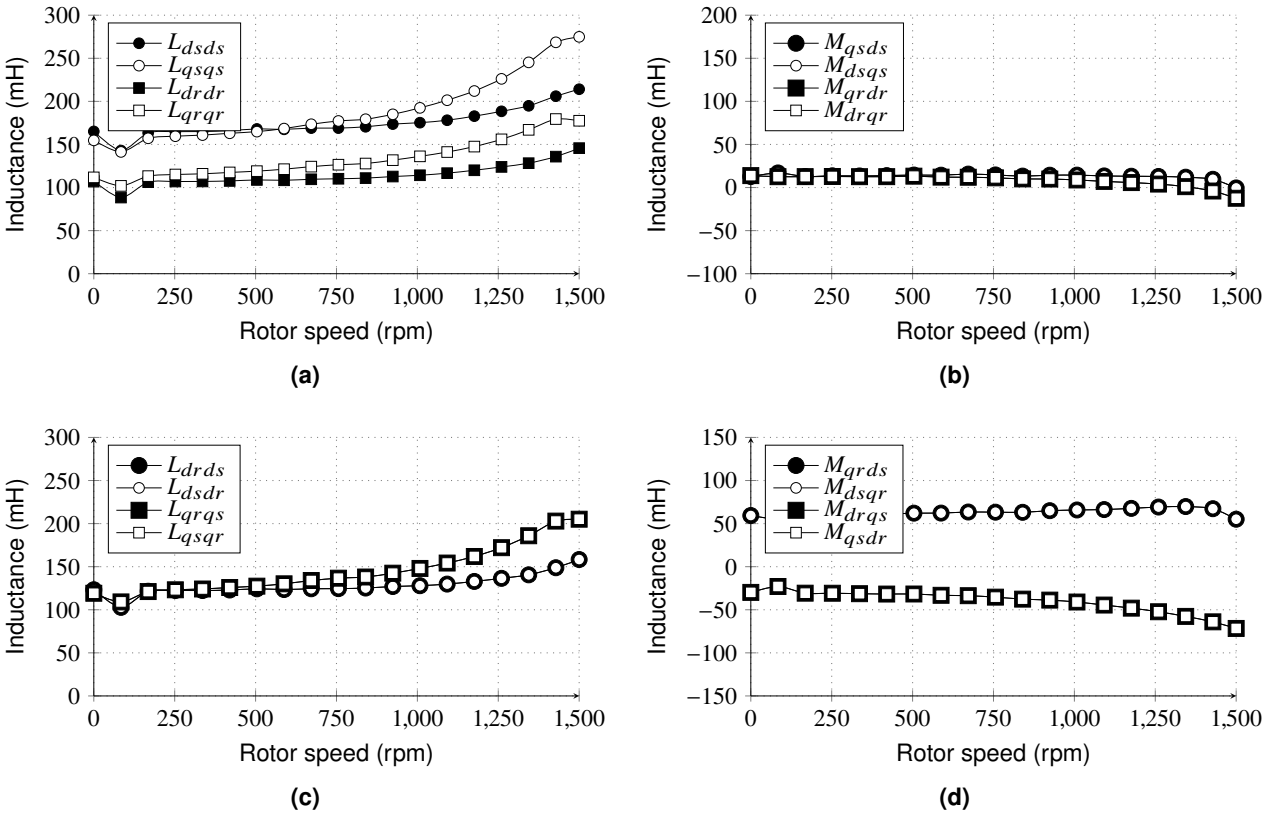

Figure 6.38: WRIM calculated inductances versus rotor speed.

from Fig. 6.38, the following equalities can be drawn

$$\begin{cases} M_{qsds} = M_{dsqs}, & L_{drds} = L_{dsdr}, \\ M_{qrdr} = M_{drqr}, & L_{qrqs} = L_{qsqr}, \\ M_{qrds} = M_{dsqr}, & M_{drqs} = M_{qsdr}. \end{cases} \tag{6.6}$$

From the results of Fig. 6.38(b) it can be observed that the considered motor does not suffer significantly from the effect of stator and rotor cross-magnetisation. However, it is wrong to assume zero mutual inductances, i.e. M_{qsds}, M_{dsqs}, M_{qrdr}, M_{drqr}. Following the results of Fig. 6.38, the flux linkage matrix of (3.6) can be rewritten as

$$\begin{bmatrix} \Lambda_{ds} \\ \Lambda_{qs} \\ \Lambda_{dr} \\ \Lambda_{qr} \end{bmatrix} = \begin{bmatrix} L_{dsds} & M_{qsds} & L_d & M_{qd} \\ M_{qsds} & L_{qsqs} & M_{dq} & L_q \\ L_d & M_{dq} & L_{drdr} & M_{qrdr} \\ M_{qd} & L_q & M_{qrdr} & L_{qrqr} \end{bmatrix} \begin{bmatrix} I_{ds} \\ I_{qs} \\ I_{dr} \\ I_{qr} \end{bmatrix}, \tag{6.7}$$

where $L_q = L_{drds} = L_{dsdr} = L_d$, $L_{qrqs} = L_{qsqr}$, $M_{qd} = M_{qrds} = M_{dsqr}$ and $M_{dq} = M_{drqs} = M_{qsdr}$. Equation (6.7) illustrates that it is wrong to assume that the self and mutual inductances of the stator and rotor are equal. With the simplified flux linkage components of (6.7) the torque components of (3.74) in(3.73) simplify to

$$\begin{cases} T_r = 1.5p[(M_{qd}I_{qr} + L_dI_{dr})I_{qs} - (M_{dq}I_{dr} + L_qI_{qr})I_{ds}], \\ T_s = 1.5p(L_{dsds} - L_{qsqs})I_{ds}I_{qs}, \\ T_m = 1.5pM_{qsds}(I_{qs}^2 - I_{ds}^2). \end{cases} \tag{6.8}$$

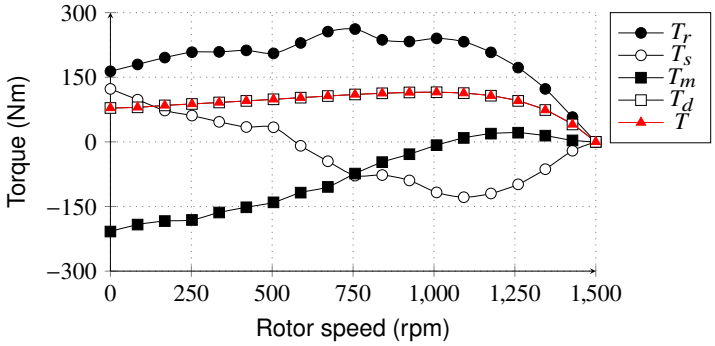

Figure 6.39: WRIM torque versus rotor speed.

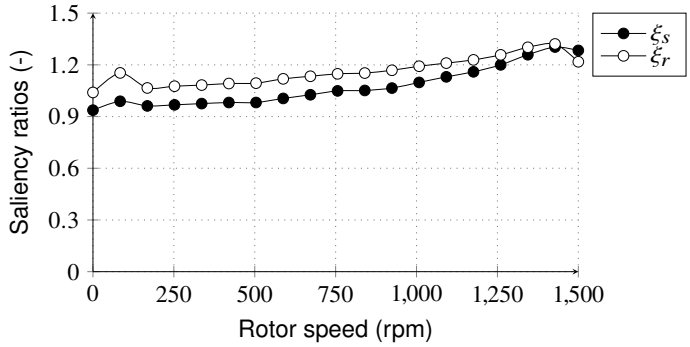

Figure 6.40: WRIM stator and rotor saliency ratios versus rotor speed.

Figure 6.39 shows torque components of (6.8) calculated from the current and inductance parameters of Figs. 6.36 and 6.38 respectively. In Fig. 6.39, T is the actual torque of the motor calculated by means of the magnetic stress tensor method. It is important to note that the parameter and performance depicted in this section are for a single rotor position. It is evident from the results of Figs. 6.36-6.39 that cross-magnetisation and saturation saliency have a significant effect on the test WRIM motor, hence, these effects must be included on the modelling of the motor type.

Figure 6.40 shows the stator ξ_s and rotor ξ_r saliency ratio variation with the motor speed given by

$$\begin{cases} \xi_s = \dfrac{L_{qsqs}}{L_{dsds}} \\ \xi_r = \dfrac{L_{qrqr}}{L_{drdr}}. \end{cases} \tag{6.9}$$

Classically, for a uniform air-gap, WRIM ratios of (6.9) are taken as $\xi_s = \xi_r = 1$, which is not correct as is shown in Fig. 6.40. As the motor speed increases, both ξ_s and ξ_r increase steadily to a ratio above one, i.e. $L_{qsqs} \geq L_{dsds}$ and $L_{qrqr} \geq L_{drdr}$ from (6.9). Thus (6.9) can be used to show severity of the effects of saturation on the motor.

Further studies on transient start up performances of the WRIM are given in Appendix B.5 in which starting methods in improving the starting torque quality are given on the grid-connected motor type following [86].

6.6. Chapter conclusions

This chapter presents an experimental validation of the proposed model approaches in performance prediction of WRSM and WRIM motor types. The proposed model approaches appear to be successful (as also proved using a commercial FEM package in Chapter 4) in that they give excellent results when compared to the experimental measurements.

The continuous accessibility of the motor parameters using the method in all the tests especially the short-circuit test, is used as an effective and powerful tool in explaining the measured results. The results are explained in terms of the severity and effect of parameter changes and torque components. This give a good and clear understanding of the saturation saliency, asymmetric saturation and cross-axes magnetisation significance impact on the prototyped motors.

Chapter 7

Industrial application: Grid-connected 6 MW mill motor

This chapter gives a detailed approach of the application of the grid-connected WRIM proposed model in Chapter 3 on a 6 MW grid-connected WRIM used for milling purposes. Practical and literature considerations are utilised in the establishment of the motor model. The design optimisation techniques explained in Chapter 5 alongside the proposed model approaches are then used in search of the 6 MW optimum motor. The effect of the skin effect in the motor conductor is also discussed.

7.1. Introduction

Over time, involvement with the design of the WRIMs has led to an extraordinary amount of learning about the analytical and numerical algorithms of these motors, consolidating every particular aspect of the motor such as saturation, heating and cooling. It has been demonstrated throughout the years of research and furthermore, in this study, in Chapter 3, that utilising these algorithms, important motor parameters such as efficiency, power factor, winding heating and torque characteristics can be estimated with a very high degree of accuracy. While the process of analysing the WRIM is vital, the designing of these motors for the best possible industrial utilisation is of even greater importance. Explicitly, for high power and voltage industry use, the WRIMs are manufactured to the customers' requirements yet constrained by the manufacturer's design tools with respect to practical structure of the motor. Hence, this chapter of this study discusses the analysis and design optimisation of a high power 6 MW and high voltage 11 kV grid-connected WRIM shown in Fig. 7.1, used for milling. The focus is on the establishment of the motor model involving practical and theoretical considerations to obtain the motor geometry and performance.

Figure 7.1 shows a 7 MW slip-ring mill motor from ACTOM South Africa which is typically the same size and structure as the 6 MW mill motor under study in this chapter. The wound stator core shown in Fig. 7.2 comprises of packets of laminations isolated by radial ventilation ducts. Because the stator is large, the laminations are manufactured in sections. The stator insulated coils are formed from annealed copper strips. The coil ends form an inflexible self supporting structure which is equipped to withstand the mechanical forces delivered by the full voltage direct line starting. The complete stator with all coil insulation, slot liners, separators and wedges are then welded into the motor frame. Figure 7.3 shows the cylindrical wound-rotor core of the mill motor stator core shown in Fig. 7.2. The

Figure 7.1: ACTOM South Africa 7 MW slip-ring mill motor [4].

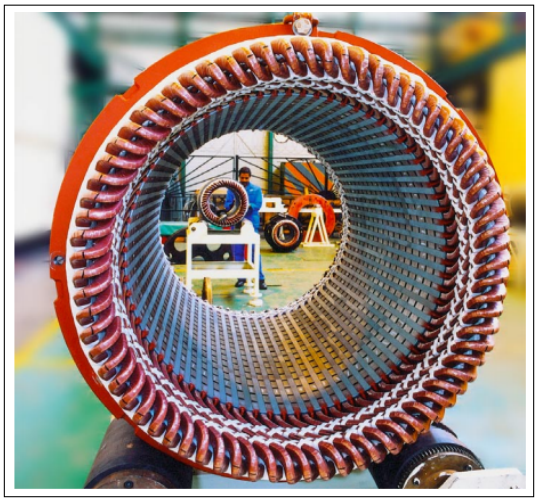

Figure 7.2: ACTOM South Africa 7 MW mill motor wound stator core [4].

Figure 7.3: ACTOM South Africa 7 MW mill motor wound rotor core [4].

rotor core also comprises of packets of laminations isolated by radial ventilation ducts. The rotor core is built up from sectioned laminations which are dovetailed and keyed directly on the spider [4].

The windings of the rotor are copper strips bar-wave type insulated and wedged into semi-closed slots. The rotor end-windings are likewise secured solidly to avoid any movement due to rotational forces. The rotor winding leads are then connected the terminal through the slip rings [4]. Table 7.1 gives the specification of the mill motor under study provided by the manufacturer, ACTOM South

Table 7.1: ACTOM SOUTH AFRICA 6 MW MILL MOTOR RATED PARAMETERS

rated parameter	symbol	value	unit
power	P_o	6	MW
voltage	V_L	11	kV
current	I_L	373	A
efficiency (%)	η	97	%
power factor	$\cos(\phi_s)$	0.88	-
pole pairs	p	3	

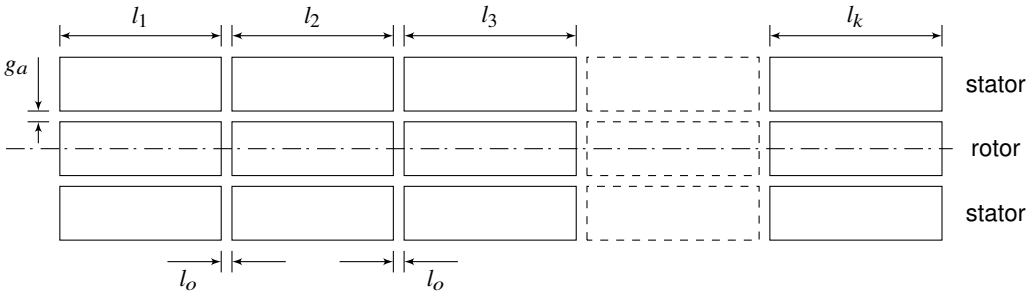

Figure 7.4: 6 MW mill motor cut-off top view of stator and rotor radial ventilation ducts.

Africa. It is important to state that in this document other motor specifications such as insulation and slot shapes information are not provided because of the manufacturer's privacy policy. However, what is given is the mill motor lamination volume and slot heights which are utilised alongside other suggestions from cited designers for the construction of the motor under study.

7.2. Establishment of the practical 6 MW mill motor

The establishment of the 6 MW grid-connected mill motor discussed in Section 7.1 is accomplished mostly by utilising the practical consideration. In addition, detailed literature provided by various citations and the analysis tools concluded from Chapters 2-6 are utilised.

The mill motor stator, Fig. 7.2 and rotor, Fig. 7.3 have radial ventilation ducts. This is because, practically speaking, as a result of the long stack length, it is hard to supply the central parts of the motor with cooling air. Hence, radial ventilation ducts are used. Both stator and rotor ducts are similar and aligned with each other, as represented as in the schematic drawing of Fig. 7.4.

The approach to incorporate the impact of radial ventilation ducts in the motor modelling is similar to that of slotting [15]. Thus, since the stator and rotor are assumed to be of the same stack length and number of ducts, the stator effective stack length including the effect of fringing due to ducts is given by [78]

$$l_t = l_i + 2g_a + kl_o(\frac{5}{l_o + 5g_a})^2 \tag{7.1}$$

where

- k - stator or rotor number of radial ventilation ducts
- l_o - length of each radial ventilation duct
- g_a - air-gap length.

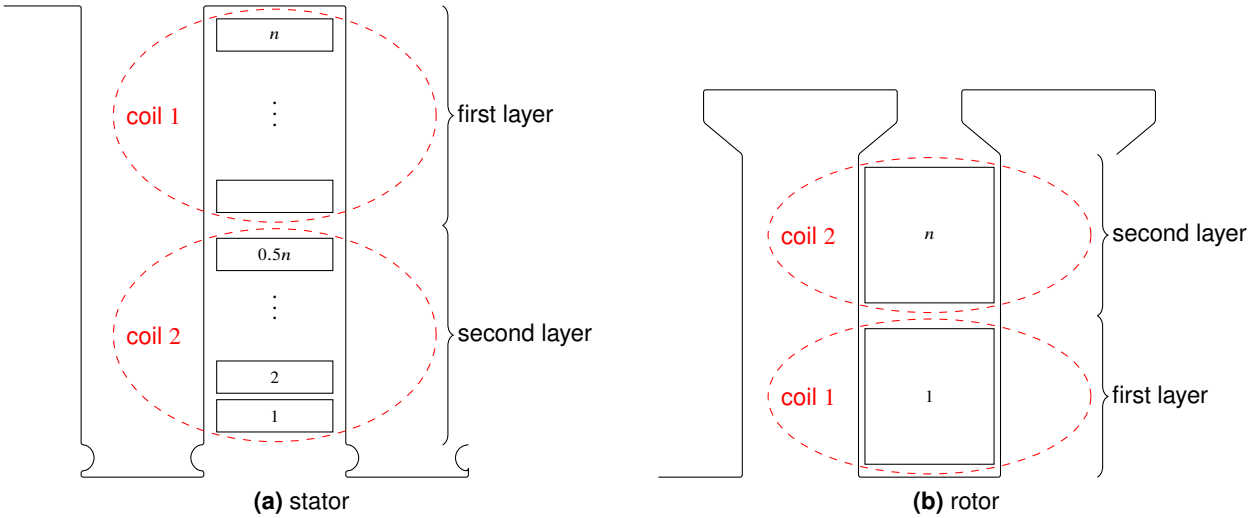

(a) stator **(b)** rotor

Figure 7.5: 6 MW mill motor adapted (a) stator and (b) rotor slot layout.

and

$$l_i = l_1 + l_2 + \cdots + l_{(k+1)}. \tag{7.2}$$

Thus knowing k, l_o and g_a, the effective stack length of the mill motor used in the simulation can be calculated from (7.1). In this study, k is taken as 18 and l_o is calculated from the manufacturer provided stack length $l = 1\ 130$ mm.

Another issue in large wound-rotor motors is the increase in copper losses with frequency as discussed in Sub-section 2.3.1. The phenomenon is caused by the combination of proximity and skin effects [68]. As a way to reduce the phenomenon, citations such as [6,59,60] suggest the location of the conductors in the slot to be taken into consideration in design since they have a great impact on the copper losses.

In electric motors, proximity copper losses are due to proximity currents. These currents are induced by flux leakages. Since flux leakages are high at slot opening, it follows that proximity copper losses are high in those conductors close to the slot opening. However, the proximity losses can be greatly reduced by the use of magnetic wedges as suggested in [14,139], or a space between the coil and slot opening [78] and or slot shape [15]. In the selection of the shapes of slots for the mill motor in this study, slot wedges are taken as air and the open slots are used in the stator and semi-closed in the rotor to reduce these flux leakages. Hence, it is applicable to ignore these losses during modelling since they are at a minimum.

As clarified in Sub-section 2.3.1, the skin effect is viably reduced when the coil conductor dimensions are kept lower than the skin depth (2.67) so that the path for eddy currents along the conductor is cut off. This is done practically in a large power level motor type by cutting up coil conductor [99]. Even though this lessens the copper losses in the active part and increases them in the end-connections [14], overall the total losses are lessened by this practice. However, care has to be taken in some cases where the practice actually increases the total copper losses [14]. In order reduce the skin copper losses in the considered mill motor, the technique of splitting the solid conductor coil is adapted as shown in Fig. 7.5. The arrangement of Fig. 7.5(a) is identical to Lammeraner's shown in Fig. 2.13. However, two layers of $\frac{n}{2}$ insulated identical rectangular conductors arranged above each other in the slot are considered in the mill motor. The mill motor two layered rotor slots have one rectangular coil, i.e. $n = 2$ as shown in Fig. 7.5(b). This coil design is to withstand large currents flow and forces when subjected to tension. Since in practice the solid rotor conductor as

Table 7.2: 6 MW MILL MOTOR ADAPTED WINDING INFORMATION

windings	stator	rotor
parallel paths	1	1
coil/phase/pole	12	10
turns per coil	15	1
strands in parallel	1	1
number of layers	2	2
coil pitch	16	15

in Fig. 7.5(b) is difficult to form, most manufacturing companies split the coil conductor into parallel connected strands. However, the effects of splitting the rotor rectangular coil is not considered in the scope of this document. In both stator and rotor, a two layer slot arrangement is adopted than one layer to decrease losses and make it easy to wind [14].

Table 7.2 gives the adapted winding information of the 6 MW mill motor to be analysed. The indicated attributes in this section in terms of the effective stack length of (7.1), slot shape and winding layout of Fig. 7.5 are used in the following sections to simplify the model approach of the practical mill motor, while at the same time incorporating all the important effects on the motor for an accurate improved performance calculation.

7.3. Model approach of the 6 MW mill motor

This section gives the model approach of the 6 MW mill motor considering the described attributes in Section 7.2 while maintaining accuracy and simplicity. The mill motor model approach is the adapted approach of Section 3.5. In the model approach of Section 3.5, it is explained that one of the important calculations for grid-connected motor types is to compute the excitation current required for the motor under a given load. This is because when using FEM based approaches, the current is normally an input which generally complicates the analysis of grid-connected motors when using FEM since it is the terminal voltages which are known, not the currents. However, the unknown currents are solved by the use of iterative processes in which FEM models are solved in conjunction with the motor phasor diagram equations.

That said, it is easy to perceive that the current solution for the grid-connected mill motor is of (3.67) given by

$$[I] = [Z]^{-1}[V] \tag{7.3}$$

in which the excitation currents $[I]$ are calculated using the iterative processes of Fig. 3.10. Using (7.3) makes the equivalent circuit diagram of Fig. 2.11 to be applicable in the analysis of the mill motor. Hence, the calculation of the equivalent circuit parameters in Section 2.3 is intensively followed, in which the equivalent circuit parameters are redefined to incorporate the effects of eddy currents.

The skin effect on the mill motor winding is included in the iterative process of Fig. 3.10 by following the ac resistance calculation flow diagram shown in Fig. 7.6. From Sub-sections 2.3.1 and 2.3.3, it is important to state that the main and end winding operating temperature, coil turns and conductor cross-section area are respectively assumed to be equal to each other in ac resistance calculation. Thus when the frequency is high and the conductor dimensions are big enough, current in the conductor is focussed close to the surface with the skin depth defined and characterised by

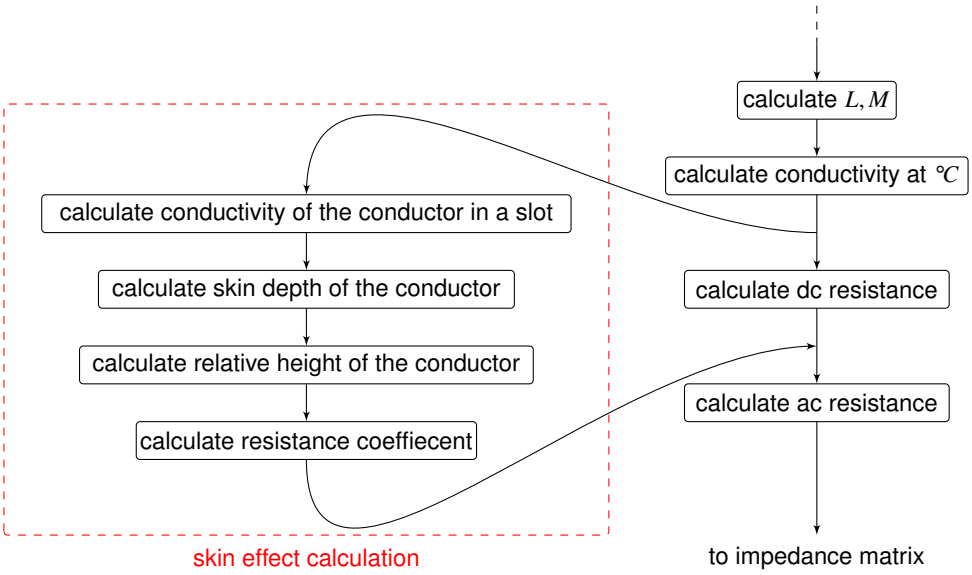

Figure 7.6: 6 MW mill motor ac resistance calculation.

(2.67), and given as

$$\delta = \sqrt{(\frac{1}{\pi f \mu_0 \mu_r \sigma})}, \tag{7.4}$$

where the electric conductivity $\sigma = (\rho)^{-1}$ and f is either stator or rotor circuitry frequency. Considering the mill motor conductor arrangement of Fig. 7.7, ρ is the electric resistivity at a winding operating temperature of $\mathcal{C}$ calculated from (2.66) as

$$\rho_s = 2\rho_{\mathcal{C}} \frac{b_{vs}}{b_s}, \tag{7.5}$$

and

$$\rho_r = \rho_{\mathcal{C}} \frac{b_{vr}}{b_r}, \tag{7.6}$$

for the stator and rotor windings in an insulated slot respectively. Equations (7.5) and (7.6) take into account the effect of winding insulation in the calculation of the conductor conductivity.

To analytically include skin effect in the mill motor analysis, the ac resistance is calculated from (2.68) and (2.79) using the dc resistance of (2.65) and (2.77) as

$$R' = k_r R, \tag{7.7}$$

where $k_r = k_{er} = k_{mr}$ is the resistance coefficient from (2.69) in which the dc resistance R increment due to the skin effect. The resistance coefficient following (2.69) in (7.7) is given by

$$k_r = \frac{[3\varphi(\xi) + (0.81n^2 - 1)\psi(\xi)]l_m^2 + 3l_e}{3(l_m + l_e)}. \tag{7.8}$$

In (7.8), the relative height ξ is of (2.70) for the stator and rotor, calculated from the skin depth of (7.4) using slot heights h_s, h_r in Fig. 7.7 respectively. The real functions $\varphi(\xi)$ and $\psi(\xi)$ of (7.8) are as of

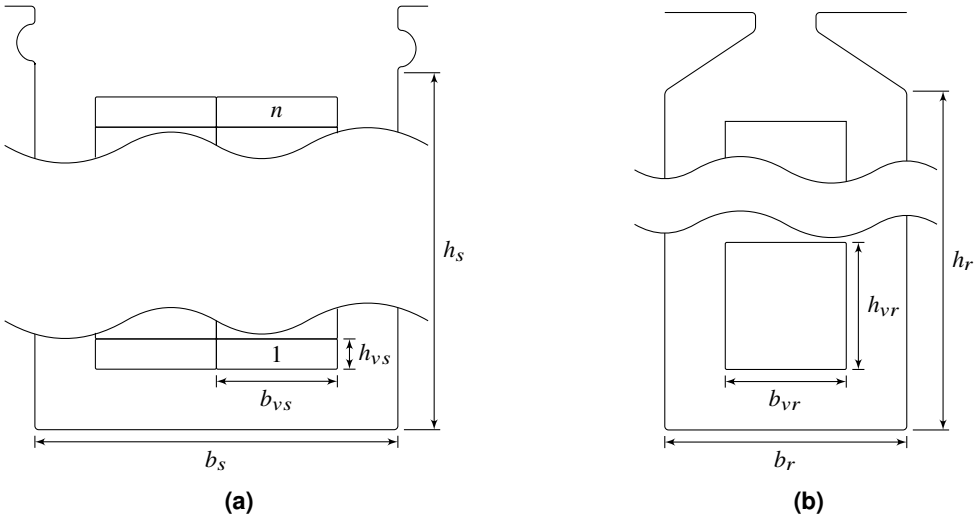

Figure 7.7: 6 MW mill motor coil location and slot variable of (a) stator and (b) rotor.

(2.71).

Following Fig. 7.6, it is the ac resistance of (7.7) and inductance parameters which are used in the assembling of the impedance matrix $[Z]$ during the iterative calculation process of the excitation currents of (7.3) as described in Section 3.5.1. With the currents, the performance of the motor, i.e. power factor of (2.21) and efficiency of (3.69) can be easily calculated. However, it is important to point out that the estimation of core losses in the calculation of efficiency is generally difficult [66] and the power loss equation of (3.44) is adapted. The proximity copper losses in both stator and rotor slots are ignored as they are assumed negligible because of the considered conductor-to-slot opening distance, slot shapes and used wedges.

7.4. Dimensions and performance search of the 6 MW mill motor

The fact that most of the important parameters of the mill motor are unknown complicates the simulation process. Henceforth, in this section, the dimensions and rated performance of the motor are searched by utilising the optimisation algorithms as in Chapter 5 directly with the model approach of Section 7.3. The obtained dimensions and performance are then compared with the rated parameters of Table 7.1.

To implement the above described, NSGA-II is utilised to determine the dimensional parameters of Fig. 7.8. From the optimisation problem function defined in Section 5.2, a total of seven design variables are selected, i.e. five dimensional design variables in Fig. 7.8 given by

$$[x] = \begin{bmatrix} x_1 \\ x_2 \\ \vdots \\ x_5 \end{bmatrix}, \tag{7.9}$$

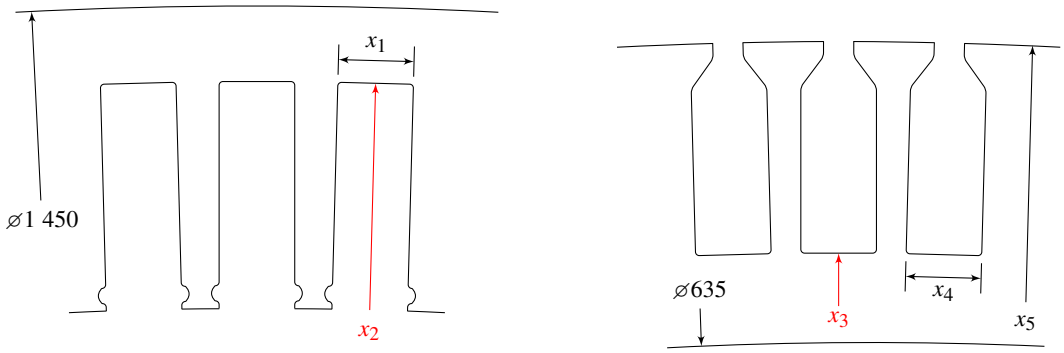

(a) stator **(b)** rotor

Figure 7.8: 6 MW mill motor adapted design dimension variables to be optimised for the rated performance. Dimensions in mm.

and two additional loading variables given by

$$[x] = \begin{bmatrix} x_6 \\ x_7 \end{bmatrix} = \begin{bmatrix} n_s \\ f_\Delta \end{bmatrix}. \tag{7.10}$$

In (7.10), n_s is the number of the stator winding turns per slot and f_Δ the motor slip frequency.

The selected objective of the optimisation process is to better achieve or fully achieve the rated efficiency and output power of the mill motor. Hence, the objective matrix is defined as

$$[f] = \begin{bmatrix} f_1 \\ f_2 \end{bmatrix} = \begin{bmatrix} P_o \\ \eta \end{bmatrix}, \tag{7.11}$$

where

$$P_o = 2\pi(f_s - f_\Delta)T_d, \tag{7.12}$$

is the motor output power calculated from torque of (3.73) and η is the efficiency of (3.69). In the optimisation process, the constraint matrix contains three selected constraint functions which are stator J_s, and rotor J_r peak current densities and power factor $\cos(\phi_s)$ defined as

$$[g] = \begin{bmatrix} g_1 \\ g_2 \\ g_3 \end{bmatrix} = \begin{bmatrix} J_s \\ J_r \\ \cos(\phi_s) \end{bmatrix}. \tag{7.13}$$

The current densities are to be less than $\sqrt{2}\times 6$ Amm^{-2}. The power factor in (7.13) is set to be greater than the rated, i.e. $\cos(\phi_s) \geqslant 0.88$. The use of design variables of (7.9), and (7.10) and objectives, and constraint functions of (7.11) and (7.13) in the geometry construction and performance calculation for the design optimisation are generally as described in Section 5.7.

7.5. 6 MW mill motor optimisation results

This section shows the simulated defined problem function described in Section 7.4 in search of the 6 MW mill motor dimensions and performance. Figure 7.9 shows the normalised converged Pareto optimal solution results using NSGA-II in *VisualDoc* optimisation results. These results are obtained after maximising the objective functions of (7.11) subjected to constraint functions of (7.13) at a winding temperature of $75\,°C$.

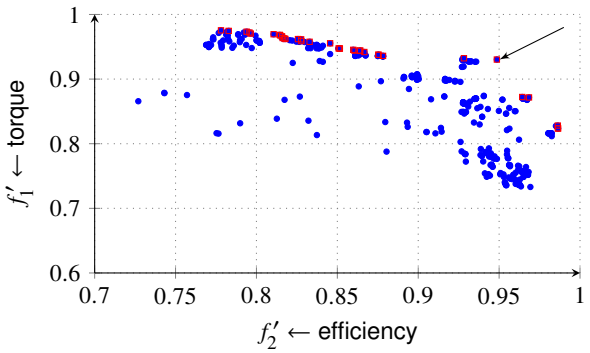

Figure 7.9: 6 MW mill motor characteristics of normalised optimisation results performance space. □ and ● scatter points represent all Pareto-optimal and feasible solutions respectively.

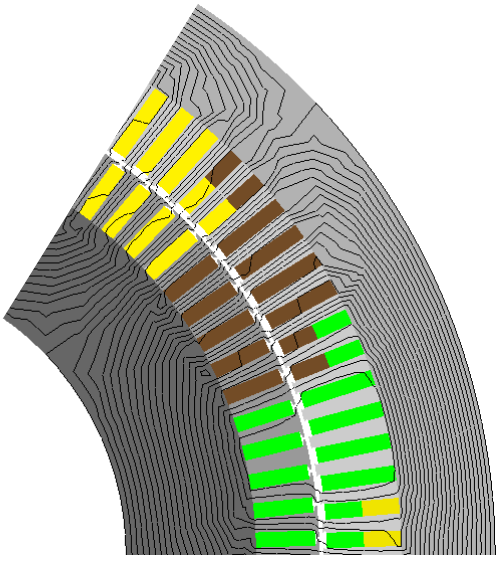

Figure 7.10: 6 MW mill motor model obtained from NSGA-II optimisation. phase A/a, phase B/b, phase C/c.

Table 7.3: OBTAINED AND RATED 6 MW MILL MOTOR PERFORMANCE

parameter	symbol	rated	obtained
voltage, (kV)	V_L	11	
power, (MW)	P_o	6	6.1
current, (A)	I_L	373	386
efficiency, (%)	η	97	95
power factor	$\cos(\phi_s)$	0.88	0.88
speed, (rpm)	n_r	–	980

The results of Fig. 7.9 are due to limited limited space in dimensional values, hence, the NSGA-II struggled to obtain more Pareto optimum solutions. However, one Pareto optimal solution, close to the mill motor rated performance highlighted in Fig. 7.9 is chosen. Figure 7.10 shows the selected optimum IHFEM pole axial view model which resulted from the NSGA-II optimisation. The three phases in the stator windings are short pitched and the rotor windings are full pitched. This can be observed from the pole face of the IHFEM model shown in Fig.7.10. The rated performance of the obtained mill motor is given in Table 7.3. Table 7.3 also gives the rated performance of the motor in Table 7.1 for comparison purposes. Indeed, the approach managed to locate the dimensions of the rated 6 MW mill motor, however at a lower performance. The reason behind the lower performance is the over estimation of some of the design parameters such as core losses, operating temperature, winding insulation and perhaps duct effects, which make it difficult to establish the motor model.

Table 7.4: NORMALISED SLOT HEIGHTS FOR THE RATED AND OBTAINED 6 MW MILL MOTOR

normalised dimension parameter	normalised value	
	rated	obtained
x_1'	0.7998	0.7531
x_3'	0.671137	0.6822

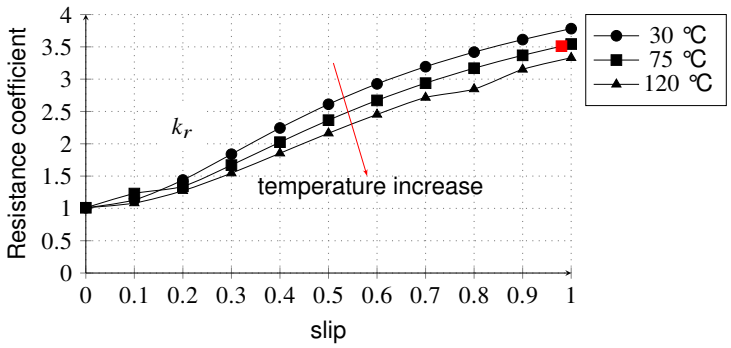

Figure 7.11: Obtained 6 MW mill motor rotor resistance coefficient versus slip with winding temperature as a parameter.

Furthermore, the normalised slot heights of Fig. 7.8 of the obtained and rated mill motor were compared as given in Table 7.4. The rated slot heights values were provided by ACTOM South Africa. The given values of Table 7.4 confirm the feasibility of the obtained mill motor since these values are in the same range.

7.6. Skin effect on the 6 MW mill motor

The analysis in this section is a discussion of the skin effect on the considered mill motor model in Section 7.3. It is essential to note that, despite the input IHFEM current in the stator and rotor slots considered homogenised, the copper losses are accurately estimated because of the accurate calculation of the effective resistance of (7.7) using k_r and incorporating insulation. Because of accurate estimation of the copper losses, it is unnecessary to independently put each conductor including insulation between them in the motor model. This improves and saves simulation time, and the size of the FEM file on the considered model, except if further investigations are to be done as in [47, 108].

Since the mill motor stator has stranded windings (skin effect ignored), Figure 7.11 shows only the rotor resistance coefficient k_r of (7.8) versus the slip at operating temperatures of 30, 75 and $120\,℃$. The k_r values are calculated using conductor dimensions calculated from the given insulation information considering the obtained dimensional parameters of Fig. 7.10. The k_r value signifies how the skin effect incorporated in the mill motor model increment the dc resistance. From the skin depth equation of (7.4), the motor stator will experience less or high skin effect copper losses depending on the temperature $℃$ for the considered conductor height, i.e. h_{vr} in Fig. 7.7. The resistance coefficient behaviour is expected, since the rotor frequency varies with slip as

$$f_r = \frac{f_s}{s}, \tag{7.14}$$

where

s - slip.

Hence, from (2.70), $\frac{h_{vr}}{\delta}$ is proportional to $\sqrt{s}$, therefore, k_r is a function of slip or rotor frequency and also decreases with temperature rise. Furthermore, considering the uniform temperature in the coil turns, causes errors. It can also be observed that at low slip the resistance of the rotor winding will tend to be close to that of the dc resistance, i.e. $k_r = 1$.

7.7. Chapter conclusions

The chapter presents a successful application of the model approaches in Chapter 3 on a 6 MW cylindrical WRIM used for milling purposes. The chapter shows how attributes from manufacturing companies and cited literature can be used to establish the mill motor. The attributes, which consist analytical formulation and practical considerations, are considered when looking at the 6 MW motor dimensions and performance. Even though the practical mill motor under performs the obtained motor, the procedure of modelling the motor is considered a useful tool especially when provided with all the information from the manufactured. The latter includes information such as operating slip, operating temperature, winding layout and slot shape.

Chapter 8

Assessment of the work

This chapter gives a summary overview of the work presented in this study. The chapter continues to itemise the aspects of the detailed examinations presented in this study which are considered to be unique. The conclusions of other selected relevant authors are also presented here.

8.1. Summary overview

The study herein details new approaches to the analysis, design by optimisation, prototyping and testing of the grid-connected cylindrical WRSM and WRIM motor types. Although the work focusses on the two motor types separately, the general goal of the study is to promote synchronous-induction motors as a feasible alternative to large power level grid-connected electric motors with better starting and operating performance.

The work begins with the technology overview setting out the motivation of the subject work including the background information. An overview of the classical electric motor model is given in which common techniques used to represent the effects of saturation and eddy currents in the motor types' analysis are assessed. The assessment leads to the findings that the available models may not be used with enough reliance to model the grid-connected motor types under different steady-steady operating points. In response to the problem statement, compatible and fast iterative based FEM processes that can be relied on are developed to accurately include all the major effects of saturation on the motor types for steady-state operation. In the proposed models the shifted motor magnetic axis due to saturation is defined and used to modify the classical model. In the defined magnetic axis, model parameters are accurately calculated using the FEM based on freezing the motor core permeance. The validation of the proposed models with the selected commercial FEM proves not only accuracy but speed and simplicity. The application of the proposed models alongside different optimisation algorithms results in satisfying optimum results. The results give confidence in the application of the proposed models in the design of energy efficient motor types. The motor types are built and tested. The performance of the proposed models results closely with the test results which confirms that the proposed models can be used as useful guideline tools in the design and operating test of the motor types. Furthermore, the continuous accessibility of motor parameters when using the proposed models is used as a powerful and effective tool to explain the motor types' behaviour at different operating points for a clear and better understanding of saturation effects in the test motor types. The successful application of the proposed models on the 6 MW slip-ring mill

motor is also demonstrated. The proposed models can be easily modified to incorporate addition copper losses which are caused by complex eddy current effects in large power applications. The assessment summarised above shows the rarity of the subject work.

8.2. Aspects considered to be original

The following aspects of the work in this dissertation are considered by the author as original:

1. Although classical textbooks introduce dq-axes expressions for flux linkages to realise equations for the motor type, it is understood the approach herein differs wholly from the classical textbooks, so that the analysis of the magnetic axis definition in Section 3.2 of Chapter 3 must be considered new. This relates to truly defining the magnetic axis on the motor under load which takes into account all the important effects such as saturation-saliency and cross-magnetisation in the motor during modelling. Hence, the classical textbooks' expressions for flux linkages cannot be used and must be adapted as of (3.5) and (3.6) for the WRSM and WRIM respectively. To this end, the developed expressions and conclusions of [81] and [82] are considered as a contribution to the literature on the two-axes electrical motor model of the cylindrical WRSMs and WRIMs respectively.

2. In Sections 3.4 and 3.5 of Chapter 3, the way in which the FEM model is solved in conjunction with the phasor diagrams using compatible iterative processes to accurately obtain the operation parameter and performance of the WRSM and WRIM respectively, is considered to be unique. Both stator and rotor matrices for the motor excitation can be solved by iteratively updating the impedance matrix for a set of the stator (grid) and rotor terminal voltages. The parameter and performance characteristics maps are then extracted utilising multi-processes. The simple, fast and accurate developed models in [85] and [82] for prediction of the parameters and performance of the WRSM and WRIM respectively, are seen as a further added theory of grid-connected motor types.

3. The proposed model applied for the first time, also works well in the design optimisation of energy efficient motors in terms of accuracy in parameter calculation and time efficiency in performance prediction. This is well demonstrated in Chapter 5 where mathematical formulations for the MFFD and NSGA-II (for Pareto-formation) optimisation algorithms are utilised for the optimum designs of the motor types. Hence, the developed optimisation model procedure and conclusions in [83] are seen as important contribution literature on the design optimisation of wound-rotor motor types.

4. The most crucial aspect in modelling is developing models which give a good correlation between estimated and tested results. The correlation depends on how good the model represents the test motor and how the test conditions are accounted for in the model. Chapter 6 confirms that the proposed model can be used as a useful guideline tool in the design and operating tests of the motor type. Thus a unique test prediction process in Sections 6.4 and 6.5 for the WRSM and WRIM respectively, can be used in parameter estimating for motor condition monitoring, since the proposed models accurately give the parameters of the healthy motor. For this, the developed parameter and performance model in [84] is a contribution to the prediction and test analysis of wound-rotor motor types.

5. Although the analysis, design, optimisation and building of large power level motors involves a complicated process, the proposed model of the mill motor in Chapter 7 makes it conceivable for the designers to analyse and synthesise the motor type. Without difficulty, the additional

losses due to skin effects are perfectly incorporated in the motor parameter and performance calculations. Thus the successful application of the proposed model on the 6 MW mill motor design is an attribute for industrial application.

6. Finally, but not part of the main focus of the study work, is the mentioning of the analysis of controlled switching in improving the transient torques of WRIMs as given in Appendix B.5 and [86]. The analysis, for the first time, gives and explains the switching times of the controlled phases. Hence, a unique motor switching method namely simultaneous-rotor controlled switching, to reduce transient torques, is introduced. To this end, the developed explanations and methods in [86] for controlled switching are seen as important research literature on improving the transient torques of induction motors by controlled switching especially for large power level applications.

It is of great importance to state that the methods that are developed in this work can now be also used for cage-rotor induction machine design, and also for the design of other synchronous machines.

8.3. Consideration of the work against others

The design principles behind electric motors utilised today were to a great extent developed during the 19^{th} century and they have evolved consistently since then by attracting on advances enabling the technology of design, material and production technologies [15, 48, 63, 78, 93, 109, 127]. The utilisation of electromagnetic field analysis in electric and magnetic design is viewed as the most significant design and analysis technology for motor types in this study [10, 108]. Quasi 2D analysis was first used in the 1960s and the analysis using edge-element-based FEM is now widely used. Over many decades, calculation speeds have likewise been improved, not only due to digital computing but also through the adaption of various calculation procedures. Several reports and articles have been published proposing quick and precise strategies for ascertaining motor parameters that are valid for a motor running under steady-state saturated conditions.

The author gives great appreciation to N. Bianchi and S. Bolognani [11] for the introduction of the frozen permeability method in 1998 to decompose the field contribution by excitation sources when the motor is saturated. In the author's opinion on the subject work, the contribution of Bianchi [11] should be considered as the most successful. A benchmark problem is described in [11] in which interior permanent magnet IPMSM parameters are computed by a FEM. Bianchi's [11] proposed method successfully managed to evaluate the apparent inductances of the saturated IPMSM from the FEM field solution. During the evaluation process, the total flux linkages are decomposed by fixing and storing the iron magnetic permeability of each element such that the non-linear problem is transformed into a linear one. The frozen permeability method is also verified by D.G. Dorrell [131] in terms of accuracy on the IPMSM. To date, the method is followed by different authors such as Z. Q. Zhu [76] and M. Ge [44] in the analysis of PMSMs, especially in flux decomposition for torque components' calculation. Bianchi's [11] flux linkage derived model equation findings correlate with the results shown in Chapter 3 of this study. Although the application of the frozen permeability method is applied to the WRSM and WRIM motor types for the first time in this study, thus not PM motors, the method is considered successful in that it effectively gives a good and clear understanding of the saturation saliency, asymmetric saturation and cross-coupling impact on the motor type parameters and performance. The conclusions drawn in the analysis results should not be considered as general as they contradict the classical analysis for cylindrical motor modelling (i.e. the two-axes are decoupled). The flux linkages equations are also, for the first time, taken further in the analysis of grid-connected WRSM and WRIM motor type in solving currents using the frozen permeability method, as detailed in Chapter 3.

Although not time-efficient and accurate, the approach presented by J. Pang in [97] is well appreciated in this study in terms of finding the saliency and field shift angles of (3.7) and (3.9) respectively. However, the way [97] extracts the phase inductances lacks clarity and accuracy. Apart from excluding leakage inductances as illustrated by V. Rallabandi [101], in Pang's formulations, his approach only considers up to the second harmonic component of the inductance. In this study, however, the total flux linkages in Sub-section 2.3.2 which include high-order harmonic and leakage fluxes produced by the winding, slotted air-gap fluxes, and the effect of magnetic saturation are used in the formulation, which all guarantee accuracy. Thus, the formation of the magnetic axis shift in cylindrical synchronous machines is well analysed when using the frozen permeability method. In this matter, the relationship between non- and classical models can be deduced, which is crucial in the motor design and control.

The contribution of M. G. Say [109] is also well documented in this study on the modelling of both the synchronous and induction motors. His theory in [109] introduces a basic way of accurately writing down a three-winding machine into a two-axes format in matrix form. He considered a synchronous motor with single phase dc and dumping windings on the rotor. In the model, he collaborated what he calls "simple rules" in setting up the impedance matrix with rows of the matrix related to the voltages and the columns to the corresponding currents. His equations are nearly identical to those represented by equations (3.23) and (3.51) in this study. Say's "simple rule" founds the methodology used by the author in simulating both the WRSM and WRIM using the principle of frozen permeability. In Chapter 3 of this study case, Say's rotor three-phase damping winding and single-phase dc windings model is modified to suit the condition for WRSM and WRIM rotor connection for excitation.

To the author's literature, Say, Graffin [48] and Rawcliffe [102] are the only authors who explain further about transforming three-phase winding to dc winding. They introduce more than ten transformed winding connections for rotor dc excitation in which the pros and cons are clearly stated. Even though this study considers only one rotor connection on the WRSM for excitation as in Fig. 4.3, the results in [81] demonstrate further the importance of involving these rotor connections in the dimensional and performance optimisation of the motor type.

A lot of work has been done in literature to confirm the existence and improve transient torque of induction motors [34, 35, 116, 134]. C. C. Brozio [18] found that for high quality starting torque, the motor stator phases A and C must be connected to the supply 6.8 ms after the zero-voltage of phase A, and phase B must then be switched on 4.8 ms later. Brozio has no explanation of the switching times. The starting method of Brozio is used in Appendix B.5 of this study. Although the starting methods are not new, the author is the first to give and explain the actual switching times of the phases for the reduction of starting transient torques in WRIMs. In Appendix B.5, a new technique for rotor switching is also introduced which greatly improves transient torques.

The author gives acknowledgement also to I. Boldea [15], J. Pyrhonen [63] and T. A. Lipo [78] on their contribution theory of electrical machine design, essentially electrical and geometric sizing of machines. Their theory is intensively followed such as Boldea's [15] parallel stator tooth sizing equations in small machines applied in stator and rotor as given in Appendix B.4 of this study. The sizing equations result in a maximum area of the slot for a given tooth flux density. Further explanation of the equations is given in this study which was not clearly explained by Boldea. Further acknowledgement is given to the considerations not found in literature shared by ACTOM South Africa of the 6 MW WRIM used for milling purposes. Although some of the information is public protected, ACTOM South Africa motor volume specifications are used in Chapter 7.

References

[1] "IEEE Guide for Synchronous Generator Modeling Practices and Applications in Power System Stability Analyses," *IEEE Std 1110-2002 (Revision of IEEE Std 1110-1991)*, pp. 1–72, 2003.

[2] ABB. "Slip-ring modular motors". ABB, 2017. [Online]. Available: https://new.abb.com/motors-generators/high-voltage-induction-motors/slip-ring-modular-motors.[Accessed: June,5,2017]

[3] ABB. "Synhronous motors". ABB, 2018. [Online]. Available: https://new.abb.com/motors-generators/synchronous-motors.[Accessed:December,17,2018]

[4] ACTOM, *"Medium voltage electric motors"*. ACTOM Electrical Machines, 2016.

[5] J. C. Akiror and W. E. Lynch, "Model for core loss prediction at high frequency and high flux density," Masters thesis, Canada: University of Concordia, 2012.

[6] G. J. Atkinson, B. C. Mecrow, A. G. Jack, D. J. Atkinson, P. Sangha, and M. Benarous, "The analysis of losses in high-power fault-tolerant machines for aerospace applications," *IEEE Transactions on Industry Applications*, vol. 42, no. 5, pp. 1162–1170, September 2006.

[7] K. B, T. N, and N. B, "Design of permanent magnet-assisted synchronous reluctance motors with maximum efficiency-power factor and torque per cost," in *2018 XIII International Conference on Electrical Machines (ICEM)*, September 2018, pp. 2465–2471.

[8] B. Stumberger, G. Stumberger, D. Dolinar, A. Hamler and M. Trlep, "Evaluation of saturation and cross-magnetization effects in interior permanent-magnet synchronous motor," *IEEE Transactions on Industry Applications*, vol. 39, no. 5, pp. 1264–1271, September 2003.

[9] N. Barbosa, "The invention of the electric motor 1800-1854 a short history of electric motors -part 1," *Electrotechnisches Institute*, June 2018.

[10] J. Bastos and N. Sadowski, *Electromagnetic Modeling by Finite Element Methods*, ser. Electrical and Computer Engineering. CRC Press, 2003.

[11] N. Bianchi and S. Bolognani, "Magnetic models of saturated interior permanent magnet motors based on finite element analysis," in *Conference Record of 1998 IEEE Industry Applications Conference. Thirty-Third IAS Annual Meeting*, vol. 1, Oct 1998, pp. 27–34.

[12] N. Bianchi, S. Bolognani, J. H. Jang, and S. K. Sul, "Comparison of pm motor structures and sensorless control techniques for zero-speed rotor position detection," in *2006 37th IEEE Power Electronics Specialists Conference*, June 2006, pp. 1–7.

[13] K. J. Binns, "Permanent magnet machines with line start capabilities: their design and application," in *IEE Colloquium on Permanent Magnet Machines and Drives*, February 1993, pp. 5/1–5/5.

[14] I. Boldea, *The Electric Generators Handbook Variable speed generators*, ser. Electric Power Engineering Series. CRC Press, 2006.

[15] I. Boldea and S. Nasar, *The Induction Machine Handbook*, ser. Electric Power Engineering Series. CRC Press, 2010.

[16] I. Boldea and L. N. Tutelea, *Electric Machines Steady State, Transients, and Design with MATLAB*, 1st ed. CRC Press Boca Raton, 2009.

[17] G. Bramerdorfer, J. A. Tapia, J. J. Pyrhönen, and A. Cavagnino, "Modern electrical machine design optimization: Techniques, trends, and best practices," *IEEE Transactions on Industrial Electronics*, vol. 65, no. 10, pp. 7672–7684, October 2018.

[18] C. Brozio and F. Van der Merwe, "Reduction of transient forces in induction motors by controlled switching," Thesis, Stellenbosch University, 1989.

[19] H. C and H. I, "Modeling of an ipmsm with short-circuited rotor winding for sensorless position estimation by fea using the frozen permeability method," in *IECON 2017 - 43rd Annual Conference of the IEEE Industrial Electronics Society*, Oct 2017, pp. 2067–2072.

[20] C. Hittinger and I. Hahn, "Modeling of an IPMSM with short-circuited rotor winding for sensorless position estimation by fea using the frozen permeability method," in *IECON 2017 - 43rd Annual Conference of the IEEE Industrial Electronics Society*, Oct 2017, pp. 2067–2072.

[21] E. S. Calvo and D. Potoradi, "Synchronous reluctance motors with and without permanent magnets for high performance low cost electrical drives," in *2015 5th International Electric Drives Production Conference (EDPC)*, September 2015, pp. 1–7.

[22] A. Castagnini, T. Känsäkangas, J. Kolehmainen, and P. S. Termini, "Analysis of the starting transient of a synchronous reluctance motor for direct-on-line applications," in *2015 IEEE International Electric Machines Drives Conference (IEMDC)*, May 2015, pp. 121–126.

[23] J. Chen, J. Li, R. Qu, and M. Ge, "Magnet-frozen-permeability fea and dc-biased measurement for machine inductance: Application on a variable-flux pm machine," *IEEE Transactions on Industrial Electronics*, vol. 65, no. 6, pp. 4599–4607, June 2018.

[24] W. Q. Chu and Z. Q. Zhu, "Average torque separation in permanent magnet synchronous machines using frozen permeability," *IEEE Transactions on Magnetics*, vol. 49, no. 3, pp. 1202–1210, March 2013.

[25] A. T. de Almeida, F. J. T. E. Ferreira, and G. Baoming, "Beyond induction motors—technology trends to move up efficiency," *IEEE Transactions on Industry Applications*, vol. 50, no. 3, pp. 2103–2114, May 2014.

[26] H. W. De Kock, "Dynamic control of the permanent magnet assisted reluctance synchronous machine with constant current angle," Masters thesis, Stellenbosch: University of Stellenbosch, 2006.

[27] K. Deb, A. Pratap, S. Agarwal, and T. Meyarivan, "A fast and elitist multiobjective genetic algorithm: Nsga-ii," *IEEE Transactions on Evolutionary Computation*, vol. 6, no. 2, pp. 182–197, April 2002.

[28] M. Degano, M. DiNardo, M. Galea, C. Gerada, and D. Gerada, "Global design optimization strategy of a synchronous reluctance machine for light electric vehicles," in *8th IET International Conference on Power Electronics, Machines and Drives (PEMD 2016)*, April 2016, pp. 1–5.

[29] D. G. Dorrell, "Are wound-rotor synchronous motors suitable for use in high efficiency torque-dense automotive drives?" in *IECON 2012 - 38th Annual Conference on IEEE Industrial Electronics Society*, October 2012, pp. 4880–4885.

[30] C. J. Dunlop and J. P. Harbour, "Modeling magnetic core loss for sinusoidal waveforms," Masters thesis, U.S.A: Massachusetts Institute of Technology, 2008.

[31] N. K. E and R. K, "Separation of torque components using frozen permeability and maxwell stress tensor," in *2017 IEEE Transportation Electrification Conference and Expo (ITEC)*, June 2017, pp. 720–723.

[32] F. M. A. El-Kader and S. M. Osheba, "Improving transient performance of reluctance motors," *IEEE Transactions on Energy Conversion*, vol. 4, no. 1, pp. 74–80, March 1989.

[33] A. M. El-Serafi and A. S. Abdallah, "Effect of saturation on the steady-state stability of a synchronous machine connected to an infinite bus system," *IEEE Transactions on Energy Conversion*, vol. 6, no. 3, pp. 514–521, September 1991.

[34] N. C. Enslin, W. M. Kaplan, and J. L. Davies, "Influence of transient switching currents and fluxes on the torque developed by a squirrel-cage induction motor," *Electrical Engineers, Proceedings of the Institution of*, vol. 113, no. 6, pp. 1035–1043, June 1966.

[35] N. C. Enslin and F. S. van der Merwe, "Improving the open-loop torque step response of induction motors," *IEE Proceedings B - Electric Power Applications*, vol. 134, no. 6, pp. 317–323, November 1987.

[36] A. S. Erasmus and M. J. Kamper, "Multi-objective design optimisation and pareto front visualisation of radial-flux eddy current coupling for a wind generator drivetrain," in *2016 IEEE Energy Conversion Congress and Exposition (ECCE)*, September 2016, pp. 1–8.

[37] H. Eskandari and C. D. Geiger, "A fast pareto genetic algorithm approach for solving expensive multiobjective optimization problems," *Journal of Heuristics*, vol. 14, no. 3, pp. 203–241, Jun 2008.

[38] W. Fei, P. C. K. Luk, D. Miao, and J. Shen, "Investigation of torque characteristics in a novel permanent magnet flux switching machine with an outer-rotor configuration," *IEEE Transactions on Magnetics*, vol. 50, no. 4, pp. 1–10, April 2014.

[39] F. Fiorillo and A. Novikov, "An improved approach to power losses in magnetic laminations under nonsinusoidal induction waveform," *IEEE Transactions on Magnetics*, vol. 26, no. 5, pp. 2904–2910, September 1990.

[40] Fitzgerald, *Electric machinery*. McGraw-Hill Education (India) Pvt Limited, 2002.

[41] T. Frenzke, "Impacts of cross-saturation on sensorless control of surface permanent magnet synchronous motors," in *2005 European Conference on Power Electronics and Applications*, September 2005, pp. 10 pp.–P.10.

[42] W. N. Fu, S. L. Ho, and P. Zhou, "Reduction of computing time for steady-state solutions of magnetic field and circuit coupled problems using time-domain finite-element method," *IEEE Transactions on Magnetics*, vol. 48, no. 11, pp. 3363–3366, Nov 2012.

[43] H. Ge, B. Bilgin, and A. Emadi, "Global loss minimization control of pmsm considering cross-coupling and saturation," in *2015 IEEE Energy Conversion Congress and Exposition (ECCE)*, Septmeber 2015, pp. 6139–6144.

[44] M. Ge, J. Li, R. Qu, Y. Lu, and J. Chen, "A synthetic frozen permeability method for torque separation in hybrid pm variable-flux machines," *IEEE Transactions on Applied Superconductivity*, vol. 28, no. 3, pp. 1–5, April 2018.

[45] M. Ge, J. Li, R. Qu, Y. Lu, and J. Chen, "A synthetic frozen permeability method for torque separation in hybrid pm variable-flux machines," *IEEE Transactions on Applied Superconductivity*, vol. 28, no. 3, pp. 1–5, April 2018.

[46] S. Gerber, *SEMFEM User's Manual*, Stellenbosch University, May 2014.

[47] D. A. Gonzalez and D. M. Saban, "Study of the copper losses in a high-speed permanent-magnet machine with form-wound windings," *IEEE Transactions on Industrial Electronics*, vol. 61, no. 6, pp. 3038–3045, June 2014.

[48] J. Griffin, *The synchronous induction motor*. Macdonald, 1954.

[49] G. Hahn and S. Shapiro, *Statistical Models in Engineering*, ser. Wiley Classics Library. Wiley, 1994.

[50] M. Y. Hassan, M. S. Majid, and H. A. Rahman, "Application of energy efficient motor in malaysian industries," in *2000 TENCON Proceedings. Intelligent Systems and Technologies for the New Millennium (Cat. No.00CH37119)*, vol. 2, September 2000, pp. 97–102 vol.2.

[51] R. L. Haupt and S. E. Haupt, *Practical Genetic Algorithms*. New York, NY, USA: John Wiley & Sons, Inc., 1998.

[52] S. L. Ho, S. Niu, and W. N. Fu, "Reduction of numerical errors of time-stepping finite element analysis for dynamic simulation of electric machines," *IEEE Transactions on Applied Superconductivity*, vol. 20, no. 3, pp. 1864–1868, June 2010.

[53] V. B. Honsinger, "Permanent magnet machines: Asynchronous operation," *IEEE Transactions on Power Apparatus and Systems*, vol. PAS-99, no. 4, pp. 1503–1509, July 1980.

[54] E. Hughes, J. Hiley, I. McKenzie-Smith, and K. Brown, *Hughes Electrical and Electronic Technology*. Pearson Education Limited, 2016.

[55] M. Humphries, "Rare earth elements: The global supply chain," Report, Congressional Research Service, 30 Septmber 2010.

[56] C. Hurst. China's rare earth elements industry: What can the west learn? Institute for the Analysis of Global Security, Potomac, MD, USA, 2010. [Online]. Available: http://www.iags.org/rareearth0310hurst.pdf

[57] A. Ibrahim, S. Rahnamayan, M. V. Martin, and K. Deb, "Elitensga-iii: An improved evolutionary many-objective optimization algorithm," in *2016 IEEE Congress on Evolutionary Computation (CEC)*, July 2016, pp. 973–982.

[58] IEC. (2010) Iec 60050-the international electronical vocabulary. Aceessed: January, 1, 2018. [Online]. Available: http://www.electropedia.org/

[59] M. J. Islam, J. Pippuri, J. Perho, and A. Arkkio, "Time-harmonic finite-element analysis of eddy currents in the form-wound stator winding of a cage induction motor," *IET Electric Power Applications*, vol. 1, no. 5, pp. 839–846, September 2007.

[60] S. Iwasaki, R. P. Deodhar, Y. Liu, A. Pride, Z. Q. Zhu, and J. J. Bremner, "Influence of pwm on the proximity loss in permanent-magnet brushless ac machines," *IEEE Transactions on Industry Applications*, vol. 45, no. 4, pp. 1359–1367, July 2009.

[61] B. J, D. K, M. K, and S. R, *Multiobjective Optimization*. Springer Science, 2017.

[62] D. Jones, "The workhorse of industry: The induction motor," *Power Transmission Engineering*, pp. 76–77, December 2013.

[63] J.Pyrhoenen, T.Jokinen, and V.Hrabovcova, *Design of rotating electrical machines*. Wiley, November 2013.

[64] T. Jung, C. Yun, H. Cha, H. Kim, H. Nam, and J. Hong, "The rotor conductor design for starting stability of line-start synchronous reluctance motor," in *IECON 2006 - 32nd Annual Conference on IEEE Industrial Electronics*, November 2006, pp. 1107–1112.

[65] K. Kaiser, *Electromagnetic Compatibility Handbook*, ser. Electrical engineering handbook series. Taylor & Francis, 2004.

[66] M. J. Kamper, "Design optimisation of cageless flux barrier rotor reluctance synchronius machine," PhD dissertation, Stellenbosch University, December 1996.

[67] M. Kamper, "The design criteria and development of a design program for turbo-induction motors for use in the load area," Master's thesis, Stellenbosch University, December 1987.

[68] H. V. Khang and A. Arkkio, "Eddy-current loss modeling for a form-wound induction motor using circuit model," *IEEE Transactions on Magnetics*, vol. 48, no. 2, pp. 1059–1062, February 2012.

[69] M. A. Khlifi and B. M. Alshammari, "A method to saturation modeling of synchronous machines in d-q axes," *International Journal of Electrical, Computer, Energetic, Electronic and Communication Engineering*, vol. 9, no. 9, pp. 1060 – 1066, 2015.

[70] P. Kundur, N. Balu, and M. Lauby, *Power System Stability and Control*, ser. Discussion Paper Series. McGraw-Hill Education, 1994.

[71] J. Lammeraner and M. Štafl, *Eddy Currents [by] Jiří Lammeraner and Miloš Štafl. English Translation Edited by G.A. Toombs [Translated by Miloš Štafl].*, 1966.

[72] L. Lavrinovicha and J. Dirba, "Comparison of permanent magnet synchronous motor and synchronous reluctance motor based on their torque per unit volume," in *2014 Electric Power Quality and Supply Reliability Conference (PQ)*, June 2014, pp. 233–236.

[73] F. Lazăr, A. Simion, L. Livadaru, and I. Daniel, "F.e.m. analysis of a 3 kw line-start permanent magnet synchronous machine," in *2014 International Conference and Exposition on Electrical and Power Engineering (EPE)*, October 2014, pp. 402–405.

[74] M. learning plus. (2015, October) Python parallel programming solutions. [Online]. Available: http://docs.scipy.org/doc/scipy/reference/tutorial/interpolate.html

[75] S. T. Lee, T. A. Burress, and L. M. Tolbert, "Power-factor and torque calculation with consideration of cross saturation of the interior permanent magnet synchronous motor with brushless field excitation," in *2009 IEEE International Electric Machines and Drives Conference*, May 2009, pp. 317–322.

[76] G. J. Li, Z. Q. Zhu, X. Y. Ma, and G. W. Jewell, "Comparative study of torque production in conventional and mutually coupled srms using frozen permeability," *IEEE Transactions on Magnetics*, vol. 52, no. 6, pp. 1–9, June 2016.

[77] X. Liang, S. O. Faried, and A. M. El-Serafi, "Space harmonics of synchronous machines calculated by finite element method," in *2015 IEEE/IAS 51st Industrial Commercial Power Systems Technical Conference (I CPS)*, May 2015, pp. 1–12.

[78] T. A. Lipo, *Analysis of synchronous machines*. CRC Press, June 2012.

[79] X. Liu, J. Jiang, Y. Gong, and Y. Ding, "Simulation of permanent magnet synchronous motor with dual closed loop by time-stepping finite element model," in *2006 CES/IEEE 5th International Power Electronics and Motion Control Conference*, vol. 2, August 2006, pp. 1–5.

[80] X. Lu, K. L. V. Iyer, K. Mukherjee, and N. C. Kar, "Development of a novel magnetic circuit model for design of premium efficiency three-phase line start permanent magnet machines with improved starting performance," *IEEE Transactions on Magnetics*, vol. 49, no. 7, pp. 3965–3968, July 2013.

[81] M. Mabhula and M. J. Kamper, "Saliency and mutual inductance effect in cylindrical wound-rotor synchronous motor," in *2017 IEEE Workshop on Electrical Machines Design, Control and Diagnosis (WEMDCD)*, April 2017, pp. 152–157.

[82] M. Mabhula and M. J. Kamper, "Computational efficient parameter and performance prediction of wound-rotor induction motor," *IEEE Transactions on Magnetics*, vol. PP, no. 99, pp. 1–7, 2018.

[83] M. Mabhula and M. J. Kamper, "Design optimization of cylindrical-rotor synchronous-induction motors," in *2018 IEEE Energy Conversion Congress and Exposition (ECCE)*, September 2018, pp. 5778–5785.

[84] M. Mabhula and M. J. Kamper, "Model parameter and performance calculation of cylindrical wound-rotor synchronous motors," *IEEE Transactions on Industry Application*, no. submitted and under review, 2019.

[85] M. Mabhula and M. J. Kamper, "Steady-state performance analysis of direct-on-line cylindrical wound-rotor synchronous motor," in *2019 IEEE Workshop on Electrical Machines Design, Control and Diagnosis (WEMDCD)*, vol. 1, April 2019, pp. 89–95.

[86] M. Mabhula and M. Kamper, "Improving starting torque quality of wound-rotor induction motor for geared fan loads," *Southern African Universities' Power Engineering Conference (SAUPEC), Vaal University of Technology, Association, South Africa*, January 2017.

[87] S. Mukerji, A. S. Khan, and Y. Singh, *Electromagnetics for Electrical Machines*, 1st ed. CRC Press, March 2015.

[88] P. Murty, "Chapter 23 - voltage and reactive power control," in *Electrical Power Systems*, P. Murty, Ed. Boston: Butterworth-Heinemann, 2017, pp. 731 – 781. [Online]. Available: http://www.sciencedirect.com/science/article/pii/B9780081011249000231

[89] S. S. Murty, C. S. Jha, and L. Shridhar, "Experience with design optimisation of induction motors driving pumpsets for energy conservation," in *TENCON '91. Region 10 International Conference on EC3-Energy, Computer, Communication and Control Systems*, vol. 1, August 1991, pp. 117–121.

[90] M. Mutluer and O. Bilgin, "Design optimization of pmsm by particle swarm optimization and genetic algorithm," in *2012 International Symposium on Innovations in Intelligent Systems and Applications*, July 2012, pp. 1–4.

[91] T. N, L. B, and M. S, "An approach to compute saturated induction motors in steady state," in *IEEE International Electric Machines and Drives Conference, 2003. IEMDC'03.*, vol. 3, June 2003, pp. 1646–1650 vol.3.

[92] J. Naidoo. "Largest motor of its type" . EE publishers, 7 November 2018. [Online]. Available: http://www.ee.co.za/article/largest-motor-of-its-type.html.[Accessed:December,17,2018]

[93] V. Ostovic, *Dynamics of Saturated Electric Machines*. Springer-Verlag New York, 1989.

[94] Y. Ouazir, N. Takorabet, R. Ibtiouen, and M. Benhaddadi, "Time-stepping fe analysis of cage induction motor with air-gap interface coupling taking into account phase-belt harmonics," *IEEE Transactions on Magnetics*, vol. 45, no. 3, pp. 1384–1387, March 2009.

[95] R. B. B. Ovando-Martinez, M. A. Arjona Lopez, and C. Hernandez Flores, "A finite-element variable time-stepping algorithm for solving the electromagnetic diffusion equation," *IEEE Transactions on Magnetics*, vol. 48, no. 2, pp. 647–650, February 2012.

[96] S. Palho, "Structural optimisation of an induction motor using a genetic algorithm and a finite element method," PhD dissertation, Helsinki University of Technology, August 1996.

[97] J. Pang, W. Liu, N. Jiao, J. Wang, and P. Ma, "Calculation of cross-coupling inductance and electromagnetic torque in wound-rotor synchronous starter/generator," *IEEE Transactions on Industrial Electronics*, vol. 66, no. 7, pp. 5115–5123, July 2019.

[98] G. Pellegrino, T. Jahns, N. Bianchi, W. Soong, and F. Cupertino, *The Rediscovery of Synchronous Reluctance and Ferrite Permanent Magnet Motors: Tutorial Course Notes*, ser. SpringerBriefs in Electrical and Computer Engineering. Springer International Publishing, 2016.

[99] A. D. Podoltsev, I. N. Kucheryavaya, and B. B. Lebedev, "Analysis of effective resistance and eddy-current losses in multiturn winding of high-frequency magnetic components," *IEEE Transactions on Magnetics*, vol. 39, no. 1, pp. 539–548, January 2003.

[100] P. Ponomarev, I. Petrov, N. Bianchi, and J. Pyrhonen, "Additional Losses in Stator Slot Windings of Permanent Magnet Synchronous Machines ," *ResearchGate*, pp. 1–11, May 2015.

[101] V. Rallabandi, N. Taran, D. M. Ionel, and P. Zhou, "Inductance testing for ipm synchronous machines according to the new ieee std 1812 and typical laboratory practices," *IEEE Transactions on Industry Applications*, vol. 55, no. 3, pp. 2649–2659, May 2019.

[102] G. H. Rawcliffe, "The secondary circuits of synchronous induction motors," *Journal of the Institution of Electrical Engineers*, vol. 87, no. 525, pp. 282–298, September 1940.

[103] R. Ridley and A. Nace, "Modeling ferrite core lossses," February 2006.

[104] H. Roux and M. Kamper, "Starting of cylindrical wound-rotor synchronous motor for fan loads," *Southern African Universities' Power Engineering Conference (SAUPEC), Vaal University of Technology, Association, South Africa*, January 2016.

[105] M. Ruba, F. Jurca, C. Martis, R. Martis, and P. F. Piglesan, "Analysis of maximum torque per ampere control strategy for variable reluctance synchronous machines for traction applications," in *2014 International Conference and Exposition on Electrical and Power Engineering (EPE)*, October 2014, pp. 322–326.

[106] S. Gerber. (2015, March) "Welcome to SEMFEM's domcumentation". Aceessed January, 15, 2016. [Online]. Available: http://www0.sun.ac.za/semfem/index.html

[107] S. Mezani, T.Hamiti, L. Belguerras, T. Lubin and C. Gerada, "Computation of wound rotor induction machines based on coupled finite elements and circuit equation under a first space harmonic approximation," *IEEE Transactions on Magnetics*, vol. 52, no. 3, pp. 1–4, March 2016.

[108] S. Salon, *Finite Element Analysis of Electrical Machines*, ser. Power Electronics and Power Systems. Springer US, 2012.

[109] M. G. Say, *Alternating current machines*, 5th ed. Longman Scientific and Technology, 1992.

[110] T. Schuhmann, B. Cebulski, and S. Paul, "Comparison of time-harmonic and transient finite element calculation of a squirrel cage induction machine for electric vehicles," in *2014 International Conference on Electrical Machines (ICEM)*, Sep. 2014, pp. 1037–1043.

[111] G. Scutaru, A. Negoita, and R. M. Ionescu, "Three-phase induction motor design software," in *2010 IEEE International Conference on Automation, Quality and Testing, Robotics (AQTR)*, vol. 3, May 2010, pp. 1–4.

[112] R. Sebastian. (2014, June) An introduction to parallel programming using python's multiprocessing module. [Online]. Available: https://sebastianraschka.com/Articles/2014_multiprocessing.html

[113] K. Shin, K. Hong, H. Cho, and J. Choi, "Core loss calculation of permanent magnet machines using analytical method," *IEEE Transactions on Applied Superconductivity*, vol. 28, no. 3, pp. 1–5, April 2018.

[114] K. Shin, K. Hong, and H. Cho and J. Choi, "Core loss calculation of permanent magnet machines using analytical method," *IEEE Transactions on Applied Superconductivity*, vol. 28, no. 3, pp. 1–5, April 2018.

[115] C. Singh and D. Sarkar, "Practical considerations in the optimisation of induction motor design," *IEE Proceedings B - Electric Power Applications*, vol. 139, no. 4, pp. 365–373, July 1992.

[116] R. D. Slater and W. S. Wood, "Constant-speed solutions applied to the evaluation of induction-motor transient torque peaks," *Electrical Engineers, Proceedings of the Institution of*, vol. 114, no. 10, pp. 1429–1435, October 1967.

[117] A. C. Smith, S. Williamson, and J. R. Smith, "Transient currents and torques in wound-rotor induction motors using the finite-element method," *IEE Proceedings B - Electric Power Applications*, vol. 137, no. 3, pp. 160–173, May 1990.

[118] J. Stallcup and J. Stallcup, *Generator, Transformer, Motor, and Compressor*, ser. 2011 NEC Stallcup Series. Jones & Bartlett Learning, 2011.

[119] C. P. Steinmetz, "On the law of hysteresis," *Transactions of the American Institute of Electrical Engineers*, vol. IX, no. 1, pp. 1–64, January 1892.

[120] E. Strangas, "Notes for an introduction course on electrical machines and drives," February 2017.

[121] N. Stranges, "Calculation of the starting performance of solid pole synchronous motors by the time-stepping finite element method," in *2008 IEEE Power and Energy Society General Meeting - Conversion and Delivery of Electrical Energy in the 21st Century*, July 2008, pp. 1–4.

[122] B. Stumberger, G. Stumberger, D. Dolinar, A. Hamler, and M. Trlep, "Evaluation of saturation and cross-magnetization effects in interior permanent-magnet synchronous motor," *IEEE Transactions on Industry Applications*, vol. 39, no. 5, pp. 1264–1271, Sept 2003.

[123] K. Tang, L. Zhou, J. Wang, Y. Xiao, and S. Wang, "Rotor design and optimization of the single-phase line-start synchronous reluctance motor," in *2017 20th International Conference on Electrical Machines and Systems (ICEMS)*, August 2017, pp. 1–4.

[124] J. K. Tangudu, T. M. Jahns, A. M. El-Refaie, and Z. Q. Zhu, "Segregation of torque components in fractional-slot concentrated-winding interior pm machines using frozen permeability," pp. 3814–3821, 2009.

[125] H. A. Toliyat and G. B. Kliman, *Handbook of Electric Motors*, 2nd ed., ser. Engineering and Technology. CRC Press, 2004.

[126] G. F. Uler, O. A. Mohammed, and C.-S. Koh, "Design optimization of electrical machines using genetic algorithms," *IEEE Transactions on Magnetics*, vol. 31, no. 3, pp. 2008–2011, May 1995.

[127] S. Umans, A. Fitzgerald, and C. Kingsley, *Electric Machinery: Seventh Edition*. McGraw-Hill Higher Education, 2013.

[128] Vanderplaats Research and Development, Inc. (2008, June) "VisualDOC: Software for Process Integration and Multidiscipline Design Optimization". Aceessed June, 30, 2017. [Online]. Available: http://www.vrand.com/products/visualdoc/

[129] B. D. Varaticeanu, P. Minciunescu, and S. Matei, "Design of permanent magnet assisted synchronous reluctance motor for light urban electric vehicle," in *2014 International Symposium on Fundamentals of Electrical Engineering (ISFEE)*, November 2014, pp. 1–6.

[130] G. Vinsard and B. Laporte, "A new formulation for induction machine computation," *IEEE Transactions on Magnetics*, vol. 30, no. 5, pp. 3693–3696, Sep. 1994.

[131] J. A. Walker and D. Dorrell, "Verification of the frozen permeabilities method of calculating the interior permanent magnet motor," in *INTERMAG Asia 2005. Digests of the IEEE International Magnetics Conference, 2005.*, April 2005, pp. 715–716.

[132] J. A. Walker, D. G. Dorrell, and C. Cossar, "Flux-linkage calculation in permanent-magnet motors using the frozen permeabilities method," *IEEE Transactions on Magnetics*, vol. 41, no. 10, pp. 3946–3948, October 2005.

[133] Y. Wang, D. Ionel, D. G. Dorrell, and S. Stretz, "Establishing the power factor limitations for synchronous reluctance machines," *IEEE Transactions on Magnetics*, vol. 51, no. 11, pp. 1–4, November 2015.

[134] W. S. Wood, F. Flynn, and A. Shanmugasundaram, "Transient torques in induction motors, due to switching of the supply," *Electrical Engineers, Proceedings of the Institution of*, vol. 112, no. 7, pp. 1348–1354, July 1965.

[135] F. Wurtz, M. Richomme, J. Bigeon, and J. C. Sabonnadiere, "A few results for using genetic algorithms in the design of electrical machines," *IEEE Transactions on Magnetics*, vol. 33, no. 2, pp. 1892–1895, March 1997.

[136] L. X, F. S, O, and E.-S. A, M, "Space harmonics of synchronous machines calculated by finite-element method," *IEEE Transactions on Industry Applications*, vol. 52, no. 2, pp. 1193–1203, March 2016.

[137] X.-S. Yang, *Optimization Algorithms*, 01 1970, vol. 356, pp. 13–31.

[138] Y. Yao, Q. Lu, X. Huang, and Y. Ye, "Fast calculation of detent force in pm linear synchronous machines with considering magnetic saturation," *IEEE Transactions on Magnetics*, vol. 53, no. 6, pp. 1–4, June 2017.

[139] X. Yi, L. Weili, W. Purui, and Z. Xiaochen, “Influence of magnetic slot wedge on electromagnetic parameters and magnetic field distribution of turbo-generator,” in *2016 IEEE Conference on Electromagnetic Field Computation (CEFC)*, November 2016, pp. 1–1.

[140] X. Yu and M. Gen, *Introduction to Evolutionary Algorithms*, ser. Decision Engineering. Springer London, 2010.

[141] G. Zaccone. (2017) Parallel processing in Python. [Online]. Available: https://www.machinelearningplus.com/python/parallel-processing-python/

Appendix A

WRSM and WRIM motor model

This chapter in Appendix A gives more details of the concepts illustrated in Chapter 2. The details include the Park Transformation, torque equation formulation and finite element method vector potential and properties of magnetic materials. The important literature for the subject matter is also cited.

A.1. Park Transformation

R.E. Doherty and R.H. Park developed a mathematical transformation (dq transformation) from the work of Andre Blondel (two-reaction method) in which the time varying stator quantities (voltages, currents and flux linkages) can be transformed into time invariant d and q axes quantities [70, 127]. The dq transformation matrices from the ABC reference frame to the dq are given by

$$[T] = \frac{2}{m}\begin{bmatrix} \cos(\theta_e - k\beta_e) & \cos(\theta_e - (k+1)\beta_e) & \dots \\ -\sin(\theta_e - k\beta_e) & -\sin(\theta_e - (k+1)\beta_e) & \dots \end{bmatrix} \tag{A.1}$$

$$[T]^{-1} = \begin{bmatrix} \cos(\theta_e - k\beta_e) & \sin(\theta_e - k\beta_e) \\ \cos(\theta_e - (k+1)\beta_e) & -\sin(\theta_e - (k+1)\beta_e) \\ \vdots & \vdots \end{bmatrix}, \tag{A.2}$$

where

- m - stator or rotor number of phases,
- θ_e - electrical transformation angle,
- β_e - electrical phase shift angle,

and $k|k \in \mathbb{N}, 0 \leqslant k < m$.

A.2. Torque equation

The WRSM and WRIM stator voltage equations of (2.5) given by

$$\begin{bmatrix} v_{ds} \\ v_{qs} \end{bmatrix} = \begin{bmatrix} r_s & 0 \\ 0 & r_s \end{bmatrix} \begin{bmatrix} i_{ds} \\ i_{qs} \end{bmatrix} + \frac{d}{dt} \begin{bmatrix} \lambda_{ds} \\ \lambda_{qs} \end{bmatrix} + \begin{bmatrix} 0 & -\omega_s \\ \omega_s & 0 \end{bmatrix} \begin{bmatrix} \lambda_{ds} \\ \lambda_{qs} \end{bmatrix}, \tag{A.3}$$

are directly related to the flux linking the stator windings. These flux linkages depend on the currents in the stator windings and other properties such as motor geometry and magnetisation characteristics of the stator core. The currents producing the flux linkages as of (2.13) in (2.15), however, depend on the stator phase position θ_s. Hence, the stator flux linkages are a function current and the phase position expressed as

$$\begin{cases} \lambda_{ds} = \lambda_{ds}(i_{ds}, \theta_s) \\ \lambda_{qs} = \lambda_{qs}(i_{qs}, \theta_s). \end{cases} \tag{A.4}$$

By applying (A.4), (A.3) results in

$$\begin{bmatrix} v_{ds} \\ v_{qs} \end{bmatrix} = \begin{bmatrix} r_s & 0 \\ 0 & r_s \end{bmatrix} \begin{bmatrix} i_{ds} \\ i_{qs} \end{bmatrix} + \begin{bmatrix} \frac{\partial}{\partial i_{ds}}\lambda_{ds} & \frac{\partial}{\partial i_{qs}}\lambda_{ds} \\ \frac{\partial}{\partial i_{ds}}\lambda_{qs} & \frac{\partial}{\partial i_{qs}}\lambda_{qs} \end{bmatrix} \frac{d}{dt} \begin{bmatrix} i_{ds} \\ i_{qs} \end{bmatrix} + \begin{bmatrix} \frac{\partial}{\partial \theta_s}\lambda_{ds} \\ \frac{\partial}{\partial \theta_s}\lambda_{qs} \end{bmatrix} \frac{d}{dt}\theta_s + \begin{bmatrix} -\lambda_{qs} \\ \lambda_{ds} \end{bmatrix} \frac{d}{dt}\theta_s. \tag{A.5}$$

The terms of (A.5) that contribute towards the developed torque (and also developed power) of the motor are speed voltages and change in flux linkages due to the phase position angle i.e. rotor position. Using only torque contribution terms, (A.5) becomes

$$[e_{dqs}] = \begin{bmatrix} e_{ds} \\ e_{qs} \end{bmatrix} = \omega_s \{ \begin{bmatrix} \frac{\partial}{\partial \theta_s}\lambda_{ds} \\ \frac{\partial}{\partial \theta_s}\lambda_{qs} \end{bmatrix} + \begin{bmatrix} -\lambda_{qs} \\ \lambda_{ds} \end{bmatrix} \}. \tag{A.6}$$

For average developed torque, the variation of the flux linkages due to rotor position can be ignored, thus

$$\begin{bmatrix} e_{ds} \\ e_{qs} \end{bmatrix} = \omega_s \begin{bmatrix} -\lambda_{qs} \\ \lambda_{ds} \end{bmatrix}. \tag{A.7}$$

Now, the developed power in the ABC reference frame must be equal to the power in the dq-axes reference frame, therefore

$$\begin{aligned} P_d &= [e_{ABC}]^T [i_{ABC}] \\ &= ([T]^{-1}[e_{dqs}])^T ([T]^{-1}[i_{dqs}]) \\ &= [e_{dqs}]^T ([T]^{-1})^T [T]^{-1} [i_{dqs}] \\ &= [e_{dqs}]^T \begin{bmatrix} 1.5 & 0 \\ 0 & 1.5 \end{bmatrix} [i_{dqs}]. \end{aligned} \tag{A.8}$$

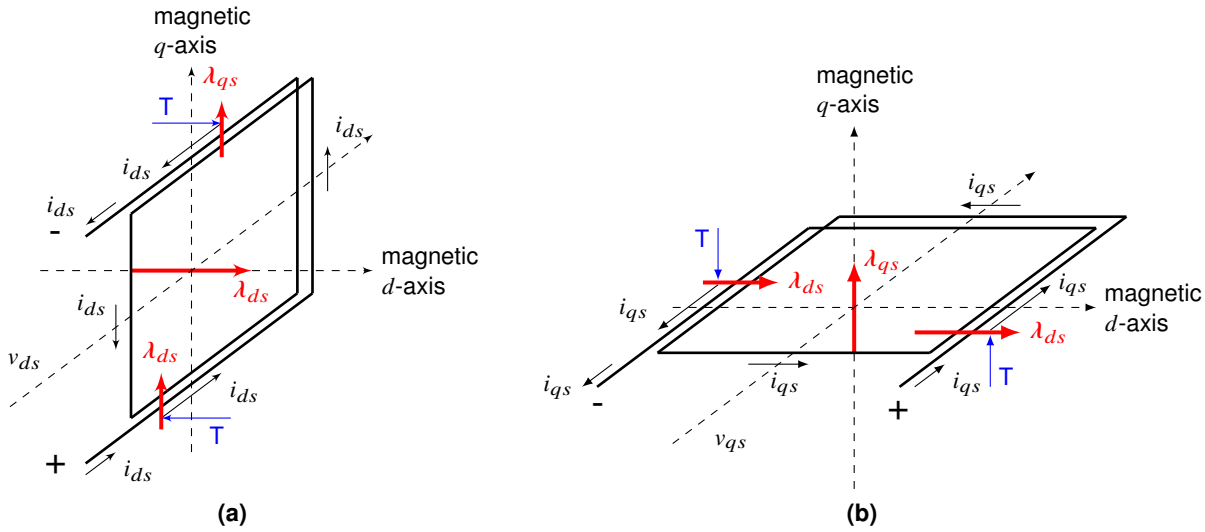

Figure A.1: Three dimensional views for (a) d-axis winding and (b) q-axis winding for torque production concept.

Using (A.7), (A.8) becomes

$$\begin{aligned} P_d &= \omega_s \begin{bmatrix} -\lambda_{qs} & \lambda_{ds} \end{bmatrix} \begin{bmatrix} 1.5 & 0 \\ 0 & 1.5 \end{bmatrix} [i_{dqs}] \\ &= 1.5\omega_s(\lambda_{ds} i_{qs} - \lambda_{qs} i_{ds}). \end{aligned} \tag{A.9}$$

Thus, the developed torque is related to the developed power by the mechanical angular speed ω_m as

$$T_d = \frac{1}{\omega_m} P_d, \tag{A.10}$$

in which the mechanical speed is related to the electrical angular speed ω_s by pole pairs p as

$$\omega_m = \frac{1}{p} \omega_s. \tag{A.11}$$

Hence, using (A.9)-(A.11), the developed torque is given by

$$T_d = 1.5p(\lambda_{ds} i_{qs} - \lambda_{qs} i_{ds}), \tag{A.12}$$

which explains the power equaliser $k = 1.5$ of (2.23).

A.3. Torque production

De Kock [26] gave a good three dimensional view of two windings in the dq-axes used for better understanding of torque production concept in electrical motors. In Fig. A.1(b), the flowing q-axis current is caused to flow by the applied q-axis voltage to the motor. The flowing current is restricted by the stator winding resistance r_s. A magnetic field is created due to this current which moves perpendicular to the area spanned by the winding. The direction of the magnetic flux is given by the RHR. Also in Fig. A.1(a) the flowing d-axis current is caused by the applied d-axis voltage to the motor. A magnetic field is also produced due to the d-axis current flowing which moves perpendicular to the area spanned by the winding. In both instances only one pole-pair machine is shown since only one d and q-axis are shown which rotates at the same speed. Because the direction of the torque

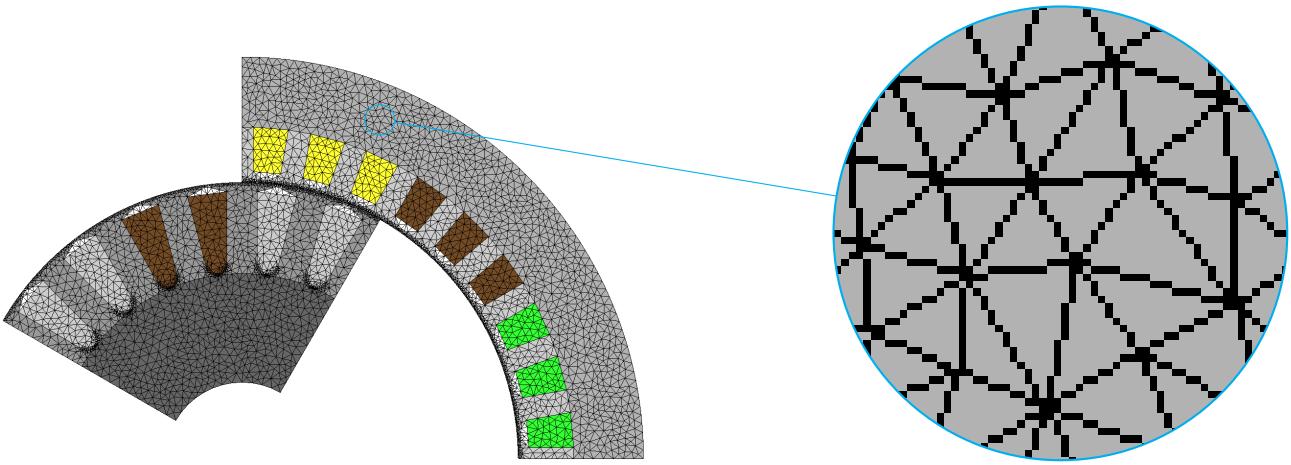

Figure A.2: Mesh representing elements and nodes in FEM.

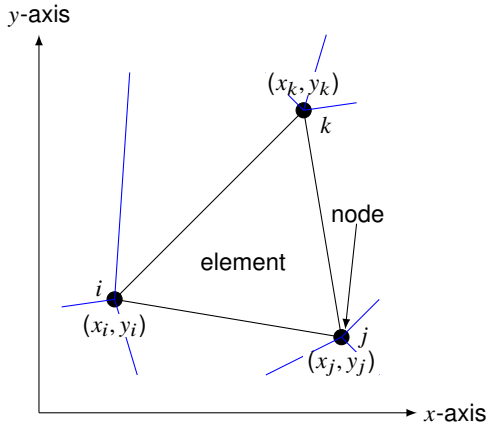

Figure A.3: An element in a triangular mesh and Cartesian coordinate system.

is given by the RHR as once stated, the interaction of the d-axis flux linkage with q-axis currents gives a positive torque while the q-axis flux linkage with d-axis currents gives negative torque in Fig. A.1. Conventionally, positive torque is anti-clockwise in direction and negative torque is clockwise in direction.

A.4. Vector potential using FEM

In the FEM, the solution domain is subdivided into triangular finite element meshes. The meshes are made up of point nodes defining the triangle shapes. The advantage of triangular elements is the flexibility in complex geometries even though they are less accurate when compared to quadrilateral elements [108]. Figure A.2 represents a wound-rotor motor geometry with mesh elements and nodes in the FEM.

Figure A.3 shows the triangular element nodal points (i, j, k) in the xy plane. The potential varies linearly between the nodal points, hence, the current density which is the derivative of the potential,

is constant in the triangle. The vector potential at each of the three nodes can be expressed as

$$\begin{aligned}\vec{A}_i &= C_1 + C_2 x_i + C_3 y_i \\ \vec{A}_j &= C_1 + C_2 x_j + C_3 y_j \\ \vec{A}_k &= C_3 + C_2 x_k + C_3 y_k.\end{aligned} \tag{A.13}$$

Equation (A.13) results in three unknowns i.e. C_1, C_2, C_3 which are solved in terms of the vector potential and geometry using Cramer's Rule as

$$C_1 = \frac{\begin{vmatrix}\vec{A}_i & x_i & y_i \\ \vec{A}_j & x_j & y_j \\ \vec{A}_k & x_k & y_k\end{vmatrix}}{\begin{vmatrix}1 & x_i & y_i \\ 1 & x_j & y_j \\ 1 & x_k & y_k\end{vmatrix}} = \frac{\vec{A}_i \begin{vmatrix}x_j & y_j \\ x_k & y_k\end{vmatrix} + \vec{A}_j \begin{vmatrix}x_k & y_k \\ x_i & y_i\end{vmatrix} + \vec{A}_k \begin{vmatrix}x_i & y_i \\ x_j & y_j\end{vmatrix}}{2\triangle}, \tag{A.14}$$

$$C_2 = \frac{\begin{vmatrix}1 & \vec{A}_i & y_i \\ 1 & \vec{A}_j & y_j \\ 1 & \vec{A}_k & y_k\end{vmatrix}}{\begin{vmatrix}1 & x_i & y_i \\ 1 & x_j & y_j \\ 1 & x_k & y_k\end{vmatrix}} = \frac{\vec{A}_i \begin{vmatrix}1 & y_k \\ 1 & y_j\end{vmatrix} + \vec{A}_j \begin{vmatrix}1 & y_i \\ 1 & y_k\end{vmatrix} + \vec{A}_k \begin{vmatrix}1 & y_j \\ 1 & y_i\end{vmatrix}}{2\triangle}, \tag{A.15}$$

and

$$C_3 = \frac{\begin{vmatrix}1 & x_i & \vec{A}_i \\ 1 & x_j & \vec{A}_j \\ 1 & x_k & \vec{A}_k\end{vmatrix}}{\begin{vmatrix}1 & x_i & y_i \\ 1 & x_j & y_j \\ 1 & x_k & y_k\end{vmatrix}} = \frac{\vec{A}_i \begin{vmatrix}1 & x_j \\ 1 & x_k\end{vmatrix} + \vec{A}_j \begin{vmatrix}1 & x_k \\ 1 & x_i\end{vmatrix} + \vec{A}_k \begin{vmatrix}1 & x_i \\ 1 & x_j\end{vmatrix}}{2\triangle}, \tag{A.16}$$

where $\triangle$ is the area of the triangle. Using the results of (A.14)-(A.16), the vector potential at any point on the element is given by

$$\vec{A} = \frac{N_i \vec{A}_i + N_j \vec{A}_j + N_k \vec{A}_k}{2\triangle}. \tag{A.17}$$

The coefficients N of the nodal potential are shape functions given by

$$\begin{aligned}N_i &= x_j y_k - x_k y_j + x(y_j - y_k) + y(x_k - x_j) \\ N_j &= x_k y_i - x_i y_k + x(y_k - y_i) + y(x_i - x_k) \\ N_k &= x_i y_j + x_j y_i + x(y_i - y_k) + y(x_j - x_i).\end{aligned} \tag{A.18}$$

Following the above, the potential is the sum of shape functions multiplied by the nodal potential

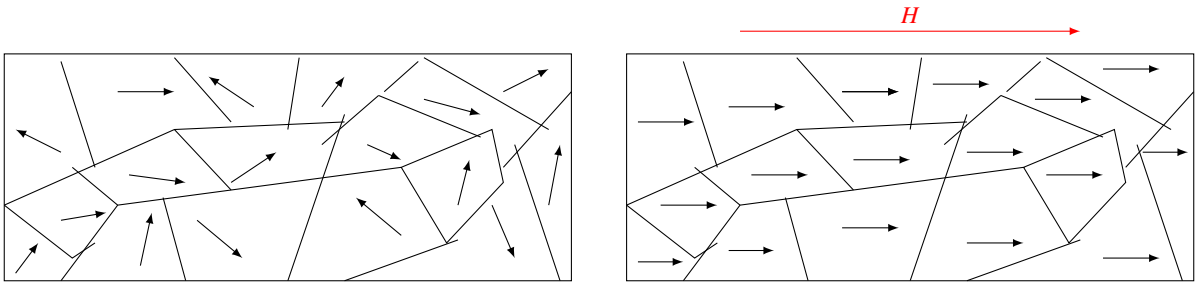

(a) Random orientation domain magnetisation moments

(b) Aligned domain magnetisation moments

Figure A.4: Ferromagnetic material sample (a) before and (b) after magnetisation.

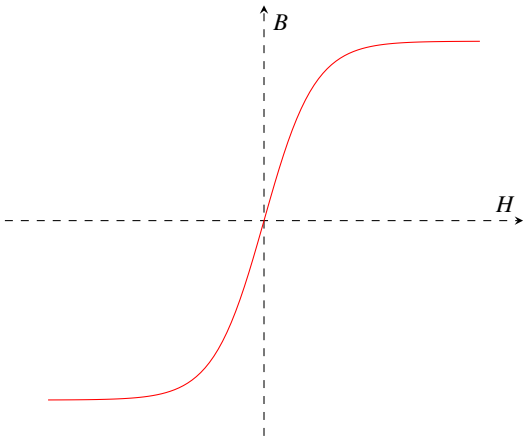

Figure A.5: Saturation in ferromagnetic materials.

expressed as

$$\vec{A} = \sum_{i=1}^{z} N_i(x, y)\vec{A}_i, \tag{A.19}$$

where z is the number of nodes in an element.

A.5. Magnetic saturation and hysteresis

With extensive reference to [127], the properties of ferromagnetic materials are described. In unmagnetised ferromagnetic materials the domain magnetic material are randomly oriented as shown in Fig. A.4(a) with zero net magnetic flux. When an external magnetic field H is applied to the material, the domain magnetic moments rapidly align as shown in Fig. A.4(b) and adding up with the applied field to produce a higher flux density B. This results in the effective permeability given by

$$\mu = \frac{B}{H}, \tag{A.20}$$

to be larger when compared to the permeability of free space μ_0. As H increases, this described behaviour is continuous until all the domain magnetic moments are aligned with H. At this state called saturation, the magnetic moments no longer contribute to the increasing B. Figure A.5 shows the concept of saturation on a BH curve when hysteresis is neglected.

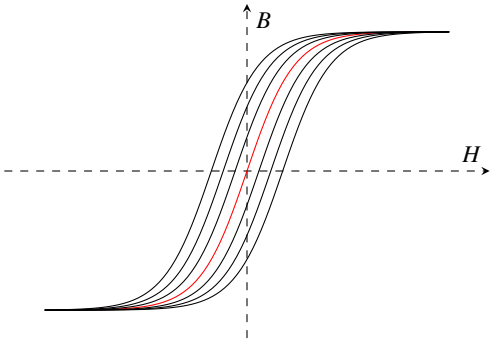

Figure A.6: Hysteresis loops and saturation in ferromagnetic materials.

When H is reduced from the saturation state, the domain magnetic moments naturally align to the direction of easy magnetism nearest to that of the applied H. Due to the natural alignment phenomenon at zero H, the magnetic domain moments no longer totally randomly oriented as they were initially, resulting in a net B. This behaviour, i.e. hysteresis is presented as in Fig. A.6, where the B value for a given value of the H starts to also depend on the history of B [120]. Figure A.6 can also be used to explain hysteresis losses in the ferromagnetic materials. When a sinusoidal current changes from i to $-i$, a point on the BH curve travels around the curve. The power, i.e. hysteresis losses proportional to the loop area, is transferred to the material during this time.

A.6. End-winding inductance variables

The end-winding inductance formulation variables of (2.80) are as given according to Kamper [67]. The formulation takes into account the end-winding coils' shape represented by index u which when

- $u = 1$ implies V-shaped coils,
- $u = 2$ implies elliptical-shaped coils and
- $u = 3$ implies rectangular coils.

The ordinary distribution factor k_d for the fundamental three phase winding of q turns per phase per pole is given by

$$k_d = \frac{\sin(\frac{\pi}{6})}{q \sin(\frac{\pi}{6q})}. \tag{A.21}$$

The factor $k_{p(u)}$ of (2.80) is an end-winding pitch factor for a coil shape u given by

$$\begin{cases} k_{p(1)} = \dfrac{3 \sin(\frac{\pi \tau_c}{6q})}{4 - (\frac{\tau_c}{3q})^2} \\ k_{p(2)} = \sin(\frac{\pi \tau_c}{6q}) \\ k_{p(3)} = \dfrac{k_{p(1)} + k_{p(2)}}{2}, \end{cases} \tag{A.22}$$

in which τ_c is the coil pitch in terms of number stator or rotor slots. The shape factor $V_{(u)}$ for a coil shape u for double and single layer windings are respectively given by

$$\text{single layer winding}: \begin{cases} V_{(1)} = 600 \\ V_{(2)} = 1\ 180 \\ V_{(3)} = 1\ 400 \end{cases} \tag{A.23}$$

$$\text{double layer winding}: \begin{cases} V_{(1)} = 465 \\ V_{(2)} = 960 \\ V_{(3)} = 1\ 040. \end{cases} \tag{A.24}$$

A.7. Python scripting parallel programming

The literature [74, 112, 141] is extensively followed in this Section. The default python interpreter is designed with simplicity in mind and has a thread-safe mechanism, the so called global interpreter lock GIL. In order to prevent conflicts between threads, it executes only one statement at a time, so called serial processing or single threading. In order to avoid some of the GIL's drawbacks, the python multiprocessing module is used in this study. The Python multiprocessing package offers the pool class which offers a convenient means of paralleling the execution of a function across multiple input values. The object distributes the input data across, i.e. data parallelism.

Even though threads can be used in parallel programming, the technique is not reliable. For example, if jobs are submitted to different threads, those jobs can be pictured as sub-tasks of a single process and those threads will usually have access to the same areas, i.e. shared memory. If processes are writing to same memory location at the same time, the approach can easily lead to conflicts in the case of improper synchronisation.

Following the above mentioned, turning to multiprocessing is a safe approach. Multiprocessing submits multiple processes to complete separate memory locations, i.e. distributed memory, with every process running completely independently from each other. However, the approach comes with an additional overhead due to the communication overhead between separate processes.

Figure A.7 illustrates the approach of parallel processing for further understanding. It is the use of more than one processor core, i.e. worker, to execute a program, i.e. job. Ideally, the program runs faster because of more engines running the program. In Fig. A.7, a single task is allocated to workers, thus the big task is distributed to four processes running at the same time.

As stated earlier in this section the python multiprocessing package offers the pool class which can be used to provide more convenient approaches for simple parallel processing tasks. The four methods provided by the class that can be looked at are

- *pool.apply*,
- *pool.map*,
- *pool.apply_async* and
- *pool.map_async*.

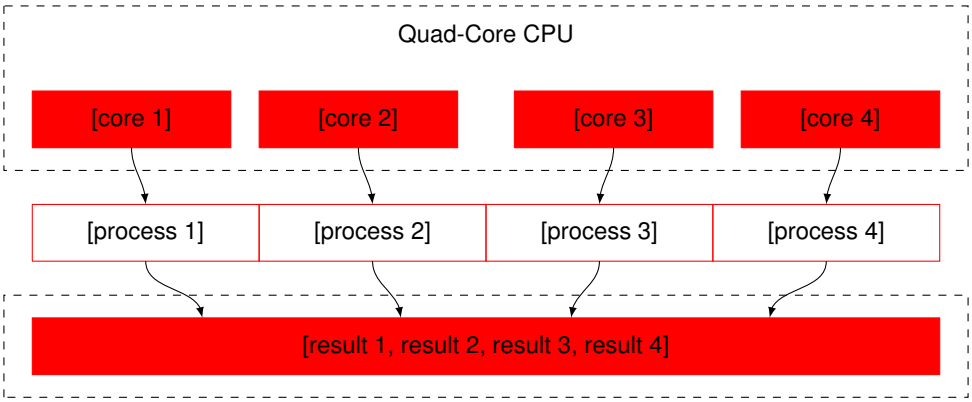

Figure A.7: Illustration of parallel processing.

The *pool.apply* and *pool.map* lock the main program until a process is finished, which is useful if results are to be obtained in a particular order for a certain application. The *async* variants submit all processes at once and retrieve the results as soon as they are finished, which is useful if results of the finished process are to be returned immediately.

Appendix B

WRSM and WRIM motor model approach

This chapter in Appendix B gives more details of the concepts illustrated in Chapter 3. The details include m400-50Aa lamination steel data, core loss equation constants calculations, IHFEM geometry creation and soft starting techniques of induction motors to improve torque quality. The important literature for the subject matter is also cited.

B.1. Lamination steel data

Figure B.1 and Table B.1 show the m400 50a lamination material information given from the manufacturer.

B.2. Core loss equation constants calculation

Core loss equation constants are calculated to present the relationship between the total loss versus the flux density of frequency. Manufacturers of core materials always provide curves of total loss versus flux density or frequency as in Section B.1, instead of giving the core loss equations constants. To extract these constants, there are various numerical approaches which have been used [**?**, 5, 30, 39, 43, 103, 114, 119]. Be that as it may, there are always contradictions between the measured and calculated losses due to lack of the formulation of numerical approaches. Consequently, numerical formulation of core loss is still an on-going examination.

Genetic optimisation algorithms which utilise digital computing to find and solve problems, have

Table B.1: IRON DATA ESTIMATED BY EMETOR

manufacturer	Surahammars Bruk
material	sura m400-50a
frequency	50 Hz
density	7 600 kg/m^3
stacking factor	0.96
lamination thickness	0.5 mm
resistivity	4.2(10)^7 Ω/m

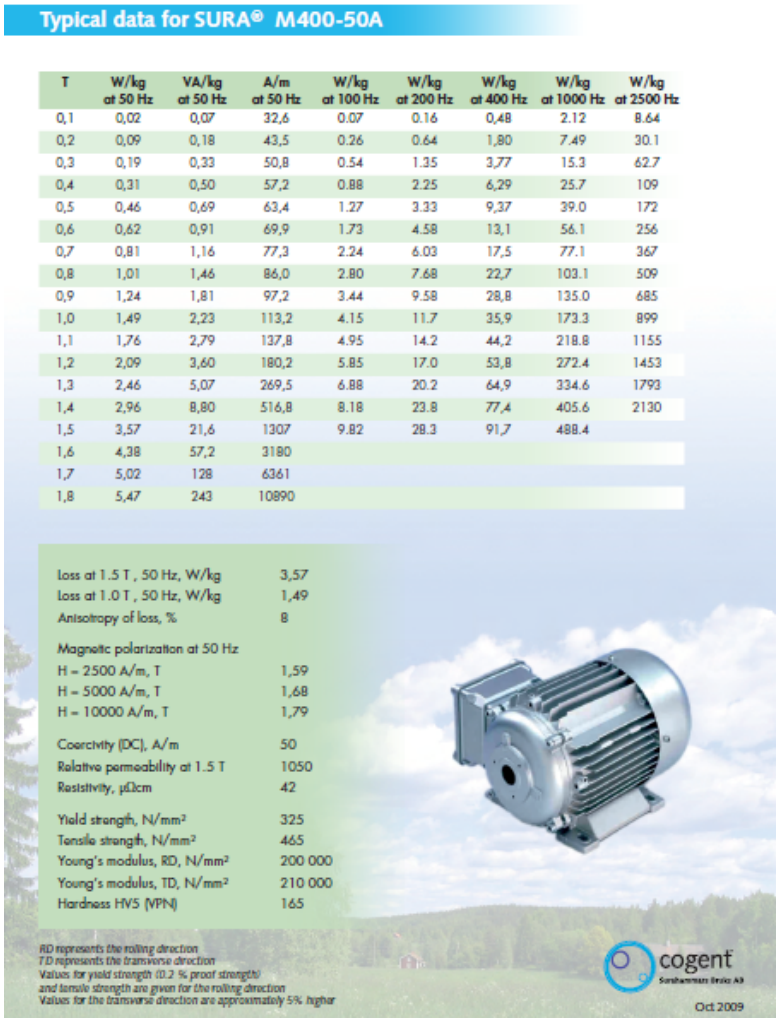

Typical data for SURA® M400-50A

T	W/kg at 50 Hz	VA/kg at 50 Hz	A/m at 50 Hz	W/kg at 100 Hz	W/kg at 200 Hz	W/kg at 400 Hz	W/kg at 1000 Hz	W/kg at 2500 Hz
0,1	0,02	0,07	32,6	0.07	0.16	0,48	2.12	8.64
0,2	0,09	0,18	43,5	0.26	0.64	1,80	7.49	30.1
0,3	0,19	0,33	50,8	0.54	1.35	3,77	15.3	62.7
0,4	0,31	0,50	57,2	0.88	2.25	6,29	25.7	109
0,5	0,46	0,69	63,4	1.27	3.33	9,37	39.0	172
0,6	0,62	0,91	69,9	1.73	4.58	13,1	56.1	256
0,7	0,81	1,16	77,3	2.24	6.03	17,5	77.1	367
0,8	1,01	1,46	86,0	2.80	7.68	22,7	103.1	509
0,9	1,24	1,81	97,2	3.44	9.58	28,8	135.0	685
1,0	1,49	2,23	113,2	4.15	11.7	35,9	173.3	899
1,1	1,76	2,79	137,8	4.95	14.2	44,2	218.8	1155
1,2	2,09	3,60	180,2	5.85	17.0	53,8	272.4	1453
1,3	2,46	5,07	269,5	6.88	20.2	64,9	334.6	1793
1,4	2,96	8,80	516,8	8.18	23.8	77,4	405.6	2130
1,5	3,57	21,6	1307	9.82	28.3	91,7	488.4	
1,6	4,38	57,2	3180					
1,7	5,02	128	6361					
1,8	5,47	243	10890					

Loss at 1.5 T , 50 Hz, W/kg	3,57
Loss at 1.0 T , 50 Hz, W/kg	1,49
Anisotropy of loss, %	8
Magnetic polarization at 50 Hz	
H = 2500 A/m, T	1,59
H = 5000 A/m, T	1,68
H = 10000 A/m, T	1,79
Coercivity (DC), A/m	50
Relative permeability at 1.5 T	1050
Resistivity, μΩcm	42
Yield strength, N/mm²	325
Tensile strength, N/mm²	465
Young's modulus, RD, N/mm²	200 000
Young's modulus, TD, N/mm²	210 000
Hardness HV5 (VPN)	165

RD represents the rolling direction
TD represents the transverse direction
Values for yield strength (0.2 % proof strength) and tensile strength are given for the rolling direction
Values for the transverse direction are approximately 5% higher

cogent
Oct 2009

Figure B.1: WRSM and WRIM lamination iron data.

been used to improve system performance and help to accomplish a period arranged objective. The algorithms generate new solutions in the search space by applying operators to current solutions and statistically moving towards more optimal regions of the search space. The algorithms rely on intelligent search of large but finite solution space using statistical methods. Additionally, the algorithms do not require taking objective derivatives and can thus deal with discrete variables and non-continuous objective functions [51].

Here, the NSGA-II genetic algorithm utilised in Chapter 5 is used to determine the core loss constants of the M400-50A steel lamination of Fig. B.1 at 50 Hz. Thus, to accurately reflect the core loss data provided by the manufacturer, c, x and y of (3.44) must be optimised to reduce errors. To implement the latter using the genetic algorithm, the power loss equation of (3.44) is modified as the core loss density given by

$$p_v = m f^n B^o, \tag{B.1}$$

where m is a variable coefficient of c and n, and o are frequency and flux density exponential variables of x and y, respectively.

Table B.2: NSGA-II SETUP PARAMETERS FOR CORE LOSS EQUATION CONSTANTS

parameter	symbol	value
crossover and mutation probabilities	p_c, p_m	0.95, 0.33
crossover and mutation distribution index	n_c, n_m	20, 20
Population and iterations	N, G	8, 600

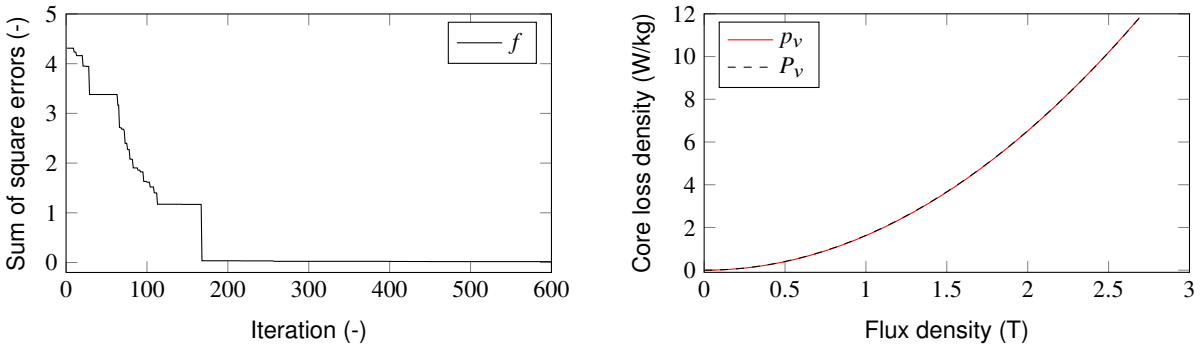

(a) **(b)**

Figure B.2: Obtained (a) the NSGA-II convergence and (b) loss curves at 50 Hz.

Following Section 5.5, the normalised design variables of (B.1) are defined by

$$\begin{bmatrix} x_1 \\ x_2 \\ x_3 \end{bmatrix} = \begin{bmatrix} m \\ n \\ o \end{bmatrix}. \tag{B.2}$$

The aim is to reduce deviation between manufacturer data and estimation loss curves, thus the objective function following Section 5.5 is defined by

$$f = \sum_i [P_{vz} - (m_z f_z^n B_z^o)]^2. \tag{B.3}$$

Equation (B.3) is the core loss sum square error function to be minimised where P_{vz} $m_z f_z^n B_z^o$ is the z^{th} point on the manufacturer and estimated density loss curve. From (B.2), the core loss equation constants are obtained by

$$\begin{cases} c = mN_c \\ x = nN_x \\ y = oN_y, \end{cases} \tag{B.4}$$

where N_c, N_x and N_y are normalising factors of c, x and y respectively. Figure B.2 shows the obtained results with NSGA-II parameters shown in Table B.2 using m400-50a steel loss curve. The obtained core loss constants are

$$\begin{cases} c = 0.017997 \\ x = 0.150467 \\ y = 2.007, \end{cases} \tag{B.5}$$

which are constants estimated as in [83]. It can be noticed in results of Fig: B.2(b) that (B.1) defined

by the obtained constants fits well within the manufacturer data.

B.3. IHFEM software package

The IHFEM is an open source FE software package which can simulate magneto static, electrostatic and current flow problems [46, 106]. The most important components of the IHFEM package for this study are

- libSEMFEM :
  - which is the primary library containing all functions of the IHFEM. The library is written in $Fortran$ and C and utilises $OpenMP$ to execute some functions in parallel,
- semfem.py :
  - file used as a Python interface for calling functions from the $Fortran/C$ libSEMFEM and
- fl2 :
  - utilised as a graphical viewer for reviewing drawing and mesh.

B.4. IHFEM problem domain geometry creation

The problem domain geometry creation (i.e. stator, rotor, air-gap) using FEM is performed during the computer-aided analysis. The problem domain is first converted into a geometric represented by a collection of elements of lines and arcs. This step is easily done using the IHFEM components given in Section B.3. During this step, simulation time can be reduced by employing symmetry on the geometry and modelling in 2D. In the second step, the material properties are then assigned to the model followed by the problem boundaries and loading points. Lastly, the problem domain geometry created is discretised into finite elements (mesh) in which the solution can be approximated in each element as explained in Appendix A.4. The used triangular mesh elements accuracy depends on how fine they are. The drawback is finer elements increase computational time for the solution of the defined problem.

Figures B.3 and B.4 show the main points applied in the problem domain geometry creation using the above mentioned steps. In this study, the stack volume of the motor is fixed, hence, the main dimensions are taken as the stator outer diameter D_s, rotor inner diameter d_r and the stack length l. The stator and rotor problem domains are divided into a number of sections equal to half teeth pitch given by the angles ζ_s, ζ_r as

$$\begin{cases} \zeta_s = \dfrac{\pi}{Q_s} \\ \zeta_r = \dfrac{\pi}{Q_r}, \end{cases} \tag{B.6}$$

where Q_s and Q_r denotes stator and rotor number of slots respectively. The half slot on both stator and rotor are constructed, mirrored about the y-axis and then mirror rotated about the origin by the number equal to $\dfrac{Q_s}{2p}$ and $\dfrac{Q_r}{2p}$ for both stator and rotor because of symmetry. The slots are constructed using only five main points ($\vec{p}_{s1}$ to $\vec{p}_{s5}$ for stator Fig. B.3 and $\vec{p}_{r1}$ to $\vec{p}_{r5}$ for rotor Fig. B.4), with straight

Table B.3: STATOR CARTESIAN SLOT POINT VARIABLES

Point	x-axis coordinate	y-axis coordinate
Cartesian	x	y
$\vec{p}_{s1}$	$x_{s1} = 0.5b_{os}$	$y_{s1} = 0.5d_s \cos[\sin^{-1}(\frac{b_{os}}{d_s})]$
$\vec{p}_{s2}$	$x_{s2} = 0.5b_{os}$	$y_{s2} = 0.5(d_s + 2h_{os})$
$\vec{p}_{s3}$	$x_{s3} = 0.5b_{s1}$	$y_{s3} = 0.5[d_s + 2(h_{os} + h_{ws})]$
$\vec{p}_{s4}$	$x_{s4} = 0.5b_{s2}$	$y_{s4} = 0.5[d_s + 2(h_{os} + h_{ws} + h_s)]$
$\vec{p}_{s5}$	$x_{s5} = 0$	$y_{s5} = 0.5[d_s + 2(h_{os} + h_{ws} + h_s)]$

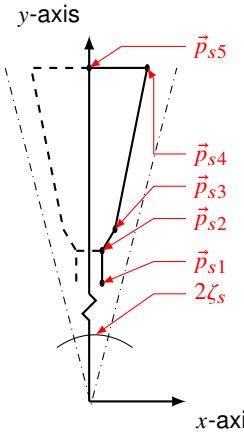

Figure B.3: Stator slot point geometry.

Table B.4: ROTOR CARTESIAN SLOT POINTS VARIABLES

Point	x-axis coordinate	y-axis coordinate
Cartesian	x	y
$\vec{p}_{r_1}$	$x_{r_1} = 0.5b_{or}$	$y_{r_1} = 0.5D_r \cos[\sin^{-1}(\frac{b_{or}}{D_r})]$
$\vec{p}_{r_2}$	$x_{r_2} = 0.5b_{or}$	$y_{r_2} = 0.5(D_r - 2h_{or})$
$\vec{p}_{r_3}$	$x_{r_3} = 0.5b_{r2}$	$y_{r_3} = 0.5[D_r - 2(h_{or} + h_{wr})]$
$\vec{p}_{r_4}$	$x_{r_4} = 0.5b_{r1}$	$y_{r_4} = 0.5(D_r - 2(h_{or} + h_{wr} + h_r)]$
$\vec{p}_{r_5}$	$x_{r_5} = 0$	$y_{r_5} = 0.5[D_r - b_{r1} - 2(h_{or} + h_{wr} + h_r)]$

$D_r = d_s - 2g$

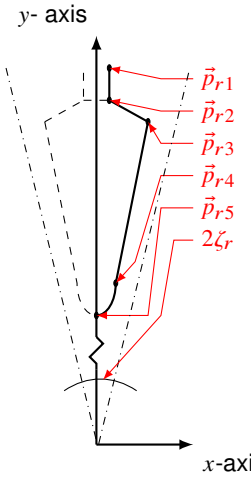

Figure B.4: Rotor slot point geometry.

lines and arcs applied in the construction. Tables B.3 and B.4 gives the stator and rotor Cartesian variable points for the IHFEM problem domain geometry creation respectively. Refer to Section B.3 for the IHFEM package components files.

B.5. Improving starting torque quality of a grid-connected WRIM

The work present here is a summary of the author work published in [86]. The start-up of the grid-connected WRIM results in huge transient torques [104]. To improve these transient torques, two controlled switching techniques, namely non-simultaneous stator controlled switching (NSS-CS) and simultaneous rotor controlled switching (SR-CS) are compared in the following sections with the conventional simultaneous-stator-controlled switching (SS-CS), i.e. grid-connected in terms of starting torque quality on a geared fan load system.

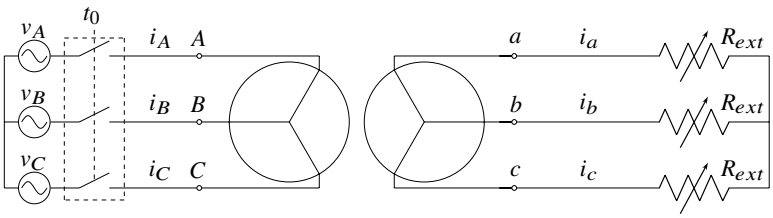

Figure B.5: Grid-connected WRIM SS-CS circuit diagram.

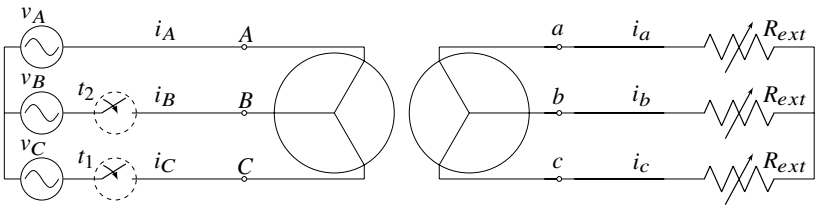

Figure B.6: Grid-connected WRIM NSS-CS circuit diagram.

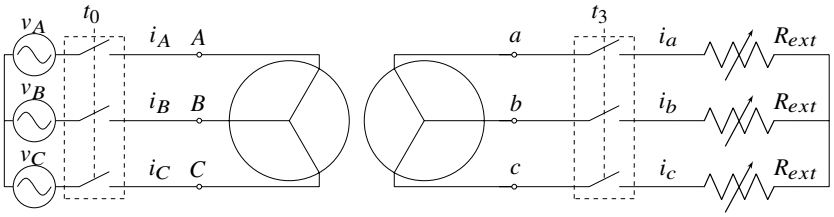

Figure B.7: Grid-connected WRIM SR-CS circuit diagram.

B.5.1. Controlled switching circuit diagrams

Three different switching techniques employed are shown in Figs. B.5-B.7. Figure B.5 shows the conventional starting SS-CS circuit diagram of the grid-connected WRIM. In this switching, the supply is switched on simultaneously to all the stator terminals at time t_0. Figure B.6 shows the proposed system of [18] for NSS-CS of a star connected grid-connected WRIM to reduce starting transient torques. In the switching sequence, phase A of the motor is always connected to the supply. The first switching is done by connecting phase A and C of the motor to the supply at time t_1. The second switching is done by considering a certain delay before connecting phase B of the motor to the supply at time t_2. The switching times are precise and therefore thyristors must be used. This technique can also be used for cage-rotor induction motors. Figure B.7 shows a proposed system for SR-CS to improve the starting transient torques of the grid-connected WRIM. In this switching sequence, the stator phases are switched on simultaneously to the motor at a time t_0. The rotor phases, however, are at first open-circuited for a considerable time before they are short-circuited at time t_3.

B.5.2. MATLAB-Simulink results

Figure B.8 shows the quality of torque versus time and speed for the three controlled switching techniques discussed above. SR-CS torque plot is shifted to the left by 0.285 s for comparison reasons.

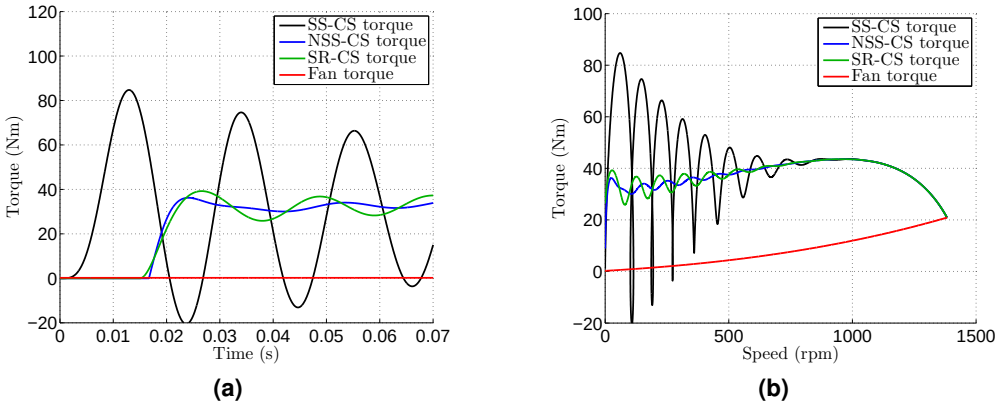

Figure B.8: Grid-connected WRIM (a) transient torque versus time and (b) induced torque versus speed of the three controlled switching techniques.

B.5.3. Conclusions drawn

Proof for the stability in the starting torque when using the NSS-CS and SR-CS methods is shown in Fig. B.8(a). Furthermore, Fig. B.8(b) shows that large torque oscillations continue up to a motor speed of 750 rpm when using the SS-CS method. The results of Fig. B.8 highlight what enormous peak torques, and also sometimes negative peak torques, are seen by the gearbox of a geared-fan load when using the conventional dol switching of all phases.

The presented work in which two controlled switching techniques NSS-CS and SR-CS are compared with the conventional SS-CS (dol start) in terms of starting torque quality is essential for geared loads. Although not all starting torque oscillations are eliminated, it is shown that the two controlled switching methods greatly improve the starting torque quality of the motor. Since the implementation of the NSS-CS is not easy, because it requires fast and accurate switching, the SR-CS can be concluded to be the best option because it is simple and uses normal mechanical switchgear. Care, however, should be taken with the SR-CS that the induced open circuit rotor voltage, when the stator is on, is within rated values.

Appendix C

WRSM and WRIM motor types manufacturing and laboratory measurements

This chapter in Appendix C gives more details of the concepts illustrated in Chapter 6. The details include the winding configurations and mechanical drawings of the prototyped WRSM and WRIM motor types.

C.1. Distributed winding configuration

In the distributed winding configuration, conductors are placed in several slots under a single pole as shown in Fig. C.1 for the three-phase two pole pair motor. This is to obtain a smooth sinusoidal

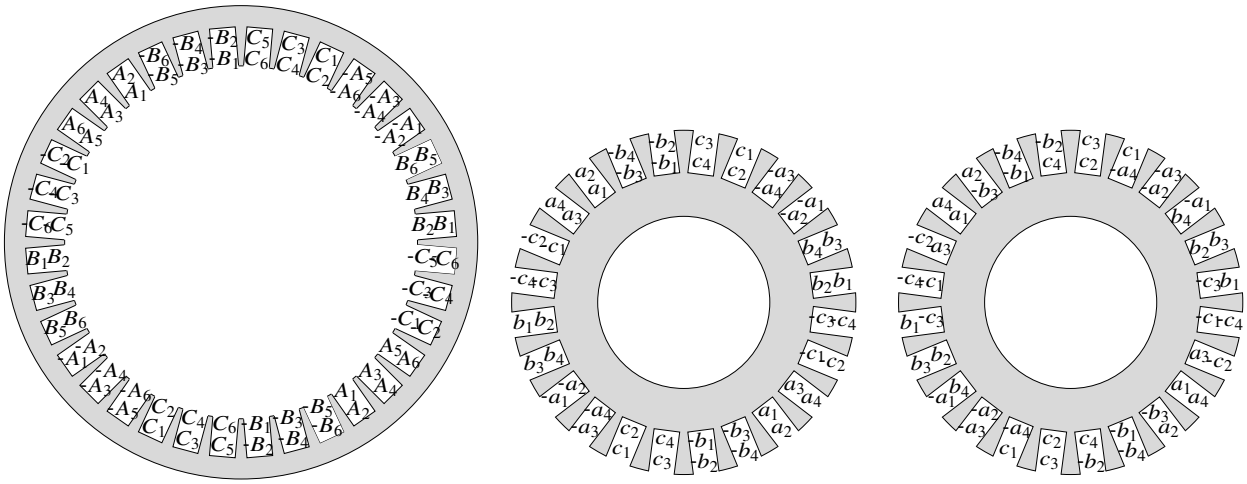

(a) stator full pitch winding **(b)** rotor full pitch winding **(c)** rotor short pitch winding

Figure C.1: Distributed four pole, three phase winding configuration.

electro magneto force emf. For simpler end connections and for a motor which is more economical to manufacture, the double layer winding is also adopted.

In the distributed winding configuration as shown in Fig. C.1(a) for the stator, one side of a coil in

a pole, for example A_1 is placed in the top of a slot and the other side, -A_1 in an adjacent pole placed in the bottom of another slot. All coil sides which are in adjacent slots and associated with same phase, e.g. A_1-A_3 and A_5 or A_2, A_4 and A_6, constitute phase belts which are the same for all phases. For the full pitch winding as in (a) and (b) of Fig. C.1, the individual coils span a full pole pitch ($180°$ electrical). The latter winding configuration is adopted for the stator and rotor of the WRSM. If all the coil sides in the bottom of the slots in the rotor are shifted counter-clockwise by one slot, any coil will span only $\frac{5}{6}$ of the pole pitch. This is illustrated in (c) of Fig. C.1 and adopted for the rotor of the WRIM.

C.2. Mechanical drawings

The author gives acknowledgement to Kenan Cloete (email: `kenan@sun.ac.za`) for all the mechanical drawings given in this section. Figures C.2-C.5 show the mechanical drawings used in the prototyping of both the WRSM and WRIM motor types. Please refer to the next pages for the mechanical drawings.

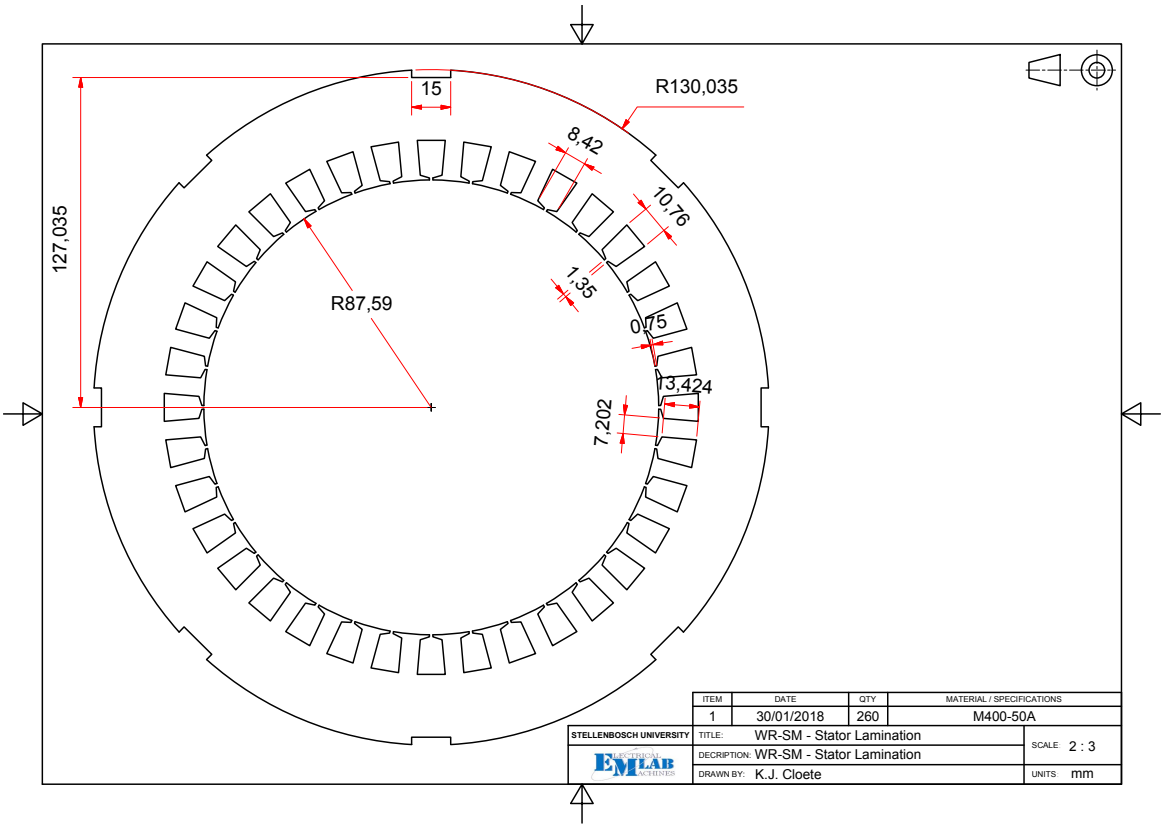

(a) WRSM stator lamininationcutting

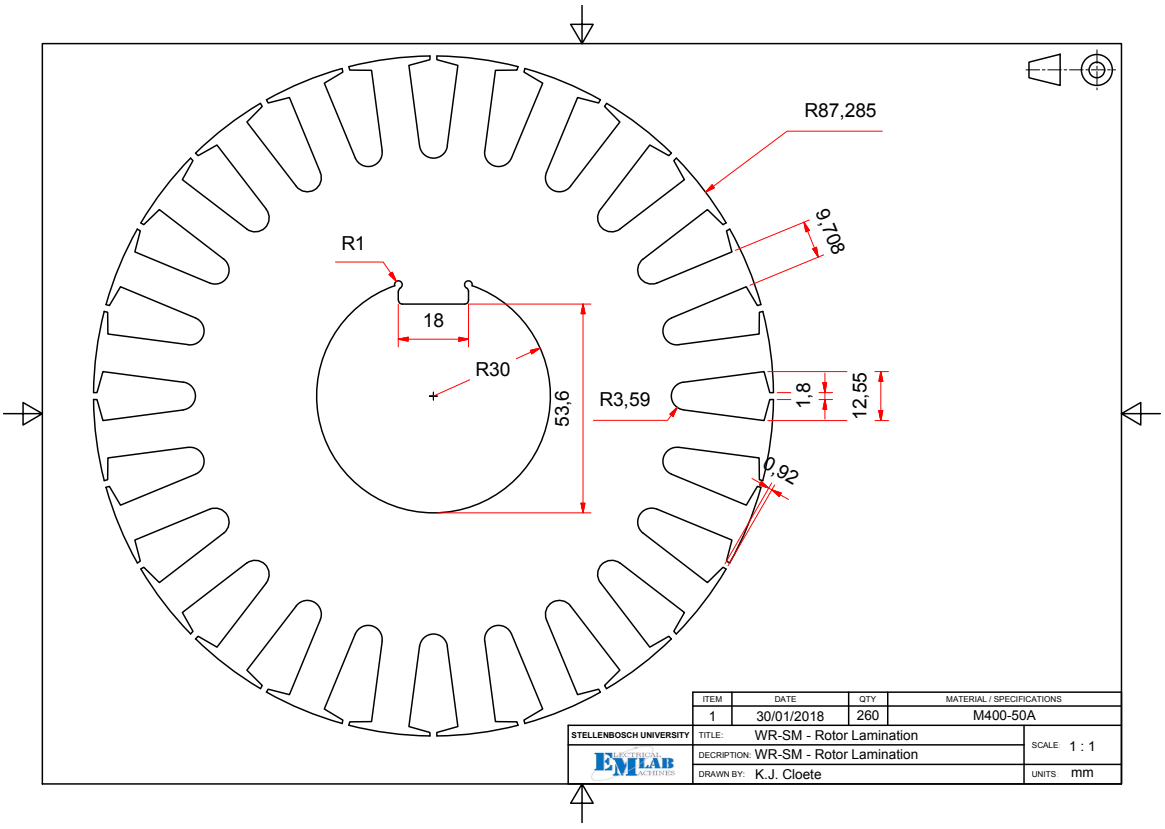

(b) WRSM rotor lamininationcutting

Figure C.2: Prototyped WRSM (a) stator and (b) rotor lamination cuttings.

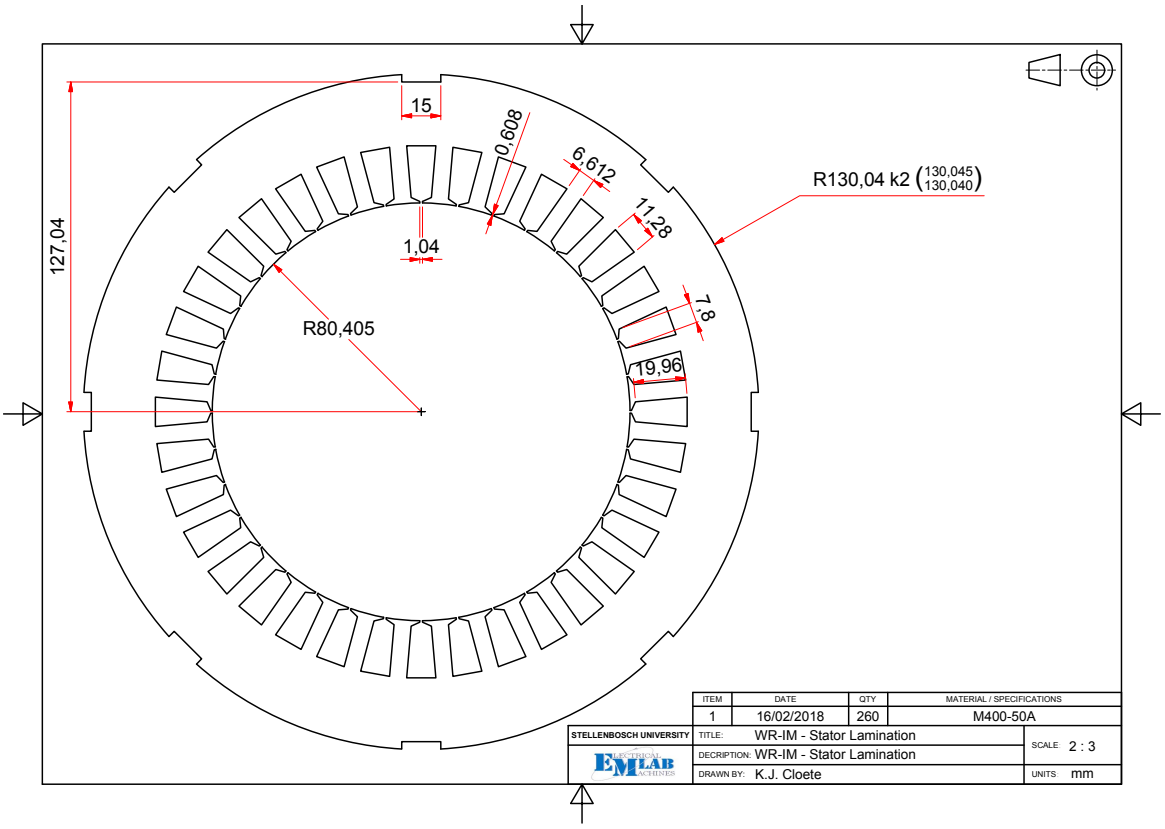

(a) WRIM stator laminination cutting

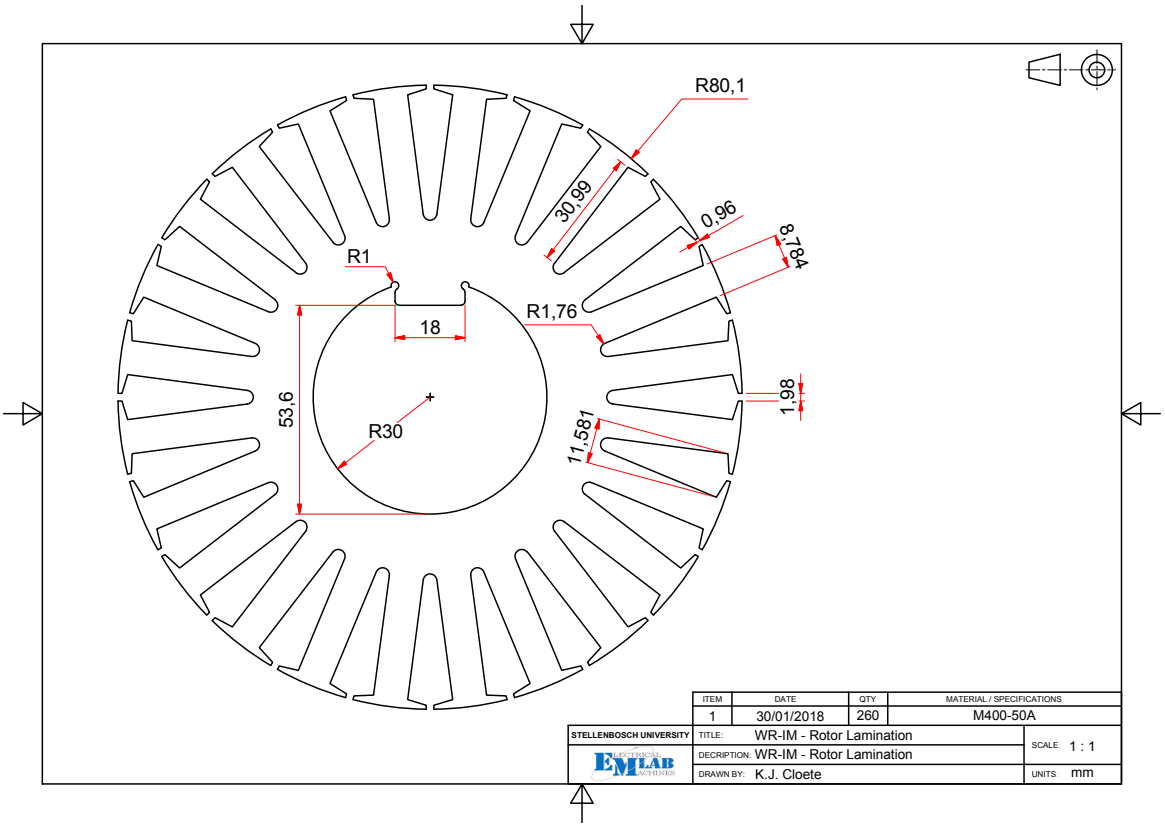

(b) WRIM rotor laminination cutting

Figure C.3: Prototyped WRIM (a) stator and (b) rotor lamination cuttings.

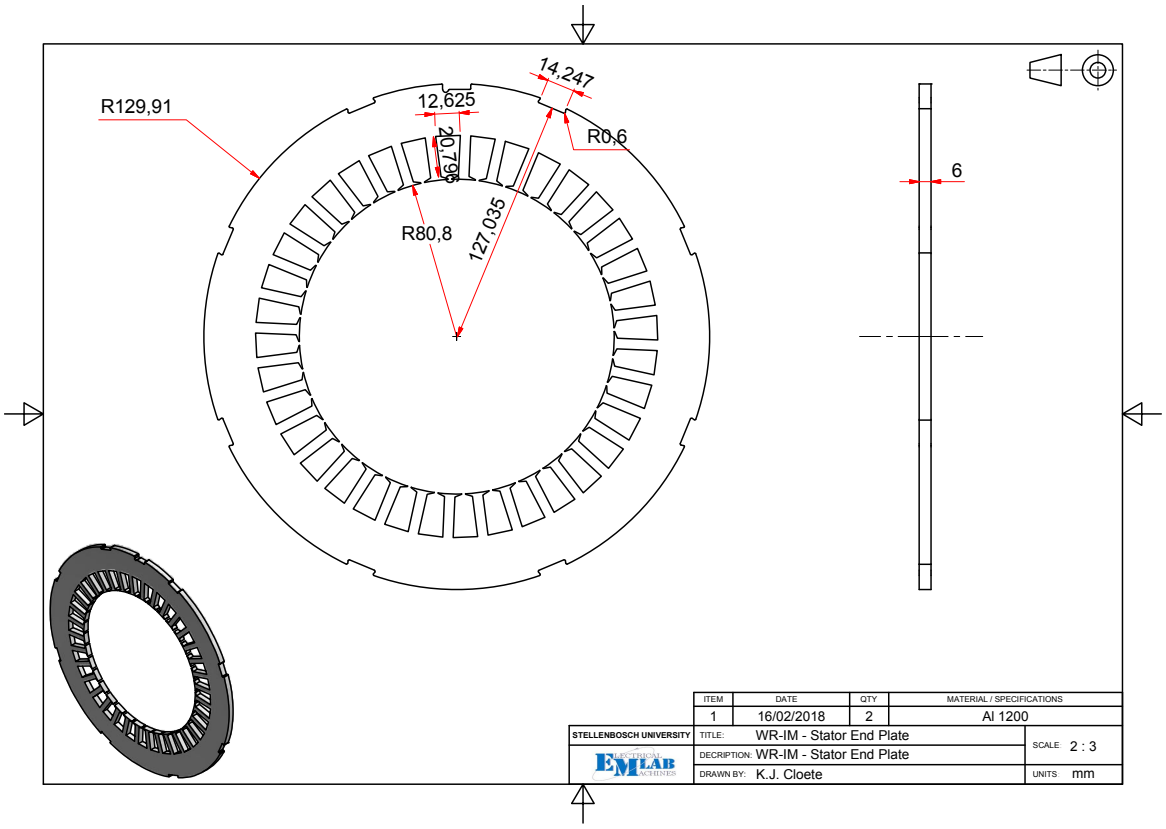

(a) WRIM Stator end ring

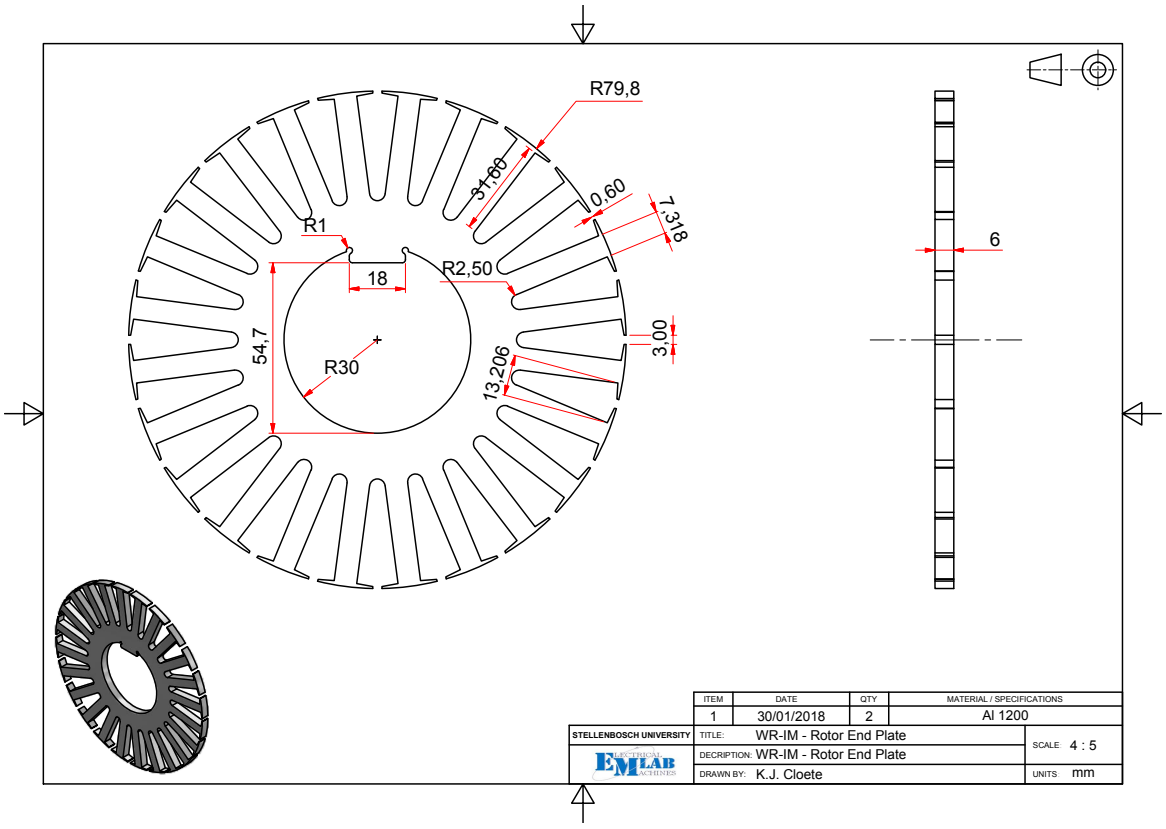

(b) WRIM rotor end-ring

Figure C.4: Prototyped WRIM (a) stator and (b) rotor end-rings.

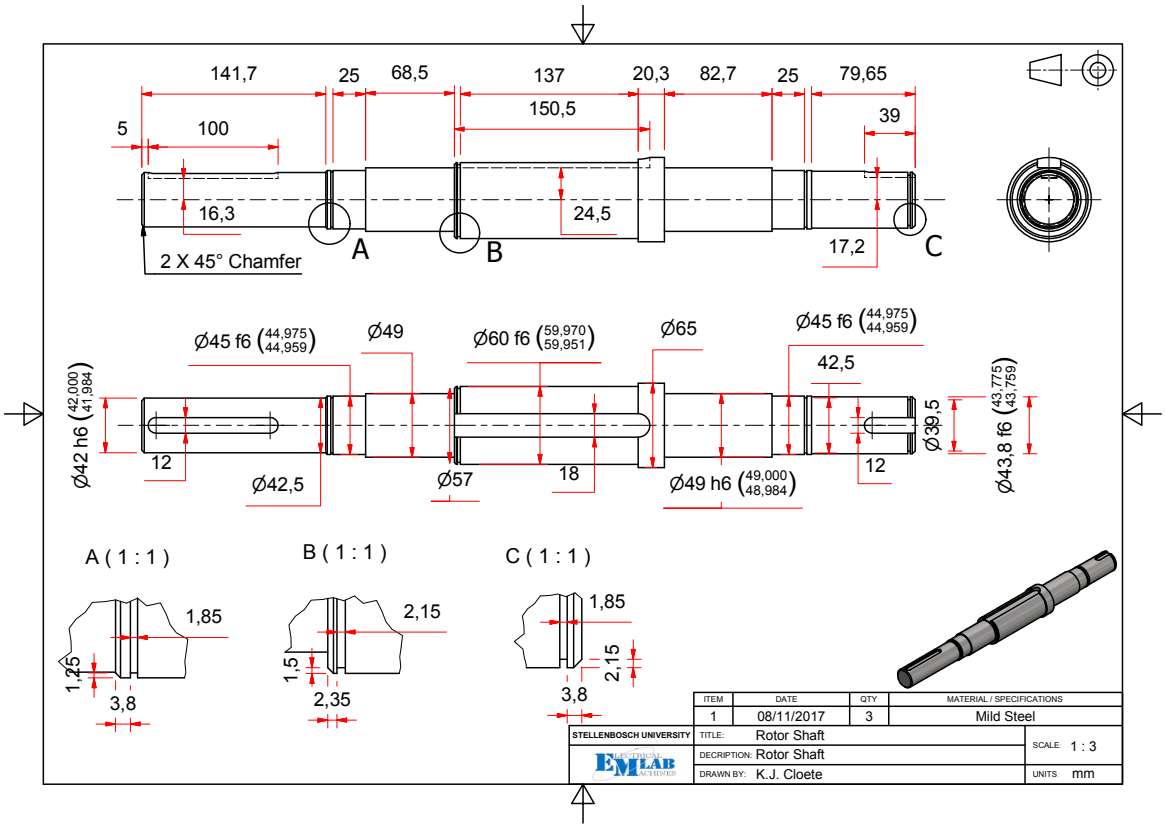

(a) shaft

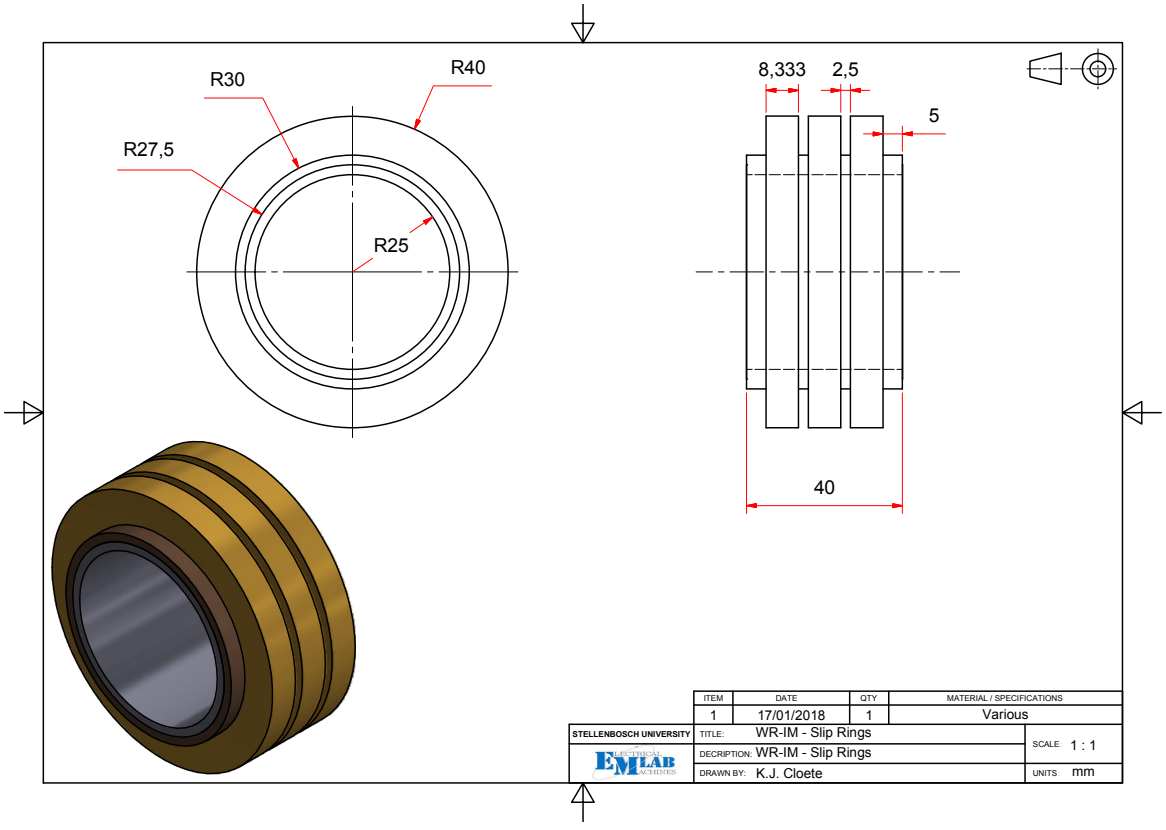

(b) slip rings

Figure C.5: Prototyped (a) shaft and (b) slip rings.

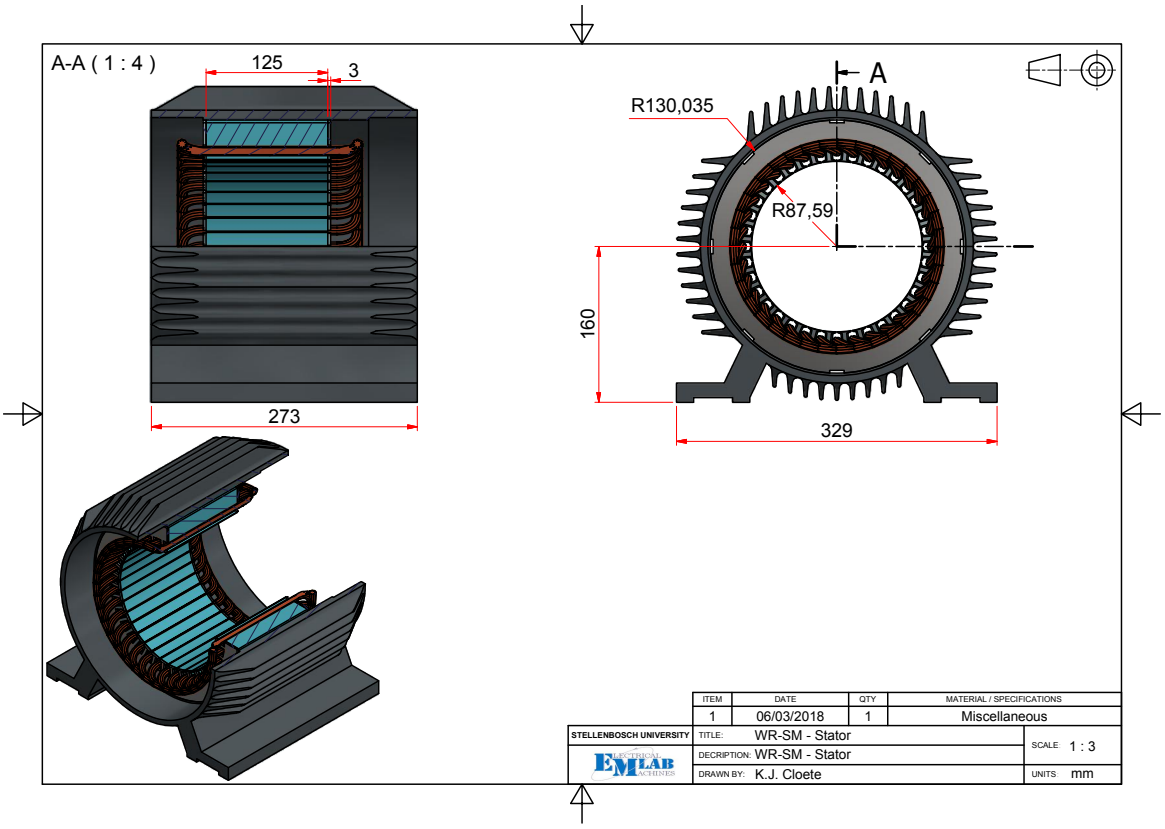

(a) WRIM stator assembly

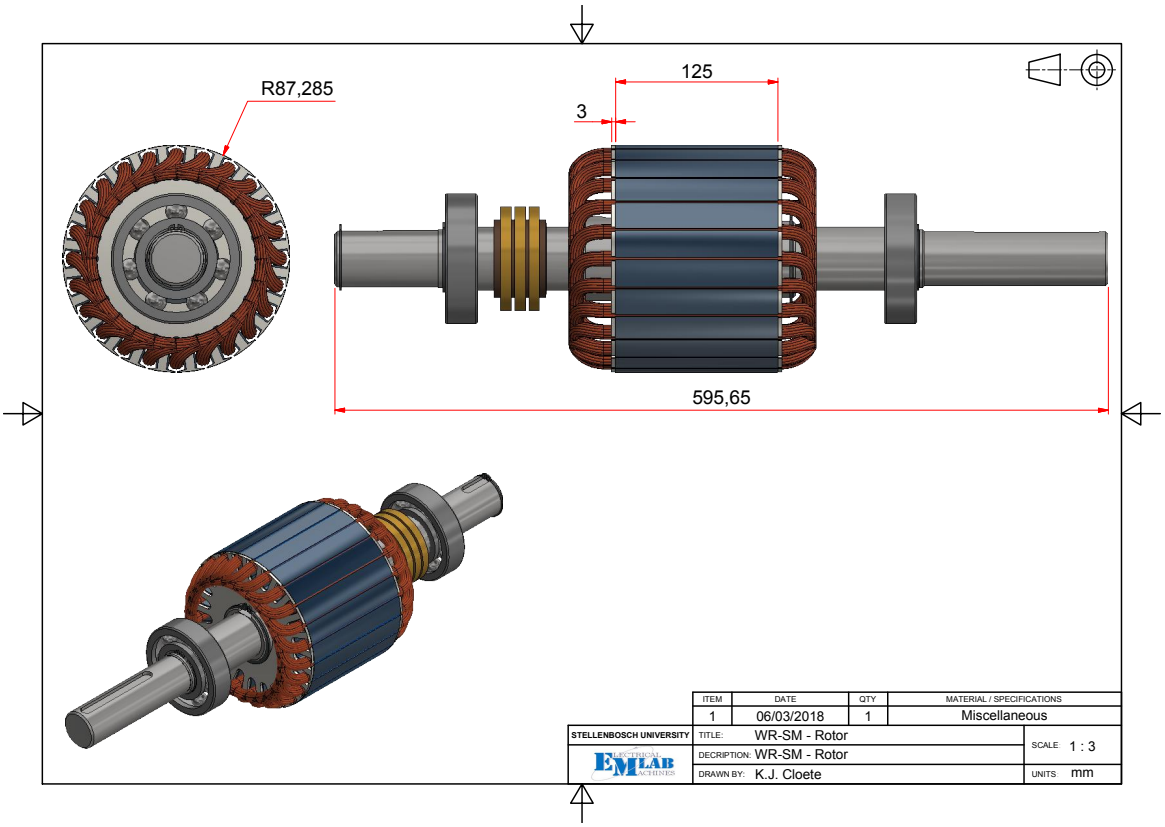

(b) WRSM rotor rotor assembly

Figure C.6: Prototyped WRSM (a) stator and (b) rotor assembly.

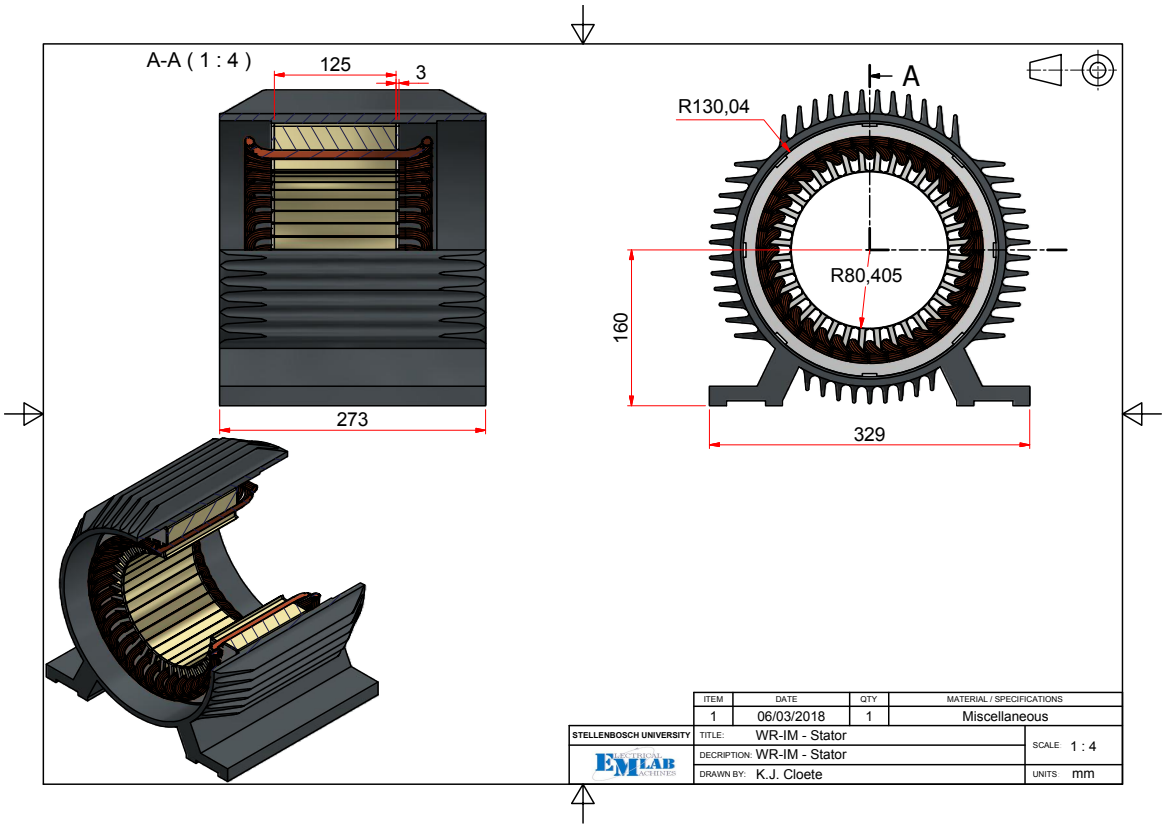

(a) WRIM stator assembly

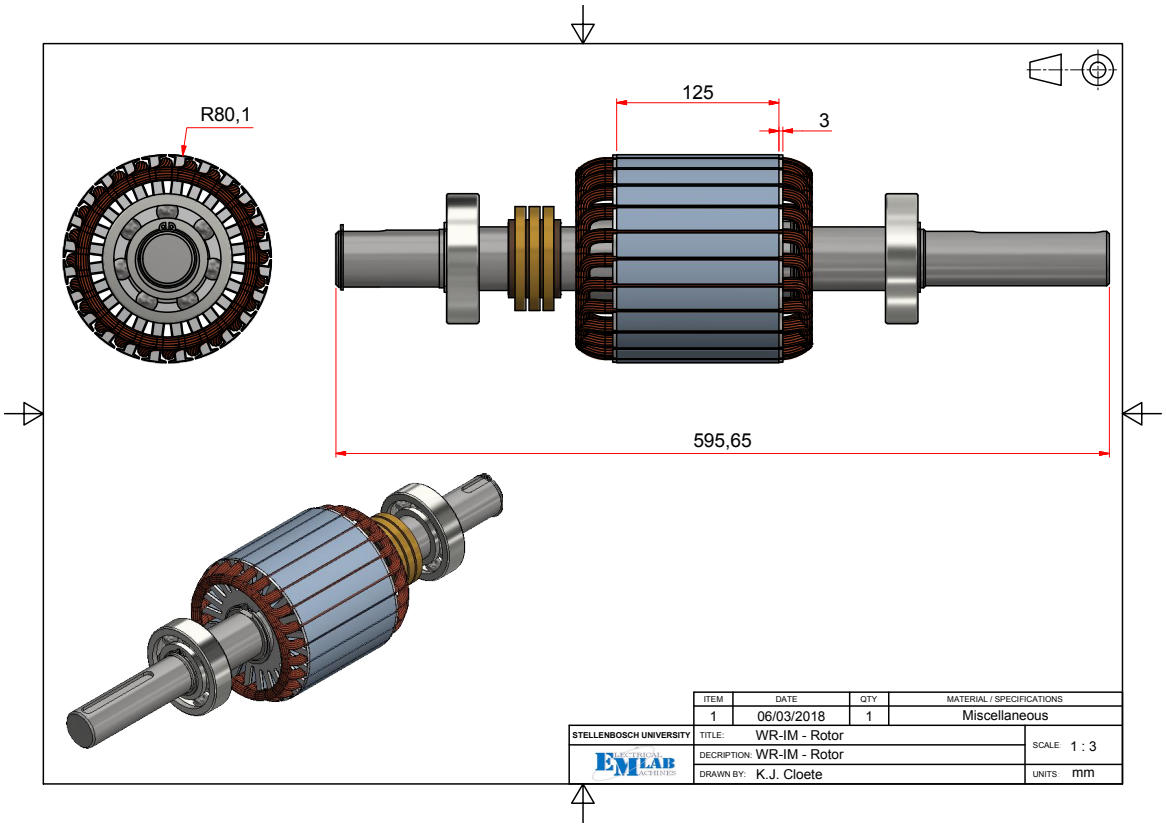

(b) WRIM rotor rotor assembly

Figure C.7: Prototyped WRIM (a) stator and (b) rotor assembly.